PACIFIC EARTHQUAKE ENGINEERING RESEARCH CENTER

# Earthquake Engineering for Resilient Communities: 2012 PEER Internship Program Research Report Collection


Heidi Tremayne, Editor
Stephen A. Mahin, Editor
Collin Anderson
Dustin Cook
Michael Erceg
Carlos Esparza
Jose Jimenez
Dorian Krausz
Andrew Lo
Stephanie Lopez Cruz
Nicole McCurdy
Paul Shipman
Alexander Sturm
Eduardo Vega



PEER 2012/07
DECEMBER 2012

# Earthquake Engineering for Resilient Communities:

# 2012 PEER Internship Program Research Report Collection


**HEIDI TREMAYNE, EDITOR**

**STEPHEN A. MAHIN, EDITOR**

**COLLIN ANDERSON**

**DUSTIN COOK**

**MICHAEL ERCEG**

**CARLOS ESPARZA**

**JOSE JIMENEZ**

**DORIAN KRAUSZ**

**ANDREW LO**

**STEPHANIE LOPEZ CRUZ**

**NICOLE MCCURDY**

**PAUL SHIPMAN**

**ALEXANDER STURM**

**EDUARDO VEGA**



PEER Report 2012/07
Pacific Earthquake Engineering Research Center
Headquarters at the University of California, Berkeley

December 2012

# CONTENTS

# Introduction

Recent earthquakes in the United States and around the world have repeatedly shown that earthquake resilience is essential to building and sustaining urban communities. Earthquake resilience will play an increasingly important role in the professions associated with earthquake hazard mitigation, thus there is a need to educate the next generation of these professionals. To address this need, the Pacific Earthquake Engineering Research Center (PEER) coordinates a summer internship program for undergraduate students that focuses on the theme of earthquake-resilient communities. With funding from the National Science Foundation (NSF), twelve interns from a variety of backgrounds and universities participated in the 2012 program.

Achieving earthquake-resilient communities is a challenge that requires the interaction of many disciplines from engineering to public policy. To show the importance of multidisciplinary cooperation and collaboration, PEER assigns participating undergraduate interns with a project in one of the following disciplines: structural engineering, geotechnical engineering, risk analysis, urban planning, or public policy. The interns are then assigned faculty and graduate student mentors who help them complete a unique research project at one of the three partnering research sites: University of California Davis, University of Washington, and University of California Berkeley.

In 2012, the participating students (listed in alphabetical order with their home university) were:

- Collin Anderson, University of California, Davis
- Dustin Cook, California State University, Chico
- Michael Erceg, Widener University
- Carlos Esparza, University of Texas at Arlington
- Jose Jimenez, University of California, Irvine
- Dorian Krausz, University of California, Los Angeles
- Andrew Lo, Rice University
- Stephanie Lopez Cruz, University of Puerto Rico at Mayaguez
- Nicole McCurdy, University of California, Davis
- Paul Shipman, California State University Sacramento
- Alexander Sturm, University of California, Davis
- Eduardo Vega, Cal Poly Pomona

Many faculty and graduate student mentors made this program a success for the interns, and PEER extends its sincere thanks to the participating mentors listed below:

- Jay Lund, University of California, Davis
- Jason DeJong, University of California, Davis
- Ross Boulanger, University of California, Davis
- Steve Kramer, University of Washington
- Marc Eberhard, University of Washington
- John Stanton, University of Washington
- Jeffrey Berman, University of Washington
- Jack Moehle, University of California, Berkeley
- Stephen Mahin, University of California, Berkeley
- Nathan Burley, University of California, Davis
- Adam Price, University of California, Davis
- Samuel Sideras, University of Washington
- Olafur Haraldsson, University of Washington
- Jonathan Weigand, University of Washington
- Duy Vu To, University of California, Berkeley
- Vesna Terzic, University of California, Berkeley

During the ten-week summer research experience, each intern conducted a research project while also regularly engaging with the full intern cohort during weekly web-meetings to discuss and learn how each of their projects related to earthquake resiliency. Students learned how to conduct independent research and how to participate effectively as a member of a research team. Supplemental activities, including a two-day orientation program with multiple skill-building workshops and participation in a research poster session at the 2012 PEER Annual Meeting, were conducted to broaden the intern experience and inspire them to make future contributions to the field of earthquake engineering and related research.

As a final research deliverable, each intern was required to prepare a final research report. This PEER report, "Earthquake Engineering for Resilient Communities: 2012 PEER Internship Program Research Report Collection" is a compilation of the final research papers written by the 2012 interns. These reports follow this Introduction. A list of the institutions, projects, interns, and mentors is listed below:

**University of California, Berkeley**

- "Ductility of Reinforced Concrete Shear Wall Boundary Elements in Compression" was completed by intern Dustin Cook under the supervision of the following mentors: Professor Jack Moehle and Duy Vu To.

- “Exploring Behavior of Thin Shear Wall Boundary Elements in Compression” was completed by intern Andrew Lo under the supervision of the following mentors: Professor Jack Moehle and Duy Vu To.
- “The Seismic Performance Observatory” was completed by intern Dorian Krausz under the supervision of the following mentors: Professor Stephen Mahin and Dr. Vesna Terzic.
- “Maximizing Learning from Real Earthquakes” was completed by intern Eduardo Vega under the supervision of the following mentors: Professor Stephen Mahin and Dr. Vesna Terzic.

**University of California, Davis**

- “Stimulating *In Situ* Soil Bacteria for Bio-Cementation of Sands” was completed by intern Collin Anderson under the supervision of the following mentor: Professors Jason DeJong.
- “The Effect of Plasticity on Intermediate Soil Compressibility” was completed by intern Nicole McCurdy under the supervision of the following mentors: Professors Jason DeJong and Ross Boulanger, and Adam Price.
- “Risk-Based Levee System Analysis with Multiple Failure Modes” was completed by intern Paul Shipman under the supervision of the following mentors: Professor Jay Lund and Nathan Burley.
- “Multi-Mode Probability of Levee Failure Curves” was completed by intern Alexander Sturm under the supervision of the following mentors: Professor Jay Lund and Nathan Burley.

**University of Washington**

- “Exploration of Earthquake Intensity Measure Relationships with Pore Pressure and Liquefaction” was completed by intern Michael Erceg under the supervision of the following mentors: Professor Steve Kramer and Samuel Sideras.
- “Stainless Steel Reinforcement in Unbonded, Pre-Tensioned Bridge Bent System” was completed by intern Carlos Esparza under the supervision of the following mentors: Professors Marc Eberhard and John Stanton, and Olafur Haraldsson.
- “Bond Capacity of Steel Epoxy-Coated and Uncoated Pre-Stressing Strands” was completed by intern Jose Jimenez under the supervision of the following mentors: Professors Marc Eberhard and John Stanton, and Olafur Haraldsson.
- “Testing the Integrity of Steel Gravity Frames subjected to large Vertical Deflections: Connection Component and Bolt Tests” was completed by intern Stephanie Lopez Cruz under the supervision of the following mentors: Professor Jeffrey Berman and Jonathan Weigand.

Funding for the 2012 PEER Internship Program is provided by the National Science Foundation under Grant No. EEC-1063138, as a part of NSF’s Research Experiences for Undergraduate (REU) Program. Any opinions, findings and conclusions or recommendations expressed in this material are those of the author(s) and do not necessarily reflect the views of the National Science Foundation (NSF) or the Pacific Earthquake Engineering Research Center (PEER). For more information about the 2012 PEER Internship Program, visit: *http://peer.berkeley.edu/education/summer_internship_program2012.html*

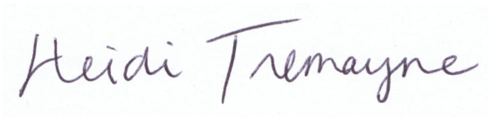


Heidi Tremayne
Outreach Director, PEER
PEER REU Coordinator

Stephen A. Mahin
Director, PEER
PEER REU Principal Investigator (PI)

# 1. Ductility of Reinforced Concrete Shear Wall Boundary Elements in Compression

## DUSTIN COOK

### ABSTRACT

As a result of the poor performance of shear walls in the 2010 Chile earthquake, questions have been raised about the performance of reinforced concrete boundary elements designed to current ACI standards. Testing done in 2010 showed that the current standards for special reinforced concrete boundary elements produced specimens that had non-ductile failure under pure compressive loading. This report suggests two strategies to improve the compressive ductility of these boundary elements: tighter spacing of the transverse reinforcement and an increased overall thickness of the shear wall boundary element. Four full-scale reinforced concrete shear wall boundary element specimens were constructed and tested under a compressive load. After testing it was found that neither increased specimen width or tighter transverse reinforcement spacing increased the ductility of the boundary elements. Further research and testing is required to devise a method that effectively increases the ductility of reinforced concrete shear walls.

### 1.1 INTRODUCTION

The main purpose of this research is to examine the compressive ductility of the boundary elements of a reinforced concrete (RC) shear wall. Damage sustained by RC bearing wall buildings during the 2010 Chilean earthquake raised questions regarding shear wall boundary elements. Structures in that earthquake experienced wide spread compressive damage and buckling of the shear wall boundary elements due to slender walls and lack of transverse reinforcement. This test described herein examined the effects of shear wall slenderness and transverse reinforcement spacing on the overall strength, ability to buckle and ductility of shear wall boundary elements in compression. This test was not an attempt to replicate conditions or code requirements in the 2010 Chile earthquake. Instead, it was based on the construction and design of the shear wall specimens in compliance with the ACI code *Building Code Requirements for Structural Concrete and Commentary* [2008].

The objectives of this research were reached through construction and testing of four RC shear wall boundary element specimens. The specimens were constructed in Davis Hall at the University of California, Berkeley (UCB), under the oversight of Professor Jack Moehle, and then tested at the Richmond Field Station in the 4-million-pound-capacity universal testing machine. The specimens were instrumented in order to measure buckling and deformation so that a stress-strain relationship could be plotted to quantify ductility. Ductility was measured by how well the specimen strain hardens once it began to fail. The current code intends for shear walls to be ductile and gain strength after yielding. This research was conducted to determine if in fact the shear wall design meets the code's intent. Most previous testing has been conducted on column specimens and not on slender shear walls. The results from this research will provide new and insightful information on performance of shear wall design and capacity.

## 1.2 BACKGROUND

In order to more fully understand the questions posed herein, several background topics must be explored. First, what exactly happened in the 2010 Chilean earthquake, and how does that lead into the study of shear wall boundary elements? Second, how do shear walls work? What are their boundary elements and what does ACI 318 require? Lastly, review of previous testing for similar specimens in order to gain fundament knowledge was conducted.

### 1.2.1 2010 Chilean Earthquake

On 27 February 2010 at 3:34 AM, a moment magnitude 8.8 earthquake struck just off the Chilean coast, causing widespread damage in a 50,000 km$^2$ area. The earthquake took a toll on the Chilean people with a recorded 521 deaths, 56 missing persons, 370,000 homes damage or destroyed, and an estimated cost of $30 billion (roughly 17% of the GDP) [Moehle et al. 2010]. This earthquake is the fifth most energetic earthquake ever recorded. Figure 1.1 below shows the epicenter location as well as the affected area of the Chilean countryside. Damage from this earthquake was seen in many buildings, roadways, and small rural towns, including damage from a tsunami that followed the earthquake [USGS 2011].


**Figure 1.1 Map showing affected area and epicenter of the 2010 Chile earthquake [Franklin and Gabbatt 2010].**

Even though the region experienced such a high energy earthquake and much damage was seen in adobe structures and small towns, most engineered buildings performed exceedingly well. An estimated 0.5% of buildings taller than three stories and 2.8% of building taller than 9 stories experienced failure, which exceeds the code requirement of a probability of 10% chance of collapse when experiencing maximum considered shaking. Among those buildings that were damaged, high concentrations of them were RC shear wall structures [Moehle et al 2010]. Failure in these walls was examined to be crushing and buckling of either the rebar or entire wall of the boundary elements of these shear walls. Figure 1.2 shows an example of one of many shear wall failures in the earthquake region. These failures were speculated to be due to two issues: the thin nature of Chilean shear walls—6 in. thick on average—and the low amount of transverse reinforcement and hooks required by the code in the walls. Adopted in 1996, the Chilean code is fairly similar to U.S. code with a few exceptions.

**Figure 1.2 Typical shear wall failure in the 2010 Chile earthquake [Moehle et al 2010].**

Section 5.1.1 of the Chilean code, NCh433 [1996] regulates the design of RC wall buildings to be based on their satisfactory behavior during the Chilean earthquake of March 1985, which had a moment magnitude of 7.8. The buildings in the 1985 earthquake performed exceedingly well yet lacked boundary element confinement. This led to section B.2.2 in the Chilean code, which states: "when designing RC walls, it is not necessary to meet the provisions of paragraphs 21.6.6.1 through 21.6.6.4 of ACI 318-95 code." That section provides boundary element confinement to RC walls as cited in the U.S. code.

Many structures in the earthquake region saw this kind of shear wall failure. Figure 1.3 shows an example of a building in Santiago that had crushing of its concrete shear walls. This building was designed to have compression and buckling in the boundary elements on one side of the shear wall while the other side was in tension, which shows that the shear wall had rotated around its vertical neutral axis causing the boundary element compression action. The tension side of the structure is believed to be the only thing holding the building up. Another structure, shown in Figure 1.4, was believed to have a similar shear wall failure, except after the shear wall in compression failed, the side in tension could not hold the weight of the building and failed, causing the building to topple.

Although the majority of engineered buildings in the 2010 Chilean earthquake performed very well, that does not mean learning and further development cannot be achieved by careful examination and research into the damaging effects of this earthquake. The main structural damages sustained by this earthquake can be attributed to ground motions exceeding code design levels, slender walls experiencing high axial stress, lack of transverse reinforcement in RC shear walls, and in some cases vertical irregularities.

**Figure 1.3 Building in Santiago that experienced shear wall boundary element compression and buckling [Moehle et al 2010].**

**Figure 1.4 Building located in Concepcion that experienced complete shear wall failure and toppled over [Moehle et al 2010].**

### 1.2.2 Shear Walls and ACI 318

Used both in the U.S. and Chile, RC shear walls are a common lateral force resisting system. They are designed to successfully transfer lateral earthquake and wind loads from a diaphragm to the foundation. Reinforced concrete shear walls add strength, stiffness, and ductility to a structural system when designed correctly. Since shear failure is a brittle failure mode for RC shear walls, most walls are designed so that flexural hinging occurs around a neutral axis before shear failure can occur. This flexural hinging action creates large compression and tension forces in the boundary elements of the shear walls, especially in compression. The weight of the structure is already a large compression force on the shear walls, and when the flexural compression is added it creates failures similar to the ones seen in Chile in 2010. To compensate for these large forces and in an attempt to create ductile failure, ACI 318 places special requirements on the transverse reinforcement spacing in the boundary elements. Several equations in ACI 318-11 [2011] govern the transverse reinforcement spacing in RC shear wall boundary elements. These equations are derived from the equations that govern the transverse reinforcement spacing of RC columns, Equations (1.1) through (1.3). ACI 318-11 21.6.4 states that the least of these will govern the transverse reinforcement spacing. The equations for the transverse reinforcement spacing in shear wall boundary elements are simply exceptions to Equations (1.1) through (1.3). ACI 318-11 21.9.6.4 states that the for shear wall boundary elements, Equation (1.1) need not be used, and that only one third of the minimum member dimension be met.

**ACI 318-11 21.6.4.3**

(a) One-quarter of the minimum member dimension;
(b) Six times the diameter of the smallest longitudinal bar; and
(c) $s_o$, as defined by the following equation

$$s_o = 4 + \left(\frac{14 - h_x}{3}\right) \tag{1.1}$$

**ACI 318-11 21.6.4.4**

$$A_{sh} = 0.3\frac{sb_c f'_c}{f_{yt}}[(\frac{A_g}{A_{ch}}) - 1] \tag{1.2}$$

$$A_{sh} = 0.09\frac{sb_c f'_c}{f_{yt}} \tag{1.3}$$

This research project based its transverse reinforcement requirement on these equations, and tested to see if in fact these requirements would provide a ductile response of the boundary element in compresion. This project also tested to see if providing a tighter transverse reinforcement spacing would increace ductilty of the specimen. The tighter reinforcement spacing would be governed by a lifting of the exceptions stated in section 21.9.6.4 of ACI 318-11 for RC boundary elements and requiring them to have the same transverse reinforcement spacing as RC columns.

### 1.2.3 Previous Research

This research project has a foundation in preceding research done in 2010 by PEER interns Ariel Creagh [2010] and Christian Acevedo [2010]. Their research looked into non-special boundary elements and special boundary elements in shear walls tested under a cyclical load as well as a pure compression load. Creagh's research specifically targeted special reinforced boundary elements; the same as was tested in this research project. Her research not only found that a boundary element yielded in tension first, then loaded in compression and experienced much less load capacity than a specimen loaded in pure compression, but also that the specimen loaded in pure compression, designed to ACI 318-08 standards, did not have a ductile response. This very surprising conclusion gave rise to this research project, which takes her research one step further and asks if the current requirements don't result in a ductile response, then will tighter reinforcement spacing or thicker width increase ductility?

## 1.3 METHODS

Several RC shear wall boundary element specimens were constructed in the Davis Hall laboratory at UCB. Although four total specimens were constructed, this report only covers the testing and results from two of them. These two specimens were both full-scale models of the boundary element section of a RC shear wall. Both specimens had an overall size of 6 ft tall × 3 ft wide × 1ft deep, and both included additional heads of 2 ft tall × 4ft wide × 20 in. deep. Figure 1.5 shows a layout of the overall size and dimensions of the tested specimens. The purpose of the addition of heads to the specimens was to ensure the uniform loading of the specimen under a compressive load and to give the transverse reinforcement enough development length.

The construction process for the specimens included; form construction, rebar assembly, concrete casting and cylinder testing, instrumentation placement, and testing set up. The specimens were constructed to standard construction practices and were inspected for quality by Professor Jack Moehle. Pictorial documentation of the specimen construction can be seen below in Figure 1.6.

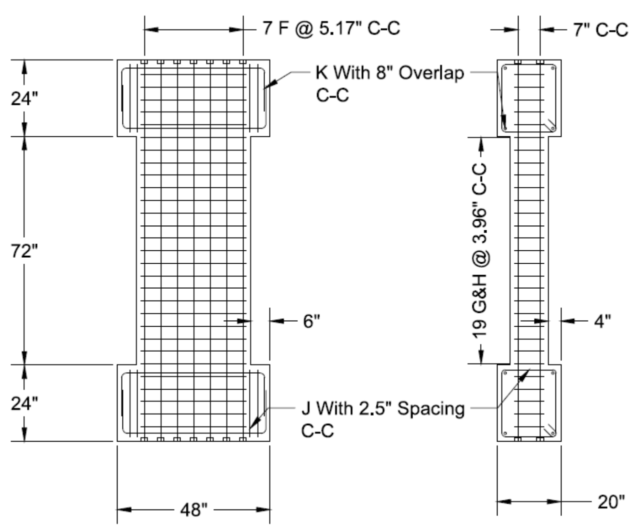


**Figure 1.5 Detailed drawing of the tested specimen's size and reinforcement layout.**


**Figure 1.6 Pictures show different stages in the construction process for the tested specimens**

### 1.3.1 Reinforcement Arrangement

Two separate reinforcement arrangements were used for the two specimens covered in this report. While both specimens contained #8 longitudinal reinforcement and #4 transverse reinforcement, the specimens had separate transverse reinforcement spacing. One specimen's transverse reinforcement was spaced at 2.61 in. center-to-center, based on Equation (1.2), while the other was spaced at 3.96 in. center-to-center, based on Equation (1.3). Transverse hooks were also placed at every transverse reinforcement bar and on every other longitudinal bar. A cross section view of the specimen's reinforcement layout can be seen below in Figure 1.7. Threaded heads were also attached to the ends of each longitudinal reinforcement bar in the specimen to ensure a proper development length over a short distance.

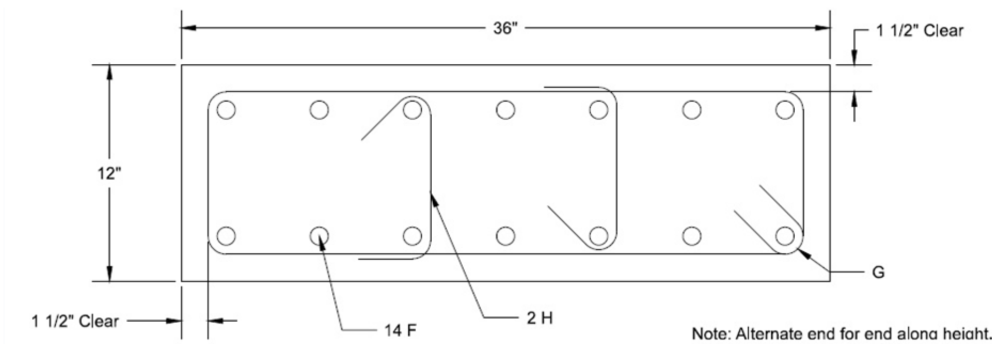


**Figure 1.7 Cross section showing the reinforcement arrangement of the specimen.**

### 1.3.2 Concrete

The two specimens that were tested for this project had a compressive strength of 3711 psi. This strength was chosen because the Universal Testing Machine (UTM) at the Richmond Field Station has a capacity of 4 million pounds. Based on the size and reinforcement of the specimen, the UTM wouldn't allow a specimen with a concrete strength much past 5500 psi to fail. The concrete mix was fairly standard with no additives or cement substitutes. The mix produced a water-cement ratio of 0.56 and ran a slump of 5 in.

Concrete cylinders were tested along with the curing specimens as well as an earlier batch, which was mixed and tested before the specimens were cast in order to determine concrete strength and ensure that the strength would not exceed 5500 psi. The forms were removed from the specimen at 7 days after casting and then air cured until they reached their 28-day strength.

### 1.3.3 Instrumentation

Because this test was designed to study the ductility of concrete shear wall members, a stress-strain curve is essential for quantifying ductility. To obtain a stress-strain curve from the testing of these specimens, instrumentation was needed to collect data. Stress on the specimen would be recorded from the loading patterns of the UTM while testing, but strain had to be recorded from specific instrumentation on the specimen itself. Two types of data collectors were used: strain gauges and displacement transducers. Three strain gauges were placed in each specimen: one on a longitudinal reinforcement bar, one on a transverse reinforcement bar, and another on a transverse hook.

The displacement transducers were attached to the specimen in six locations along the face. Beyond the six transducers along the face, one displacement transducer spanned the entire length of the testing region. As the specimen deforms, the transducers will read its overall and relative displacement allowing the specimens strain to be calculated. A final transducer was placed perpendicular to the specimen in order to read out of plane deformation and buckling.

A digital image correlation (DIC) was also used to observe micro-strain over the face of the entire specimen during testing. It measures the change observed in black Sharpie pen marks scattered over the specimen face through comparing high-resolution pictures taken throughout the course of testing. The change in the black dots is then converted to micro-strain on the face by using finite element analysis software. Figure 1.8 shows the program output of micro-strain right before rupture and the specimen after testing.

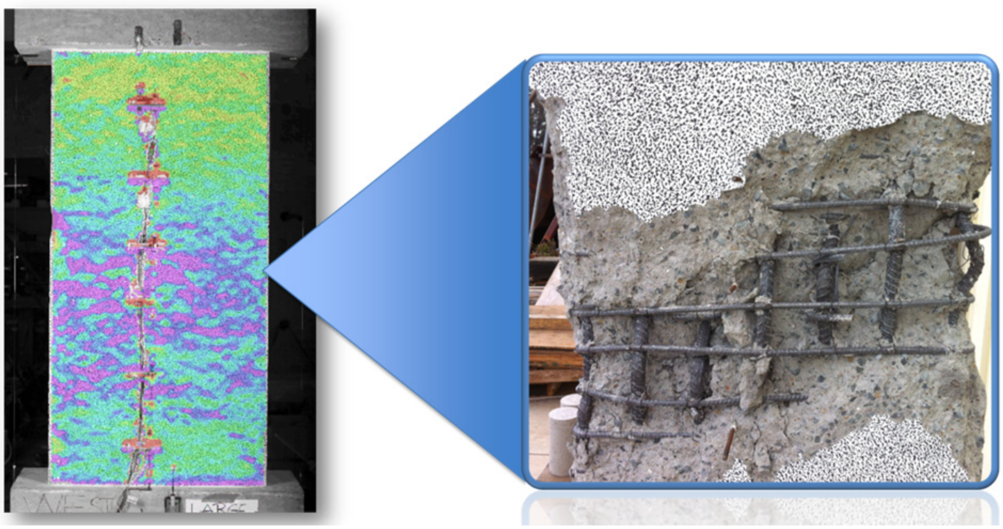

**Figure 1.8** **Purple area on left indicates area with the highest strain as calculated by digital image correlation. Concrete spalled and specimen ruptured in that exact spot.**

## 1.4 RESULTS

The specimens were loaded in uniaxial compression until rupture in the 4 million pound capacity UTM at Richmond Field Station. Unfortunately, the large specimen with a transverse reinforcement spacing of 2.61 in. (the tighter spacing) experienced serious construction errors during concrete casting and could not be tested before this report and will have to be reconstructed. The large specimen with a spacing of 3.96 in. was tested, and its results were analyzed and compared with its predicted results, and the results from the testing of the smaller two specimens.

### 1.4.1 Calculated Results

Before the specimen was tested, expected results were calculated using equations from Professor Moehle's CE 244 reader, which predicted that the specimen would have a ductile failure, with the confined core taking the load at about 1900 kips and gaining strength until it gave way at a strain of about .0204 in/in. Buckling calculations done on the specimen predicted that it would not buckle. The predicted results can best be summed up in an axial load versus deformation graph seen in Figure 1.9. In this graph it can be seen that the specimen continued to gain strength even after yielding, thus classifying it as a ductile failure.

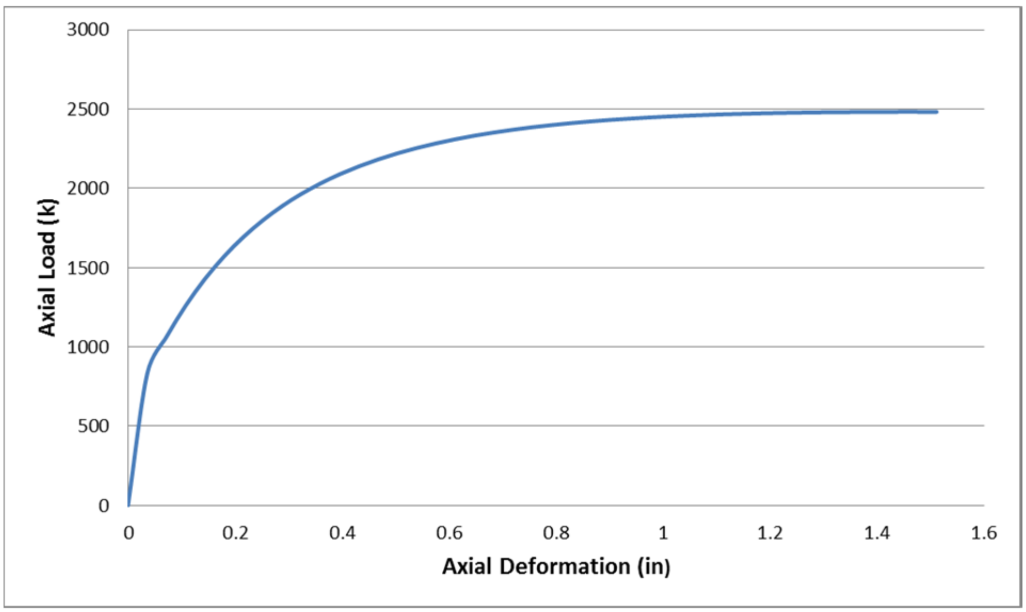


**Figure 1.9 Axial versus deformation graph of the predicted results of the large specimen with transverse reinforcement spacing of 3.96 in.**

### 1.4.2 Test Results

The results from the actual test did not match the predicted results. The actual specimen broke in a brittle manner. Although it was much stiffer than predicted, it had no strength gain after yielding occurred. The concrete core was not stronger than the overall wall section, thus resulting in failure soon after the concrete cover spalled off. A comparison of the predicted results versus the actual test results are shown in Figure 1.10. During testing when the concrete cover spalled off, it took more of the concrete core than just the 1.5 in. of concrete cover, thus reducing the cross-sectional area of the confined core and drastically reducing the amount of concrete holding back the 135°hooks on the transverse reinforcement. This resulted in unhooking of the transverse reinforcement and a release of the confining force on the longitudinal reinforcement that caused it to buckle, and finally axial failure of the entire specimen. Pictorial documentation of the testing results can be seen in Figure 1.11.

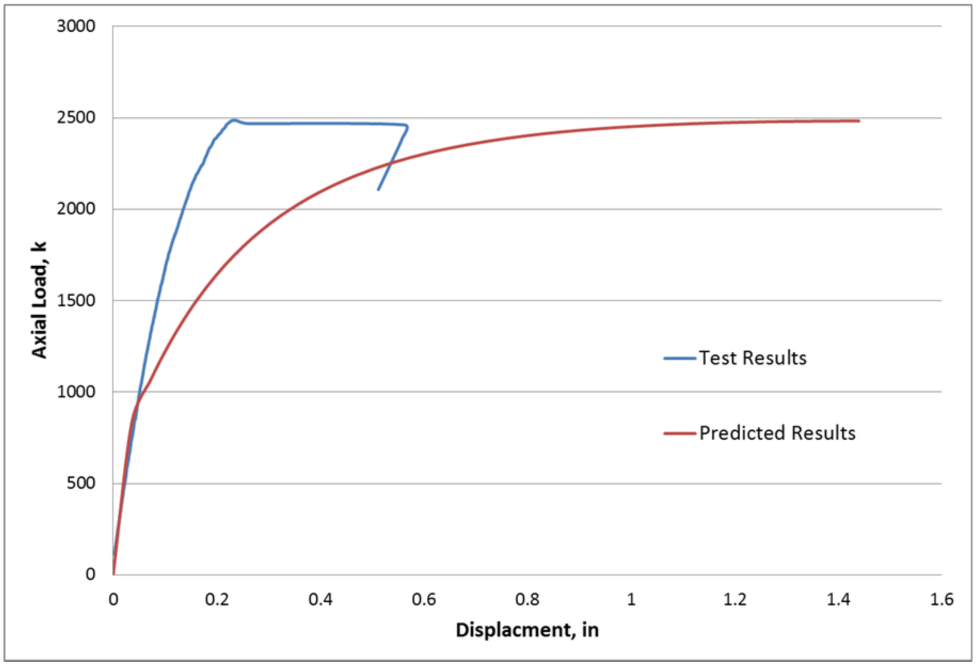


**Figure 1.10 Comparison of predicted and actual testing results.**

**Figure 1.11 Specimen failure after being loaded in compression at Richmond Field Station.**

When comparing the results of the large specimen with the two smaller specimens that were constructed and tested by my research partner, Andrew Lo, we can see that both of those specimens failed in a similar non-ductile way. The tighter reinforcement spacing had no effect on ductility; even though the large specimen reached a higher strain than the smaller specimens, there was still no strength gain after yielding, thus classifying it as non-ductile. A graph showing a comparison of all the tested specimens is shown in Figure 1.12.

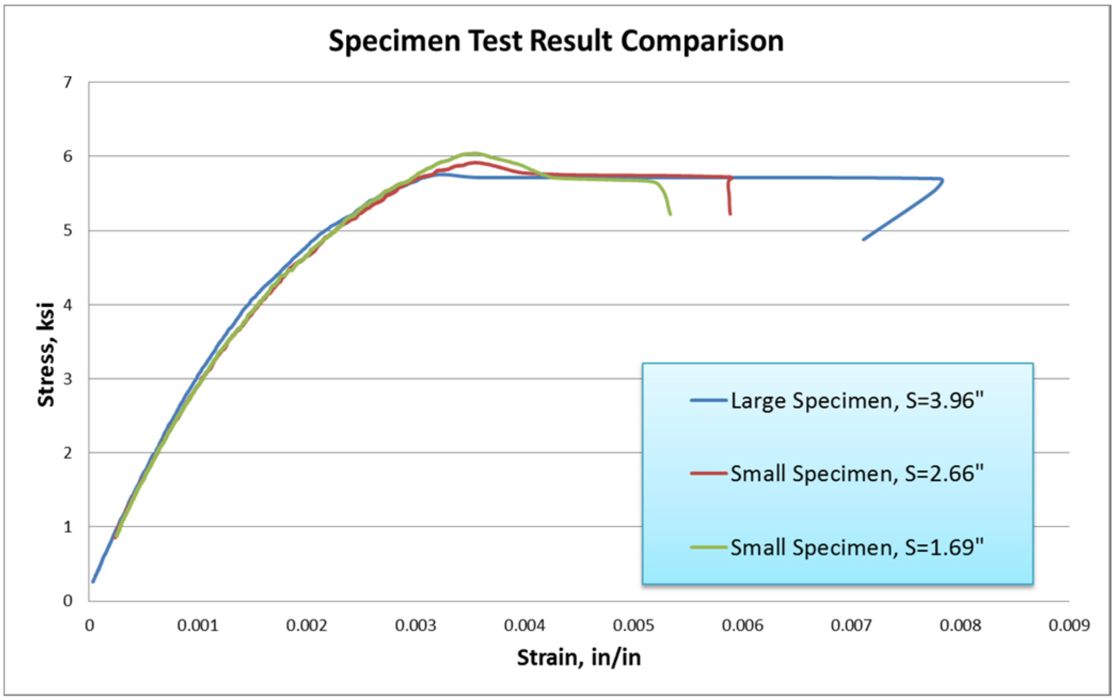


**Figure 1.12 Comparison of large specimen against small specimens constructed and tested by PEER intern Andrew Lo.**

## 1.5 CONCLUSIONS

From these results, along with the preceding research on special reinforced boundary elements done in 2010, it can be said that current ACI requirements for RC boundary elements do provide ductile members for a shear wall yielding through a flexural hinge, and that small increases in width or tightening of the transverse reinforcement spacing will not increase ductility. Further research is taking place in order to provide enough testing data to amend the current code, including a full size shear wall test placed under an earthquake load via actuators. Other research on ways of increasing the ductility of these members is necessary so that shear walls will continue to be an effective structural system. Some ideas include using fiber-reinforced concrete, reducing the concrete cover dimension to around 3/4 in. instead of 1.5 in., or requiring tie back hooks on all of the longitudinal reinforcement bars instead of every other.

## ACKNOWLEDGMENTS

I would like to thank PEER for the opportunity to participate in this research project. I learned so much during my summer internship and gained a new love and respect for the world of research. I would also like to thank the rest of my research team; Professor Jack Moehle for his trustworthy experience and his down-to-earth way of explaining things, Duy To for his hands-on leadership and patience with my understanding and mistakes, and Andrew Lo for making this project fun through his friendship and love for life. I had so much support from many of the lab technicians at the Davis Hall lab and at RFS, and greatly appreciate their friendliness and help. And finally I would like to thank Heidi Tremayne for all the work she did to make the PEER internship a reality. This project would not be possible without funding from the National Science Foundation.

## REFERENCES

ACI Committee 318 (2008) (2011*). Building Code Requirements for Structural Concrete and Commentary*, American Concrete Institute,, Farmington Hills, MI.

Andrus RD, and TL Youd (1987). Subsurface investigation of a liquefaction-induced lateral spread Thousand Springs Valley, Idaho, *Misc. paper GL-87-8*, U.S. Army Corps of Engineers.

Acevedo C (2010). Seismic vulnerability of non-special boundary element of shear wall under axial force reversals, in *PEER Report 2011/10*, Pacific Earthquake Engineering Research Center, Berkeley, CA.

Bray JD, and RB Sancio (2006). Assessment of the liquefaction susceptibility of fine-grained soils, *J. Geotech. Eng*., 132(9):1165–1177.

Creagh A (2010). Seismic performance of concrete special boundary element, in *PEER Report 2011/10*, Pacific Earthquake Engineering Research Center, Berkeley, CA.

DWR (2011). *Delta Risk Management Strategy*, Department of Water Resources, accessed Sept.ember 1, 2011, *http://www.water.ca.gov/floodmgmt/dsmo/sab/drmsp/*.

Franklin J, and A Gabbatt (2010). Rescuers continue search for Chile earthquake survivors, The Guardian, Guardian News and Media, accessed January 24, 2013, *http://www.guardian.co.uk/world/2010/feb/28/hundreds-feared-dead-chile-earthquake*.

Holzer TL, MJ Bennett, DJ Ponti, and JCI Tinsley (1999). Liquefaction and soil failure during 1994 Northridge earthquake, *J. Geotech. Eng.*, 125(6):438–452.

Idriss IM, and RW Boulanger (2008). *Soil Liquefaction during Earthquakes*, Earthquake Engineering Research Institute, Oakland, CA, 261 pgs.

Instituto Nacional de Normalizacion (1996). *Earthquake-resistant Design of Buildings*, Official Chilean code, NCh433.Of196.

Kramer SL (1996). *Geotechnical Earthquake Engineering*, New Jersey: Prentice Hall.

Moehle JP (2009). *Reader for CE 244: Reinforced Concrete Structures,* Dept. of Civil and Environmental Engineering, University of California, Berkeley, CA.

Moehle JP (2010). *27 March 2010 Offshore Maule, Chile Earthquake Presentation,* Pacific Earthquake Engineering Research Center, Berkeley, CA.

Moehle JP, K. Kelson, J Bray, M Yashinsky, and W Holmes (2010). Chile EERI/PEER Reconnaissance Briefing, Berkeley, CA, accessed January 24, 2013, *http://peer.berkeley.edu/events/2010/chile_eq_briefing.html*.

USGS (2011). Report on the 2010 Chilean earthquake and tsunami response, U.S. Geological Survey, *Open-File Report 2011-1053*, Vol. 1.1, 68 pgs., *http://pubs.usgs.gov/of/2011/1053/*.

# 2. Exploring Behavior of Thin Shear Wall Boundary Elements in Compression


## ANDREW LO



### ABSTRACT

Following the 2010 Chile earthquake, shear wall boundary element crushing failures were observed in structures all over the nation, despite the otherwise good performance of structures at large. These failures were presumptively caused by building geometry, shear wall thinness, and lack of confinement from transverse reinforcement in the boundary elements. Confined concrete is used in earthquake engineered structures to provide ductility and increased axial capacity to members in compression. However, the Chilean building code, NCh433 [1996], specifically excludes confinement requirements due to satisfactory performance of shear walls in the 1985 Chilean earthquake. These shear walls did not perform as well this time, with the aforementioned boundary element crushing failures prevailing through many buildings. This research project looks to explore behavior of boundary elements in compression given confinement, as required by ACI 318-11 [2011].

Four specimens were constructed in order to test the ACI 318-11 requirements for confinement of boundary elements. This report focuses on the smaller two of the four considered, both with 8-in.-thick boundary elements. These two specimens shared all geometry, with the exception of transverse spacing. Specimen 1 was constructed to the specifications of the ACI 318-11, while Specimen 2 was constructed to specifications that were beyond current code requirements for boundary elements. The specimens were tested in compression at the University of California, Berkeley's Richmond Field Station. Data was taken via displacement transducers, strain gages on specified rebar, and digital image correlation technology.

Despite both the code and calculations predicting increased capacity and ductility in both specimens, neither specimen performed as expected. In spite of transverse spacing differences, axial-versus-deformation plots showed that both specimens behaved almost identically, characterized by brittle failure. Transverse reinforcement, which was expected to provide confinement, failed to engage as expected.

The results show that the current ACI 318-11 requirements for boundary elements are ineffective in providing confinement. Decreasing the required spacing between transverse bars also failed to provide any significant changes to the specimen. This implies that the failure of these specimens may be tied to specimen geometry. Further research exploring other methods of

offering confinement, such as decreasing cover, changing boundary element geometry, or utilizing different types of concrete, is necessary

## 2.1 INTRODUCTION

Under the mentorship of Professor Jack Moehle and graduate student Duy Vu To, Pacific Earthquake Engineering Research (PEER) Center interns Dustin Cook and Andrew Lo designed, constructed, instrumented, casted, and tested four shear wall boundary elements. This report discusses the development of two of the boundary element specimens and results of the compression tests on those two specimens. This research focused on the effect of the spacing of the transverse reinforcement and its ability to affect ductility, confinement, and overall capacity. As such, the two specimens varied only in transverse reinforcement spacing, based on ACI 318-11 [2011], with all other dimensions and design factors remaining the same.

The purpose of this project was to explore the behavioral differences of these boundary elements in compression, particularly in failure. The study is part of a larger project on shear walls, which will include additional testing of boundary elements in tension-compression-tests with the intention of later developing recommendations to ACI Committee 318 on the shear wall design code. This umbrella project is run by Professors Dawn Lehman, and Laura Lowes (of the University of Washington), Jack Moehle (University of California, Berkeley), and John Wallace (University of California, Los Angeles).

## 2.2 BACKGROUND

### 2.2.1 2010 Chile Earthquake

On 27 February 2010, Chile experienced an earthquake off the coast of the Maule region, with shaking that lasted about three minutes. With a moment magnitude of 8.8 and a fault-rupture zone of 100 km × 100 km, this event was felt throughout a large portion of the country. A map of the affected areas is shown in Figure 2.1. The event is currently ranked as the sixth largest earthquake by magnitude to ever be recorded by a seismograph. Damage caused by the earthquake, as well as the subsequent tsunami, has been estimated to cost between $15 and $30 billion, with 525 lives lost and 25 people missing.

Following the 2010 Chile earthquake, the Earthquake Engineering Research Institute (EERI) sent a reconnaissance team led by Professor Jack Moehle to survey the damage caused by the disaster. Engineered buildings built between 1985 and 2009 were of particular interest, as the Chilean building code at the time reflected what had proved effective during the 1985 Chile earthquake. Among those buildings built between 1985 and 2009, there was a significantly low failure rate: 0.5% of buildings of three or more stories and 2.8% of buildings of nine or more stories required demolition; this was considered good performance when taking into account that current codes consider 10% probability of failure under maximum considered shaking acceptable. Despite the positive performance of many of the structures, the EERI reconnaissance team did recognize a common string of failures in reinforced concrete shear walls of many buildings [Moehle 2010].

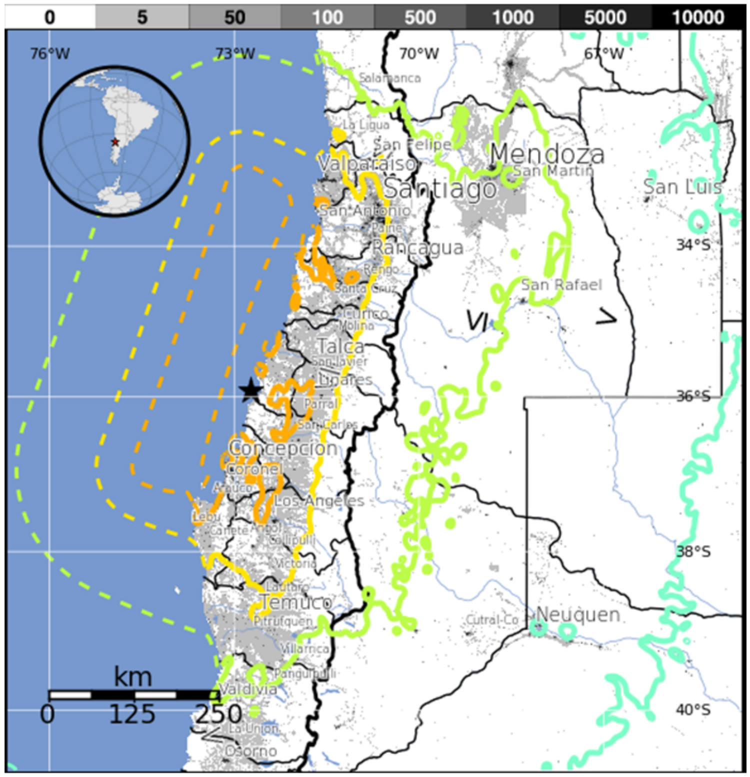


**Figure 2.1 Map of 2010 Chile earthquake [USGS 2010].**

### 2.2.2 Shear Walls

Shear walls, also known as structural walls, are structural systems that play a dual role: they are designed to resist gravity loads and in-plane lateral loads in the form of wind or seismic. In the case of reinforced concrete shear walls, longitudinal reinforcement is provided for the flexural strength of the shear wall. In order to decrease the total amount of steel used in a reinforced concrete shear wall, non-uniform distribution of flexural steel is utilized in the wall, with a majority of the steel placed towards the edges of the wall. The steel edges are often tied together with transverse ties, forming boundary elements.

Due to their stellar performance following the 1985 Chile earthquake (which had a moment magnitude of 7.8), reinforced concrete shear walls were implemented almost ubiquitously amongst Chilean buildings erected between 1985 and 2009. However, these newer buildings started to utilize shear walls of 6 in. thickness, unlike in earlier buildings where 12 in. sections were commonly observed. Another common trend in these newer buildings was to decrease the length of the transverse shear walls in underground levels in order to accommodate parking constraints.

During the 2010 event, many of the reinforced concrete buildings, mostly using structural systems comprised mainly of shear walls, saw failures in boundary elements in lower floors. The failures in boundary elements were largely crushing failures, with large amounts of spalling. These failures were observed by the EERI Reconnaissance group in buildings all across Chile and can be seen in Figures 2.2, 2.3, 2.4, and 2.5.

**Figure 2.2** Boundary element failure below grade in Av. Irarrázaval 2931, Ñuñoa, Santiago [Moehle 2010].

**Figure 2.3** Typical transverse wall crushing failure below grade in Sol Oriente, Macul, Santiago [Moehle 2010].

**Figure 2.4** **Typical boundary element failure on ground floor in 18 de Septiembre 235, Chilian [Moehle 2010].**


**Figure 2.5** **Boundary element failure at ground floor of Freire 165, Concepción.**

As mentioned above, these shear walls serve a dual role of resisting gravity and lateral loads. In the case of this seismic event, the lateral loads translated to flexural compression and tension at the boundary elements of the transverse shear walls. The combination of flexural compression and gravity load exceeded the capacity of the boundary element, causing the crushing failures seen in the figures above. These failures have been attributed to the trend toward thinning and shortening of shear walls, which would decrease axial capacity at the boundary elements and increase the flexural load to be resisted, respectively.

The four figures above also clearly display the large spacing between transverse ties, which may have also contributed to the failure. In some cases, spacing between the ties was as large as 6 in., which was equal to the thickness of the wall. This allowed for a wedge of unconfined concrete to spall out, further decreasing the capacity of the wall. Part of this project was aimed at exploring to what degree confining concrete by decreasing spacing between ties would prevent excessive loss of concrete and loss of capacity. The concepts behind confined concrete will be explored in the following section.

### 2.2.3 Confined Concrete

As concrete is loaded in compression, it undergoes Poisson's effect, where the concrete in question will tend to bulge outwards. In the case of an axially loaded reinforced concrete member with transverse reinforcement, such as the boundary elements mentioned above, the concrete bulging stresses will be opposed by the transverse ties and hooks. That is to say that the transverse reinforcement will provide "confinement stresses" that act on the concrete core. As confinement stresses are applied on the concrete, the axial and strain capacity increase greatly. The effect is analogous to loading a free standing heap of sand (unconfined scenario) and loading a bucket full of sand (confined scenario). A comparison of unconfined and confined concrete can be seen in Figure 2.6. Because of the increased load capacity and ductility, confined concrete is often utilized in earthquake-resisting structures.

In laboratory settings, confinement stresses can be imparted by hydrostatic oil pressures, similar to those in confined compression tests of soil samples. This is called active confinement and is impractical for real world applications. Instead, passive confinement through transverse reinforcement is utilized, where confinement occurs only following axial load. When considering passive confinement in the linear-elastic range, experiments have shown that stresses from passive confinement are ineffective. Concrete needs to reach its normal load capacity and enter a plastic region in order to take advantage of confinement stresses. A problem presents itself, as unrestrained concrete, e.g. concrete cover, in the plastic region will spall off. This leads to a decrease in concrete area, a decrease in load capacity, and one might expect failure to follow. In members with well-confined concrete, the loss of axial capacity due to spalling is offset by gains in axial capacity from passive confinement taking effect. That is to say, in an optimally confined member, axial capacity remains the same or increases following the loss of the cover concrete. Failure in a confined member is then attributed to failure in the transverse ties, when bulging stresses exceed confinement stresses and subsequently fracture the transverse ties. This point of strain is denoted as $\varepsilon_{cu}$ in Figure 2.6.

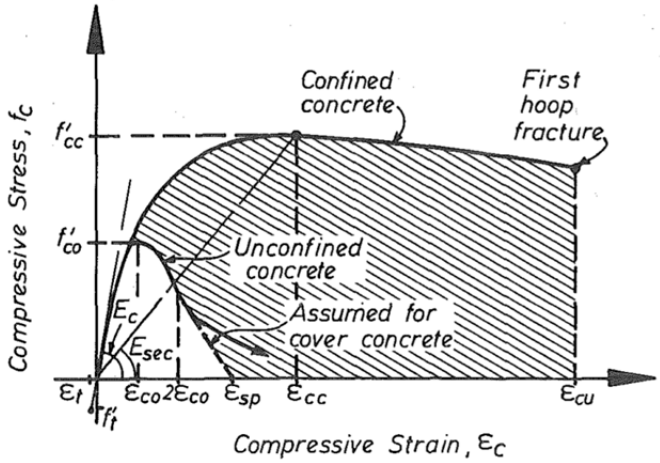


**Figure 2.6 Stress-strain relation of unconfined and confined concrete (after Mander et al. [1988]).**

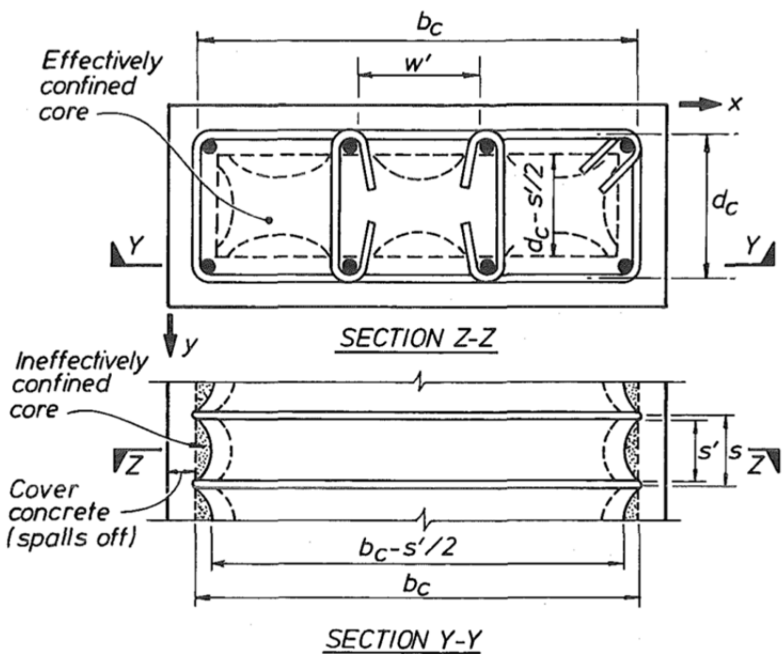


**Figure 2.7 Arching action on rectangular section (after Mander et al. [1988]).**

Confinement effectiveness is largely affected by reinforcement organization. Flexural rigidity of transverse ties is ineffective in providing restraint against outward bulging pressures of the confined concrete core. The expansion of the core in compression is only effectively resisted by the axial rigidity of transverse tie hoops and hooks. Expansion is also unrestrained between transverse ties in the longitudinal direction. Upon the spalling of concrete, it can be expected that these unrestrained areas will tend to spall off as well, causing what is known as an arching effect. Figure 2.7 shows the arching effect in a rectangular section, and Figure 2.8 provides a three-dimensional perspective of the arching effect on a less-confined and a more-confined square section. Section *Z-Z* of Figure 2.7 shows clearly how the arching effect decreases the area of the effective concrete core; the concrete area is further decreased between ties as shown in Section *Y-Y* of the same figure. Confinement effectiveness is, thus, a function of reinforcement geometry, transverse spacing, and the size of the section. For this project, a model for confinement effectiveness for a long rectangular section provided by Mander et al. [1988] is utilized in later calculations.

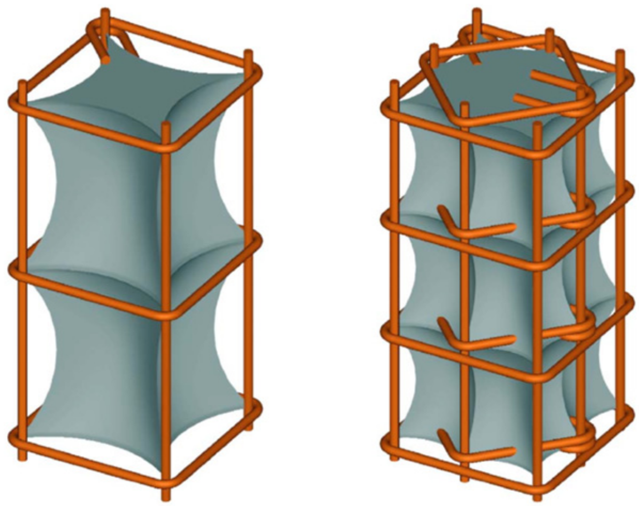

**Figure 2.8 Arching action on two square section in 3D (after Paultre and Légeron, [2008]).**

Transverse reinforcement used in a confined concrete section is recommended to utilize 135°or 180°standard hooks. As concrete spalls off a confined member, it is imperative that the hooks remain anchored in the core concrete to prevent hooks from opening. Hooks with 90° bends are ineffective for this purpose because of a lack of embedment. However, cross ties with one 135°bend and one 90° bend are allowed by some codes, such as ACI 318-08, in order to facilitate construction. As this project is focused on providing confinement for boundary elements, further discussion of the reinforcement design used on this project is provided in later sections.

### 2.2.4 Relevant Codes

As mentioned earlier, the current Chilean Building Code, NCh433 [1996] is based on satisfactory performance of structures following the 1985 Chile earthquake. Due to the lack of confining boundary element reinforcement at the time, the practice of designing without such reinforcement carried over to current buildings. In fact, NCh433 B.2.2 specifically mentions that "when designing reinforced concrete walls it is not necessary to meet the provisions of paragraph 21.6.6.1 through 21.6.6.4 of the ACI 318-95 code." This section of the ACI code specifically refers to confinement in boundary elements.

However, this project is not concerned with amending the Chilean code, but instead addresses the ACI code for the design of shear walls. The relevant ACI code for the design of shear wall boundary elements is found in Section 21.9.6.4(c), which states:

The boundary element transverse reinforcement shall satisfy the requirements of 21.6.4.2 through 21.6.4.4, except Eq. (21-4) need not be satisfied and the transverse reinforcement spacing limit of 21.6.4.3(a) shall be one third of the least dimension of the boundary element.

This project is particularly concerned with 21.6.4.3 and 21.6.4.4(b). Section 21.6.4.3 states:

Spacing of transverse reinforcement along the length $l_o$ of the member shall not exceed the smallest of (a), (b), and (c):

(a) One-quarter of the minimum member dimension;
(To be taken as one third in this case, with respect to 21.9.6.4(c) )
(b) Six times the diameter of the smallest longitudinal bar; and
(c) $s_o$, as defined by the following equation

$$s_o = 4 + \left( \frac{14 - h_x}{3} \right) \tag{1.1}$$

The value of $s_o$ shall not exceed 6 in. and need not be taken less than 4 in.

Equation (1.1) is referenced to as 21-2 in the ACI code. In the case of Equation (1.1), $h_x$ is taken to be the largest distance from centerline to centerline of tie legs in the boundary element.

The other part of the code this project is concerned with, Section 21.6.4.4(b), states:

The total cross-sectional area of rectangular hoop reinforcement, $A_{sh}$, shall not be less than required by Eq. (1.2) and (1.3)

$$A_{sh} = 0.3 \frac{s b_c f'_c}{f_{yt}} \left[ \left( \frac{A_g}{A_{ch}} \right) - 1 \right] \tag{1.2}$$

$$A_{sh} = 0.09 \frac{s b_c f'_c}{f_{yt}} \tag{1.3}$$

The code refers to Equations (1.2) and (1.3) as 21-4 and 21-5, respectively. Here:

$s$ = center-to-center spacing of transverse reinforcement
$b_c$ = cross-sectional dimension of member core measured to the outside of transverse reinforcement composing area $A_{sh}$
$f'_c$ = specific compressive strength of concrete
$f_{yt}$ = specific yield strength of transverse reinforcement
$A_g$ = gross area of concrete section
$A_{ch}$ = cross-sectional area of structural member measured to outside of transverse reinforcement

While the code specifies that Equation (1.2) may be ignored, in the design of a shear wall boundary element, this project is interested in exploring the effects of increased transverse reinforcement and its subsequent effects on the confinement and ductility of the specimen. For this reason, one of the specimens in this project was built to 21.9.6.4(c), and the other specimen was built while taking into account Equation (1.2).

## 2.3 METHODS

### 2.3.1 Specimen Design and Layout

#### *2.3.1.1 Plan and Dimension of Specimen*

The specimens were designed with three separate "regions": a specimen test region and two specimen heads. The specimen test region is the area of interest; it is designed to the aforementioned ACI 318-11 Building Code parameters for shear wall boundary elements. The specimen test region of both specimens is meant to emulate full-scale shear wall boundary elements. Both test regions had the following dimensions: of 8 in. wide, 24 in. long, and 48 in. high.

In order to ensure that failure was observed in the test region, distribute the compressive load evenly to the test region, and provide appropriate development length for the longitudinal rebar running through the test region, reinforced concrete block specimen heads were added. These blocks were 16 in. wide, 36 in. long, and 18 in. high. The full geometry of each specimen is shown in Figure 2.9.

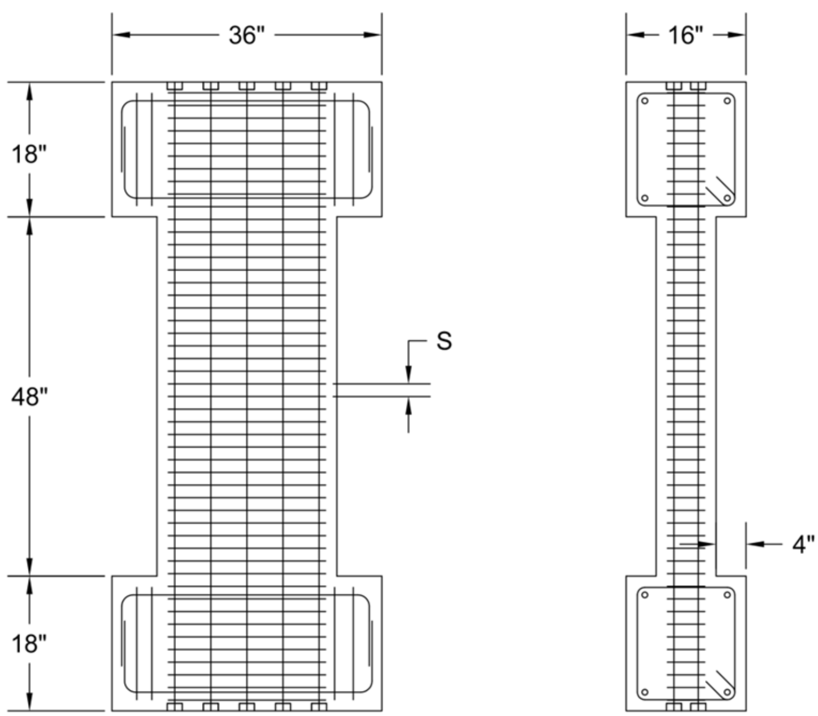


**Figure 2.9 Elevation and profile view of specimen layout.**

### *2.3.1.2 Reinforcement Layout*

Longitudinal reinforcement for boundary element was provided by ten #6 bars that stretched the full length of the specimen; they were provided in two evenly spaced rows of five. The development length for the longitudinal reinforcement is dictated by ACI 318-11 Section 12.3.2, which states that the development length "shall be taken as the larger of $(0.0003 f_y)d_b$ and $(0.0003 f_y)d_b$," where $d_b$ is the nominal diameter of the bar. For the #6 bars, a development length of 14.25 in. was needed, and to provide the development length the concrete heads were sized to be 18 in. high. To ensure that force was fully developed, headed rebar was used for the longitudinal reinforcement.

Transverse reinforcement was provided for the entire length of the specimen in two parts: transverse ties and transverse hooks. All transverse reinforcement were sized at #4 and bent, with an inside diameter of $4d_b$, or 2 in. Transverse ties enclosed all of the longitudinal bars, with two 135°bends closing the tie at one corner. As mentioned in Section 1.2.3, bends of 135°aim to increase confinement by limiting unwrapping of the transverse tie by staying embedded in the core concrete. Hooks enclosed the two middle longitudinal bars, with a 90°bend at one end and a 135°at the other end. Hooks with two 135° bent ends would have been optimal for confinement purposes, but would limit construction ease. A cross section of the test region is provided in Figure 2.10.

As mentioned earlier, this project focused on exploring the effect of transverse spacing on specimen axial capacity and ductility. Using the ACI code requirements discussed in Section 2.2.4 of this report, transverse spacing for the two specimens (referred to from this point on as Specimen 1 and Specimen 2) were calculated to be 2.66 in. and 1.69 in. center-to-center, respectively. In the case of Specimen 1, the controlling spacing value came from 21.6.4.3(a), and in the case of Specimen 2, the controlling spacing requirement came from Equation (1.3), or Eq. (21-4) of 21.6.4.4(b). Note that the transverse spacing of Specimen 1 and Specimen 2 is the only difference between the two specimens.

This project utilized Grade 60 rebar all over. A clear cover of 1.5 in. was utilized for both specimens. Additional reinforcement was provided for the concrete heads, which did not intersect the test region and is assumed to have no effect on the test results.

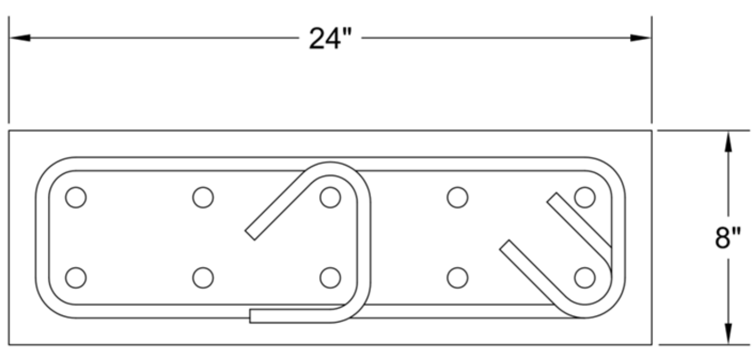


**Figure 2.10 Cross-sectional view of boundary element specimen.**

## 2.3.2 Construction and Assembly

The construction of these two specimens was composed of three main parts: the formwork, the reinforcement assembly, and the concrete pour.

### *2.3.2.1 Formwork*

After discussion with the laboratory technician about previous projects and how to approach the formwork, it seemed that the main concern for the project was to prevent the concrete from bulging out the plywood sides, causing a "wavy" pattern on the specimen. Precaution was taken in fabricating the formwork by providing extra supports and stiffeners for all of the plywood faces, as can be seen in the figures below.

For ease of construction and pouring, the specimens were constructed lying down, with the face of the wall parallel to the floor. Plywood beds were constructed first; a sheet of plywood rested on four 2 × 4 supports. To allow for the dog-bone shape of specimen, 2 × 4 ribs were placed in the center of the specimen to raise it 4 in., accounting for the difference in width between the block heads and the test region; see Figure 2.11.

The specimens were boxed in by plywood faces. In order to prevent the plywood faces from bulging, a concern mentioned earlier, 2 × 4s were nailed to the backs of each piece of plywood, to form a frame. The frame also allowed space for diagonal supports to be attached to resist lateral pressures from the concrete. Figure 2.12 shows a photograph of the specimen formwork as it was taking shape.

**Figure 2.11 Formwork beds and raised ribs.**

**Figure 2.12 Formwork partially assembled.**

**Figure 2.13 Formwork completed, with reinforcement cage placed.**

The specimen forms were pushed together, with additional pieces of bedding attached in most directions. This was done to allow for the supports to rest on the formwork bed. Also, by pushing the beds together, only a limited amount of additional bedding was needed for the supports. The specimen forms were not completed until after the reinforcement cage was laid down. (See Figures 2.13 and 2.14**)**. Because the concrete head sat 4 in. above the surface of the wall, an additional piece of formwork was added across the top face of the wall for each concrete head. These pieces were added on the pour day after the concrete was poured to the surface of the face of the wall.

**Figure 2.14 Another perspective of completed formwork with reinforcement placed.**

### *2.3.2.2 Reinforcement Assembly*

The reinforcement cage was fabricated to specifications based on the design mentioned in Section 1.3.1.2. As mentioned earlier, both transverse ties and hooks were used. In order to prevent any bias associated with reinforcement orientation, transverse ties were oriented with closing bends alternating. The same was done for the hooks.

Fabrication of the reinforcement cage for these two specimens faced some challenges. The first issue came from trying to fit the longitudinal reinforcement into the transverse tie, specifically into the corner opposite the closing bend. The problem area is shown below in Figure 2.15. Due to the required length of the bend, the corner space below became very tight, and would not accept a #6 bar slip through. In order to deal with the issue, bars were manually adjusted by bending the extra length in tighter. The additional bending was just sufficient to allow the corner space to accept a #6 bar. The bending process is shown in Figure 2.16.

Despite opening this corner space more, a second issue arose, when the headed rebar would not fit through either bend. The rebar head had a diameter of 2 in., and because an alternating pattern was chosen for the transverse ties, each of the four corners presented problems. In order to fit the rebar through, the rebar heads were unscrewed, the longitudinal rebar was slipped into the transverse ties, and the heads were reattached. The process can be seen in Figures 2.17 through 2.19.

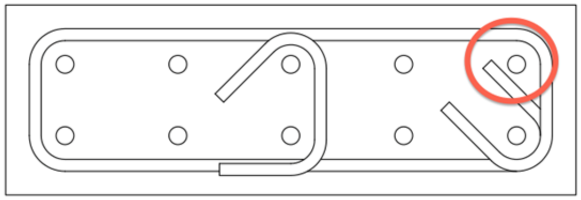

Figure 2.15 Cross sectional view showing problem area.


Figure 2.16 PEER Intern manually bending rebar with pipe extension.

Figure 2.17 PEER Intern removing head from rebar with pipe wrench.

**Figure 2.18** **Longitudinal rebar inserted into cage, prior to reattachment of heads on two bars.**

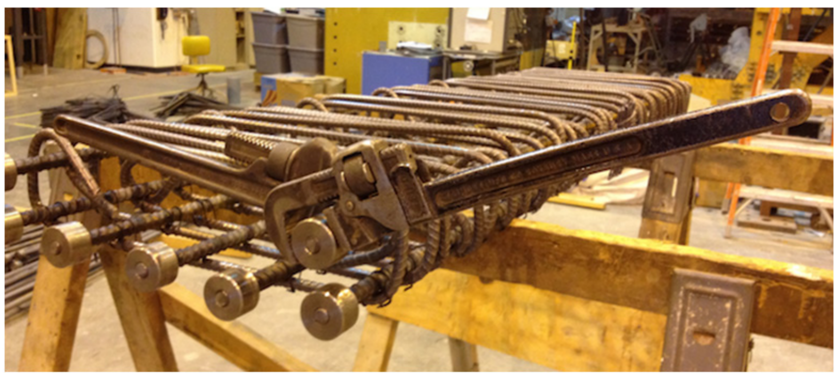

**Figure 2.19** **Reattachment of head on rebar with two pipe wrenches.**

Due to the imprecision of the tying process, the specimen reinforcement cages were also skewed to form a slight rhombus. The problem was fixed by using brute force via a forklift to push opposite corners and straighten the specimen. The process can be seen in Figure 2.20. The completed cage, while waiting to be loaded into the formwork via crane, can be seen in Figure 2.21.

**Figure 2.20 PEER Intern preparing to gage skew of specimen cage; forklift seen in upper left corner.**

**Figure 2.21 Completed reinforcement cage of Specimen 1.**

#### *2.3.2.3 Concrete Pour*

This project is paired with another project that tests two similar but larger specimens, with test region dimensions 12 in. wide, 36 in. long, and 72 in. high. The other project also utilized more longitudinal reinforcement, of fourteen #8 bars per specimen. Because of the increased size in these two alternate specimens, a limit was placed on the concrete strength allowable to ensure that all specimen tested would fail. The maximum allowable concrete strength was expected to be 5500 psi; the concrete strength prescribed was 4000 psi.

A test batch of the concrete was mixed to ensure that the concrete received would be of a similar strength. The mix used was standard with no admixtures, and a slump of 5 in. a 28-day strength of 3716 psi. The mix was deemed acceptable. The final mix used had a slump of 3.75 in. At the time of testing, Specimen 1 had a concrete strength of 4425 psi. Specimen 2 had a concrete strength of 4468 psi at time of testing. The completed specimens following the pour can be seen in Figure 2.22.

**Figure 2.22 Finished specimens.**

### 2.3.3 Instrumentation

This project was instrumented in three ways: strain gages on the reinforcement, displacement transducers, and a digital image correlation on the wall face.

#### *2.3.3.1 Strain Gage*

Three strain gages were installed in each specimen: on one longitudinal rebar, on one transverse tie, and on one transverse hook. These were placed approximately at the center of the specimen, with the assumption that a well-confined boundary element would experience failure across the entire height of the wall. The strain gages were placed along the neutral axis for the hook and tie in order to capture only axial deformation of the bars. An image of a strain gage on a transverse hook can be seen in Figure 2.23.

**Figure 2.23 Hook reinforcement, with strain gage epoxied.**

### *2.3.3.2 Displacement Transducers*

To measure axial deformation, a number of displacement transducers were utilized. The displacement transducers were attached to #3 threaded rods embedded in the boundary element specimen. Spalling was expected in these tests, and, to some degree, encouraged as spalling is required for confinement effects to occur. Too prevent the threaded rods from adding any additional confinement to the face of the shear walls, rubber sheaths were utilized.

The threaded placement rods were embedded through the formwork bed to protrude out of both faces by at least 5 in. after construction. Rubber sheaths covered both ends of the threaded rods, exposing only 1 in. of steel. The sheaths limited the concrete bonding to only that 1 in. of steel, which sat inside the core. The organization of these placement rods and their accompanying sheaths can be seen in Figures 2.24 and 2.25, respectively.

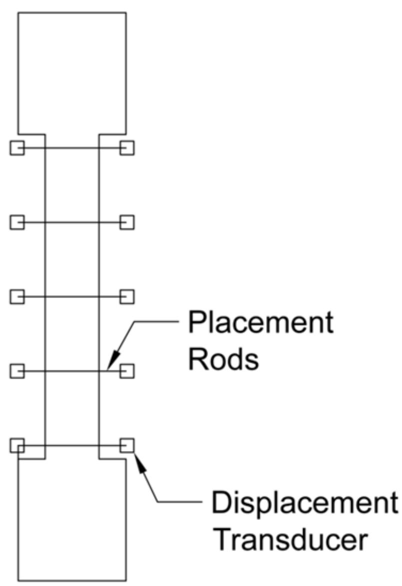


**Figure 2.24 Rough drawing of placement rod and displacement transducer orientation.**

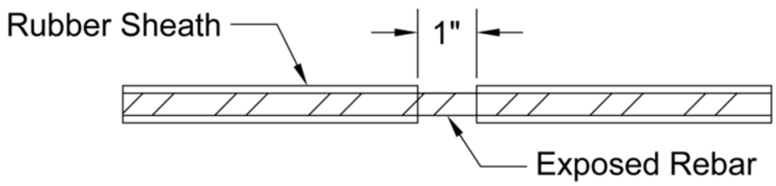


**Figure 2.25 Placement rod with sheath.**

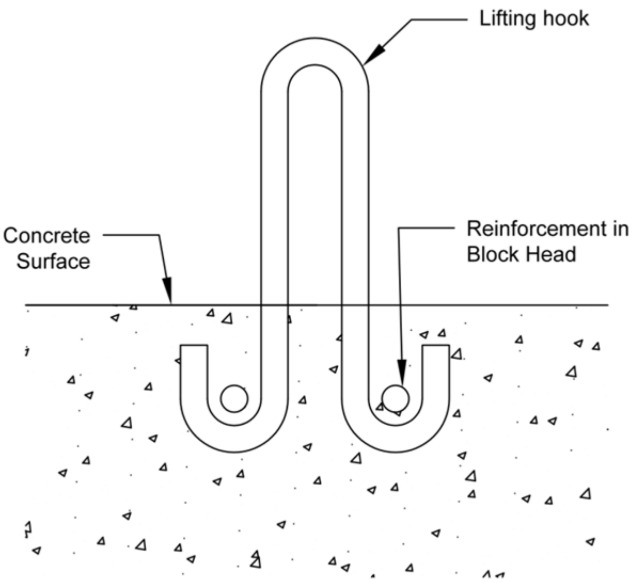


**Figure 2.26 Lifting hook drawing.**

Because the threaded rods extended through the formwork bed, this limited specimen removal after curing to vertical lifting only. Four hooks, of #4 rebar, were bent and attached to the reinforcement cages of the block heads to provide lifting spots. These hooks are shown in Figure 2.26 and can also be seen protruding through the concrete surface in Figure 2.22. The height of each face of the specimen was spanned by 5 transducers, as well as 4 transducers that each covered the full height of the specimen for a total of 14 vertical transducers. An additional transducer was attached perpendicular to the wall face to measure out-of-plane buckling. The transducer set up can be seen in Figures 2.27 and 2.28.

**Figure 2.27 Front face of wall before testing.**

**Figure 2.28 Back face of wall before testing; pieces of tape hanging on piano wire leading to lateral displacement transducer.**

### *2.3.3.3 Digital Image Correlation*

Another method of instrumentation used on this project was digital image correlation (DIC). The technology utilizes high-definition cameras to track a random pattern printed on a surface. Pictures are manually taken of the specimen. As the random pattern on the specimen face moves, software tracks the motion, translates it to strain across the surface, and provides information about the stress that the surface is experiencing. The random pattern utilized in this project was a myriad of handmade marker dots (see Figure 2.29). This technology is limited by the appearance of the dots. As concrete and the attached pattern spalls off during testing, DIC would no longer be able to provide information.

**Figure 2.29 Handmade marker dot pattern on specimen front wall.**

## 2.3.4 Test Set Up

Both specimens were brought to the Richmond Field Station to be tested under the 4 million lb. Southwark-Emery Universal Testing Machine (UTM). The test was specified to have a fixed-fixed connection to emulate conditions of the shear wall boundary elements as part of a larger, full shear wall. The concrete heads were grouted to the floor and press head to ensure a distributed load across the top and bottom faces of the specimen. The test set up for Specimen 1 can be seen in Figure 2.30**.** The test set up for Specimen 2 was identical. Both specimen were loaded at a rate of approximately 50 kips per minute in compression and were compressed past the point of failure to observe any possible ductility due to confined effects.

**Figure 2.30** **Specimen 1 grouted to floor and press head; camera and lighting for DIC behind this camera perspective.**

## 2.4 RESULTS

Prior to testing, estimates of specimen load and strain capacities were calculated using methods from Professor Jack Moehle's "CE 244 Reinforced Concrete Structures course." Based on the geometry and provided reinforcement, both specimens were expected to perform in a ductile manner. This was determined by comparing axial capacity from the gross concrete and steel area against that from a confined concrete core at the point of hoop fracture after cover spalling. In the case of confined action and ductility, the latter case was supposed to show greater axial capacity, which was the case in the calculations for both specimens. Comparisons of expected and test results for each specimen are discussed in the next sections, as well as comparisons between the response of the two specimens.

### 2.4.1 Specimen 1 Results

As mentioned above, a ductile response was expected of Specimen 1. The maximum expected axial capacity was calculated to be 1284 kips; maximum expected strain capacity was calculated to be 0.0235, or 1.13 in. The actual specimen test did not perform as well as expected. The maximum achieved load from the test results for Specimen 1 was 1136 kips, with a maximum strain of 0.00388, or 0.19 in. A comparison between the expected and achieved results can be shown in Figure 2.31. This figure has been abridged to best display the behavior of specimen under load; Figure 2.47 shows the full extent of expected ductile behavior of both specimen. Clearly, Specimen 1 did not achieve the expected ductile behavior as predicted by the model. As shown in Figure 2.32, failure was largely localized to the center portion of the test region and can be attributed to buckling of the longitudinal rebar between transverse reinforcement; see Figures 2.33 and 2.34.

As observed, the brittle failure due to rebar buckling would suggest that the transverse ties and hooks were not engaged to their full capacity. This expectation is confirmed in the data provided by the strain gage installed on the transverse reinforcements. Figures 2.35 and 2.36 plot the transverse reinforcement behavior for the transverse tie and transverse hook, respectively. Neither reinforcement was strained to the point of yielding. The transverse tie did exhibit a greater stain than the transverse hook; this may be due to longitudinal corner bars pushing against the ties as they approached the point of buckling.

The wall remained stable throughout the test. This is shown in the lateral displacement data taken by the lateral transducer. Figure 2.37 shows very little amounts of lateral displacement against axial load for the entire loading process. At the time that this report was written, no DIC data was available for Specimen 1.

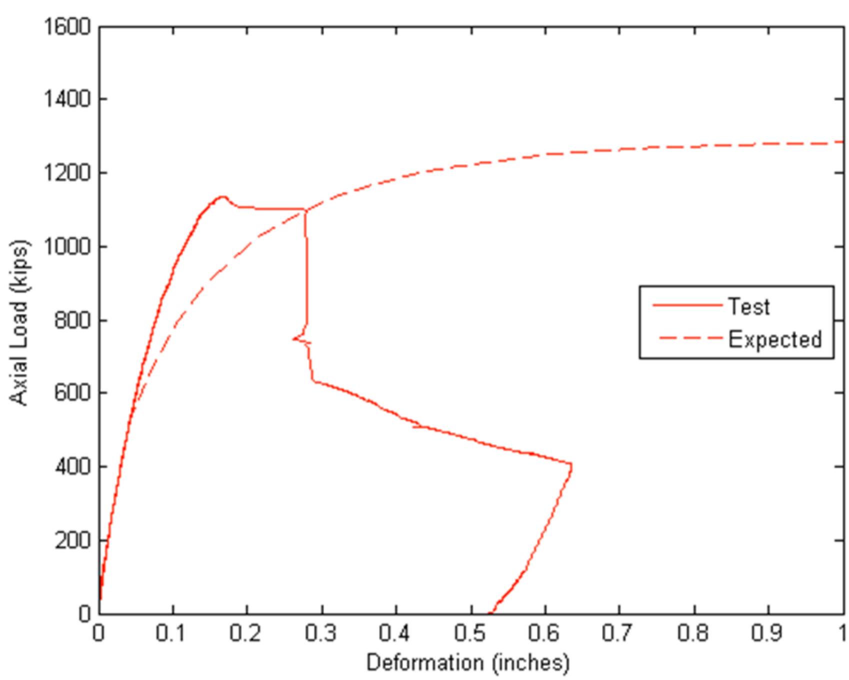


**Figure 2.31 Plot comparison of expected versus tested results of Specimen 1.**


**Figure 2.32	Specimen 1 after failure; front face.**

**Figure 2.33	Buckling of center longitudinal rebar between transverse ties; back face of Specimen 1.**

**Figure 2.34 Buckling of corner longitudinal rebar of Specimen 1.**

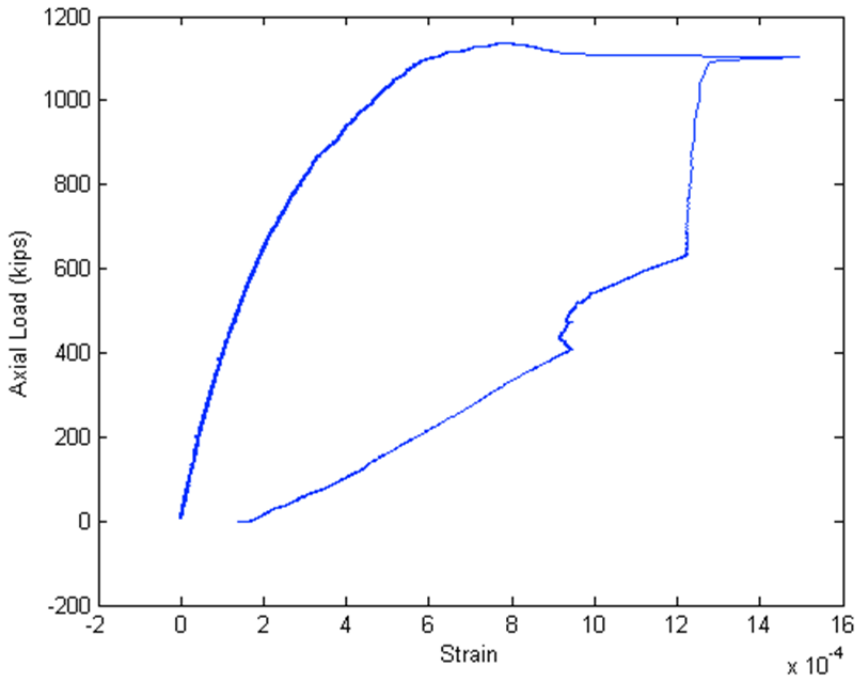


**Figure 2.35 Strain in transverse tie in Specimen 1.**

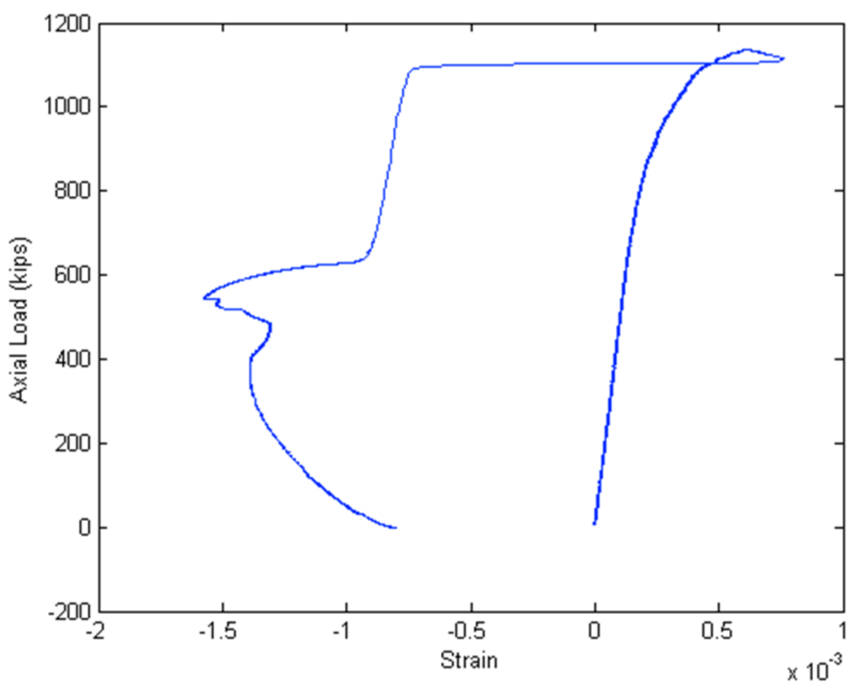


**Figure 2.36 Strain in transverse hook in Specimen 1.**

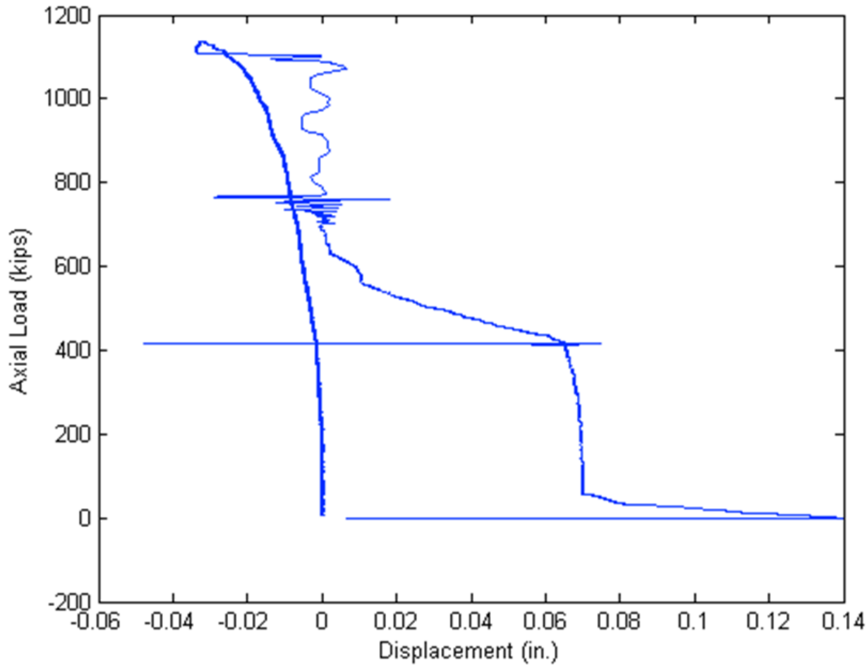


**Figure 2.37 Lateral displacement of Specimen 1.**

### 2.4.2 Specimen 2 Results

As mentioned above, a ductile response was expected of Specimen 2. The maximum expected axial capacity was calculated to be 1498 kips; the maximum expected strain capacity was calculated to be 0.0376, or 1.8 in. As with Specimen 1, Specimen 2 also did not perform as well as expected from the calculated results. The maximum achieved load from Specimen 2 was 1159 kips, with a maximum achieved strain of 0.00347, or 1.7 in. An abridged comparison of the expected and tested behaviors of Specimen 2 is provided in Figure 2.38 where the plot shows that despite expectations Specimen 2 also did not achieve a ductile response. A full comparison between Specimen 2, its ductile response, and Specimen 1 are provided in Figure 2.47.

Failure for Specimen 2 was localized in the upper portion of the test region; see Figures 2.39 and 2.40. Rebar buckling was not observed in Specimen 2. Instead, the loss of concrete area decreased the moment of inertia and allowed for global buckling to occur. Figures 2.41 and 2.42 present side views of the wall. In Figure 2.42, a level is set plumb and flush against the bottom portion of the wall. The gap between the level and the top portion of the wall is indicative of the misalignment of the top and bottom portions of the specimen, a consequence of the global buckling.

The DIC data was available for this specimen. Figure 2.43(a), was taken midway during testing. The image shows uniform strain experienced across the front face of the specimen during loading, as would be expected. Figure 2.43(b) was taken moments before failure. This image shows a collection of strain in the upper portion of the test region, indicating the area of failure that would follow.

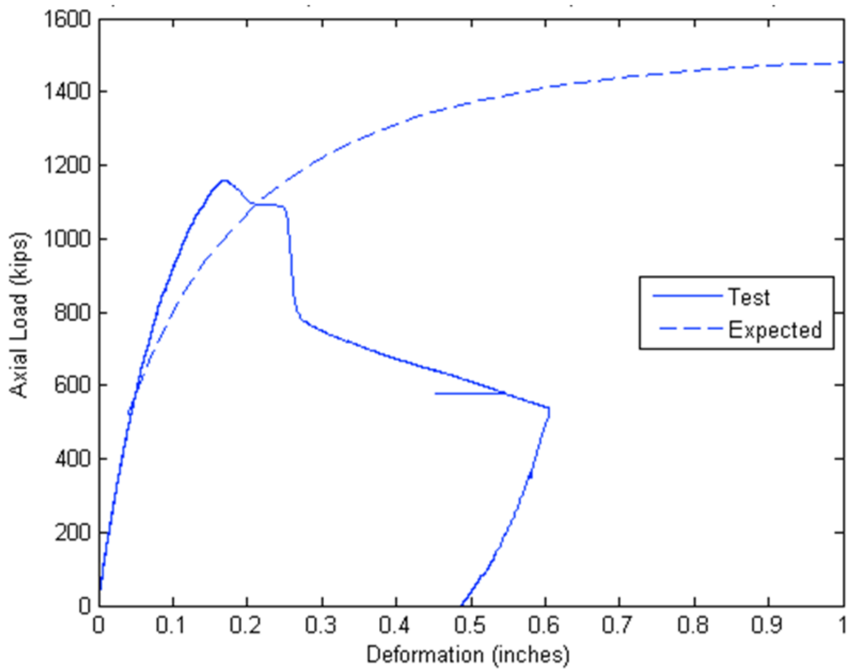


**Figure 2.38 Plot comparison of expected vs. tested results of Specimen 2.**

**Figure 2.39 Specimen 2 after failure; front face**

**Figure 2.40 Close up of failure on back face of Specimen 2.**

**Figure 2.41 Side view of Specimen 2 failure.**

**Figure 2.42 Alternate side view of Specimen 2 failure with level reference.**

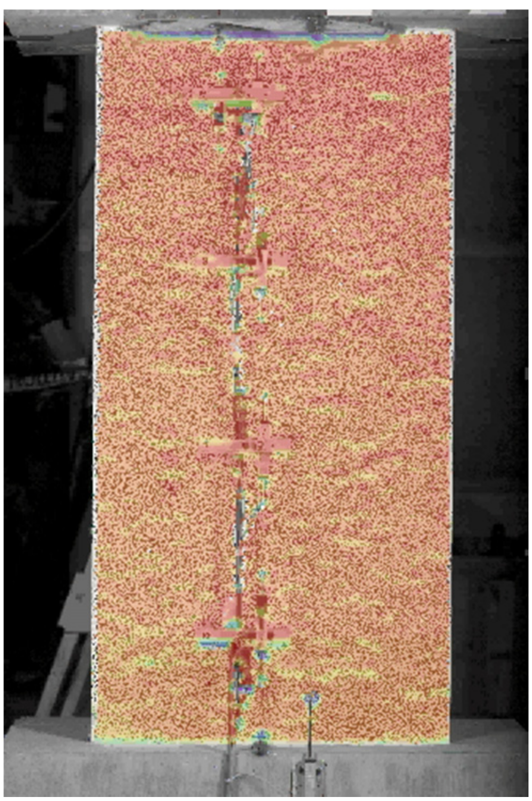

(a) Mid-way during testing

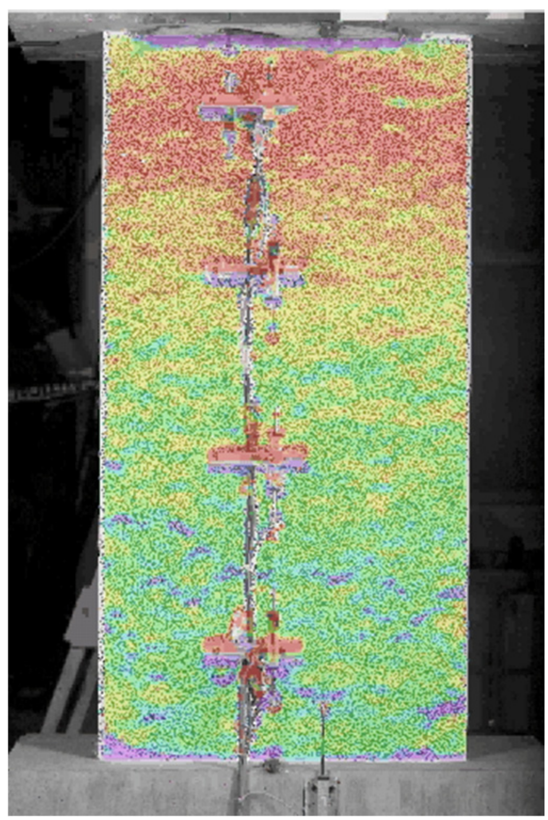

(b) Preceding failure

**Figure 2.43 DIC images of Specimen 2.**

Strain gage data for the transverse tie and hook are provided in Figures 2.44 and 2.45, respectively. Because this specimen was also not ductile, neither strain gage showed any form of yielding behavior in the steel, which would be indicative of well-confined concrete. Despite failure due to global buckling, the lateral displacement transducer was unable to capture any significant movement. The transducer measured displacement at the center of the specimen where failure occurred at the top. The data recorded from the transducer is provided in Figure 2.46, demonstrating stability throughout the test for the bottom portion of the specimen.

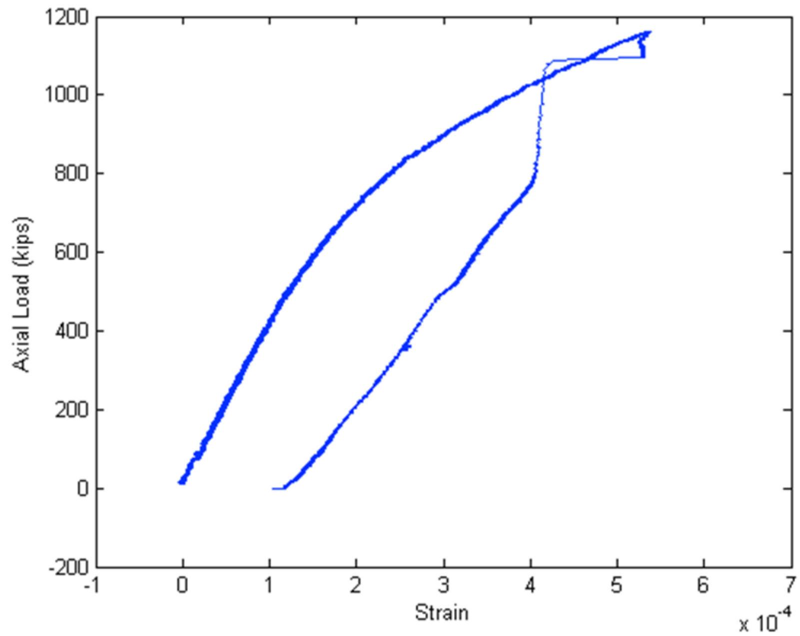


**Figure 2.44 Strain in transverse tie of Specimen 2.**

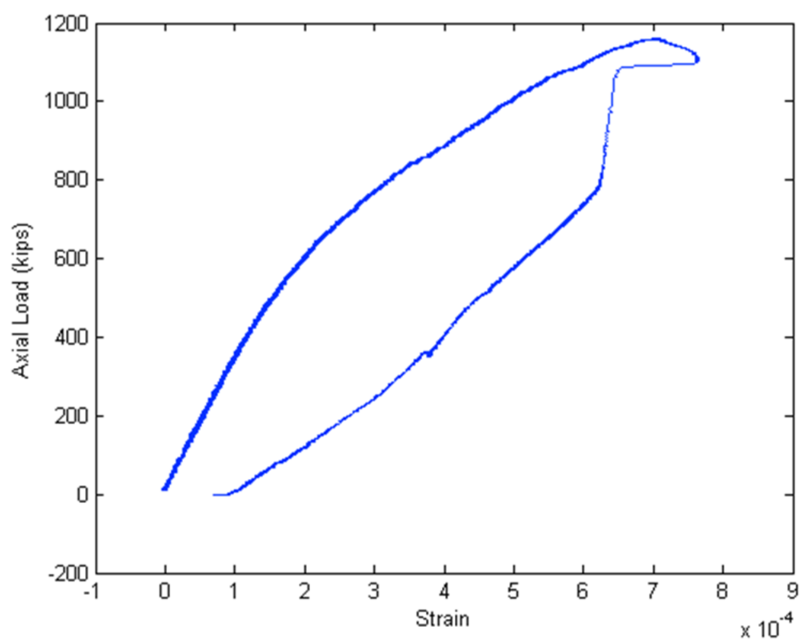


**Figure 2.45 Strain in transverse hook of Specimen 2.**

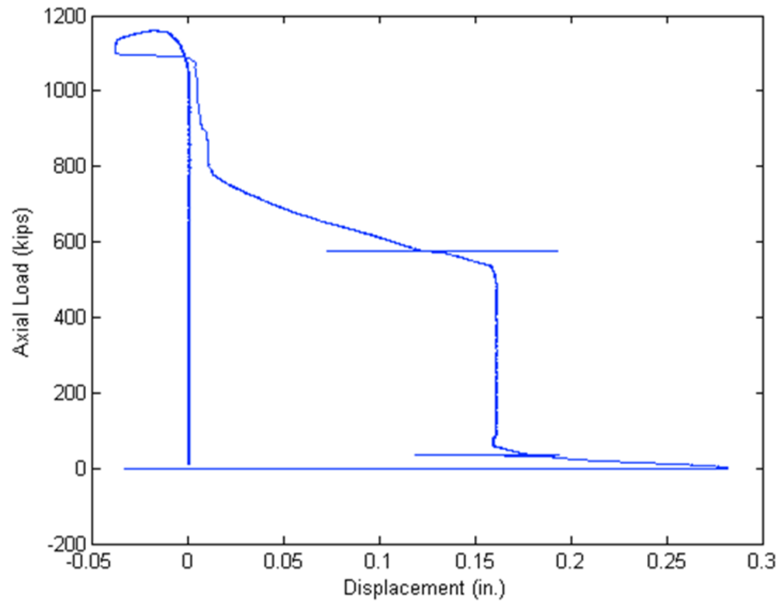


**Figure 2.46 Lateral displacement of Specimen 2.**

### 2.4.3 Comparative Analysis

Calculations on the behavior of the specimen predicted that the difference in spacing of transverse reinforcement would produce similar ductile behavior but of different magnitudes. Specimen 2 was expected to be more ductile and hold more axial load than Specimen 1. However, neither specimen performed as expected. In fact, both specimens performed very similarly. Figure 2.47 compares the test and expected behavior of both specimen. From this plot, the similarity of the behavior of Specimen 1 and 2 becomes apparent. Specimen 1 is marginally more ductile, and Specimen 2 is marginally stronger, but neither performed as was expected.

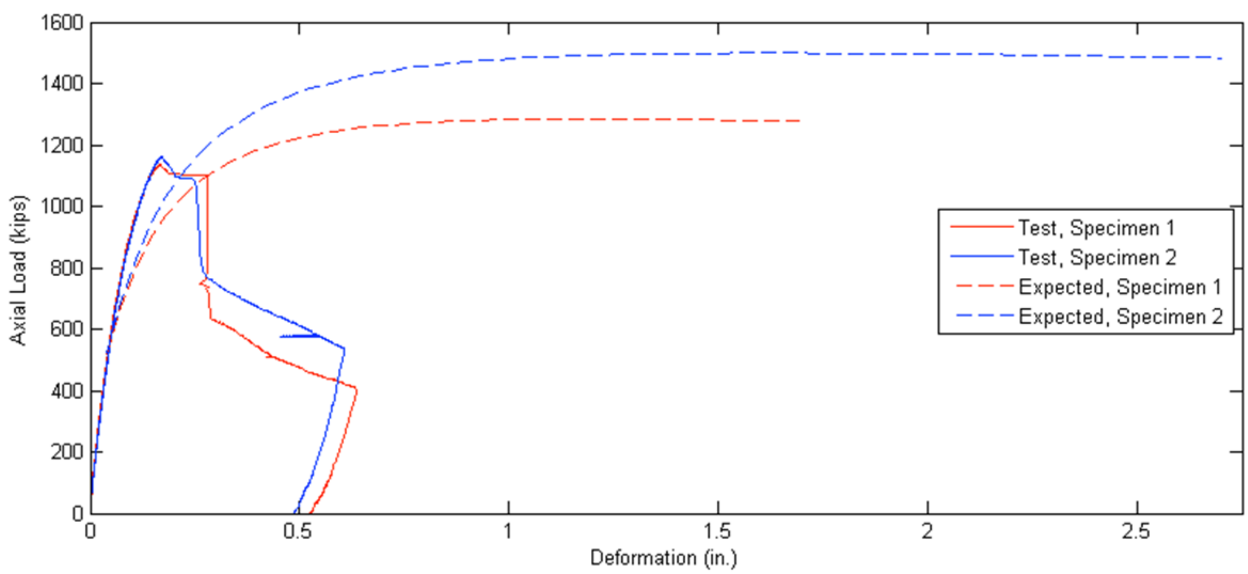


**Figure 2.47 Comparison of test and expected results for both specimens.**

## 2.5 CONCLUSIONS

The requirements set forth by ACI 318-11 used in this project were insufficient in providing confinement for shear wall boundary elements. No ductile response was observed in either test, nor were there any significant changes to the behavior of the boundary element specimen despite a difference in transverse spacing of nearly 1 in. Some form of amendment to ACI 318-11 in regards to confinement of boundary elements will be necessary, at least for 8 in-thick shear walls.

Further research will be needed to explore ways to provide ductility. The similarity in behavior between the two specimens seems to imply that the geometry of the wall, both the size and cover, are at fault for the specimen failure. As it stands, it seems unlikely that an increase in provided transverse steel by decreasing spacing will be feasible. At 1.69 in. spacing, Specimen 2 was approaching the limits of constructability.

Other possible solutions developing ductility in boundary elements should be explored in further research, including:

- Decreasing the concrete cover of the specimen, effectively increasing the area of the confined core
- Requiring hooks for all longitudinal bar to increase confinement action
- Exploring the effect of different types of concrete, such as fiber reinforced concrete
- Changing the wall geometry, for a thicker boundary element or a flanged boundary element

As this research pertains to earthquake engineering, cyclic loading of boundary elements should also be investigated.

## ACKNOWLEDGMENTS

I would like to express my very great appreciation for this research opportunity provided to me by Professor Jack Moehle, my faculty mentor. Without Professor Moehle's direction and experience, this project would not have been possible. I would also like to thank my graduate mentor, Duy To, for his support, time, and leadership provided to us through the entire project. I would like to also acknowledge Dustin Cook, my partner intern on this project. Dustin's carpentry prowess was key to the process of bringing the specimen from paper to the real world, and his companionship throughout the research was priceless. The lab technicians at Davis Hall and Richmond Field Station helped us to make and test these quality specimens, and more importantly, helped us make sure that we kept all of our fingers and toes attached firmly to our bodies, so many thanks goes out to them. Finally, I'd like to thank Heidi Tremayne, the PEER Outreach Director, for her patience and counsel. Her strong guidance and firm criticisms were priceless for a young undergraduate researcher.

This project was made possible by funding from the National Science Foundation throughout the Pacific Earthquake Engineering Research Center's Summer Research Internship.

## REFERENCES


ACI 318 Committee (2011). *Building Code Requirements for Structural Concrete (ACI 318-11) and Commentary*, American Concrete Institute, Farmington Hills, MI.

Instituto Nacional de Normalizacion (1996). *Earthquake-resistant Design of Buildings*, Official Chilean code, NCh433.Of196.

Mander JB., MJN Priestley, and R Park (1988). Theoretical stress-strain model for confined concrete, *J. Struct. Eng*., 114(8):1804–1826.

Moehle JP (2010). *Buildings and Overview*, Lectures, Chile EERI/PEER Reconnaissance Briefing at UC Berkeley from Earthquake Engineering Research Institute/Pacific Earthquake Engineering Research Center, Berkeley, CA, March 30, 2010.

Moehle JP (2009). *Reader for CE 244: Reinforced Concrete Structures*, Dept. of Civil and Enviro. Eng., University of California, Berkeley, CA.

Paultre P, and F Légeron (2008). Confinement reinforcement design for reinforced concrete columns, *J. Struct. Eng*., 134(5):738–749.

USGS (2010). PAGER - M 8.8 - OFFSHORE MAULE, CHILE, U.S. Geological Survey, Earthquake Hazards Program, *http://earthquake.usgs.gov/earthquakes/pager/events/us/2010tfan/index.html* (accessed November 16, 2012).

# 3. The Seismic Performance Observatory

## DORIAN KRAUSZ

### ABSTRACT

Hindered by a lack of available pre-earthquake data and an unsystematic method for effectively gathering and storing critical data, the earthquake engineering community is limited in its development and advancements in research. Although the importance of recording structural behavior following seismic activity and performing post-earthquake investigations is well known, there exists an equally essential counterpart that seems to have been swept aside: namely, pre-earthquake investigation methods and data collection. Without a strong baseline of information pertaining to a structure's history and original state, it is difficult to form accurate comparisons and, consequently, draw reliable conclusions or improve future structural performance. In both cases it is the method of compiling and organizing data that presents a more crucial problem to engineers and researchers studying the performance of structures. Oftentimes, the structural data gathered following an earthquake is neither stored properly nor made accessible to the public for further use and the advancement of design practice. In an effort to address these issues, the Pacific Earthquake Engineering Research (PEER) Center has begun to develop an accessible, user-friendly network, the Seismic Performance Observatory. This web-based system will provide a foundation of both visual and quantitative information, offer an advanced search engine tool, draw patterns between various types of structures and their response to ground motion, and serve as an ongoing source of data available to the public. The following report will expand on the need for such an extensive pre-earthquake archive and investigation strategy, and will present a detailed description of the intended process one should follow when contributing to this interactive, global database.

### 3.1 INTRODUCTION

The overarching notion for PEER's Seismic Performance Observatory (SPO) is to connect already existing sources of data and create a unified location from which users can easily access links to various geological maps, earthquake records, etc., as well as utilize an advanced search engine to observe patterns between similar scenarios. Unlike many existing databases, SPO is targeted towards the research community, allowing users to identify trends by using an interactive search tool to effectively describe and quantify damage in order to validate and produce computer models and fragility curves. If one were focusing on the failure of rectangular columns with the aspect ratio in the range from "X" to "Y", the axial load ratio of "Z" on soil type A, SPO's search engine would quickly locate and present cases with the requested specifications, allowing the user to more concretely formulate theories and identify patterns. Additionally, this observatory will offer a detailed pre-earthquake and post-earthquake investigation plan as well as a thorough user's manual, PEER's SPO User's Manual, discussing SPO's various interfaces.

Within this umbrella management system, there are three primary metadata classes: earthquakes, structures, and general data. Although each metadata class exists independently on the interface during the development process, the user is able to associate each class with one another in order to draw relationships between a structure, the degree of ground motion, and other critical structural features. This web-like capability fosters an interactive environment for engineers, researchers, and others associated with earthquake studies to both explore patterns of similar scenarios and communicate with one another.

It is our hope that a clear, thorough outline of how to both perform a pre- and post-earthquake investigation and will encourage others to contribute, inform the public of the importance of this unified source of data and, ultimately, improve the performance and behavior of structures during seismic activity.

## 3.2 BACKGROUND

Although there exist a number of archives based on structural performance and behavior, these documents and recordings are often inaccessible, unorganized, and, often, lost over time. If structural data *is* recorded in a systematic manner, there is no *one* environment in which the public can share such important findings. In an effort to establish a quantitative source of information that directly relates to ground motion, the Pacific Earthquake Engineering Research (PEER) Center launched a project to construct this concentrated network and investigate its potential benefits for future research.

In 2010, PEER began to develop this data management system in order to provide an interface from which users could import, search, and analyze data [Mahin et al. 2012]. The SPO is equipped with the potential to store geo-tagged annotated digital photographs and videos, point clouds, ground motion and structure instrumentation records, audio files, structural drawings, computer analysis models, and currently available visualization technologies such as Google Maps and Google Earth [Mahin et al. 2012]. With the availability of Google Earth, as shown below in Figure 3.1, users are able to layer various KML files (i.e., soil-type maps, liquefaction zones, faults, etc.) to more thoroughly analyze a structure and predict the behavior during large ground motions.

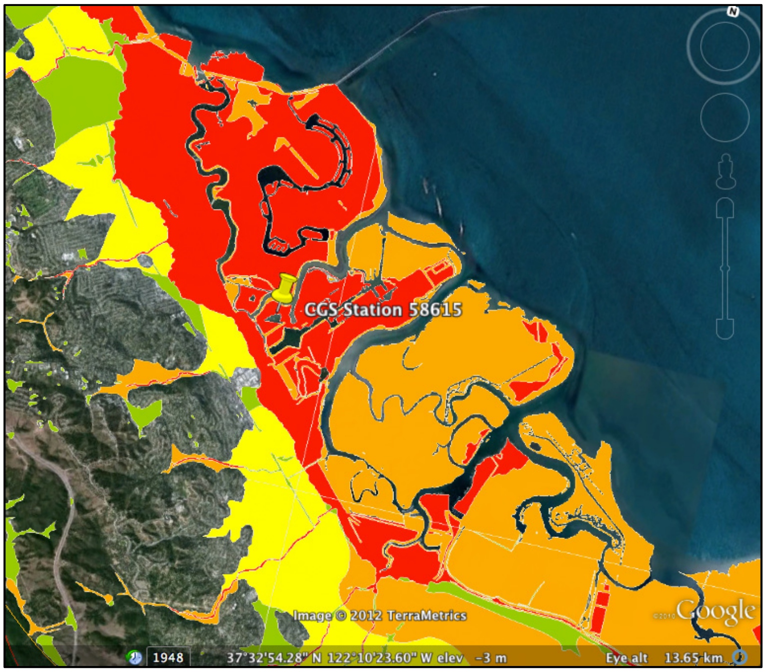


**Figure 3.1 Liquefaction rating KML layer.**

## 3.3 PRE-EARTHQUAKE INVESTIGATION

With a primary goal of offering a detailed example of how one may contribute to the growth of the SPO database, pre-earthquake investigations of instrumented buildings and bridges within the San Francisco were performed. Therefore, several instrumented structures within the Bay Area were selected for investigation, a detailed investigation plan was developed, and a list of tasks one must accomplish to populate the SPO database was established.

### 3.3.1 External Resources

In an approach to locate multiple sources of data, external agencies that hold important records and may be interested in SPO, such as US Geological Survey (USGS), California Geological Survey (CGS), and California Department of Transportation (Caltrans) were contacted. After presenting SPO's primary objectives and stage of development to a number of representatives from various agencies, PEER discussed specific resources that would most effectively serve the observatory. It was stressed that the intention is not to hold all of the data within SPO but, rather, create a safe environment that will serve as a central hub for resources and data that are closely related yet seem to be scattered, hidden, or buried over time. This type of "virtual access" creates a webbed system from which users may link to various sources of data, such as USGS shake maps and liquefaction rating maps, providing the public with a single, accessible, web-based location for critical data.

## 3.3.2 Selecting Structures

As shown in Figure 3.2, 30–40 seismically instrumented structures around the Bay Area were identified [CESMD 2011] and relevant information such as the distance to the nearest fault, type of structural system, liquefaction rating, material, function, and soil type was collected. Although it is intended to expand the database to a wider variety of structures in the near future, instrumented structures were initially chosen due to the amount of useful data that can be extracted from seismic recording instruments following the event of an earthquake. The identified instrumented structures were ranked according to their distance to the closest fault, as shown in Table 3.1, as well as the type of structural system (moment resisting frame, shear walls, braced frame, etc.) in order to obtain a sense of variety and availability. Ten to twelve structures, a representative sampling of bridges and buildings, were selected for investigation based on the following characteristics: distance to fault, structural system, soil type, material, foundation type, function, and accessibility of the structure for inspection.

The important structural features for a number of structures within the Bay Area are displayed in Table 3.1, where the red font signifies structures that lack a large amount of information. As shown in Figure 3.3, the structures selected for investigation exhibit a variety of structural systems; however, due to the locality of our investigations, they lack a range of soil types and materials. The majority of buildings with available strong-motion records were a combination of concrete and steel, ranging from concentrically braced steel frames, to reinforced concrete block shear walls, to moment resisting steel frames. All bridges considered were composed solely of concrete components.

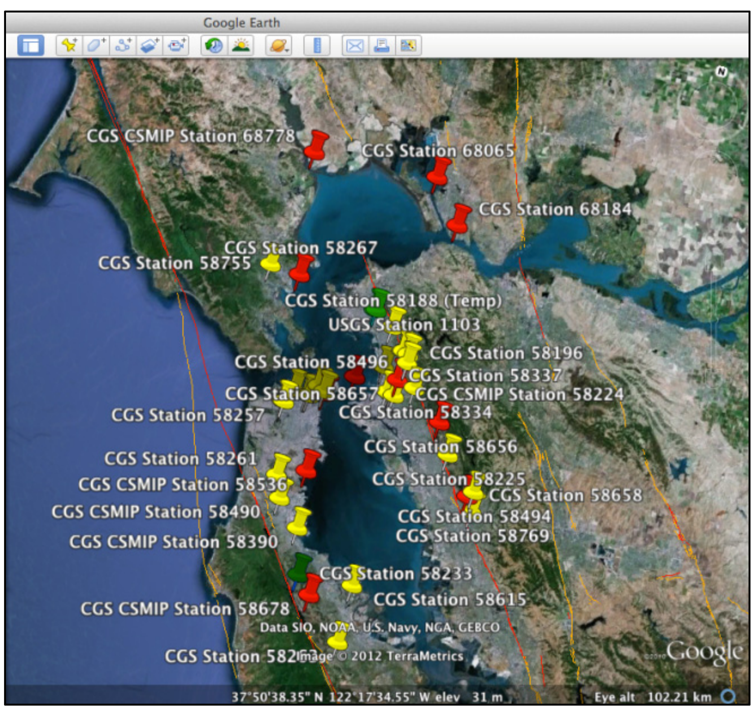


**Figure 3.2 Selected instrumented structures within the Bay Area (red markers for bridges, yellow for buildings).**

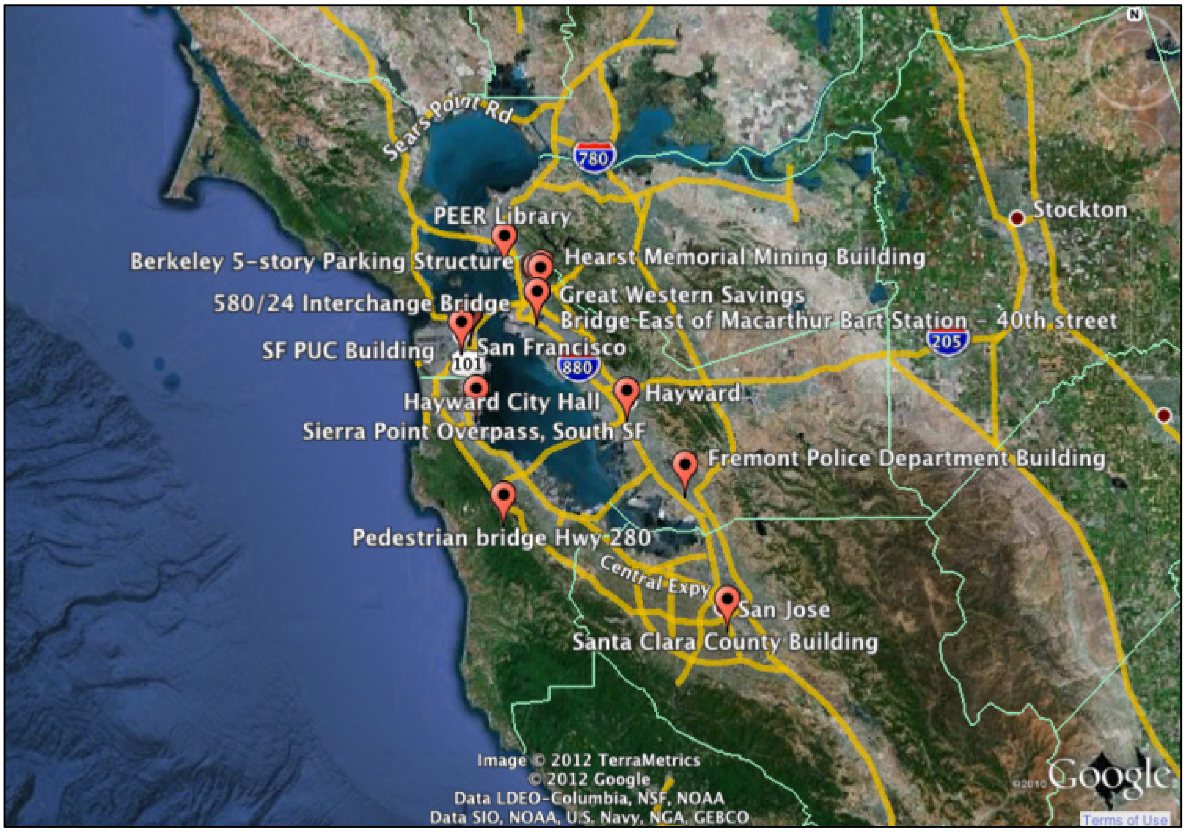


**Figure 3.3** **Instrumented structures selected for investigation.**

Table 3.1 Important features of structures within the Bay Area.

| Buildings | Station Name | Coordinates | Distance To Hayward Fault (km) | Structural System | Soil Type | Liquefaction Rating | Material | Foundation Type |
|---|---|---|---|---|---|---|---|---|
| Fremont Police Dept Bldg | CGS Station 57783 | 37.5529 N, 121.969 W | 0.08 | Steel moment frame | Stiff soil | High | RC, steel | |
| Hayward City Hall | CGS Station 58769 | 37.67086 N, 122.085 W | 0.2 | Steel brace frame | Very dense soil and soft rock | Moderate | Concrete, steel | Mat foundation |
| Schuman-Liles Clinic | CGS Station 58225 | 37.74155 N, 122.1497 W | 0.7 | | Very dense soil and soft rock | Moderate | Steel, masonry, wood | Spread footing |
| Berkeley 5-Story Parking Structure | CGS Station 58196 | 37.86 N, 122.259 W | 0.8 | Reinforced masonry shear walls | Very dense soil and soft rock | Low | Concrete, steel, reinforced masonry | |
| Berkeley Great Western Savings | USGS 1103 | 37.87 N, 122.269 W | 1.3 | | Very dense soil and soft rock | Low | | |
| Eden Medical Center | CGS Station 58494 | 37.6981 N, 122.09 W | 1.3 | Concentric ally braced steel frame | Hard rock | Very low | Concrete, steel | Mat foundation |
| Alta Bates Summit Medical Center | CGS Station 58496 | 37.8548 N, 122.257 W | 1.4 | Eccentricall y braced steel frame | Very dense soil and soft rock | Low | Concrete, steel | |
| Berkeley City Hall | USGS Station 1812 | 37.869 N, 122.271 W | 1.5 | Shear walls | Very dense soil and soft rock | Low | Concrete | |
| Piedmont Middle School | CGS Station 58334 | 37.82276 N, 122.2346 W | 2 | RC frame and RC shear walls | Hard Rock | Very low | RC | Spread footing |
| Pho 84, 2 Story Office Building | CGS Station 58224 | 37.8054N, 122.267 W | 5.5 | RC block shear walls | Very dense soil and soft rock | Moderate | Concrete, steel | |
| Harris State Building | CGS Station 58312 | 37.8063 N, 122.273 W | 5.8 | | Very dense soil and soft rock | Moderate | | |
| Oakland City Hall | CGS Station 58675 | 37.8054 N, 122.272 W | 5.8 | Concentric ally braced steel frame | Very dense soil and soft rock | Moderate | Concrete, steel | Mat foundation |
| San Jose City Hall | CGS Station 57318 | 37.3377 N, 121.885 W | 6.8 | Steel moment frame, RC shear wall | Stiff soil | Moderate | Concrete, steel | Piles |
| San Jose Government Office Building | CGS Station 57357 | 37.3522 N, 121.903 W | 7.7 | Moment resisting steel frame | Stiff soil | Moderate | Concrete, steel | |

| Bridges | Station Name | Coordinates | Distance To Hayward Fault (km) | Structural System | Soil Type | Liquefaction Rating | Material | Foundation Type |
|---|---|---|---|---|---|---|---|---|
| 580/13 Interchange | CGS Station 58656 | 37.7836 N, 122.177 W | 0.24 (Hayward) | Concrete box girder | Very dense soil and soft rock | Very Low | Concrete | |
| 580/238 Interchange | CGS Station 58658 | 37.6905 N, 122.099 W | 0.18 (Hayward) | Concrete box girder | Very dense soil and soft rock | Low | Concrete | Spread footings |
| 580/24 Interchange | CGS Station 58657 | 37.8286 N, 122.267 W | 3.8 (Hayward) | Concrete box girder | Very dense soil and soft rock | Moderate | Concrete | Piles |
| Pedestrian bridge, highway 280 | CGS Station 58678 | 37.5048 N, 122.335 W | 0.9 (San Andreas) | Concrete box girder | Very dense soil and soft rock | Low | Concrete | Spread footings |
| Carquinez /I80 East Bridge | CGS Station 68184 | 38.061 N, 122.225 W | 10.8 (Concord Fault) | Steel truss | Soft Soil | Very High | Steel | Spread footings |
| Highway 37 Napa River Bridge | CGS Station 68065 | 38.1205 N, 122.28 W | 5.3 (West Napa Fault) | Pre-stressed concrete girder | Soft Soil | Very High | Concrete | Piles and spread footings |
| Hwy 37 Petaluma River Bridge | CGS Station 68778 | 38.1157 N, 122.505 W | 8 (Rodgers Creek Fault) | Steel girder | Soft Soil | Very High | Concrete | Piles and spread footings |
| Sierra Point Overpass, South SF | CGS Station 58536 | 37.6746 N, 122.39 W | 5.5 (Serra Fault) | Steel I-beams supported by lead rubber isolation bearings | Soft Soil | Very High | Concrete | Spread footings |

Below is a list of the structures investigated during this ten-week internship. The data collected for each of the structures listed has been input into SPO and are accompanied with an extensive gallery of photos and descriptions:

**Buildings:**

- Berkeley Public Safety Building (only exterior)
- Berkeley City Hall (only exterior)
- Great Western Savings (only exterior)
- Berkeley's 5-Story Parking Garage on Durant and Telegraph
- San Francisco's Public Utilities Commission Building
- UC Berkeley's Hearst Memorial Mining Building (isolated)
- Hayward City Hall
- Fremont Police Station

**Bridges:**

- 580/24 Interchange Bridge
- Pedestrian bridge off of Highway 280
- Sierra Point Bridge, San Francisco
- 580/13 Interchange Bridge

### 3.3.3 Pre-Earthquake Investigation Plan

When approaching a pre-earthquake investigation, for comparison purposes one must consider what may be of interest *after* an earthquake occurs. Based on already existent post-earthquake plans developed by the Earthquake Engineering Research Institute (EERI) and the PEQUIT manual from Caltrans, this pre-earthquake investigation strategy incorporates many familiar procedures and underlines the key differences for evaluating bridges and buildings [EERI 2010; Caltrans 2012]. The author has included the pre-earthquake investigation plan in this report, noting that the respective post-earthquake investigation plan is extremely similar and varies only with respect to the amount of damage documented and the potential use of SPO as a reference. If a pre-earthquake investigation has been previously performed on a structure that later experiences an earthquake, one may reference the data held in SPO for comparison purposes during the post-earthquake investigation.

The following pre-earthquake investigation procedure incorporates strategies and instructions acquired from performing a number of investigations and developing the most efficient, systematic method. Although the procedure is targeted towards experienced engineers with an inspection background, the format speaks to a wide audience and clearly defines the purpose of each step with detailed guidelines. The full pre-earthquake investigation plan for both bridges and buildings is given within SPO; a synopsis is given below.

1. Collect all beneficial preliminary information about the building/bridge
    - Coordinates of structure
    - Structural system (moment resisting frame, braced frame, shear walls, post and beam frame, etc.)
    - Function
    - Material
    - Foundation type
    - Soil type
    - Liquefaction Zone
    - Details regarding instrumentation (location, type, etc.)
    - If applicable:
        - ✓ Number of stories
        - ✓ Base dimension
        - ✓ Number of bents
        - ✓ Number of columns per bent

2. Prepare a set of drawing plans (structural, mechanical, architectural, electrical, etc.)
    - Determine a specific route to follow during the investigation
    - Create naming conventions for various components of the structure (e.g., labeling columns)
    - Identify and highlight key components of the structure that may fail following an earthquake (potential damage zones)
    - Identify location of each instrumentation device
3. Collect all tools and equipment
    - Camera
        - ✓ Fish-eye lens to capture global interior shots
        - ✓ Tripod
        - ✓ Film and memory cards (plan for high capacity needs)
    - Clipboard with drawings
    - Miniature white board
    - Pens, pencils, erasers, notebook
    - Map of site and surrounding area
    - Binoculars
    - Walkie Talkies/Radio
    - Tape measure
    - Safety:
        - ✓ Hardhats
        - ✓ Vests
        - ✓ Appropriate clothing for site
        - ✓ Valid ID cards (company specific ID badge if possible to verify purpose of investigation)
        - ✓ Flash light
        - ✓ **In addition, for bridges:**
            - Lane closures
            - Physical Barriers
            - Air horns
            - Rent lights (if necessary)
            - Safety glasses or goggles
    - Smartphone
        - ✓ 360 degrees application
        - ✓ Magic plan application
        - ✓ Voice recorder

4. Photograph/Record/Film/Note:
    - Once the structural system is determined and structural drawings evaluated, follow the route previously prepared, noting important components and any existing damage

- Use the miniature white board to insert labels into the corners of each photo (specify component's label name and use cardinal directions to note the position relative to other components)

5. Create a new structure within the SPO and upload:
   - Photographs (note any damage found using the taxonomy provided)
   - Important features mentioned in Table
   - Voice recordings
   - Drawings and sketches
   - Videos
   - Scans

### 3.3.4 Input of Data into the Seismic Performance Observatory

After collecting an extensive set of photos, sketches, videos, or any other type of information, one may contribute to SPO by creating a "structure" for others to access, inserting descriptions and specifications to accompany each photograph, sketch, or video, noting the location and type of damage, and uploading any available structural drawings that may or may not have been used during the investigation.

When creating a structure, the interface will present a number of areas in which the user may enter data directly. The exact location of the specific structure with either coordinates or an address must be inputted first. The user can then specify the structural system using the SPO classification of structural types, materials, and systems, as shown in Figure 3.8. For both buildings and bridges, the user may specify the liquefaction rating, soil type, instrumentation details, inspection details, design and construction dates, building code information, and isolator and damping details, as well as any additional relevant comments. Story height, span, function, plan irregularities, and other specifications may be included when defining a building's structure. Similarly, a bridge's bent, column, and span details may be inputted in the fields provided. If documents such as structural, architectural, or electric plans exist, the user can easily upload each file to accompany the structure within SPO's profile interface. Annotated plans used during the pre-earthquake investigation should be uploaded, as they may be useful for those viewing the database after the initial input of data.

After creating a structure and inputting detailed information regarding the structural system, the user may upload photos from the investigation, use SPO's mass-assigning feature to associate a set of photographs with a specific structure and/or earthquake, and begin editing each image. The image-editing interface offers the user a "local" or "global" view option. Depending on whether the photograph is classified as a "local" or "global" shot, the user is given different damage taxonomies to specify damage, as shown in Figures 3.12 and 3.13. The user may also include the camera position details and any additional relevant comments. For a more detailed, step-by-step procedure for inputting data into SPO, please see the Appendix, Section 3.9.

## 3.4 EXAMPLES

Following the selection of 10 to 12 seismically instrumented structures within the Bay Area, all available structural drawings were gathered and an investigation route for each site was established. During the pre-earthquake investigation, global and local shots, interior and exterior shots, regions of potential failure, exposed connections, structural and nonstructural elements, and existing damage were documented. Equipped with a detailed taxonomy of structural and failure classifications, the SPO allows for a systematic and organized method for defining and quantifying data that can be used for comparison purposes. Additionally, in the process of utilizing SPO's new interface, the most ideal and user-friendly approach for inputting data was established, as described in SPO's User's Manual.

To more accurately and thoroughly convey the procedures mentioned above, detailed examples of the pre-earthquake investigation and data inputting process for both a bridge and building are included in this report. Following the steps described in Sections 3.3.3 and 3.3.4, the investigation procedure for Oakland's 580/24 Interchange Bridge and San Francisco's Public Utilities Commission Building are provided below.

### 3.4.1 Bridge

*The 580/24 Interchange Bridge, Berkeley, CA*

1. Preliminary information collected:
    - Coordinates: 37.8286 N, 122.267 W
    - Moderate liquefaction rating
    - 3.8 km from the Hayward fault
    - Located on Type C soil, very dense soil and soft rock (shear wave velocity between 1200 and 2500 ft/sec)
    - Material: concrete
    - Structural system: continuous concrete box girder
    - Instrumented in 1993; 6 accelerometers
    - Foundation type: concrete piles
    - Length: 11 m (36 ft)
    - Number of bents: 35
    - Number of columns per bent: 1 to 3
2. Gather all available plans of the structure
    - 71.3 displays the annotated plan of this bridge (each column labeled from the North abutment as well as its original label beginning with EN 24)
    - Route of investigation highlighted in pink in Figure 3.4
    - Distinguish cardinal directions
    - Become familiar with location of each instrumentation device
3. Collect all tools and equipment (see Section 3.3.3, step #3)
4. Photograph and/or note:
    - Insert the miniature white board into an appropriate location of the photograph's frame (as to not obscure any views of important components), as shown in Figure 3.5
        - Be sure the white board is labeled with the correct name, as determined by the pre-established naming convention
    - Sketch a specific bent/column system and visually identify which components you have photographed, as shown in Figures 3.6

    - In Figure 3.6, also notice how the bent's direction and the view from which the photo was taken is noted, highlighted in blue
  - Photograph any visible damage and insert corresponding labels as necessary, as shown in Figure 3.7.
5. Input findings into SPO
  - Begin by creating and defining the structure, following the provided taxonomies and instructions for bridges, as shown in Figure 3.8
    - When creating a bridge, one can provide detailed information on each column. For example, this structure contained a bent with 3 columns, each of which had different cross sectional shapes and heights. As shown in the sketch of SPO's Bridge Geometry interface, Figure 3.9, each column can be separately evaluated and thus allow for a more specific, quantitative search in relation to column behavior
  - Create a new gallery by uploading the photos and selecting a structure to which the photos will be assigned, as shown in Figure 3.10
  - Begin editing the gallery by evaluating each photo, inputting a description and type of view
    - As shown in Figure 3.11, each photo's latitude and longitude are automatically provided if the camera accessed GPS capabilities
    - Specify if it is a global or local view (global when focusing on more than a single component)
      - As shown in Figure 3.12, if the photo is a "global view," may specify the type of structural or geotechnical damage
      - As shown in Figure 3.13, if the photo is a "local view," may specify the type of damage based on a more detailed taxonomy, provided by the database
    - Within the "Description" section, may input any additional information seen as relevant or important, as shown in Figure 3.11.
    - Insert "Tags," which serve as a tool when one attempts to search the database for a specific type of structural system, type of damage, material etc.

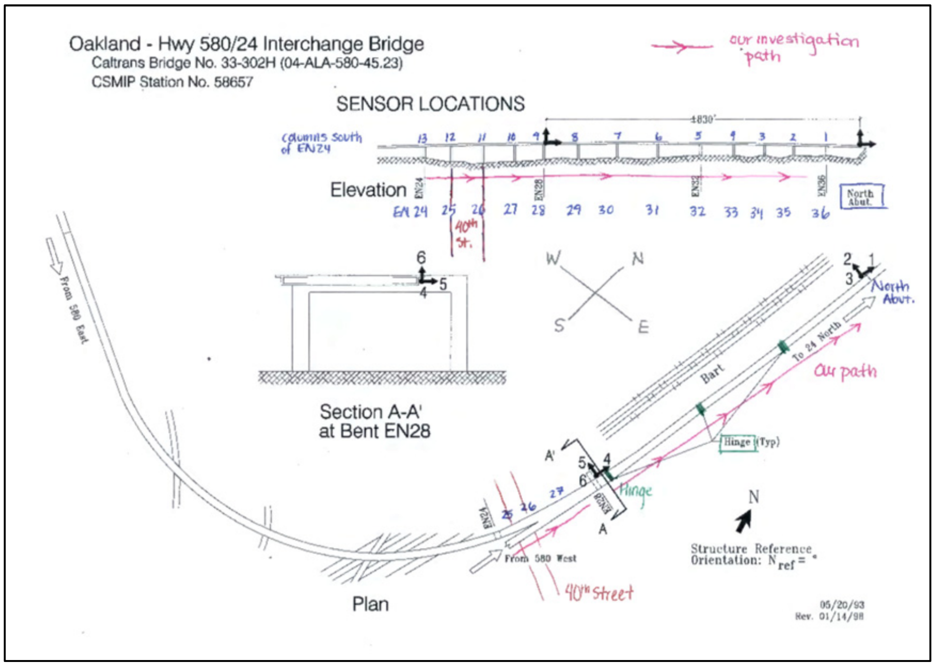


Figure 3.4 Annotated plan drawing of 580/24 Interchange Bridge.


Figure 3.5 Photograph of 580/24 Interchange Bridge bent.

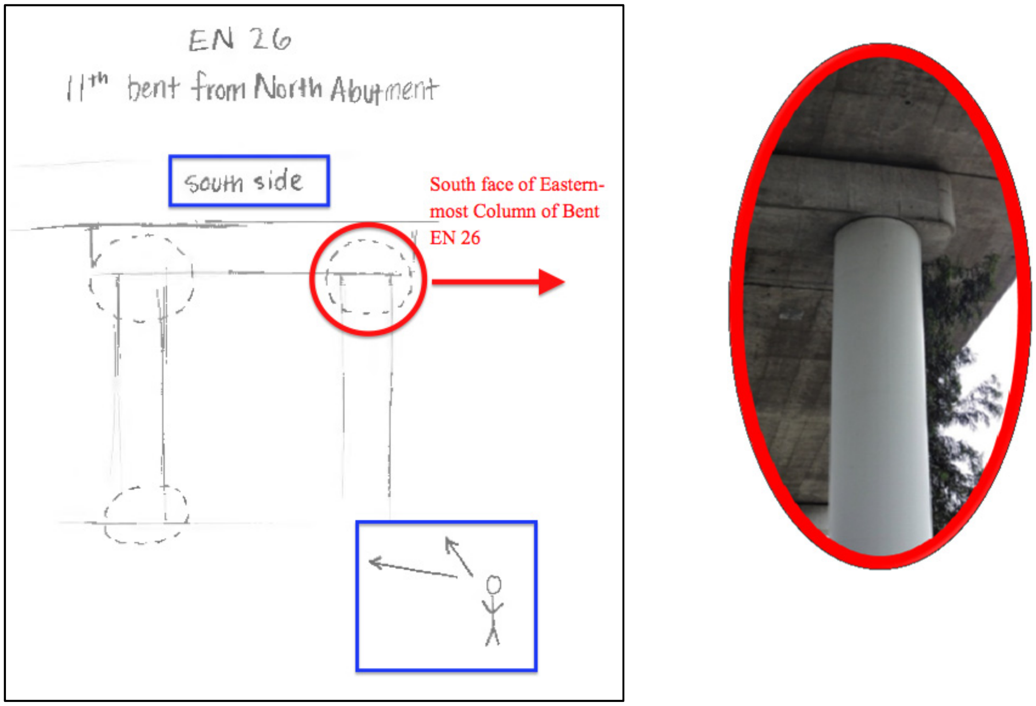


**Figure 3.6** **Sketch and photograph of connection between Bent EN 26 and the upper deck (580/24 Interchange Bridge).**


**Figure 3.7** **Documentation of shear crack failure on interchange column.**

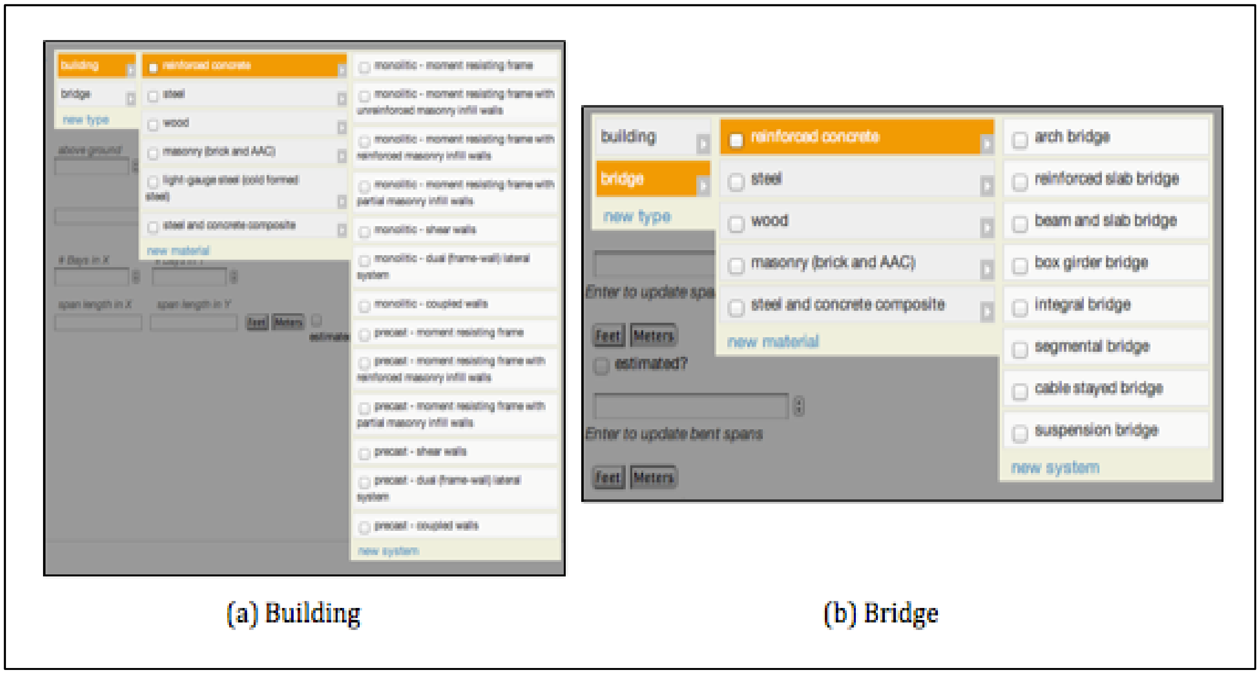

Figure 3.8 Taxonomy of defining (a) the structural system of a building and (b) a bridge.

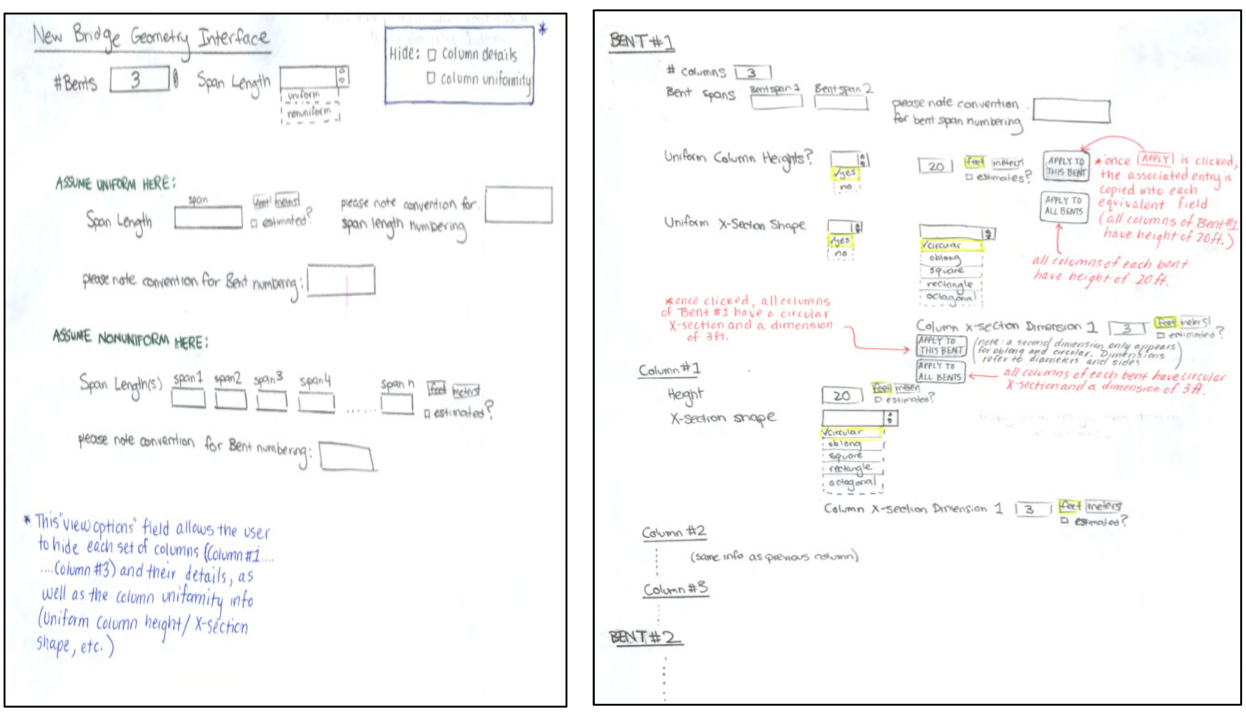

Figure 3.9 Sketch of SPO's Bridge Geometry Interface (interface design with notes in red).

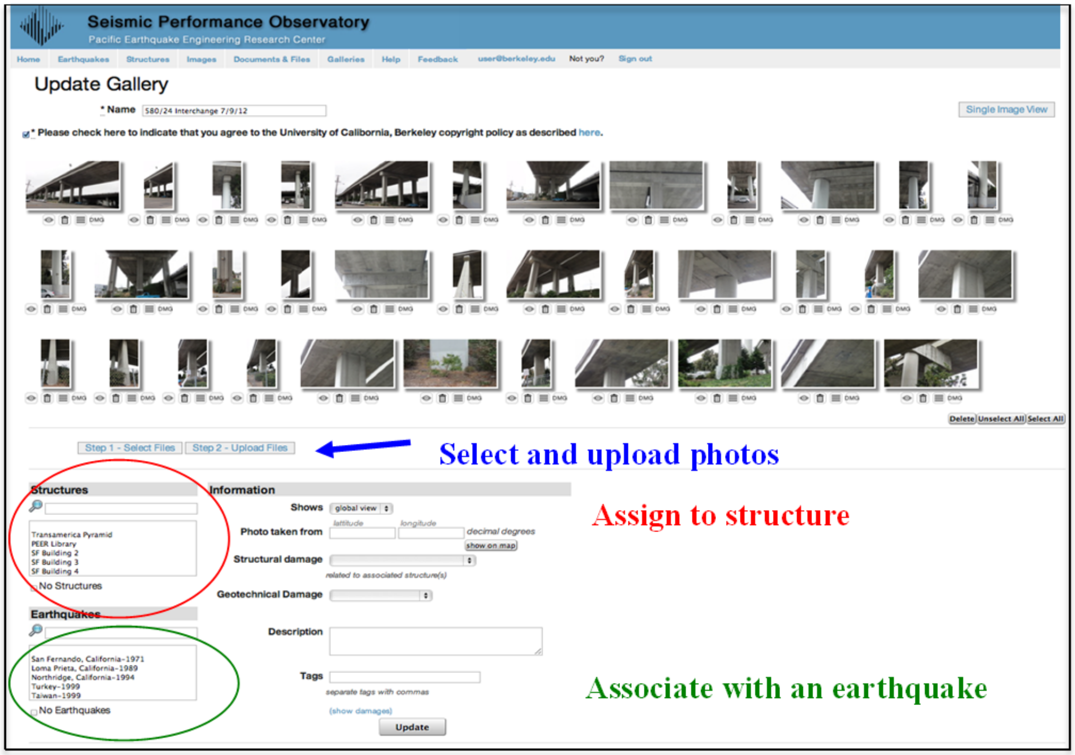


Figure 3.10 Gallery Interface, displaying the mass assigning feature.

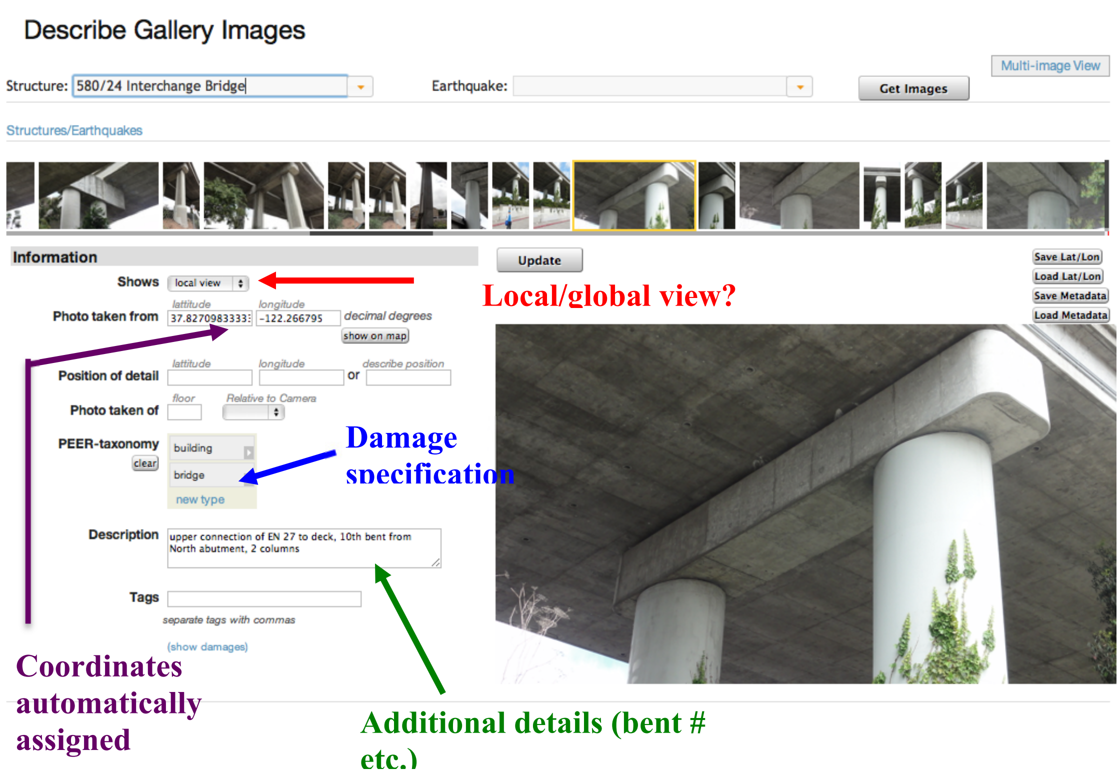


Figure 3.11 Image documentation interface.

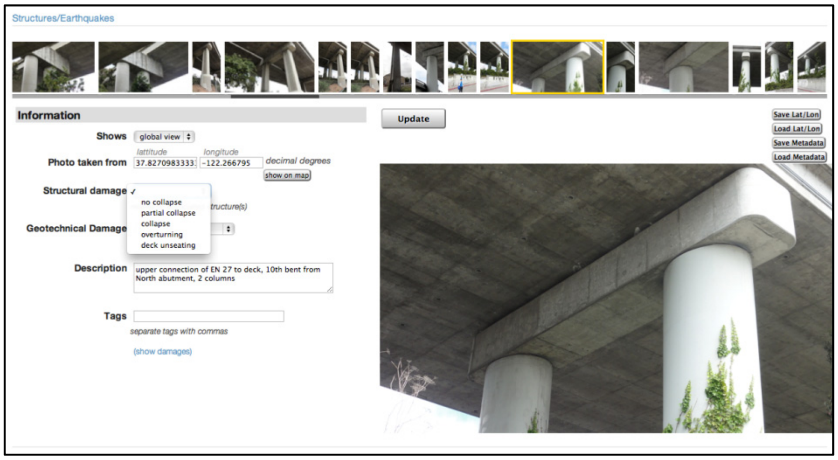


**Figure 3.12 Global view damage taxonomy.**

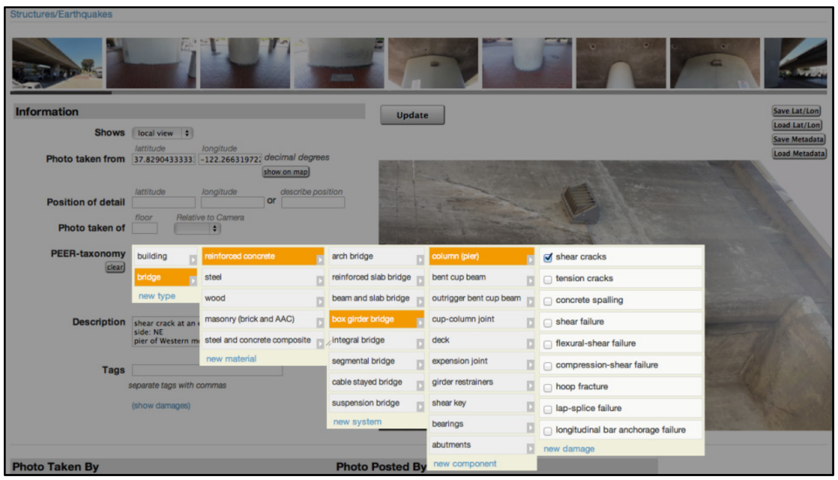


**Figure 3.13 Local view damage taxonomy (for bridges).**

### 3.4.2 Building

*San Francisco Public Utilities Commission Building, SF, CA*

1. Preliminary Information Collected:
    - Coordinates: 37.780956 N, 122.419342 W
    - Moderate liquefaction rating
    - 12.3 km from the San Andreas fault
    - Located on Type D soil, stiff soil (shear wave velocity between 600 and 1200 ft/sec)
    - Material: steel and concrete composite
    - Structural system: shear wall with steel frame and reinforced concrete infill walls. Consists of a dual (frame-wall) lateral system and steel frame with cast in-situ concrete shear walls
    - Instrumentation devices: 24 accelerometers, 2012
    - Design Date: 2009

- Construction Date: 2010-2012
- Inspected on July 13, 2012
- Seismically strengthened in 1996
- Foundation type: mat foundation
- 13 stories, 277500 sq. ft.
- Building Code: 2007 SF Building Code
- Additional Notes: A full height steel tower exists on the north side, consisting wind turbines starting on the 6th floor. There are two concrete core shear walls, which utilize a "combination of vertically post-tensioned tendons and mild steel to resist the lateral loads" ("525 Golden Gate – Your New SFPUC Sustainable Headquarters" 2011). The east core is linked to an outrigger concrete column. At the penthouse, concentrically braced steel frames resist the lateral loads.

2. Gather all available plans of the structure
    - Figure 3.14 displays the annotated plan of this structure, specifying each column and location of each instrumentation device
    - Distinguish cardinal directions
3. Collect all tools and equipment (see Section 3.3.3, step #3)
4. Photograph and/or note:
    - Use the miniature white board as described in the investigation process of the 580/24 interchange bridge above
        - Be sure the white board is labeled with the correct name, as determined by the pre-established naming convention
    - Sketch any components that may seem ambiguous to the user following the investigation
5. Input findings into SPO
    - Begin by creating a structure, following the provided taxonomies and instructions for buildings shown in Figure 3.8. The structure's database profile is shown in Figure 3.15.
    - Create a new gallery by uploading the photos and selecting a structure to which the photos should be assigned, as shown in Figure 3.10.
    - Begin editing the gallery by evaluating each photo, inputting a description and type of view
        - Please refer to the previous example to obtain a more thorough explanation on how one may input specific types of data

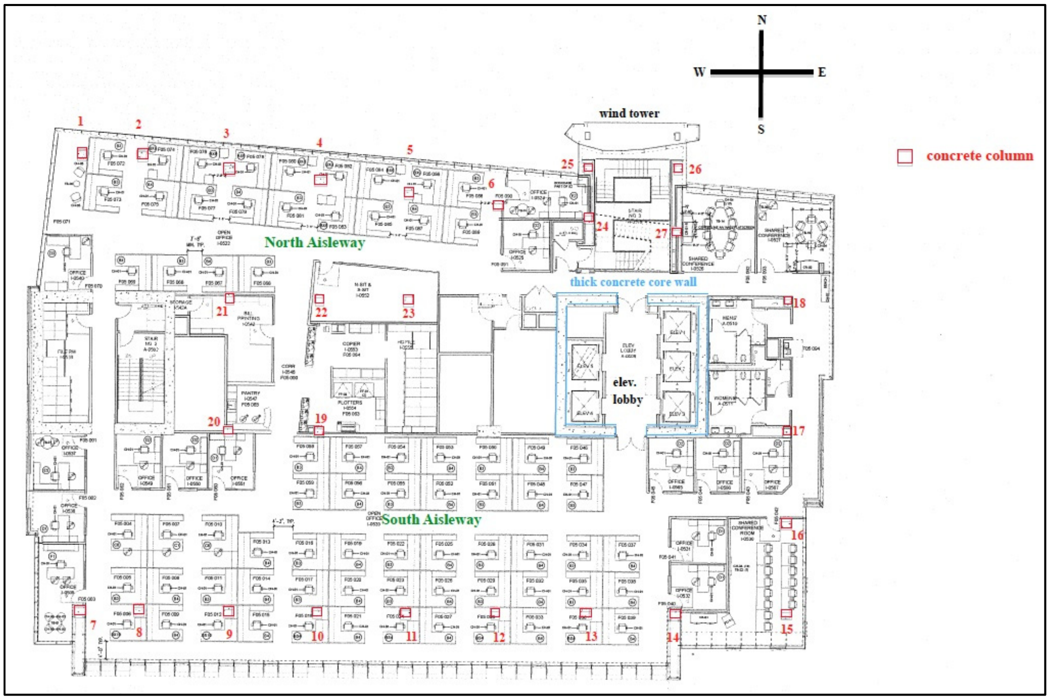


**Figure 3.14 Annotated plan of San Francisco's Public Utilities Building.**

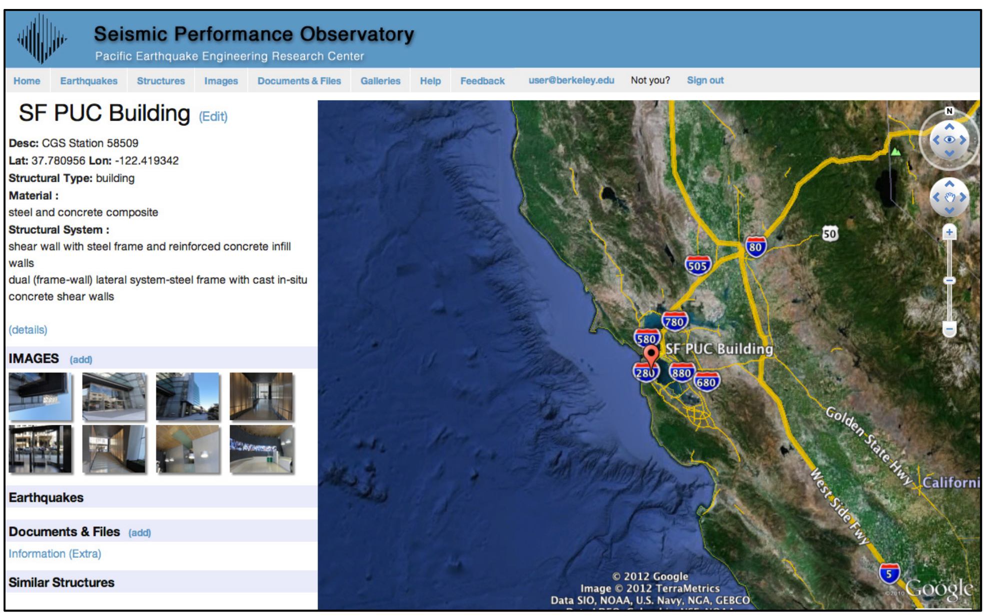


**Figure 3.15 Global view taxonomy.**

## 3.5 EARTHQUAKE DOCUMENTATION AND ANALYSIS

In addition to offering structural data sets and their relation to earthquakes, SPO also contains a metadata class for earthquake-specific information. This archive of past earthquakes will include a large variety of resources and links (detailed USGS shake maps, fault maps, instrumented structures map, stations map, inspections map, soil characterization map, etc.) and will give users the opportunity to draw trends and compare different types of information related to an earthquake and its consequences. A screenshot of the Earthquake interface within SPO is shown below in Figure 3.16.

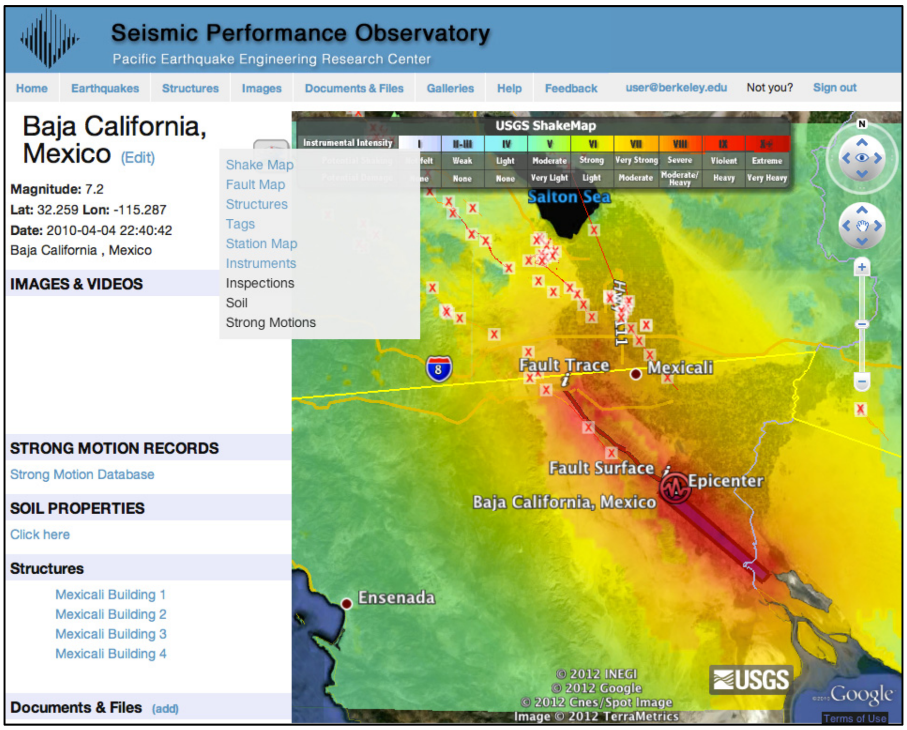


**Figure 3.16 Earthquake profile on SPO, USGS Shake Map displayed.**

## 3.6 SEARCHING CAPABILITIES

Along with SPO's invaluable data storing abilities, this observatory will offer an extremely powerful research tool – a search feature. The extensive and articulate meta-data tagging system built into the database allows users to find all available information regarding very specific qualifications. As shown in the snapshot of SPO's searching interface, Figure 3.17, the user may search for a particular type of structural component on soil type "X" that experienced "Y" type of damage, and the network will identify and present all records that fit this criteria. Users will also be given the opportunity to search for a group of structures with similar attributes, such as structural system, material, foundation type, experience of ground motion etc. SPO's web-like search feature will link together archived data from external sources and current visual data provided by engineering community members, and offer users a qualified group of structures that conform to their search specifications. This comparison tool and highly detailed search engine, enabled by the hundreds of data layers embedded into the observatory, will help users build relationships between types of structures, levels of damage, and degrees of ground motion, and allow researchers to access all available information pertaining to a very specific combination of metadata.

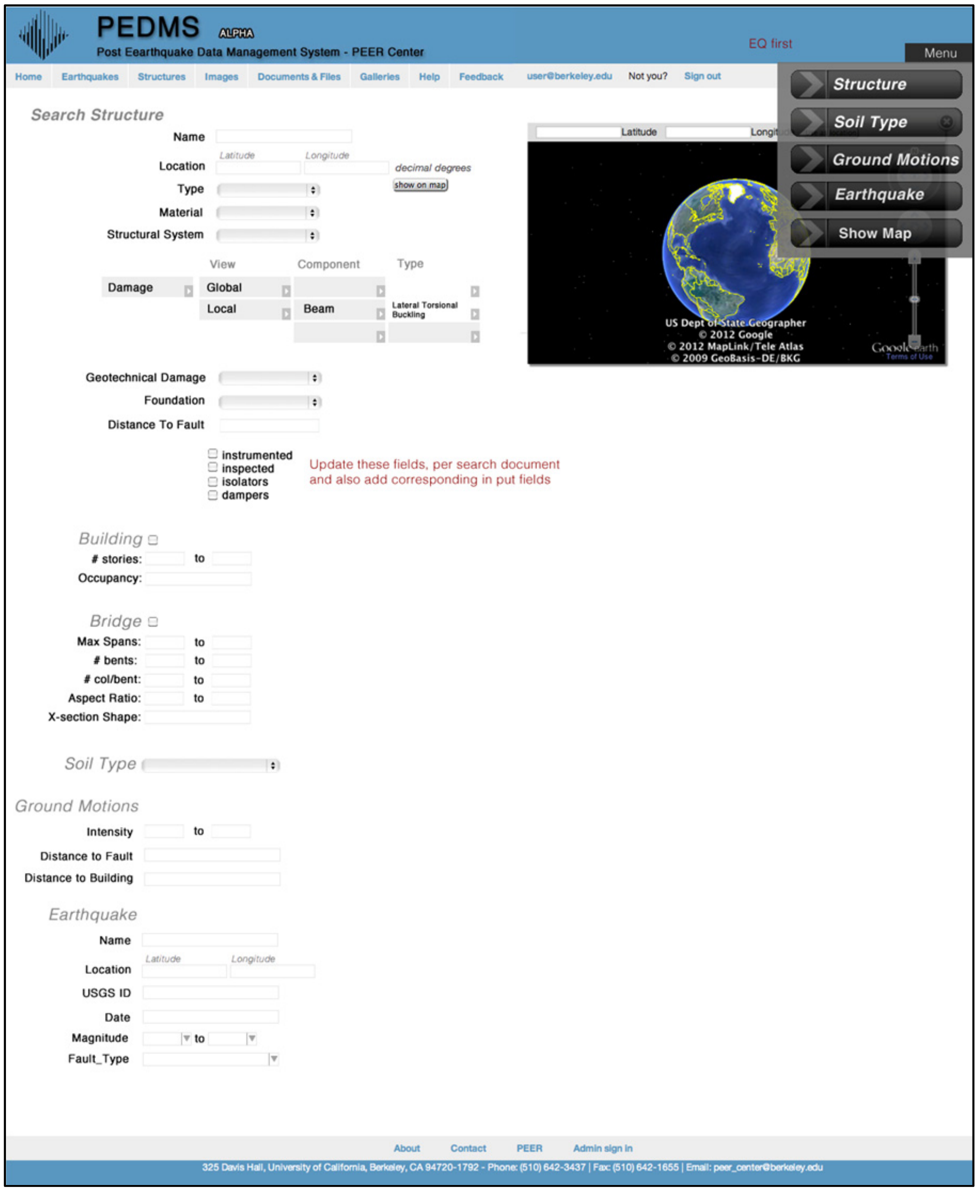


**Figure 3.17 SPO's search feature.**

## 3.7 CURRENT PROGRESS OF SPO

While performing multiple pre-earthquake investigations and continuously contributing to SPO's growing collection of data, PEER encountered multiple obstacles and concerns from external resources, performed a number of alterations to the system in an effort to create the ultimate user-friendly interface, and solidified SPO's core objectives. The various barriers, security concerns, improvements to SPO's interface, and the overarching goal of producing fragility curves based on recorded damage are expanded upon below.

### 3.7.1 Obstacles

The most common obstacle was associated with gaining permission from building managers to document interior structural and nonstructural elements. Although the project's research incentives were explained to a number of representatives, security and privacy concerns often held precedence and further permission was sought out and acquired. In addition to a general hesitance from building officials to give interior access, external agencies that PEER felt could both contribute to and benefit from SPO addressed the issue of security and public access. Security concerns, described more thoroughly in Section 3.7.2 were quickly subdued with an explanation of PEER's plan to create a layered account system within SPO that will incorporate various levels of access. Lastly, while performing pre-earthquake investigations on seismically instrumented structures and using SPO's interface to input a wealth of data, modifications were constantly made to ensure the most efficient and systematic method for approaching pre- and post-earthquake investigations as well as obtain the ultimate user-friendly environment.

### 3.7.2 Security Concerns

After presenting SPO's objectives to a number of external agencies, there arose a common concern regarding public access and various security levels. To avoid the misuse and abuse of SPO's extensive collection of data, this observatory will incorporate several layers of access, many of which will require special permission from an external source. Each new user will create an account, request the type of data desired, and then receive an email confirmation and permission from the appropriate representative. This tiered account system will ensure the safe usage of structural information and provide users with an incentive to store additional data in SPO's reliable environment.

### 3.7.3 The Ultimate User-Friendly Interface

In order to receive impactful contributions from the public, this database must be easily accessible in its vocabulary, format, and development. While pre-earthquake investigations were performed and data was collected and inputted into SPO, the database's interface experienced a number of alterations that would help improve the overall accessibility of the network. Specific modifications were sketched out, sent to PEER's database administrator, and then implemented. Figure 3.18 is a sketch of the desired alterations to the definition of a bridge's bent geometry. The content and layout is carefully displayed in each sketch, with side notes shown in red. The importance and value of an accessible, adaptable, user-friendly system is what will fuel SPO's expansion and most effectively encourage outside contributions.

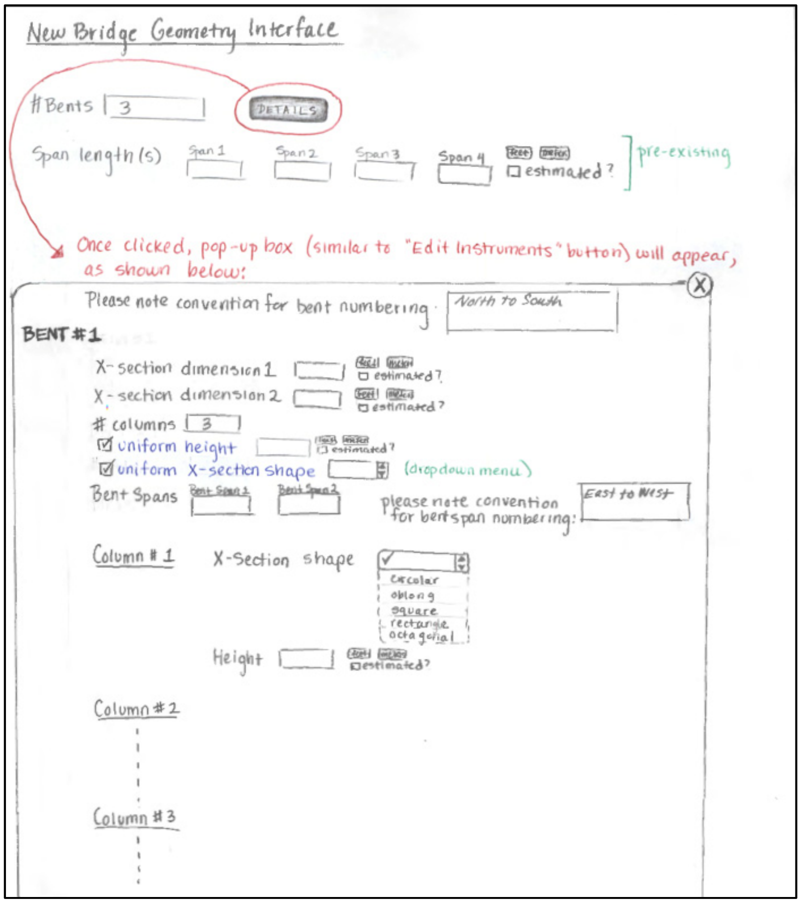


**Figure 3.18 Sketch of the interface design for bridge geometry.**

### 3.7.4 Fragility Curves

As mentioned above, one of the primary attributes of this database is its ability to describe and quantify damage, and offer a preliminary baseline of information from which engineers can draw comparisons following an earthquake. Although the recording of damage after an earthquake while invaluable, even the *lack* of damage may contribute to the development of fragility curves and the analysis of seismic vulnerability. Fragility curves, which study the relationship between probabilities of unacceptable seismic responses and levels of ground motion, serve as a key tool in performance-based design and offer researches a wealth of data [Mander 1999]. In order to produce a set of fragility curves that correlate engineering demand parameters (EDPs) with the damage state of a structural or nonstructural component, there must be access to shake maps, ground motion data, the structure's primary characteristics, and performance during an earthquake [Mahin et al. 2012]. With SPO's central, data-storing capabilities, the development and production of fragility curves seems highly plausible and would greatly benefit the earthquake engineering research community.

### 3.7.5 Immediate Source of Data

There is very little time between the actual occurrence of an earthquake and the necessity to travel to each site and analyze the behavior of various structures. Currently, the most critical concern is that directly following seismic activity, there is a limited source of data from which one can perform a successful post-earthquake investigation [Mahin et al. 2012]. As demonstrated throughout this paper, SPO will immediately offer access to a range of drawings, visual footage of the building before the event of an earthquake, specific information essential to structural analysis, and an advanced search engine that will assist those searching for patterns of structural performance. This database may also provide a tool to observe traffic information for various routes towards a site immediately following an earthquake.

## 3.8 CONCLUSIONS

With the ultimate goal of storing mass amounts of pre- and post-earthquake data as well as quantifying damage found before and after an earthquake, SPO provides researchers with the tools necessary to validate computer models and produce effective fragility curves. This organized, user-friendly database, equipped with advanced searching capabilities, offers a strong baseline of information and allows researchers and professionals to draw comparisons and identify trends. Having performed the established pre-earthquake investigation and SPO procedure for 10–12 buildings and bridges thus far, it is PEER's hope that others will use the examples provided in this report, follow the investigation plan, employ SPO's User's Manual, and actively contribute to this central location for hundreds of records, links, geological maps, pre-earthquake investigation findings, and much more.

With the intention of storing large amounts of earthquake data as well as pre-earthquake data from high earthquake risk communities, this integrated system will offer engineering research and professional communities an irreplaceable resource for data sharing. However, only with a strong pre-population of data and a continuous addition of data following seismic events will this web-based environment truly benefit the engineering community, and provide researchers with the quantitative information needed to advance performance-based design. That said, in order for the Seismic Performance Observatory to progress and for PEER's vision to be achieved, unconditional support and contributions from community members are critical.

## ACKNOWLEDGMENTS

This research was supported and funded by the Pacific Earthquake Engineering Research (PEER) Center as a part of the 2012 summer internship program and by the National Science Foundation. I would like to thank Stephen Mahin, my faculty advisor and PEER director, and Vesna Terzic, my dedicated graduate mentor, for their unconditional support and guidance. I thank my fellow intern, Eddie Vega, for his invaluable company and PEER's outreach director, Heidi Tremayne, for her incomparable organization and leadership. Additional thanks go to James Way, PEER's database administrator, for assistance in developing SPO's interface, and finally the staff at UC Berkeley's Richmond Field Station for contributing investigation equipment when needed.

## REFERENCES


Caltrans (2012). *PEQIT Manual 2012*, last modified January, 2012, accessed June 27, 2012, *http://www.dot.ca.gov/hq/esc/earthquake_engineering/PEQIT/.*

CESMD. *Strong Motion Stations in Northern California*, Center for Engineering Strong Motion Data, last modified March 23, 2011, accessed June 2012. *http://www.strongmotioncenter.org/.*

Earthquake Engineering Research Institute (2010). *Post-Earthquake Investigation Field Guide,* last modified 2010, accessed June 27, 2012, *http://www.eeri.org/site/lfe-field-guide.*

Hamburger RO (2000). *Recommended Post-earthquake Evaluation and Repair Criteria for Welding Steel Moment-Frame Buildings*, Federal Emergency Management Agency, FEMA-352, Washington D.C.

Mahin SA, HA Faison, V Terzic, and J Way (2012). Development of a system for visualization and management of information on the earthquake performance of structures, Pacific Earthquake Engineering Research Center, PEER, University of California, Berkeley, pp. 1–10.

USGS (2009). 2009 earthquake probability mapping, U.S. Geological Survey, last modified November 4, 2010, accessed June 2012, *http://geohazards.usgs.gov/eqprob/2009/index.php.*

USGS (2012). *Soil Type Map*, U.S. Geological Survey, last modified June 8, 2012, last accessed June 2012, *http://earthquake.usgs.gov/regional/nca/soiltype/.*

USGS (2012). *Liquefaction Hazard Maps*, U.S. Geological Survey, last modified June 8, 2012, last accessed June 2012. *http://earthquake.usgs.gov/regional/nca/qmap/.*

## 3.9 APPENDIX: SEISMIC PERFORMANCE OBSERVATORY USER'S MANUAL

PACIFIC EARTHQUAKE ENGINEERING RESEARCH CENTER

UC Berkeley ▪ Caltech ▪ OSU ▪ Stanford ▪ UC Davis ▪ UC Irvine ▪ UC Los Angeles ▪ UC San Diego ▪ USC ▪ U Washington

# SEISMIC PERFORMANCE OBSERVATORY

# USER'S MANUAL

Last Modified: 08/20/12

For Information and permission to use these training modules, please contact:


Stephen Mahin – mahin@berkeley.edu - (510) 642-3437

University of California Berkeley

## TABLE OF CONTENTS

## OBJECTIVE

The Seismic Performance Observatory (SPO) is a centralized web-based database for the storage and organization of data relevant to the earthquake engineering community. The purpose of this resource is to facilitate the collection and sharing of this information for use in seismic performance analyses. This manual provides users with a thorough understanding of how to use SPO by creating and editing structures and galleries, uploading and editing images and documents, and defining and inputting appropriate metadata.

## CREATING AN ACCOUNT

To be added

## CREATING AND EDITING A STRUCTURE

1. Click **Structure > New Structure**
2. Insert the Name and Location in the provided fields
    a. To specify the location, one can directly input the structure's coordinates or address
    b. To the right, a button labeled "Show on map" will direct the user to a Google Earth view. If the coordinates or address were slightly incorrect, the user may simply click on the correct location on the given map and press "Use as location" to reassign the structure's location.
3. Specify the structural system using the provided taxonomy. If the desired material or system is not offered, click "new material" or "new system" within the taxonomy field to more precisely define the structure.

**IF BUILDING:**

4. Input additional information, following the fields provided
    a. If the Story height or Span is entered in **feet**, one may select **meters** to convert the measurement, and vice versa
    b. Input soil and liquefaction information by using the given soil type and liquefaction zone KML files
    c. Specify the function of the structure, labeled **Primary Occupancy**
    d. If regularities in the plan exist, which is most likely the case, please describe them
    e. If the structure is instrumented, click **Edit Instruments**, and specify the number of instruments and the date of instrumentation mounting

f. If the structure has undergone an inspection, click **Add Inspections** and specify the type, date, inspector, earthquake associated with the inspection, and any additional comments. One may also assign a gallery of photos associated with this inspection. Click **Done** to finalize all details.
g. If the structure has isolators, click **Add Isolators** and specify the location, type, quantity, and any additional specifications or comments. Click **Done** to finalize all details.
h. If the structure has dampers, click **Add Dampers** and specify the location, type, quantity, and any additional specification or comments. Click **Done** to finalize all details.
i. If the Design and/or Construction Date are known, please input this information in the given fields
j. If the Building Code is known, please specify this in the given field
k. Any additional Notes about the structure may be inputted in the provided field labeled **Notes**

5. After inputting all relevant data, click **Create Structure** in the bottom left corner

**IF BRIDGE:**

4. Input additional information, following the fields provided
   a. Specify the number of Bents and whether or not the Span Length between the bents is uniform
      i. Please note the convention for bent numbering in the designated field (i.e., *North to South, East Abutment to West Abutment)*
      ii. If the Span Length is entered in **feet**, one may select **meters** to convert the measurements, and vice versa
   b. For each Bent, specify whether the columns have a uniform height and/or cross-sectional shape.
      i. *Uniform Column Height and Uniform Cross-Sectional Shape*: enter the height and shape and click **APPLY TO THIS BENT** (to extend this entry to only this specific bent) or **APPLY TO ALL BENTS** (to extend this entry to all bents within the bridge). These buttons are provided separately for column height and cross-sectional shape.
      ii. *Uniform Column Height and Nonuniform Cross-Sectional Shape*: enter the height and click either **APPLY TO THIS BENT** or **APPLY TO ALL BENTS**. A field for the varying cross-sectional shapes will appear beneath each column heading. Specify the column's cross-sectional dimensions, as shown below.
      iii. *Nonuniform Column Height and Uniform Cross-Sectional Shape*: select the cross-sectional shape and dimensions and click either **APPLY TO THIS BENT** or **APPLY TO ALL BENTS**. A field for the varying column heights will appear beneath each column heading.

iv. *Nonuniform Column Height and Nonuniform Cross-Sectional Shape:* A field for the varying column heights and cross-sectional shapes will appear beneath each column heading. There, you may select or enter the appropriate height, shape, and cross-sectional dimensions.

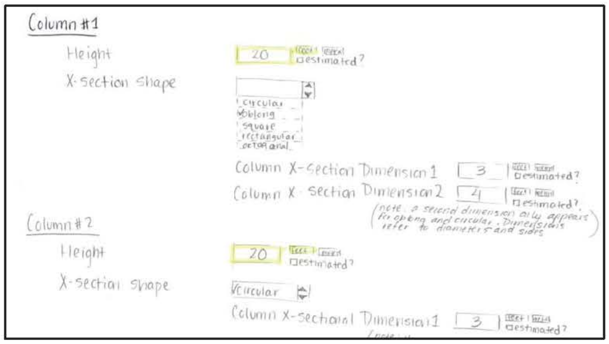


c. Input soil and liquefaction information by using the given soil type and liquefaction zone KML files
d. Specify the function of the structure, labeled **Primary Occupancy**
e. Specify the **Bearing Type**
f. If the structure is instrumented, click **Edit Instruments**, and specify the number of instruments and the date of instrumentation mounting
g. If the structure has undergone an inspection, click **Add Inspections** and specify the type, date, inspector, earthquake associated with the inspection, and any additional comments. One may also assign a gallery of photos associated with this inspection. Click **Done** to finalize all details.
h. If the structure has isolators, click **Add Isolators** and specify the location, type, quantity, and any additional specifications or comments. Click **Done** to finalize all details.
i. If the structure has dampers, click **Add Dampers** and specify the location, type, quantity, and any additional specification or comments. Click **Done** to finalize all details.
j. If the Design and/or Construction Date are known, please input this information in the given fields or select that it is unknown
k. If the Building Code is known, please specify this in the given field
l. Any additional Notes about the structure may be inputted in the provided field labeled **Notes**

5. After inputting all relevant data, click **Create Structure** in the bottom left corner

### Uploading Files to Accompany a Structure

If any drawings are available (structural, architectural, electrical etc.), click **(add drawings)** within the structure's profile interface and upload each drawing, assign a name, and add any additional comments if necessary.

**Note:**

- If any annotated plans were used during the pre-earthquake investigation, please upload these to the structure's profile.
- If any additional documents or files exist that may be useful, please click **add** to the right of the **Documents & Files** heading and upload each relevant document.

## Uploading and Editing a Gallery

To create a new gallery

1. Click **Gallery > New Gallery**
2. Assign name for the new gallery
3. Check box to agree with copyright policy

To view a gallery

1. Click **Gallery > Gallery List**
2. Select the gallery of interest

To upload images to a gallery

1. Select the gallery of interest
2. Click **Step 1 – Select Files** button
3. Browse and select all photos to be uploaded.
4. Click **Step 2 – Upload Files** button.

To edit a gallery

1. View the gallery of interest, as described above.
2. Click **Edit**.
    a. To mass edit photos, select all photos of interest
    b. Enter information into the appropriate fields shown in the following image.

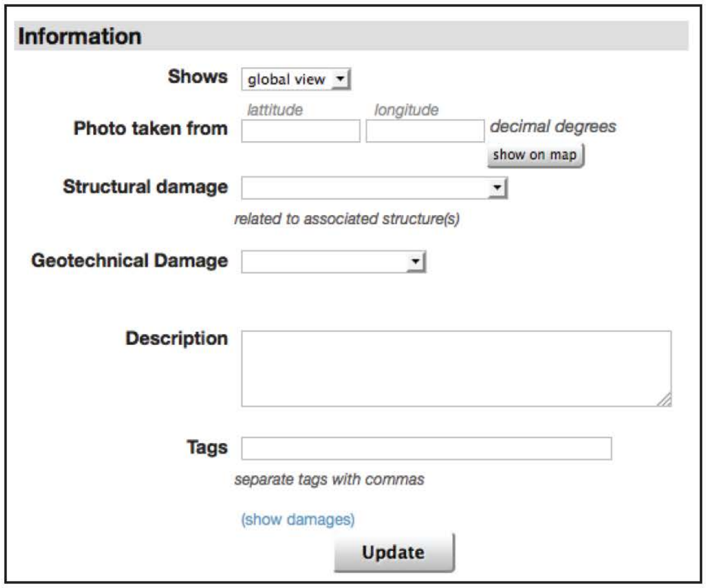


c. Click **Update**

## Assigning Gallery to Structure

1. View the gallery of interest, as previously described.
2. Select the structure to be associated with the gallery under the "Structures" section at the bottom of the page as shown below.

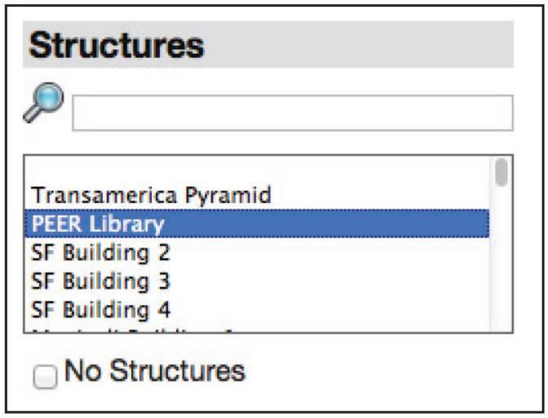


3. Click **Update**.

## Editing Images

1. View gallery.
2. Click **Edit Image** button under photo of interest.
3. Enter appropriate meta data
    a. Select either local or global view in the **Shows** field
    b. Enter latitude and longitude in the **Photo taken from** field
    c. Enter description into the **Description** field
    d. Enter tags for searching in the **Tags** field, separating different tags with commas
    e. If possible identify who posted and uploaded each photo and when, in the **Photo Taken by** and **Photo Posted by** sections near the bottom of the page.
    f. For *global views*
        i. Select any appropriate Structural Damage from the dropdown menu
        ii. Select any appropriate Geotechnical Damage from the dropdown menu
    g. For *local views*
        i. Enter the position of the detail of interest in the photo by either entering the coordinated or writing in the **describe position** field
        ii. If possible, specify the floor on which the photo was taken and select a position of the camera relative to the detail of interest in the **floor** and **Relative to Camera** fields respectively.

## Defining Damage

When editing an image:

**IF LOCAL VIEW:**

1. Under "PEER Taxonomy" select either **building** or **bridge**.
2. Continue by selecting the material, system, component, and type of damage in the options that follow, as shown in the image below. If the desired option is not found in the current list, add in the appropriate selection.

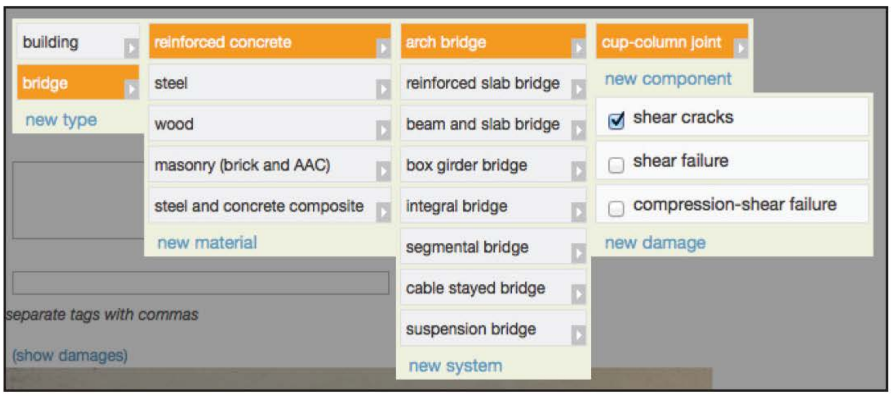


**IF GLOBAL VIEW:**

1. Select any present damage under the dropdown menus that appear under **Structural damage** and **Geotechnical damage**, as shown in the images below.

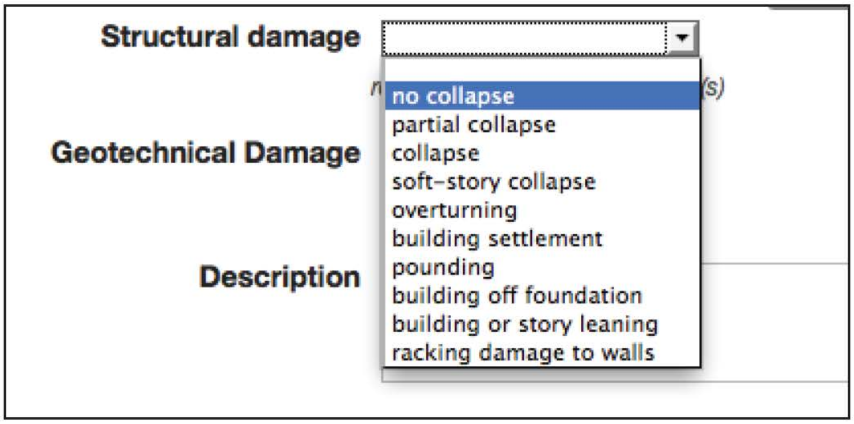


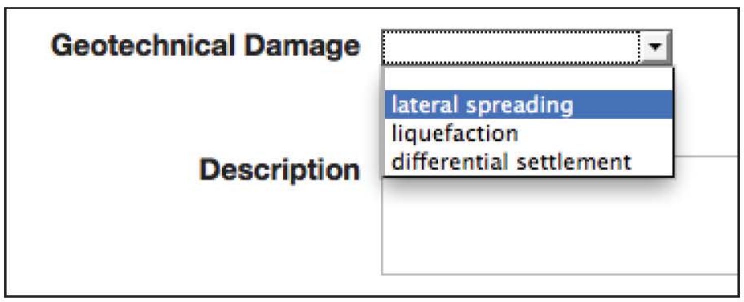


## INPUTTING EARTHQUAKE DATA

1. Click **Earthquakes > New Earthquake**
2. Input the required fields marked with an asterisk:
    a. Name
    b. Range of Time
    c. Magnitude of the earthquake
    d. Location (insert the coordinate values → click "**show on** map" → can readjust the location by clicking a different spot and pressing "**Use as location**")
3. Specify the region where the earthquake occurred as well as the Country
4. Insert the USGS ID in the specified field
5. Provide the database with any alternate names for the earthquake for a more accessible identification system

6. Click **Create Earthquake**

### Associating Structures with Earthquakes

When editing a gallery, below the images is a region for mass-assignment. Select the photos associated with the earthquake, simply click on the correct earthquake, and click **Update**. If there is no earthquake associated with the photos, check the box next to **No Earthquakes** and click **Update**.

## Utilizing the Search Engine

To be added

## Frequently Asked Questions

To be added

## Contacts

**Professor Stephen Mahin**
PEER Director
(510) 642-3437
mahin@berkeley.edu

**Vesna Terzic**
OpenSees, Transportation Systems Research Program
vesna@berkeley.edu

**James Way**
Database Administrator
(510) 665-3531
jamescway@berkeley.edu

**Dorian Krausz**
PEER Summer Intern 2012
(415) 686-2759
doriankrausz92@yahoo.com

**Eddie Vega**
PEER Summer Intern 2012
(626) 482-3770
eddie.j.vega@gmail.com

# PRE-EARTHQUAKE INVESTIGATION PROCEDURE

Last Modified: 08/20/12

For Information and permission to use these training modules, please contact:

Stephen Mahin – mahin@berkeley.edu - (510) 642-3437

University of California Berkeley

## TABLE OF CONTENTS

**Goal:** Gather both visual and quantitative pre-earthquake information that will contribute to the growing Seismic Performance Observatory database and serve as an accessible and organized resource and baseline to the public following an earthquake.

*The following plan is intended for the pre-earthquake investigation of buildings and bridges. It uses the Post-Earthquake Investigation Field Guide by EERI and the PEQUIT Manual by Caltrans as a reference ("Post-Earthquake Investigation Field Guide" 2010, "PEQIT Manual 2012" January, 2012).*

## INVESTIGATION PLAN:

### Plan:

1. Collect preliminary information about the building
   - Building/Bridge plan drawings (structural, mechanical, architectural, electrical etc)
   - Structural System
   - Material
   - Function
   - Foundation type
   - Liquefaction Zone
   - Soil Type
   - Year designed, constructed, retrofitted, and instrumented
   - Details regarding instrumentation (location, type etc.)
   - If applicable, collect:
     - ✓ Number of stories
     - ✓ Base dimension
     - ✓ Number of bents/spans
     - ✓ Number of columns per bent
2. Coordinate with other engineering groups and people of interest
   - Note: those with field investigation experience are most suitable, however, interest and availability are also of strong importance
3. Bring a set of drawing plans to the investigation site
   - Use these to draft the investigation route through and around the structure
   - Identify which components of the structure may lead to its failure during an earthquake (damage zones)
   - Tag key areas of interest on the plan
   - Use voice memo recorder to document further comments/observations for photos as necessary for future reference
4. Collect all tools and equipment needed for pre-earthquake investigation:
   - **Toolbox/Bag to hold the following items:**
     - ✓ Camera (with GPS technology)
     - ✓ Tripod
     - ✓ Film and memory cards (plan for high capacity needs)
     - ✓ Voice Recorder (and cassette tapes)

- ✓ Mini white board (for scale and photo labeling)
- ✓ White board markers and erasers
- ✓ Tape measure (100ft)
- ✓ Plumb Bob/Level
- ✓ Notebook/notepad
- ✓ Pens, pencils, erasers
- ✓ Maps of site (if available)
- ✓ Plans of site (if available)
- ✓ Radio
- ✓ Cellular phone
- ✓ Walkie-talkies
- ✓ Binoculars
- ✓ Chargers and batteries for camera, phone, etc.
- ✓ Valid ID cards (Company specific ID Badge if possible)
- ✓ Hardhats
- ✓ Orange Vests
- ✓ Appropriate clothing for site
- ✓ Food/water

- Smart phone with the following applications:
  - ✓ 360 degrees
  - ✓ Magic Plan
  - ✓ Voice Recorder
- **Safety**
  - ✓ Vest
  - ✓ Identification
  - ✓ Hardhat
  - ✓ Flash light
  - ✓ Covered clothing (close toed shoes, full length pants etc.)
  - ✓ **In addition, for Bridges:**
    - Lane closures
    - Physical Barriers
    - Air horns
    - Rent lights (if necessary)
    - Safety glasses or goggles
      - When near moving traffic or in highway work zones
    - Coveralls

5. Observe - Note - Photograph:
   - Record actual route taken during the investigation and locations of key photos/notes (mark references on the drawings)

### General Assessment for Buildings:

- ✓ Begin by photographing global views of the structure from all sides
- ✓ Photograph the building's corners, windows, and any protruding structures (piping, etc.) that connects to an exterior source
- ✓ Photograph instrumentation of each structure – if visible

- ✓ Note any nonstructural elements that are connected to structural elements (if exposed)
- ✓ Note the presence of glass, decorative screens of metal, masonry, wood, or plastic
- ✓ Large scale graphics or illuminated signs
- ✓ If large focus on interior:
    - Furniture, equipment, wall-hung objects, storage cabinets, displays, shelving systems, files
    - Suspended ceilings – if so, describe the system (material, grid system, hangers, grills, bracing etc.)
    - Computers
    - Decorative objects
    - Heating, air-conditioning systems
- ✓ General photos of neighboring structures
- ✓ **SEE THE REFERENCE LIST OF STRUCTURAL SYSTEMS BELOW TO DETERMINE WHAT ADDITIONAL OBSERVATIONS MUST BE MADE**

- ✓ **In the event of a multi-story building:**
    - Investigate the ground level, mid segment, and upper segment for each structural system separately, following the plan above
    - Focus on stairs and elevators (emergency exit strategy)
    - For structures with multiple structural systems (divided on different floors) – evaluate each segment separately

### General Assessment for Bridges:

- ✓ Take photographs of elevation views of structure to show general condition
- ✓ Residual displacements of columns and bents
    - Use plumb bobs, level, etc. for reference
- ✓ Photograph and measure cracks in the structure
    - Determine cause of crack (bending, shear, compression)
- ✓ Check abutments, piers, wingwalls, retaining walls, etc. for signs of movement, misalignment, and cracking.
- ✓ Check for indications of movement at hinges, joints, railings, and curbs.
- ✓ Damaged utilities
    - Electrical shorting, disconnected power, gas, and water lines
- ✓ Exposed piles, cracks in foundations
    - Document and photograph current condition
- ✓ Connections of widenings
    - Note and photograph conditions of key area where damage can develop
- ✓ Check for general damage that indicates structural movement
    - Scrape marks, dents, holes
- ✓ Note directions of any leanings or fallings
- ✓ Check for deformed or displaced bearings

- ✓ Note condition of equalizing bolts, restrainers, and shear keys
- ✓ Note and photograph broken welds, rivets, or bolts

### Additional Nonstructural Considerations for Both Bridges and Buildings (if applicable):

- ✓ Communication Systems:
    - Telephone, microwave towers and disks,
    - Computer centers
    - Digital switches
    - Bracing systems used to support communications equipment
    - Emergency power supplies
    - Radio and Television
        - Anchorages and bracing – ability to remain operational?
        - Antenna towers – note height, foundations, type, and materials
        - Emergency power supplies available?
- ✓ Newspapers and Magazines
        - Printing equipment
        - Storage racks
        - Stock of printing materials
- ✓ Electric Power Delivery Systems
- ✓ Gas and Liquid Fuels
- ✓ Water Delivery and Treatment
- ✓ Fire-Resisting Elements
- ✓ Internal Utilities
    - Emergency electrical power systems
    - Emergency generators
    - Natural gas supply system equipped with automatic shutoff valve?
    - Telephone and communication systems

6. Propose suggestions that may improve the structure's seismic response
    - Recommend specific areas of potential damage for more detailed post-earthquake investigations
7. Enter findings into the Seismic Performance Observatory database
8. Prepare a report based on findings

**STRUCTURAL SYSTEM REFERENCE (FOR BUILDING INVESTIGATION):**

- **Moment Resisting Frames**
  - ✓ *In General*
    - Frame as a whole, noting types of connections and loading variations
    - Nonstructural elements such as infill walls, stairs, escalators, and partitions
    - Welded, bolted, nailed, and riveted connections
  - ✓ *Reinforced Concrete Moment Resisting Frames*
    - Anticipated cracking regions and locations of brittle or ductile behavior
    - Anticipate tensile or compressive axial load cracking, shear or diagonal tension cracking
    - Columns
    - Beams – specifically bar cutoffs, splices, bottom bar anchorage
    - Joints of beams and columns
    - Reinforcing details – ties, stirrups, splices of longitudinal steel (extract from building plan)
  - ✓ *Steel Moment Resisting Frames*
    - Anticipate locations of possible buckling
    - Columns – note bases of columns (anchor bolts, connection material, grout)
    - Beams
    - Joints
    - Column splices and joints
    - More heavy jumbo sections
    - Offsets or transfer girders
    - Welds
    - Moment connections – note the type, flexibility, stiffeners, and ductility
- **Steel-Braced Frames**
  - ✓ Braces
  - ✓ Connection details
  - ✓ KL/r
  - ✓ Anticipate regions of possible distress
- **Masonry Buildings**
  - ✓ Walls and reinforcing details
  - ✓ Pier and spandrel detail
  - ✓ Floor-to-wall anchorage
  - ✓ Roof-to-wall anchorage
  - ✓ Quality of workmanship on grout, mortar etc.
- **Concrete Buildings**
  - ✓ *Precast Concrete Buildings*
    - Joint
    - Topping slab present?
    - Ties/lack of ties
    - Connections between elements and frames, and between elements and foundations
    - Quality of construction materials in concrete

- ✓ *Pre-stressed/Post-Tensioned Concrete Buildings*
  - Type of pre-stressed system
  - Grouted tendons?
  - Anchorage
  - Slab to wall details
  - Joints between horizontal and vertical elements

- **Wood Frame Buildings**
  - ✓ Shear walls
    - Nailing patterns
    - Sheathing materials
    - Hold downs
  - ✓ Connections
  - ✓ Gypsum board sheathing? Plywood?
  - ✓ Roof – spaced sheathing?
  - ✓ Masonry veneer or chimney
  - ✓ Anchorage details
- **Portable Buildings**
  - ✓ Construction materials (wood, steel, concrete, etc.)
  - ✓ Lateral load resisting system for building superstructure (wood, shear wall, steel frame)
  - ✓ Overall superstructure
  - ✓ Anchorage?
  - ✓ Type of foundation (stacked wood, masonry units, concrete, steel jackstands)
  - ✓ Connections between supports and building
  - ✓ Any earthquake bracing systems present?
  - ✓ Supports or bracing system
  - ✓ Non-structural components – ceiling tiles, ceiling grid system, light fixtures, window, furnishings
  - ✓ Utilities
- **Shear Walls**
  - ✓ *In General*
    - Number and placement of shear walls
    - Structural elements added after the initial construction of the building – do they lack adequate strengthening?
  - ✓ *Poured-in-Place Concrete Shear Walls*
    - Layout and vertical continuity of shear walls
    - Construction joints
    - Keys and dowels
    - Discontinuity of materials at construction joints
    - Joinery of shear walls, diaphragms, framing members, floors, foundations
    - Concrete quality
    - Connection of infill shear walls to the frame
  - ✓ *Precast Concrete Shear Walls*
    - Follow the checklist for poured concrete as well as:

- Types of fasteners to the frame, between units, and to diaphragms
- System of load transfer between units and the structural frame and between units and the foundation

✓ *Masonry Shear Walls*
  - Follow the checklist for poured concrete as well as:
    - Mortar and grout, type of bond
    - Note whether concrete columns were poured before or after masonry walls were constructed (pouring after has proven better bond to masonry…)
    - Connection of foundations

✓ *Wood Shear Walls*
  - Type of sheathing – blocked or unblocked plywood, straight or diagonal boards, metal straps?
  - Sheathing fasteners – type, pattern, spacing
  - Anchorage and ties, struts, chords etc.
  - Connections to foundations

✓ *Steel Shear Walls*
  - Type of wall (corrugated or stiffened sheet)
  - Connections between panels and to supports
  - Shear transfer elements to frame and foundation

▪ **Base-Isolated Structures**
  - ✓ Number, type, and size of isolators
  - ✓ Presence of back-stop devices used to limit displacements
  - ✓ External condition of isolators
  - ✓ Clearance gap around the building

▪ **Diaphragms**
  - ✓ Diaphragm system
  - ✓ Chords, drag struts, continuity ties
  - ✓ Diaphragm webs at points of concentrated loading
  - ✓ Plywood diaphragms with and without steel anchors connecting joists to walls?
  - ✓ Connections
  - ✓ Concrete topping slab on precast elements
  - ✓ Gypsum deck
  - ✓ Horizontal rod bracing system

▪ **Foundations**
  - ✓ Backfilling around structure
  - ✓ Soil type
  - ✓ Water presence
  - ✓ Subsidence
  - ✓ Attachments (stairs, walks, etc.)
  - ✓ Utility lines, piping etc.
  - ✓ Liquefaction zone?
  - ✓ Basement walls
  - ✓ Batter piles

- **Previously Repaired, Retrofitted and Strengthened Buildings**
    - ✓ Note types of repair
    - ✓ Code used if building was strengthened
    - ✓ Any inadequate repairs?
    - ✓ Anchoring?

## References

1. Earthquake Engineering Research Institute, "Post-Earthquake Investigation Field Guide." Last modified 2010. Accessed June 27, 2012. http://www.eeri.org/site/lfe-field-guide
2. Caltrans, "PEQIT Manual 2012." Last modified January, 2012. Accessed June 27, 2012. http://www.dot.ca.gov/hq/esc/earthquake_engineering/PEQIT/

## Contacts

**Professor Stephen Mahin**
PEER Director
(510) 642-3437
mahin@berkeley.edu

**James Way**
Database Administrator
(510) 665-3531
jamescway@berkeley.edu

**Eddie Vega**
PEER Summer Intern 2012
(626) 482-3770
eddie.j.vega@gmail.com

**Vesna Terzic**
OpenSees, Transportation Systems Research Program
vesna@berkeley.edu

**Dorian Krausz**
PEER Summer Intern 2012
(415) 686-2759
doriankrausz92@yahoo.com

# 4. Maximizing Learning from Real Earthquakes


## EDUARDO VEGA



### ABSTRACT

The earthquake engineering community is in need of a centralized, accessible database for seismic and structural information. The Pacific Earthquake Engineering Research (PEER) Center is developing a seismic performance database called the Seismic Performance Observatory (SPO) in order to facilitate and organize the collection of technical data from pre and post-earthquake investigations. Procedures for these investigations have been developed and applied in the field to test and determine effective methods of data collection. This report contains a summary of the development of the database and these procedures, and covers the background of the project, the methodology of the development, problems encountered, and the final state of the project.


### 4.1 INTRODUCTION

Earthquakes act as natural occurring experiments and provide a wealth of data on the seismic performance of structures. Earthquake investigations are a common practice in the collection of this data. Currently, separate organizations conduct their own investigations, using self-determined procedures and independently store and organize their data. Due to this lack of cooperation, much of the data collection efforts are not synchronized and result in redundant records, a general lack of structure in the overall compilation of data, and inefficiencies in the use of time and other resources. This has created a need for a streamlined approach for earthquake investigations, and a common hub for the archive and organization of gathered information. This project seeks to develop a database and procedure for use with pre and post-earthquake investigations. The intent of this is to foster cohesion in the rush to gather data after an earthquake and provide a central system of organization for all information relevant to the earthquake engineering community for seismic performance analyses. This purpose makes this research project somewhat unique. Rather than trying to answer a specific question, the work of this project is directed towards working towards a specific solution to the mentioned problem.

The PEER is taking an active responsibility in contributing to the earthquake engineering community and towards fulfilling this need with this project. The SPO is designed to act as the centralized system for the archiving, organization, and use of earthquake and structural information. The contents of this report cover PEER's efforts to address this necessity directly through this project. The background covers the current situation of earthquake investigation procedures and databases. The methodology section covers the planning of the earthquake investigation procedures and the development of the SPO. The results section presents the current status of the project in regards to the investigation procedures and SPO, highlights a specific investigation, and concludes with an assessment of the project and the future work needed to continue the progress and evolution of these tools that PEER has developed.

### 4.1.1 Background: Current Situation

The need for a procedure for earthquake investigations and a system to store and organize the collected data is not new. Procedures and storage systems developed by various organizations to meet their individual needs have already been developed. What is lacking in the earthquake engineering community is a centralized and shared hub for seismic performance data of structures that is easily usable for seismic performance analyses. In the development of this resource, it is important to be aware and understand what currently exists in the field regarding this need and how these tools can be improved.

### 4.1.2 Current Earthquake Investigation Procedures

Earthquake investigations are a common practice to gather seismic performance data for a structure. As such, various organizations have independently developed their own manuals and procedures for conducting these investigations. However, the majority of these pre-existing investigation protocols are only designed for post-earthquake investigations. For this project, procedures previously established by Caltrans and the Earthquake Engineering Research Institute (EERI) were referenced to develop a pre-earthquake investigation guide. One difficulty that arose with this is that were no specific references to help with the creation of a pre-earthquake examination. Despite the concern, these manuals were helpful in that by identifying areas were of specific interest in a post-earthquake investigation, they provided direction and parameters for the information necessary to perform a pre-earthquake investigation procedure. A copy of the pre-earthquake investigation procedure developed for this project can be found in PEER's Pre- and Post-Earthquake Investigation Plans (see Section 3.9 of this volume).

### 4.1.3 Seismic Performance Analysis

The significant potential use of the database is that it can act as a resource of organized and searchable data when conducting a seismic performance analysis. By cataloging photographs and other data about structures of interest and using metadata to make it searchable, patterns can be identified in structural behavior for certain criteria. For example, a hypothetical use for this database would be to search pictures of shear cracks in all concrete box girder bridges on soil type C, resulting from a magnitude 6.0 earthquake or greater in California. By creating such a vast library of pictorial structural references, more accurate assessments of seismic performance can be made by analysts. Usability of the information collected and stored in the database is what makes the SPO distinct from other similar or comparable archives.

## 4.2 METHODS: DEVELOPMENT OF PROCEDURE AND DATABASE

The main objective of this project is twofold. The development of the database and the creation and use of the investigation procedures, which are interconnected and depend on each other to progress. By testing the procedures in the field, adaptations can be made to make the process more effective and efficient, and the data collected can be inputted in the database as reference for future use. In addition, by using the database as the primary archive for data, the usability of its features and interface are tested and improved. The two goals are integral to each other and need to be developed simultaneously. With this background, the overall procedure for this project can be more accurately understandable as a continuous web, as shown in Figure 4.1. This graphic expresses that the progress of this project flows in a cycle that repeats itself as each individual aspect is developed further.

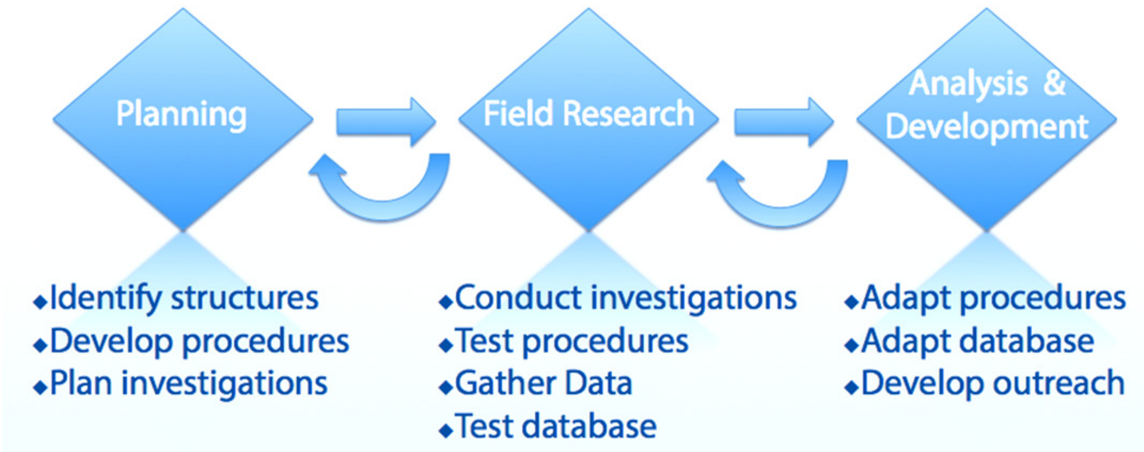


**Figure 4.1 Flow diagram of project procedure.**

The above graphic illustrates the continuous nature of the project procedure. The first phase was the preliminary research that involved gathering data to identify structures of interest and references to develop the earthquake investigation procedures. This then led to planning and conducting the investigations, which included collecting data while testing the procedures. The data was then inputted into SPO, which in itself tested out the interface and facilitated the database's development. Future investigations were adapted based off the experiences from past procedures and the planning phase repeated again. This cycle has a linear element initially, but with time forms a web where each step flows into a new phase, leading the overall development of the project.

### 4.2.1 Preliminary Research: Identifying Structures of Interest

One of the main efforts in the beginning of this project was to conduct a literature review in addition to the preliminary research. This included looking for what already existed in terms of earthquake investigation procedures and databases, and reading about what PEER has already done in the past regarding this project [Mahin et al. 2012].

Before any investigations could be tested in the field, it was necessary to identify which structures would be most valuable to study for this project. A list of potential structures was needed to act as a guide to those sites that would be most appropriate for the initial investigation.

This first step consisted of identifying what data would be relevant in a seismic performance analysis, and seeking and organizing this information. The Center for Engineering Strong Motion Data (CESMD) acted as the starting point for this effort. Due to feasibility and available resources, the first decision in criteria for these structures was that they had to be located in the Northern California, specifically the Bay Area, and that they had to be seismically instrumented. The location decision allowed for visiting the site due to their proximity to UC Berkeley. Also, the instrumentation requirement would provide a wealth of ground motion and acceleration data for a structure in the event of an earthquake. This specific data would be useful in any seismic performance analysis to be conducted after a seismic event.

Google Earth and Microsoft Excel acted as the primary mediums of this data collection and organization. By documenting the locations of every identified structure by inputting coordinates into Google Earth and using KML files from US Geological Survey (USGS), information such as liquefaction hazard, closet active fault, and distance to fault were easily gathered and documented. Figure 4.2 illustrates the use of Google Earth's interface to determine liquefaction hazard for various structures.

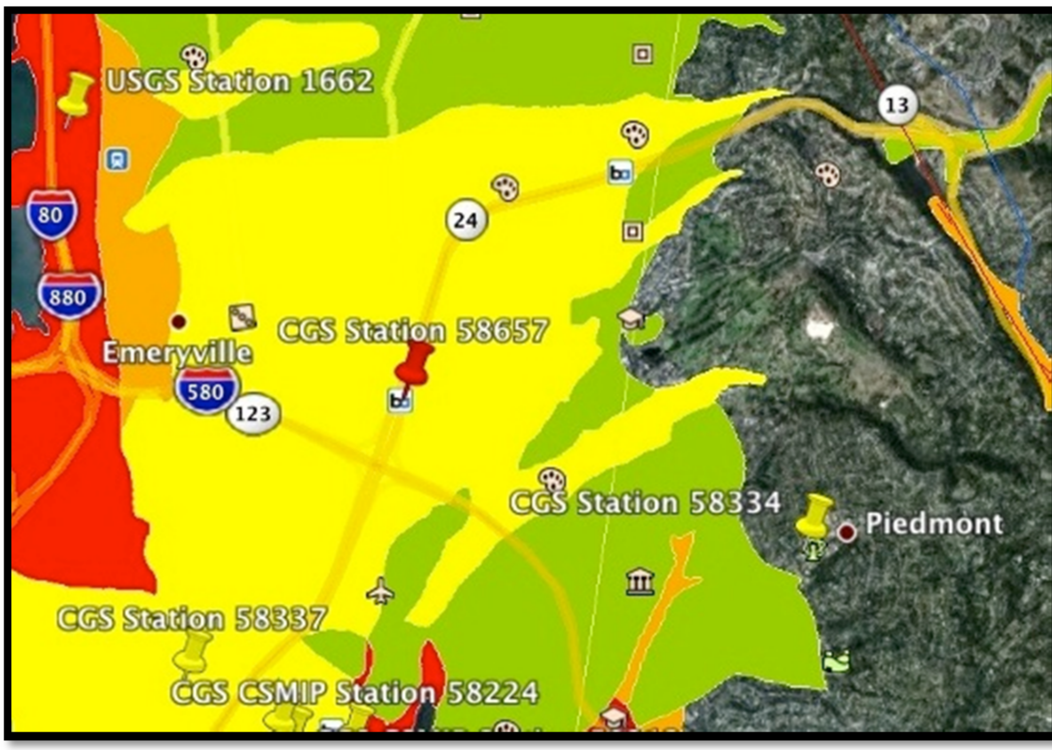


**Figure 4.2 Google Earth interface showing liquefaction hazard map.**

The data collected for each identified structure included the following: structure name, station number, coordinates, liquefaction hazard rating, closest active fault, distance to fault, soil type, plan drawings, material, structural system, function, year or construction, year of design, year of retrofit, instrumentation details, the presence of dampers and isolators, building code, foundation type, number of stories, plan shape, base dimension, bent details for bridges, bearing type, address, and contact information. The primary sources of this information came from the structural info sheets and plan drawings from the Center for Engineering Strong Motion Data ("Strong Motion Stations in Northern California" March 23, 2011) and liquefaction hazard maps ("Liquefaction Hazard Maps" June 8, 2012) and soil type maps ("Soil Type Map" June 8, 2012) from the USGS. Once this information was gathered, the structures were evaluated to determine which sites should be treated as priorities and points of interest. It was decided to select a bridge and a building from five points around the Bay Area: Berkeley, San Francisco, Oakland, Marin, and the South Bay. This plan was followed for the most part expect no structures in Marin were investigated.

### 4.2.2 Planning and Conducting Earthquake Investigations

One of the key components of developing pre- and post-earthquake procedures was to go out into the field to actually test current data collection methods. As previously mentioned, a detailed list of structures of interest was generated and used a guide for these investigations. The first locations visited where those near the UC Berkeley campus and included the PEER Library at the Richmond Field Station, Berkeley City Hall, the Berkeley Police Department, and the Great Western Savings located in downtown Berkeley. By starting off in nearby areas, it was easier to identify and apply needed adaptations to the investigation procedure.

These investigations primarily consist of photographing structural and nonstructural elements of buildings and bridges, and taking global shots to act as reference for future seismic performance studies. Since the occurrence of earthquakes cannot be controlled, all the studies conducted for this research consisted of the pre-earthquake investigations, thereby creating a reference of the condition for a structure before a major earthquake. This consists of taking global shots of the main faces of a building or bridge and its surround area, and documenting the current conditions of any potential areas of failure. By recording what damage is present before an earthquake, the amount of seismic-induced damage can be more accurately assessed when a post-earthquake investigation is conducted.

Manuals for post-earthquake investigations from various institutions such as Caltrans [2012] and the Earthquake Engineering Research Institute (EERI) [2010] were used when developing the pre-earthquake investigation procedure. These were used as a main reference in recognizing what would be considered a point of interest for a structure after an earthquake so that a reference point would be established prior to a seismic event.

Various problems were encountered during the development and application of the pre-earthquake investigations, including obtaining access to certain structures, safety hazards due to the locations of the sites, and a lack of specific references for the database and investigation procedures. Due to the nature of the investigations, it was necessary to go into many buildings to document the condition of all the structural and nonstructural elements that would be relevant to compare in a seismic performance analysis. This led to the need for permission not only to enter buildings of interest but also to photograph the interiors. This process varied from taking days to weeks for certain buildings.

One of the key tasks in developing effective pre- and post-earthquake investigations was to identify the differences in procedure when studying buildings compared to analyzing bridges. These differences include varying safety considerations and the specifics of what is important to photograph. PEER's Pre- and Post-Earthquake Investigation Plans (see Section 3.9 of this volume) contains the procedure for earthquake investigation developed in this project and provides details about the different needs and requirements for bridge and building investigations.

#### *4.2.2.1 Types of Photographs Taken during Investigations*

The primary method of documenting data and observations during the pre-earthquake investigations is through photographs. There are four different types of pictures taken during a given investigation: global shots, local shots, panoramas, and fisheye shots used to generate 360° models. Figures 4.3 through 4.6 show these various types of photos.

Figure 4.3 shows example of global shots for building and bridges. Global shots are photographs where the entire shot is the focus of the image. They are meant to document the overall and general condition of a structure and its surroundings.

Figure 4.4 shows examples of local shots that were taken as part of the pre-earthquake investigations of this project. These types of photos are the most common during an investigation as they are used to document the condition of a specific element. The focus of the picture is a specific part of the image. It can be a structural element like a column of a bridge, or a nonstructural element like a utility line or a crack on the ceiling of a parking structure.

Figure 4.5 shows example of panoramic shots taken during the investigations. These pictures serve as global shots with larger scopes and ranges. They can document more visual data since they fit more of the scene in a single image. This is useful by presenting more reference information in direct relationship to each other rather in separate shots.

Figure 4.6 shows shots that were taken using a fisheye lens. These photos are to be used to generate spherical panoramas used in developing 360°models.

**Figure 4.3 Global shots taken for pre-earthquake investigations.**


**Figure 4.4 Local shots taken for pre-earthquake investigations.**

**Figure 4.5 Panoramas taken for pre-earthquake investigations.**


**Figure 4.6 Fisheye shots taken for pre-earthquake Investigations.**

These photos act like global shots that capture everything in view from a specific point in space. The fisheye lens used captured 185°of vision. Three photos were taken at 120° spacing to capture the entire view with some overlap. The photos were dewarped using DeWarper and then stitched together using Adobe Photoshop. This process was used to generate a spherical panorama that could eventually be used to generate a 360° model similar to that in Google Streetview. These shots are useful as they provide a pre-earthquake reference for an entire room from a single point.

### 4.2.3 Developing the Seismic Performance Observatory

The Seismic Performance Observatory (SPO) is the database that PEER is developing for this project. Currently in a pre-beta form, much of the usability of the database is still under development. This aspect of the project also has multiple objectives. The first goal is to provide a centralized location for the collection of data, primarily photographs, of various structures for use by the earthquake engineering community. These raw pictures of preexisting conditions and damage act as a great resource and reference for assessing damage for a seismic performance analysis. The next goal deals with the usability of this archive. The significance of the SPO is that it makes the masses of data collected from structures in earthquake investigations usable through its use of metadata. By organizing all the data of the structures with various tags, labels, and taxonomies, it becomes searchable and useful for identifying patterns and assessing structural performance. This makes the SPO an effective tool for Performance Based Earthquake Engineering (PBEE).

One of the primary goals in the development of the SPO is to make it more user-oriented and effective in organizing relevant structural and earthquake data. With this objective, alterations were continuously made to the database throughout its use. Anytime a need for an addition or alteration was identified, it was recorded and a schematic was drawn for the interface changes to be communicated as effectively as possible. An example of one of these sketches is shown in Figure 4.7, which shows how sketches are created to communicate interface adaptations to SPO. These changes are intended to provide greater usability to the database by allowing more detailed and accurate input of data and metadata, while also making it as intuitive and user-friendly as possible.

Another goal associated with the SPO's development was to pre-populate the database with the photographs collected during the conducted investigations and the information obtained through the preliminary research of structures of interest. This provided new users with examples of what type of information needs to be inputted into the database and use it as a template for new submissions.

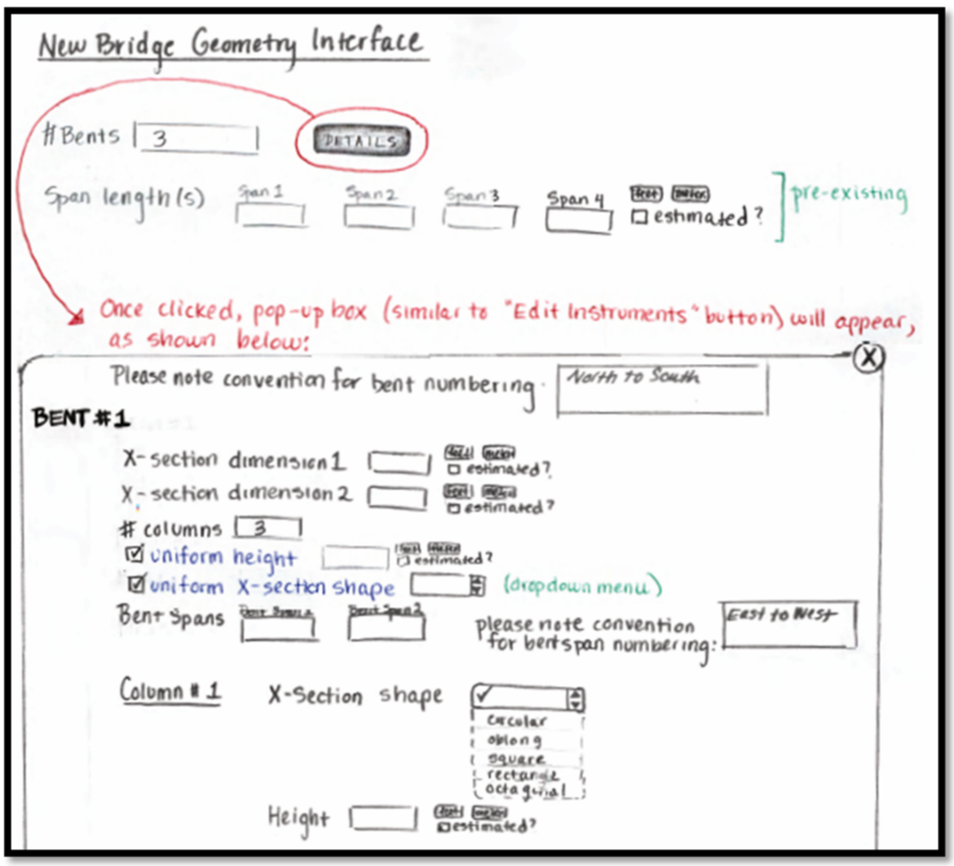


**Figure 4.7 Image of sketch for SPO interface addition.**

One of the final tasks of this project was to develop a user manual for the SPO that could be uploaded onto the database itself. The objective of this was to preserve and document all the insight for using the SPO that was obtained during its development. With different tabs and menus to navigate when inputting data from investigations, this manual is meant to guide the user to easily and effectively store and organize the photographs, documents, and other data types. The tasks involved in this process include: creating and editing structures and earthquakes, uploading photos into galleries and associating them with structures and earthquakes if applicable, labeling photo details, and classifying damage. More details on these tasks and their procedures can be found in the SPO User Manual (see Section 3.9 of this volume).

#### *4.2.3.1 Outreach*

A secondary goal of this project was to gain outside support for the project with the intention that the database and procedures developed be used by other organizations in cooperation and collaboration with PEER. The hope is that if its use goes viral, the amount of information that will be available as a shared resource will drastically increase and substantially help the earthquake engineering community. With this goal, continuous meetings were held with outside organizations like the USGS and Caltrans in order to gain feedback on the development of the project and to find support for various needs such as request to share specific data and access to certain structures to conduct investigations. Figure 4.8 presents schematic that visualizes this idea, providing a visual for the concept of data sharing with SPO. This graphic presents an idea of synching SPO with other outside databases and resources from other organizations. Additionally, another potential source of data is from individuals not associated with a specific organization. By having students or professionals able to input data individually, the wealth of data housed in the SPO can continuously expand and evolve.


**Figure 4.8 Schematic of data sharing/input for SPO.**

### 4.2.4 Identifying and Addressing Problems and Concerns

Both major aspects of this project, the conducting of pre-earthquake investigations and the development of SPO, encountered various problems and challenges. These ranged from simple logistical issues to concerns brought up from outside organizations regarding the project.

As previously mentioned, the hardest aspect of the investigations was getting permission to enter a building when necessary. Various efforts were made to deal with this including sending letters to building managers, scheduling tours with professionals in the buildings, and simply visiting structures to see as much as possible without an appointment. Another concern that arose with the investigations was safety particularly when visiting bridges. Most of the bridges were freeway interchanges and required crossing streets with fast traveling traffic and no pedestrian walkways. These conditions made it exceptionally important to be aware of the surroundings and made having two people out in the field more ideal.

A significant concern that was continuously addressed was the use of the information gathered. Many building managers would not grant permission into buildings or share structural drawings and plans unless they knew for what the data would be used and what practices would be implemented to protect it. In a society where terrorism is a relevant worry, the structural information of a building cannot be completely public due to fear of misuse.

The proposed solution to this concern is to implement security practices into the account system of SPO. There can be different accounts for students who only want to upload data from their own investigations, earthquake engineers doing research on PBEE, or professionals in industry who want to assess the seismic performance of a structure. By having tiered accounts with different levels of access, data can be more effectively protected and shared only with those who would appropriately use it.

## 4.3 RESULTS: COMPLETED INVESTIGATIONS AND SPO STATUS

Because most of this project consisted of conducting investigations and inputting data into the SPO, the results can be expressed as the completed investigations and current status of SPO. Table 4.1 shows a complete list of the structures for which a pre-earthquake investigation was completed during this project. This list of 12 investigated building and bridges exhibits a variety of structures. The types of buildings included varied from government buildings with base isolators to simple concrete parking structures. The locations of these sites included cities from Berkeley, San Francisco, to San Jose and this shows that the goal of selecting structures from all around the Bay Area was accomplished.

**Table 4.1 List of structures investigated.**

| BUILDINGS | | |
|---|---|---|
| **Structure** | **Location** | **Date Visited** |
| Berkeley City Hall | Berkeley | 7/3/12 (ext.) |
| Berkeley Police Department | Berkeley | 7/3/12 (ext.) |
| Great Western Savings | Berkeley | 7/3/12 (ext.) |
| SFPUC | San Francisco | 7/21/12 |
| Hayward City Hall | Hayward | 8/16/12 |
| Hearst Mining Building | Berkeley | 7/18/12 (ext.)<br>7/25/12 (int.) |
| Santa Clara East Wing | San Jose | 7/23/12 |
| Berkeley Parking Structure | Berkeley | 7/11/12 |

| BRIDGES | | |
|---|---|---|
| **Structure** | **Location** | **Date Visited** |
| Pedestrian Bridge | San Mateo | 7/24/12 |
| Sierra Pt. Overpass | Brisbane | 8/8/12 |
| 580/24 Interchange | Oakland | 7/9/12 |
| 580/13 Interchange | Oakland | 8/16/12 |

### 4.3.1 Specific Investigation: San Francisco Public Utilities Commission

As part of this project, the San Francisco Public Utilities Commission (SFPUC) underwent a pre-earthquake investigation on Friday, July 20, 2012. This building in located in Downtown San Francisco on 525 Golden Gate Avenue and was completed during the summer of 2012. It is LEED Platinum certified and was identified as a structure of interest for this project because it is seismically instrumented by the California Geological Survey (CGS) as Station 58509 and utilizes post-tensioned flexural concrete cores to realign the structure in the event of an earthquake. These characteristics make it valuable to have a pre-earthquake reference for this building so that after an earthquake, any structural damage can be more accurately assessed and the performance of the building can be compared to its predicted and designed response.

Figure 4.9 shows the different types of photographs that were taken as part of the pre-earthquake investigation for the SFPUC. A variety of photos were taken in the pre-earthquake investigation of the SFPUC. Photo 1 is a global shot of the exterior of the structure from the northeast corner of the intersection of Golden Gate Avenue and Polk Street. Photo 2 is a local shot of the west side of column 20 on the 13th floor. Photo 3 is a local shot of the ceiling pipe framing on the 14th floor. Photo 4 is a local shot of the seismic instrumentation located in the basement. Photo 5 is a panoramic global shot of the intersection of Golden gate Avenue and Polk Street from the northeast corner.


**Figure 4.9 Photos from SFPUC pre-earthquake investigation.**

Typically for a given investigation, the plan drawings are obtained prior and evaluated to plan a pathway for the investigative procedure. For this particular investigation, the plan drawings were not available prior to the visit. Additionally, an escort was required for the entire investigation due to the sensitive nature of the building and its operations. This condition provided a lack of flexibility in the path of the investigation but also added the benefit of having access to someone who was familiar to the layout of the building and aware of what structural elements would be useful to document. For example, Brian Wong, the escort for this investigation, previously worked as the Construction Manager of the building and was very aware of points of interest for a pre-earthquake investigation. He was able to provide direction to the seismic instrumentation and access to the areas of the building not accessible to the public, like the roof, which contained many utilities. This guidance added efficiency to the investigation, as less time was needed to find and determine points of interest due to the experience and help of an escort.

Being a very recently completed structure, no pre-existing damage was observed and documented during the investigation. This may seem like the investigation was not worthwhile, but recording the lack of damage is just as significant as documented preexisting damage. By having any reference for a structure's damage before an earthquake, the degree of damage from a seismic event can be accurately determined. It also important to remember that part of the pre-earthquake investigation procedure involves gathering important documents, drawings, plans, and documenting instrumentation locations. All this information can be used as future references in seismic performance analyses.

### 4.3.2 Current Status of SPO

Throughout the development of the Seismic Performance Observatory during this project, new features were added and adaptations were made to its interface. These adaptations are all intended to make the database as effective and detailed when storing and organizing earthquake and structural data and are meant to make this process as user-friendly as possible. There are some key features still missing from the SPO. Currently there is no search feature to identify patterns in the seismic performance of structures. As this is critical for the SPO to be used as a tool in conducting seismic performance analyses and necessary for PBEE, adding this feature is the next critical step in SPO's development.

Despite some key aspects of the SPO missing, the database has significantly progressed. It has all the features necessary to store earthquake and structure information, photos, and documents. In this way, it acts as an accessible archive that is approaching being ready for use by outside organizations. Its library of data is to be constantly expanding and its interface continuously evolving. Figure 4.10 shows a screen capture of the interface of SPO in its current form.

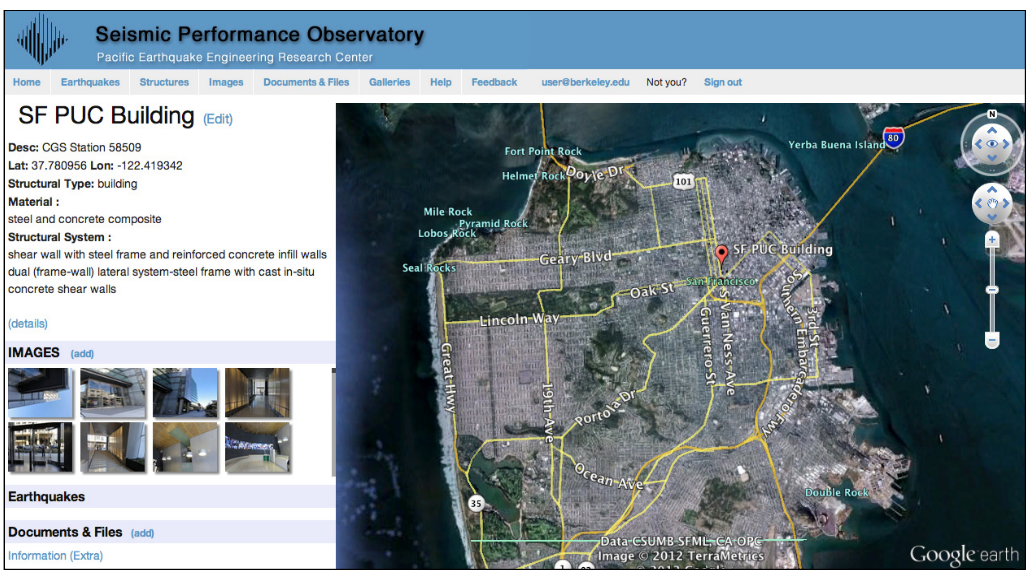


**Figure 4.10 SPO interface.**

This image shows the interface when viewing a structure in SPO, in this case, the SFPUC. It clearly organizes a summary of general information about the structure like its locations, material, and structural system, and provides access to the images associated with the structure of interest. Also shown in the figure are the links to relevant documents and earthquake data directly associated with the structure. These features are meant to allow any user to easily and seamlessly identify and access all the information needed when analyzing a specific building or bridge. Rather than simply allowing for storage and relying on the user to locate relevant data independently, SPO collects and organizes its library based of the associations established when a user initially inputs data into the database. More details on the features of SPO and instruction on its use can be found in the SPO User Manual (see Section 3.9 of this volume).

## 4.4 CONCLUSIONS: ASSESSMENT OF GOALS AND FUTURE WORK

The initial primary goals of this project were to develop a procedure for pre- and post-earthquake investigations, conduct these investigations, and use the collected data to pre-populate and develop the Seismic Performance Observatory. These goals were all met for the most part. Note that actually conducting post-earthquake inspections was not part of the scope as it was unrealistic to plan for an earthquake to occur during the project. Nevertheless, the procedure developed was intended to cover both types of investigations and can be found in PEER's Pre- and Post-Earthquake Investigation Plans (see Section 3.9 of this volume).

This development of the SPO also progressed significantly over the duration of this project. By pre-populating the database with the photos from the completed investigations and the research needed to identify structures of interest, the actual use of SPO for an archive or structural and earthquake data gained significant momentum. This drive to expand the use of the SPO is planned to continue and progress as key features are added to the database to expand its usability and role as a tool for earthquake engineering

### 4.4.1 Future Work

As this project is intended to serve as a constant tool for the earthquake engineering community, its development does not have a definitive end. It was decided that in addition to continuing the development of the SPO, the next phase of the project is to expand its scope to include areas in Southern California. This is specifically to be done by working with students Cal Poly Pomona and University of California, Los Angeles. Since the hope is that this project will find roots in organizations all over the country, it is vital that it can spread and evolve outside of PEER and UC Berkeley. By gradually expanding it to new regions of the state, data from structures all over the United States can be gathered, organized, and used for seismic performance analyses that will not only benefit the earthquake engineering community, but society everywhere.

## ACKNOWLEDGMENTS

This project can only attribute its success to the collaboration of those involved. Special thanks to faculty mentor Professor Stephen Mahin, and graduate mentor Vesna Terzic for their invaluable guidance and direction, to partner intern, Dorian Krausz, for effective and seamless collaboration, and to Heidi Tremayne, for constant support and supervision. Thanks to Caltrans and USGS for their useful feedback and encouragement, and for their hospitality. Thanks to

James Way for implementing the adaptations to the Seismic Performance Observatory's interface. Thanks to PEER interns Andrew Lo and Dustin Cook for their encouragement and support. Thanks to all the staff at Richmond Field Station and the PEER office at UC Berkeley for their assistance and aid. This project was made possible by funding from the National Science Foundation.

## REFERENCES

Caltrans (2012). *PEQIT Manual 2012,* accessed June 27, 2012. *http://www.dot.ca.gov/hq/esc/earthquake_engineering/PEQIT/.*

Center for Engineering Strong-Motion Data (2012). *Strong Motion Stations in Northern California*, accessed June 2012, *http://www.strongmotioncenter.org/.*

Earthquake Engineering Research Institute (2010). *Post-Earthquake Investigation Field Guide*, accessed June 27, 2012, http://www.eeri.org/site/lfe-field-guide.

Mahin SA., HA Faison, V Terzic, and J Way (2012). Development of a system for visualization and management of information on the earthquake performance of structures, Pacific Earthquake Engineering Research Center, University of California, Berkeley, pp. 1–10.

USGS (2012). *Liquefaction Hazard Maps*, U.S. Geological Survey, last accessed June 2012, *http://earthquake.usgs.gov/regional/nca/qmap/.*

USGS (2012). *Soil Type Map*, U.S. Geological Survey, last accessed June 2012, *http://earthquake.usgs.gov/regional/nca/soiltype/.*

# 5. Stimulating *In Situ* Soil Bacteria for Bio-Cementation of Sands

COLLIN ANDERSON


## ABSTRACT

Microbial Induced Calcite Precipitation (MICP), or bio-stimulation, has advanced tremendously in the past decade, but the likelihood of MICP progressing to field applications is largely dependent on stimulating the bacteria already present in the soil to precipitate calcite. This idea of stimulating *in situ* bacteria has been investigated by treating Folsom Lake sand from Folsom Lake, California, with four unique treatment solutions with a focus on whether or not the bacteria can be stimulated, whether calcite can be efficiently precipitated at grain boundaries, and if the resulting improvements to geotechnical properties are adequate. This pilot project has shown that the *in situ* bacteria can be stimulated to precipitate calcite, with a corresponding 600% increase in shear wave velocity and peak strength of 2.2 MPa. While this project was successful, more research is needed to optimize the treatment program and solution for MICP to be a more economical alternative to traditional ground improvement techniques.


## 5.1 INTRODUCTION

Microbial Induced Calcite Precipitation (MICP), or bio-cementation, has been shown to drastically reduce liquefaction potential in sands by reducing permeability, increasing shear strength, and increasing stiffness (as evident in increased shear wave velocity). Currently, there is a field trial of MICP in Northern California to assess the feasibility of large-scale testing using foreign calcite precipitating bacteria injected into the soil. This study aims to answer the following question: Can the *in situ* bacteria be stimulated to precipitate calcite, while avoiding chemical crash out in the pore fluid?

## 5.2 BACKGROUND

### 5.2.1 Liquefaction

Sands can significantly lose strength when exposed to cyclic loading. A small amount of cementation, even just due to aging of sands, can significantly increase liquefaction resistance. For example, Pleistocene sands (sands over 10,000 years old) have been shown to have higher liquefaction resistance than younger Holocene sands. Liquefaction occurs when stress from cyclic loading is transferred from particle-particle contacts in the soil matrix onto the pore water, resulting in the sand particles being pushed apart [Idriss and Boulanger 2008]. Once this occurs, the sand no longer behaves as a solid and can no longer support static loading.

### 5.2.2 Shear Wave Velocity in Sands

Shear wave velocity ($V_s$) is dependent on confining pressure, density, mineralogy, depth, Over Consolidation Ratio (OCR) and numerous other factors, and is fundamentally linked to a soil's shear modulus. Shear waves are small strain elastic waves whereby the particle displacement, which is perpendicular to the direction of wave motion, can be defined by the following equation:

$$V_s = \sqrt{G/\rho} \tag{5.1}$$

where $V_s$ is shear wave velocity, $G$ is the shear modulus, and $\rho$ is the density of the soil [Mitchell and Soga 2005]. Typical shear wave velocities for loose liquefiable sands are 100 to 200 m/s for the upper 30 m of a soil layer.

### 5.2.3 Microbial Induced Calcite Precipitation

Microbial induced calcite precipitation stimulates ureolytic bacteria to precipitate calcite at particle-particle contacts, resulting in a cemented sandstone-like material. This material has a higher liquefaction resistance due to an increase in shear strength and stiffness, and a reduction in permeability [DeJong et al. 2006; 2010; 2011; Wheil et al. 2010; Tobler et al. 2012; Bernardi et al. 2012]. Shear strength, measured in undrained triaxial tests, has been shown to increase from a shear ratio of 0.4 when untreated to 1.7 when treated. Stiffness, which is measured through unconfined compression and shear wave velocities, resulted in peak strengths of 2.2 MPa and increases in shear wave velocity upwards of 1000 m/sec. Permeability reductions up to 95% of initial values have also been shown in column tests of quartz sands.

Microbial induced calcite precipitation occurs through two primary reactions. The first reaction is hydrolysis of urea [Equation (5.2)] by bacteria containing urease enzymes; once calcium is injected into the pore fluid, a second chemical reaction [Equation (5.3)] results in the precipitation of calcite ($CaCO_3$). The entire process can be seen in Figure 5.1.

$$NH_2 - CO - NH_2 + 2H_2O \rightarrow 2NH_3^+ + HCO_3^- + OH^- \tag{5.2}$$

$$Ca^{2+} + HCO_3^- + OH^- \rightarrow CaCO_3 + H_2O \tag{5.3}$$

In addition to calcite precipitated at grain boundaries, it can also precipitate in the pore fluid, resulting in inefficient calcite precipitation that has little structural benefit. Known as "crash out," this can be determined by comparing calcite concentrations to strength or stiffness and if bacteria impressions are present on the crystalline structure shown in Scanning Electron Microscopy images.

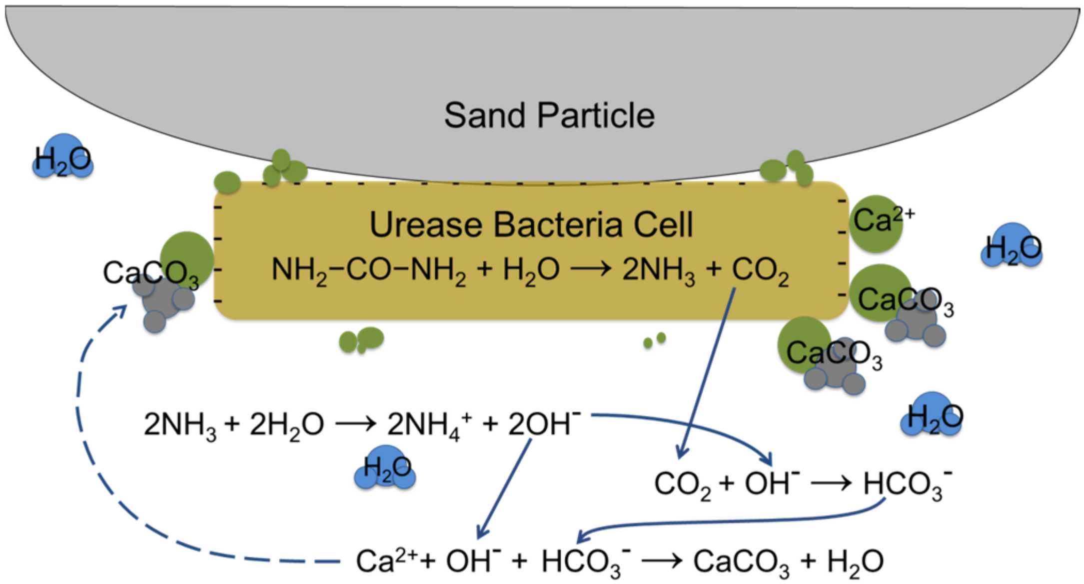


**Figure 5.1 Simplified diagram of the primary reactions for MICP.**

Microbial induced calcite precipitation can be performed through two methods: Bio-Augmentation and Bio-Stimulation. Bio-Augmentation is the process of injecting *Sporosarcina Pasteurii* (ATCC 11859) into the soil and stimulating them to precipitate calcite. This method has been useful for developing a standard treatment procedure and tools for measuring the effects of calcite precipitation as well as methods for monitoring the effectiveness of treatments. The other method, Bio-Stimulation, stimulates the urease bacteria already present in the soil to precipitate calcite. This method introduces a new challenge: spatial variability of the urease bacteria and stimulating them exclusively rather than the entire bacteria population.

## 5.3 EQUIPMENT

### 5.3.1 Folsom Lake Sand

The soil used for these experiments is well-graded silica sand with some feldspar. The soil samples were taken from the beach of Folsom Lake in Folsom, California, and wet sieved through a No. 50 sieve to remove fines. A sieve test was then performed on the post-sieved material to develop a grain size distribution curve (see Figure 5.2) to get the Coefficient of Curvature ($C_c$), Coefficient of Uniformity ($C_u$), and diameter of particles at 50% passing ($D_{50}$) of Folsom Lake sand. The $C_u$ was 3.7, the $C_c$ was 0.9 and the $D_{50}$ was 0.69 mm, and summarized in Table 5.1.

**Table 5.1 Folsom Lake sand properties.**

| $D_{50}$ | $C_u$ | $C_c$ | $D_{10}$ | $D_{30}$ | $D_{60}$ | Mineralogy |
|---|---|---|---|---|---|---|
| 0.69 | 3.70 | 0.90 | 0.23 | 0.42 | 0.85 | Silica |

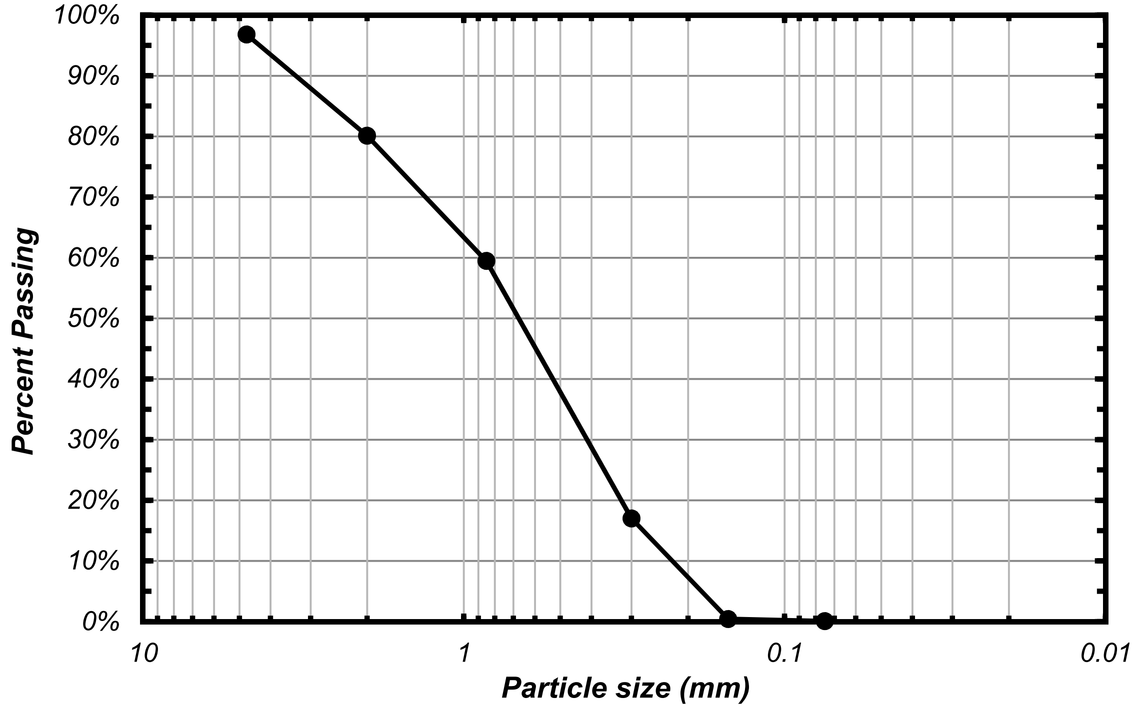


**Figure 5.2 Grain distribution curve of Folsom Lake sand after having been sieved through a No. 50 sieve (opening diameter of 0.30 mm).**

### 5.3.2 Test Cells and Injection System

The specimens, prepared in 4-in. high × 2-in.-diameter hollow acrylic cylinders, were treated through a gravity fed percolation system. The cells had two, 1-in.-diameter holes drilled at mid-height to allow for bender elements to be secured in place. There was also a half-inch-diameter hole drilled and later filled with a piece of rubber to allow the hypodermic needle to be inserted while still keeping a water-tight seal.

The gravity-fed percolation system consisted of a pump that transferred 300 mL (1.5 pore volumes) of treatment solution in 15 min to a reservoir, which then flowed into the bottom of the specimen and exited from the top. The reason for pumping the solution bottom-up was to ensure that if the cell experienced a drastic reduction in permeability it would not overflow (as the treatments were automated for the entire process). We also wanted the cells to remain saturated in-between treatments to simulate *in situ* conditions.

### 5.3.3 Bender Element Measurement System

Piezoelectric transducers, also referred to as bender elements, were utilized to measure change in shear wave velocity nondestructively during the treatment program. The bender elements, fabricated from Piezosystems Inc., were constructed in the manner specified by Montoya et al. [2010]. The shear waves were recorded using a LabView program written by Branderburg et al. [2008], and the waves produced were square waves of 9 volt amplitude and 100 Hz frequency. The receiving signal was sent through a National Instruments SCB-68, USB 6251 DAQ Box and a Krohn-Hite Model 3362 filter (see Figure 5.3). The filter consisted of a low-pass loop of 20 kHz, a high-pass loop of 1.0 kHz (to remove ambient electrical noise in the building) and an input gain of 30 times amplification. The shear wave velocities were calculated using the tip-to-tip distance in conjunction with the lag time and time of the first arrival of the shear wave.

As the treatments continued, the signal quality decreased, making first shear wave arrival difficult to detect. Because of the influence of the faster compression waves that would interfere with the receiving shear wave signal, the first arrival of the shear wave was taken to be the point of first major crossing of the wave on the *x*-axis.

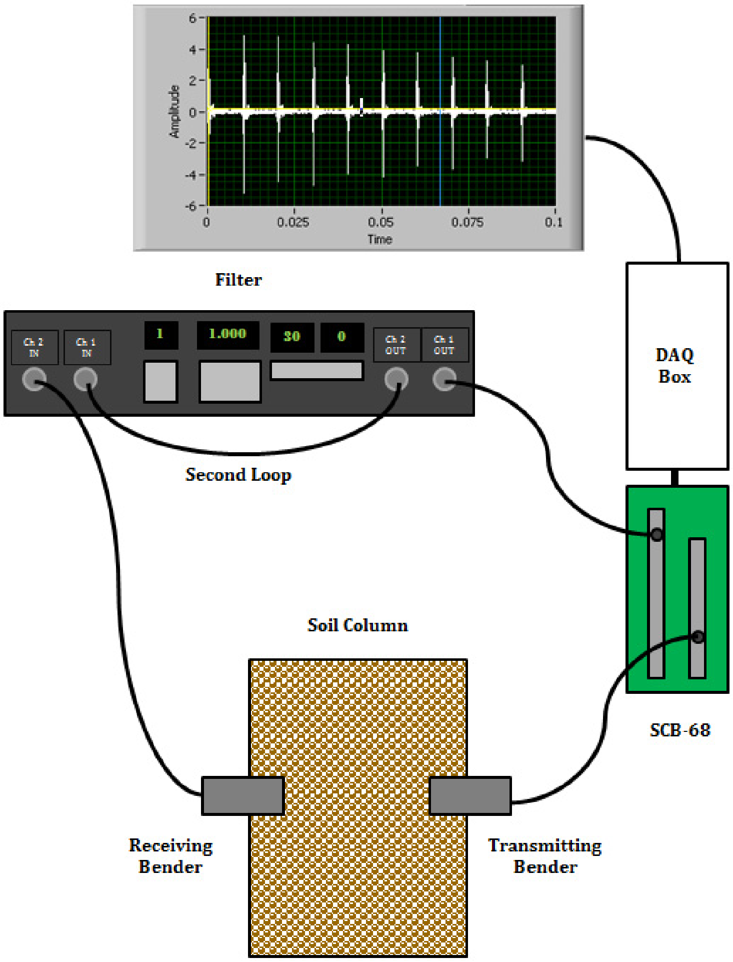


**Figure 5.3 Simplified diagram of the Bender element measurement system displaying a sample shear wave plot.**

### 5.3.4 Bacterial Queries

Bacterial activity in the specimens was measured using the optical density, pH, and bacteria counts on Agar plates of the pore fluid and effluent. Optical density measurements were performed at a wavelength of 600 nm using a Shimadzu UV160U spectrophotometer at 12-hr increments for the bacteria stimulation phase and at 24-hr increments for the calcite precipitation phase. Optical density is a measure of the turbidity, or translucency, of the fluid and a higher optical density indicates a higher turbidity (or less translucent) fluid. Bacteria plating was performed during the bacteria stimulation phase on both Nutrient Agar (pH=7) and *Sporosarcina*

*Pasteurii* Agar (pH=9) on the 48- 96-, 168-, and 228-hr treatments. Readings of pH were taken of the pore fluid before each treatment and of the effluent within the first thirty sec of pumping. Hydroxide ions are a byproduct of one of the reactions occurring in MICP, resulting in a higher pH if the urease bacteria are active.

### 5.3.5 Unconfined Compression Test

Once the samples were extruded and dried in the oven overnight, the stress-strain behavior of the specimens was tested in unconfined compression using the Geo-Tac automated load actuator. The height and diameter of the samples were recorded prior to testing and later used for calculations of force and strain. The mass of the top plate was also recorded and added to the load from the actuator in later analyses. The plate was centered on the sample and then centered under the load actuator. The test itself was performed at a strain rate of 0.025 in./min for approximately 4 min. Before the samples would fail fully, the test was stopped and the samples carefully removed and laid on their side for sampling. The specimens were divided into three samples of roughly 1.25-in. layers and saved for calcite measurements. Additional samples of cemented soil were taken and saved for SEM imaging in future analyses.

### 5.3.6 Precipitated Calcite Concentration Measurements

Calcite concentrations were measured using a Rapid Calcite Analyzer (RCA) and by acid washing soil samples after performing unconfined compression tests. After the unconfined compression tests, the samples taken were put into a total of 12 mason jars with a No.-200 sieve epoxied onto the cap. The jars were weighed before and after adding the dried samples. Five Molar HCl was then poured into each Mason jar to a level just above the sample and stirred six times for roughly 20 sec at 10-min intervals. The Mason jar was then filled with de-ionized (DI) water, capped with the No.-200 sieve and poured into a waste container. A total of 10 dilutions (adding DI water) were performed, and the waste water was neutralized using Potassium Hydroxide pellets, to a pH between 6 and 8, before being poured into the drain with running water. The samples were dried and the final mass was recorded, and the difference between the initial and final mass was taken to be the mass of calcite.

The RCA was used in conjunction with ASTM D4373 and a calibration curve was developed using reagent grade $CaCO_3$. This curve (see Figure 5.4) was used for calculating the mass of calcite in the sample tested. Because the pressure generated from the crashed out calcite was not expected to create a significant enough increase in pressure, samples from Specimen 1 and 3 were not tested using this procedure. Five gram samples were used in this experiment, and 30 mL of 1 M HCl were used to react with the samples. The soil was placed in the RCA chamber, and the HCl was placed in the small plastic container to prevent the reaction from occurring prematurely. The chamber was then sealed with the pressure gauge and tilted so that the HCl would pour out of the container and begin reacting with the soil sample. The pressure generated from the reaction was then recorded and used with the calibration curve resulting in the mass of calcite. The samples were watered down and neutralized using Potassium Hydroxide and poured down the drain once the pH was between 6 and 8.

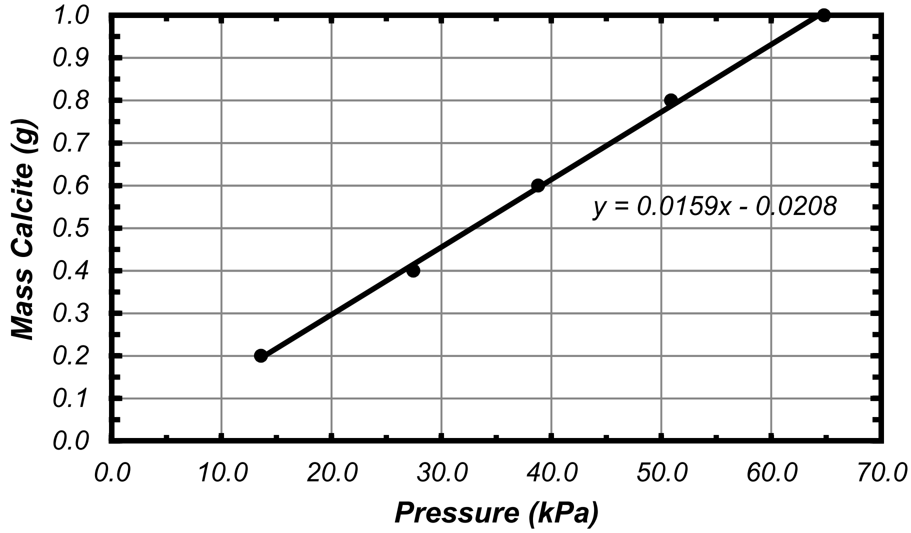


**Figure 5.4: Calibration curve used for calculating mass of calcite for RCA calcite Analysis with corresponding linear trend line.**

## 5.4 SAMPLE PREPARATION AND TREATEMENT PROGRAM

### 5.4.1 Testing Set Up and Sample Preparation

Four identical soil columns were constructed to test the four treatment solutions listed in Table 5.2. The benders were encased in a silicone puck and secured to the rigid cells using zip ties and vacuum greased to ensure a water-tight seal. The acrylic cylinder was then attached to a bottom cap with a nozzle for fluid flow and a rubber O-ring for a water-tight seal. The POREX plastic (opening diameter = 125 μm) was placed at the bottom of the sample followed by roughly 150 g of soil placed and then tamped 25 times. The hypodermic needle was inserted and a small POREX plastic (opening diameter = 45–90 μm) was attached to the end. Two more layers of approximately 150 g were placed and tamped 25 times each with care taken to not damage the bender elements and needle; a POREX plastic (opening diameter = 125 μm) was placed on top of the final layer. The cap was then secured in place with silicone oil and a rubber O-ring to allow the overburden load to transfer to the soil and not the acrylic cylinder.

**Table 5.2 Table of variance for the stimulation phase of the treatment program.**

| Specimen No. | Method | Concentration of Solution |
|---|---|---|
| 1 | Control | 12.5 mM $NH_4Cl$ + 0.1g/L Bacto |
| 2 | Urea | 333 mM +control solution |
| 3 | Sodium Acetate | 170 mM + control solution |
| 4 | Urea + Acetate | 333mM Urea and 170mM Acetate + control solution |

An overburden pressure of 100 kPa was applied to the top of the samples and the influent and effluent tubes were attached to the spouts at the bottom and top, respectively, of the specimen. The transmitting bender wire was attached to the SCB-68 and the receiving bender wire was connected to a port that could be attached to the filter depending on which specimen's shear wave velocity was being recorded.

### 5.4.2 Bacterial Stimulation

As shown in Table 5.2, to stimulate *in-situ* bacteria treatments were applied at 12-hr intervals for ten days. These treatments were taken from the method developed by Burbank et al. [2011], but divided into the constitutive parts to determine if chemical crash out would be evident in the pore fluid. During this phase of testing, samples of the pore fluid and effluent were taken immediately before each treatment began. These samples were used for bacterial queries on nutrient and *Sp pas* Agar, optical density, and pH readings. Shear wave measurements were taken as well to determine a base line for the calcite precipitation phase of treatments.

### 5.4.3 Calcite Precipitation

Calcium chloride anhydrous ($CaCl_2$) at a concentration of 250 mM was added to the treatments for ten days at 12-hour intervals to precipitate calcite. Samples of the pore fluid and effluent were taken every 24 hours, and used for optical density and pH readings with 1 mL of fluid saved for later analysis if needed. Shear wave measurements were taken during this phase to monitor increases in stiffness with time.

## 5.5 RESULTS AND ANALYSIS

### 5.5.1 Evidence of Bacterial Growth

Ureolytic bacteria growth was evident in the specimens treated with urea by monitoring bacteria counts, optical density, and pH of the pore fluid and effluent. A total of 108 plates, 54 Nutrient Agar and 54 *Sporosarcina Pasteurii* Agar, were plated with pore fluid samples. The final counts of colonies/mL for plating were $10^7$ on Nutrient Agar (NA) and $10^7$ on *Sporosarcina Pasteurii* Agar (SA) for Specimen 1, $10^6$ on NA and $10^8$ on SA for Specimen 2, $10^6$ on NA and $10^7$ on SA for Specimen 3 and $10^7$ on NA and $10^7$ on SA for Specimen 4. The counts for samples supplemented with urea were higher on *Sp pas* Agar than Nutrient Agar because there were more urease bacteria in the sample that would not grow on the lower pH Agar plates (urease bacteria are alkaliphilic). Samples not treated with urea showed a higher bacteria count on Nutrient Agar than *Sp pas* Agar, indicating the urease bacteria were not stimulated. As shown in Figure 5.5, these results correspond with the pH readings conducted during the stimulation phase. The pH began increasing in Specimen 2 and 4 after 24 hours and reached a pH of 9 by 36 and 48 hours, respectively. Specimen 1 and 3 never exceeded the pH of the influent, agreeing with the Agar data. Optical density measurements of the influent and effluent were sporadic during most of the testing, as shown in Figure 5.6, but were consistently above the optical density of the influent, indicating there was some sign of microbial growth in the specimen. Overall, the pH and bacteria plating were most effective in monitoring bacterial growth.

Results of performing a urease potential test on the bacteria colonies collected on the Agar plates indicated the bacteria were not urease positive meaning they are not capable of performing ureolysis. This can be attributed to the *Sp pas* Agar plates not having a source of Nitrogen, but still having a pH 9. This leads researchers to believe the Agar plates were not supplemented with the proper chemicals and will need to be improved for future tests.

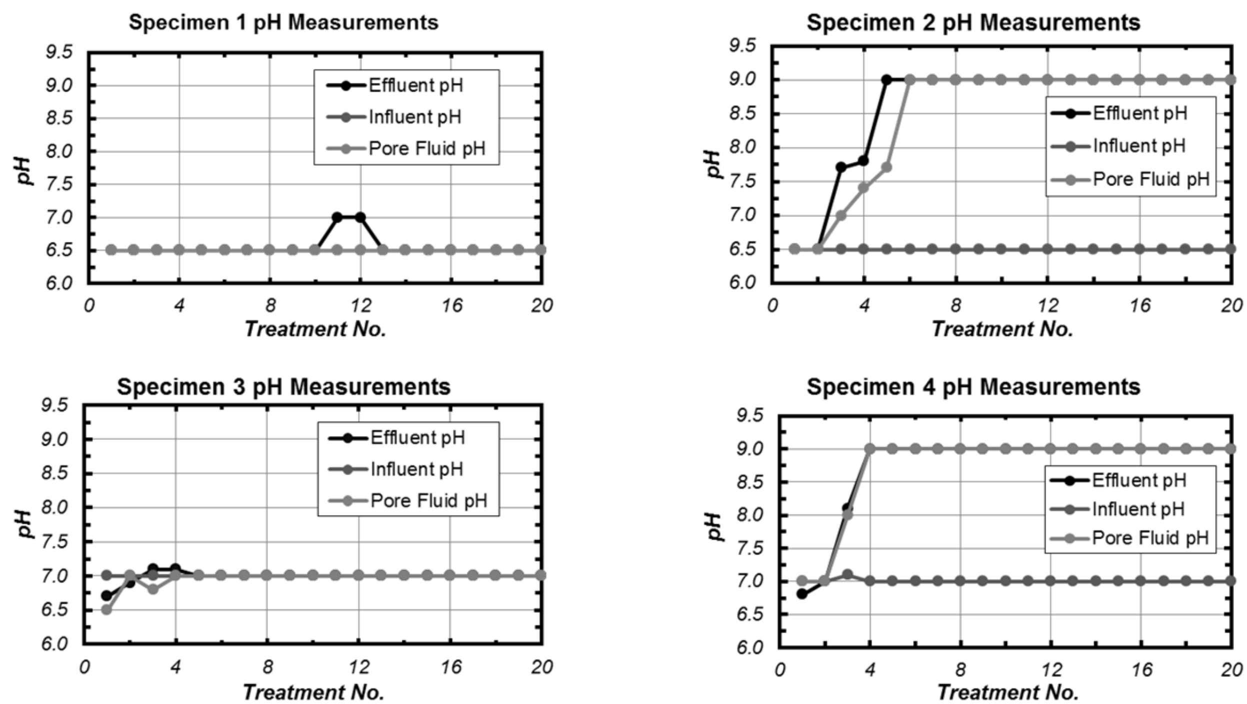


**Figure 5.5 pH measurements of the four specimens during the stimulation.**

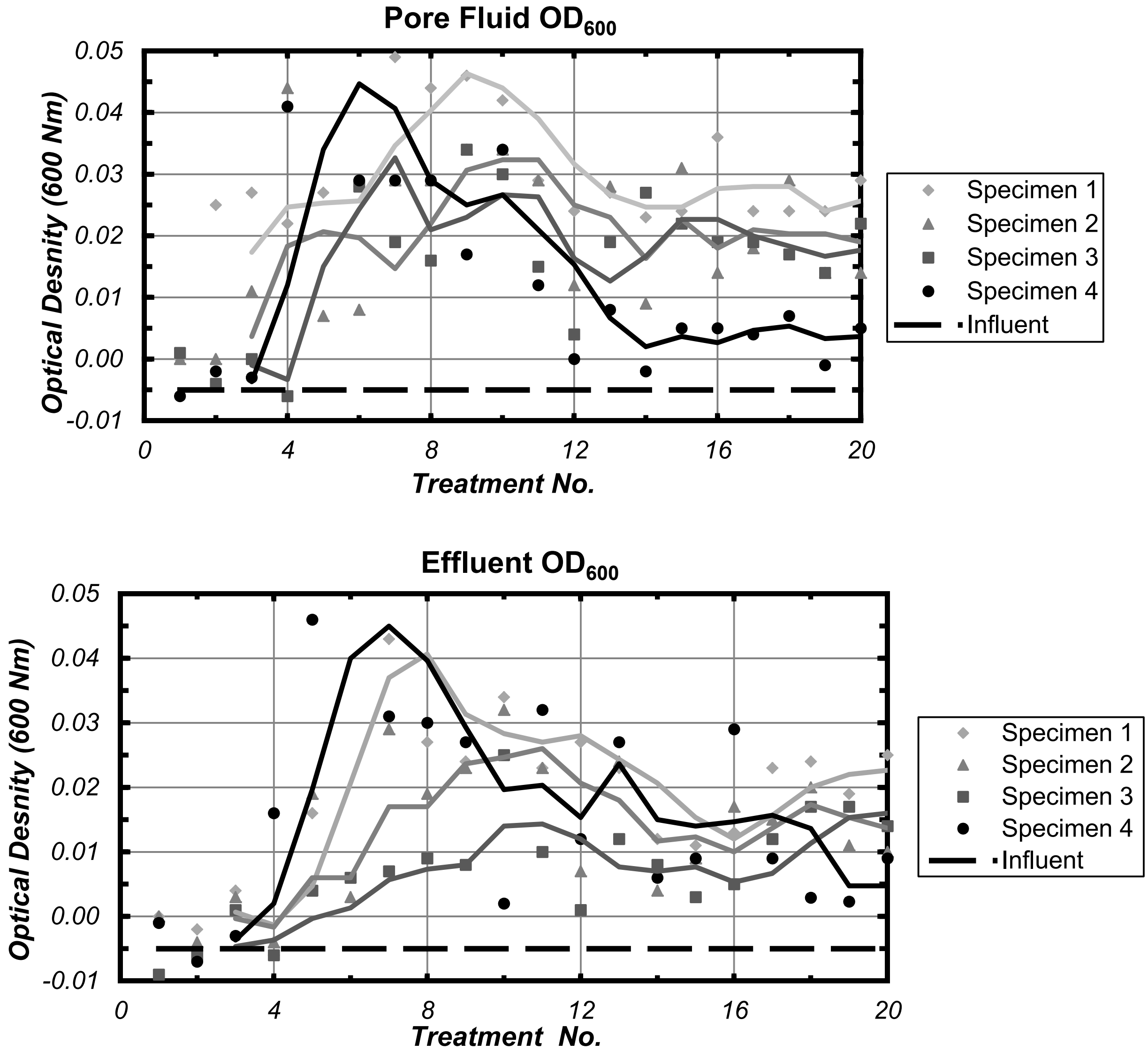


**Figure 5.6** **Optical density measurements of both the pore fluid and effluent of all four specimens during the stimulation phase. The trend lines are a three-period moving average.**

### 5.5.2 Shear Wave Velocity

Shear wave velocity increased up to 400% and 600% for Specimens 2 and 4, respectively, and remained at roughly 150 m/sec for the others. As can been seen in Figure 5.7, the only samples that experienced an increase in $V_s$ were the samples treated with urea. This correlates well with the data from the bacterial plating of pore fluid on the *Sp pas* Agar and Nutrient Agar plates. Due to a leak around the silicone pucks, the control sample experienced a decrease in shear wave velocity due to reconstructing of the sample on day ten. As stated previously, the only variables that affect the shear wave velocities in these tests are density and shear modulus; therefore, an increase in $V_s$ correlates to an increase in density and therefore stiffness. Experimental error did result in the last reading of Specimen 2 cell to be removed, and it is believed that the bender elements themselves began to degrade, which was due to degradation of the protective PVC coating by the high pH of the pore fluid or numerous other electrical errors. Initially the reading was much lower, but Specimen 2 was extruded, and $V_s$ readings were taken again with different bender elements and tip-to-tip distances, which resulted in a significantly higher $V_s$ measurement for the urea cell (620 m/sec) rather than the lower initial measurement (410 m/sec).

### 5.5.3 Stress Strain Behavior

Initial stiffness ranged from 2200 kPa to 1700 kPa and relates directly to the final shear wave velocities of the specimens. Specimen 1 and 3 were not plotted in Figure 5.8 as Specimen 1 was destroyed before beginning the unconfined compression test and Specimen 3's strength was insignificant compared to Specimens 2 and 4. The results from $V_s$ can be correlated to the stiffness of the two samples and the higher $V_s$ readings correspond to the higher stiffness. Specimen 4 experienced a brittle failure, with a significant reduction in load carrying capacity after it reached its peak strength. Specimen 2 experienced a more ductile failure, reaching a higher strain at its peak strength and taking longer to dissipate its load carrying capacity. The E50 values (see Figure 5.9), taken as a secant of the stress-strain curve at 50% of the peak strength, were 60.2 MPa for Specimen 2 and 78.2 MPa for Specimen 4. Three points were used for these calculations to remain consistent.

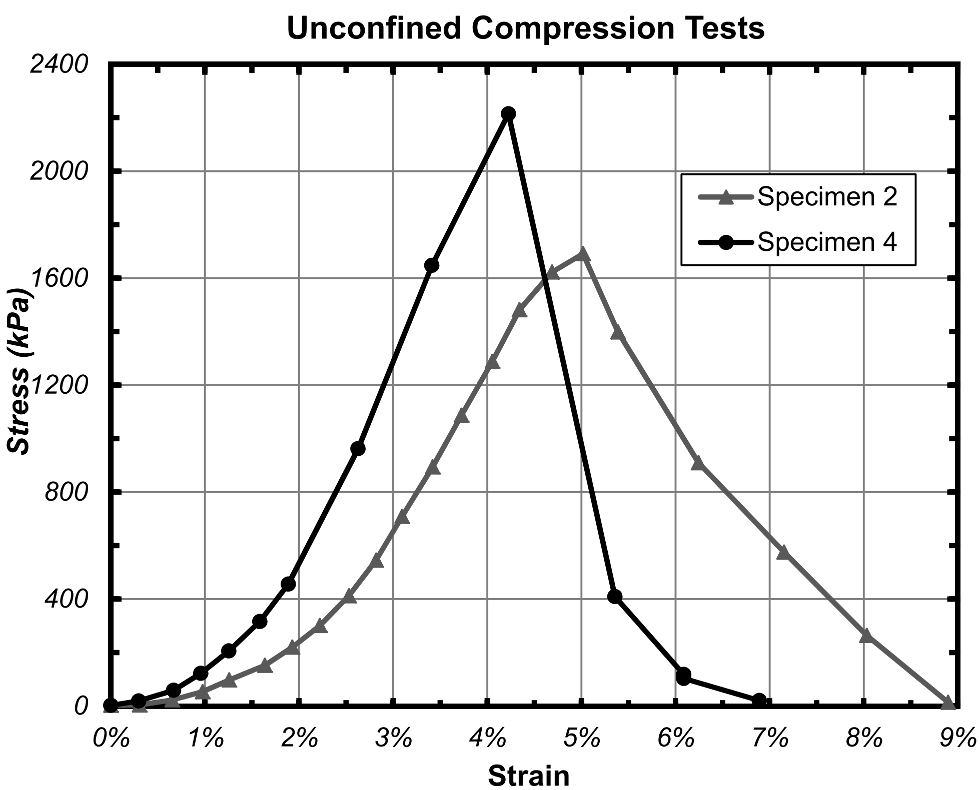


**Figure 5.8 Results from unconfined compression showing peak strengths of 2.2 MPa for Specimen 4 and 1.7 MPa for Specimen 2.**

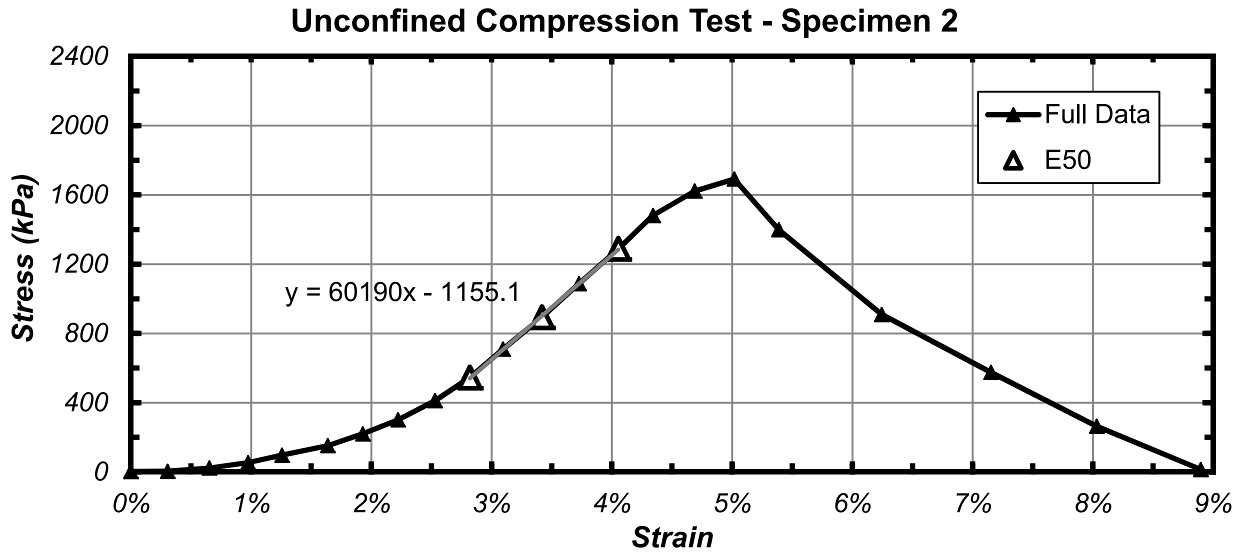


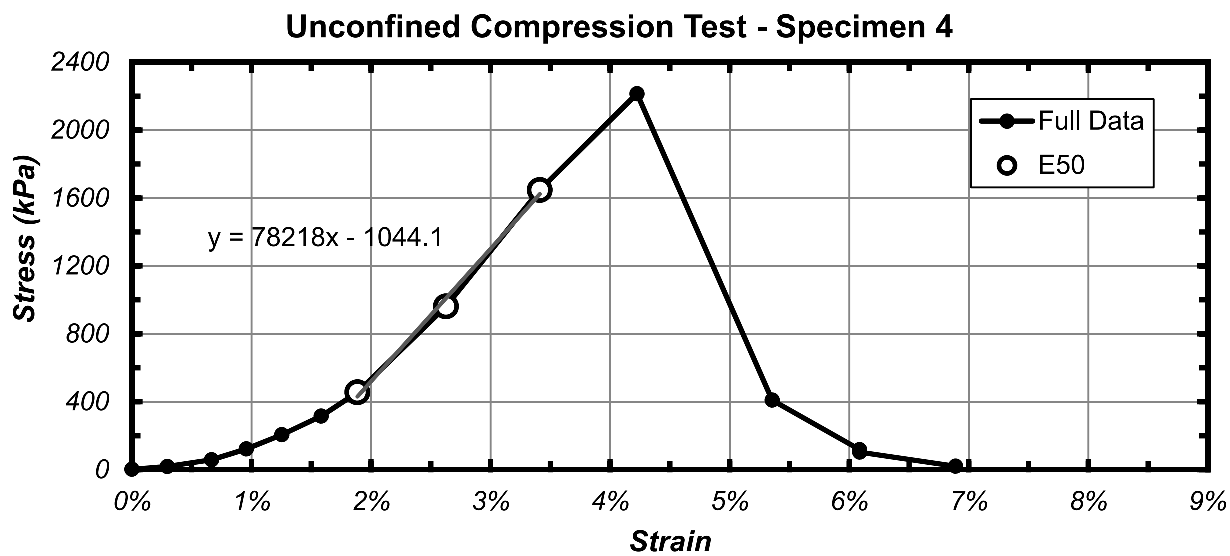


**Figure 5.9** **Points used for calculating $E_{50}$ with the slope of the trend line taken as the $E_{50}$ of each specimen.**

The resolution of the data is not ideal, due to a complication in how the data was stored. As a result there may be error in the calculations of the E50 and peak strength values; however, the data was still analyzed in a consistent manner. Although the numerical values may be in question, the trends and comparisons between the samples remain well defined.

## 5.5.4 Calcite Percent by Mass

Calcite concentrations range from 6.7% to 14.5% and show evidence of chemical crash out in Specimens 1 and 3. As shown in Figures 5.10 and 5.11, Specimen 2 and 4 show a noticeable calcite concentration. The results shown in Figure 5.10 were subjected to the acid-wash method, and the results shown in Figure 5.11 were subjected to the RCA method. Specimens 1 and 3 were not analyzed using the RCA method because the pressure increase from the small amount of crashed out calcite would not result in a measureable value. Interestingly, Specimen 2 had a relatively uniform calcite concentration throughout both analyses and showed a decrease of calcite concentration from the injection point. Specimen 4 on the other hand had quite varied results, which could be attributed to the spatial variability of the bacteria.

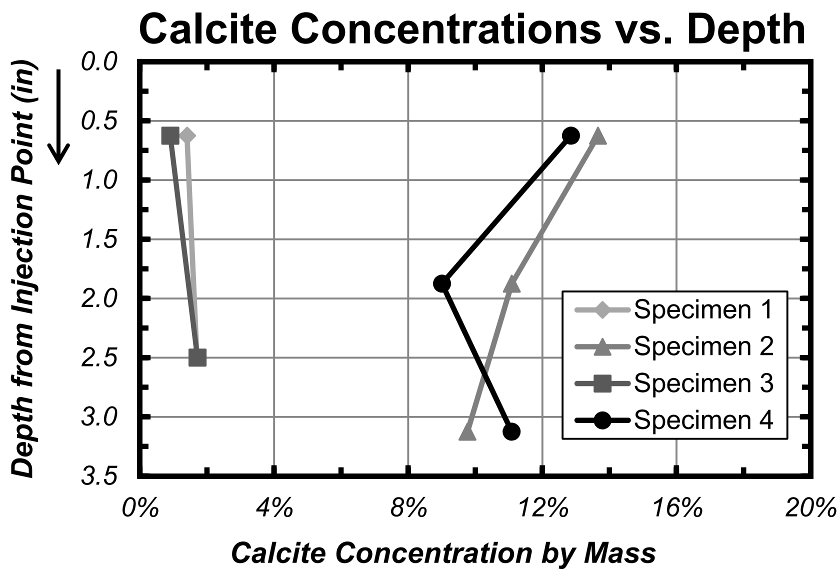


**Figure 5.10:** **Calcite concentrations for all four specimens using the Acid Wash method.**

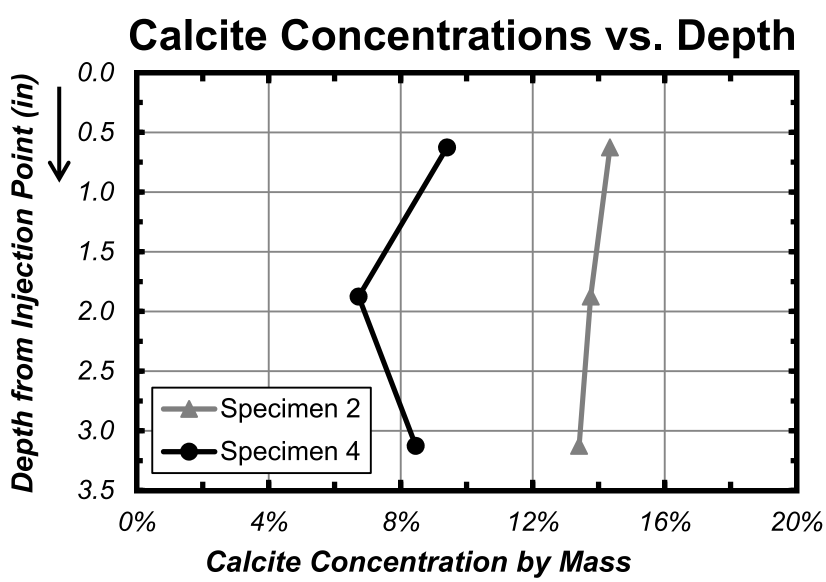


**Figure 5.11** **Calcite concentrations for Specimens 2 and 4 using the Rapid Calcite Analysis method.**

Comparing Calcite concentrations (see Figures 5.10 and 5.11) to stress-strain (Figure 5.8) and $V_s$ (Figure 5.7), a few results appear irregular, which could be the result of chemical crash out. First, although the $V_s$ and stress-strain correlate well, they do not correlate to the calcite concentrations. Second, looking at just the calcite concentrations, it would be expected that Specimen 2 would have a higher stiffness and shear wave velocity, which is particularly true for the samples at 1.875 in., (where the bender elements were located and shear wave velocities measured). This is a strong indication that chemical crash out of calcite in the pore fluid occurred in Specimen 2, resulting in a large calcite concentration; however, this crash out did not result in a significant increase in shear wave velocity and compressive strength.

## 5.6 CONCLUSIONS

This pilot research project has demonstrated the feasibility of stimulating bacteria that exist naturally in soil, thereby eliminating the need to inject additional bacteria within soil. All treatment solutions stimulated growth of *in situ* bacteria, as was evident in bacteria plating and optical density measurements. Only soils supplemented with urea stimulated growth of alkaliphilic bacteria in excess of other *in situ* bacteria after comparing the bacteria counts of the Nutrient and *Sp pas* Agar plates.

This pilot project has also demonstrated that calcite precipitation is possible in soil with stimulated natural bacteria. The increase in shear wave velocity up to 600% of initial values for soils stimulated with urea and no increase in $V_s$ in Specimens 1 and 3 indicates that to induce calcite precipitation urea needs to be present in the pore fluid. The results of the unconfined compression tests showed brittle behavior for urea-treated soils, with high initial stiffness and peak strengths of about 2 MPa and allow for a good correlation between $V_s$ and compressive strength. The Calcite concentrations were 10% and 14% by mass for urea treated soils, 1.6% and 1.3% for Specimen 1 and 3, and do not correlate directly to $V_s$ or compressive strength. The calcite results also provide strong indication of chemical calcite crash out in Specimens 1, 2, and 3, proving that calcite measurements alone are not good indicators of soil property improvement.

## ACKNOWLEDGMENTS

Special thanks to Jason DeJong, Department of Civil and Environmental Engineering at UC Davis, for providing valuable guidance and patience during the summer and past year, Doug Nelson, Department of Microbiology at UC Davis, and his lab staff for teaching me the nuances of microbiology and performing Agar plating. Finally I would like to thank the National Science Foundation for funding this project and Heidi Tremayne for supporting and assisting myself and the other interns throughout the ten-week internship.

## REFERENCES

ASTM (2007). *Standard Test Method for Rapid Determination of Carbonate Content of Soils*, American Society for Testing and Materials, *Standard D4373*, PA.

Burbank, M, T Weaver, T Green, B Williams, and R Crawford (2011). Precipitation of calcite by indigenous microorganisms to strengthen liquefiable soil, *Geomicrobio. J.*, 28(4):301–312.

Burbank M, T Weaver, B Williams, and R Crawford (2012). Urease activity of ureolytic bacteria isolated from six soils in which calcite was precipitated by indigenous bacteria, *Geomicrobio. J.*, 28:389–395.

DeJong, JT, MB Fritzges, and K Nusslein (2006). Microbial induced cementation to control sand response to undrained shear, ASCE, *J. Geotech. Geoenviro. Eng.*, 132(11):1381−1392.
DeJong, JT, BM Mortensen, BC Martinez, and DC Nelson (2010). Bio-mediated soil improvement, *Ecological Eng.*, 36:197–210.
Mortensen, BM, R Gerhard, JD DeJong, M Weil, BC Martinez, JT Waller, and L Pederson (2010). Fabrication, operation, and H=health monitoring of bender elements for aggressive environments, *ASTM Geotech. Testing J.*, in review.
Tobler, DJ, E Maclachlan, and VR Phoenix (2012). Microbially mediated plugging of porous media and the impact of differing injection strategies, *Ecological Eng.*, 42:270–278.
Weil, MH, JT DeJong, BM Mortensen, and BC Martinez (2010). Resistivity and seismic measurements for real-time monitoring of microbially induced calcium carbonate precipitation in sands, *ASTM Geotech. Testing J.*, in press.

# 6. The Effect of Plasticity on Intermediate Soil Compressibility

NICOLE MCCURDY


## ABSTRACT

Earthquake-induced liquefaction has the potential to cause devastating ground deformations. Soil susceptibility to this phenomenon can be predicted through triggering curves that plot the tip resistance of a Cone Penetration Test (CPT) against the cyclic resistance of soil. Predicting the location of a given soil with respect to the curve requires testing the tip resistance and cyclic resistance independently, based on their contributing properties. This project focuses on the CPT tip resistance, and, more specifically, how soil of various plasticity levels compresses when subjected to a force similar to that produced by a penetration rod pushing soil aside. Soil compressibility is depicted by a Limiting Compression Curve (LCC) based on one-dimensional compressive test results. The LCC describes when and how particle crushing occurs and is unique to each soil type. It is independent of initial density and aids in calibration of the MIT-S1 constitutive model to predict the CPT tip resistance. The yield point and slope of the LCC depend on the plasticity of the soil, so different compositions of ground silica silt and kaolin clay were used to track the effect of plasticity and fines content on the LCC.


## 6.1 INTRODUCTION

Liquefaction is a potentially devastating occurrence for civil infrastructure built in loose, cohesionless, saturated soil. The Cone Penetration Test (CPT) is a common *in situ* test used to help determine soil susceptibility to this event. Modeling such tests allows the results to be predicted without actually performing the test. Constitutive models are used to mathematically represent how material behaves under different loading conditions. The equations used for the model allow specific factors to be individually tested to determine their influence and significance. Calibrating the model requires various lab tests to determine the contributing factors and their respective numerical parameters. One of the calibration factors used to model CPT results depends on compressibility. The soil properties and conditions that affect compressibility are known, but some, such as plasticity, are still being understood.

The first step in modeling soil behavior is performing Atterberg limits tests to find the plasticity index (PI) of various soil mixtures. Soil composition is chosen based on the desired plasticity level and samples are prepared at liquid limit (LL) for compression testing. One dimensional compression tests provide data that create a limiting compression curve (LCC) of slope $\rho c$ in the log-effective stress, log-void ratio graph. $\rho c$ is one of thirteen necessary parameters used to calibrate MIT-S1, the constitutive model created by Pestana and Whittle [1999]. The equations included in this model are used in a finite element program to simulate the CPT tip resistance expected from that particular soil. The values can be plotted on predetermined triggering curves to predict whether liquefaction would occur under cyclic conditions.

## 6.2 BACKGROUND

### 6.2.1 Liquefaction

Earthquakes induce seismic waves that propagate through soil and apply cyclic loading throughout the soil profile. One effect of cyclic loading is liquefaction. Liquefaction is the loss of strength in saturated soil deposits due to the transfer of stress between soil particles onto pore water, causing effective stress to approach zero [Idriss and Boulanger 2008]. The total stress is the combination of effective stress (stress carried by the soil skeleton) and the pore water pressure (stress carried by the pore fluid). The liquefaction process begins when a rupture in bed rock induces vibration in loose, cohesionless soils, causing particles to want to shift into a denser packing. The soil would contract if drainage conditions were present, but rapid loading does not provide time for water to drain from the deposit. If water cannot drain, volume is held constant and there is a transfer of stress from the soil matrix to pore water as the soil particles attempt to contract. Effective stress felt by the particles reduces to zero and there is a loss of soil strength. Liquefaction can result in large strains and displacements depending on site geometry and soil-structure interaction. Figure 6.1 shows an example of this behavior, in which a building in Kocaeli, Turkey, tipped during a 7.6 magnitude earthquake in 1999. The building remained structurally sound, but the soil beneath the foundation liquefied, causing failure.


**Figure 6.1 Kocaeli, Turkey [USGS 1999].**

### 6.2.2 Cone Penetration Test

Due to the damaging effects of liquefaction, there is a need to predict where this phenomenon will occur. A CPT is a common, relatively simple test that measures soil conditions to determine site stratigraphy and engineering properties about a soil profile. A penetration rod is pushed into the ground at a constant rate, taking continuous readings of tip resistance, pore pressure, sleeve friction, and other values depending on the type of sensors used. Recorded data is displayed with respect to depth, indicating the type of soil in the profile. Figure 6.2 shows an example of a tip resistance profile obtained from a CPT as well as the soil behavior type it corresponds to.

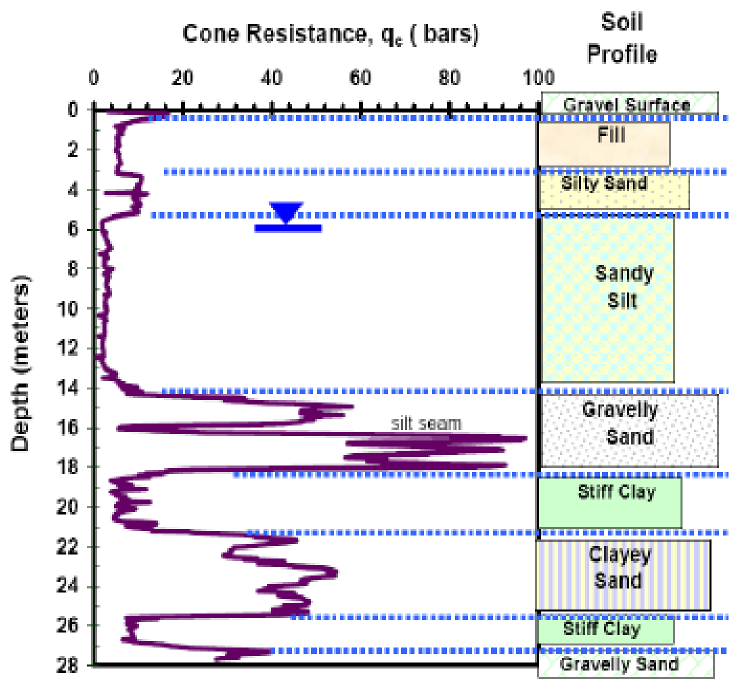


**Figure 6.2 CPT soil profile [Chien-Hsun et al. 2008].**

As the tip resistance increases, the number of loading cycles required to induce liquefaction also increases. This causes shear stress to build until the soil loses strength, causing liquefaction. The ratio between the shear stress, $\tau_{cyc}$, and the initial effective confining stress, $\sigma'_{vc}$, at this point is called the cyclic resistance ratio (CRR). The CRR is a very specific value of cyclic stress ratio (CSR), shown in Equation (6.1), which requires a certain tip resistance to cause liquefaction [Idriss and Boulanger 2008]

$$CSR = \frac{\tau_{cyc}}{\sigma'_{vc}} \tag{6.1}$$

Calculation of the CSR is necessary for plotting triggering curves, shown in Figure 6.3, which depict the boundary line between conditions where liquefaction is expected to occur and where it is not. These plots use a tip resistance that is normalized with respect to atmospheric pressure and corrected to represent the equivalent resistance obtained if the vertical effective stress were one atm, in order to make the plot applicable to more situations. Filled points on the graph indicate locations in the field where liquefaction has been observed and open points indicate where it has not. If a tip resistance is recorded at a CSR above the curve, liquefaction will likely occur under cyclic conditions.

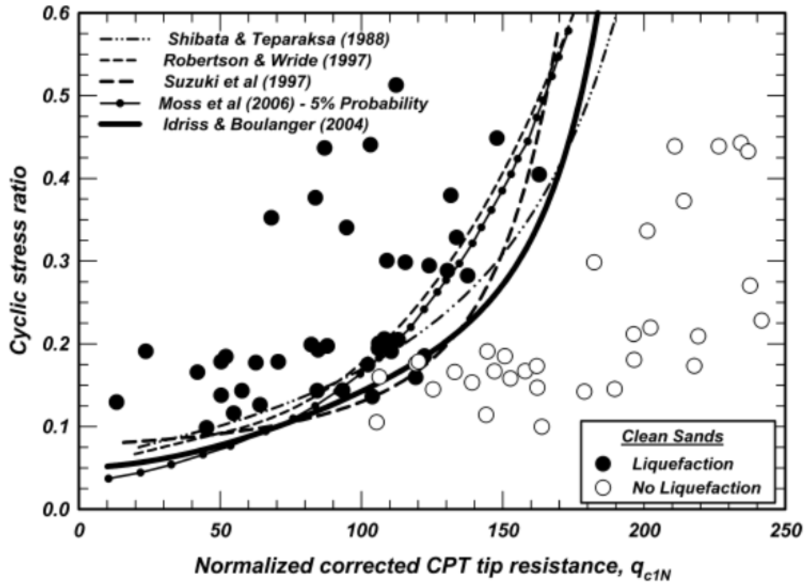


**Figure 6.3 Triggering curve [Idriss and Boulanger 2008].**

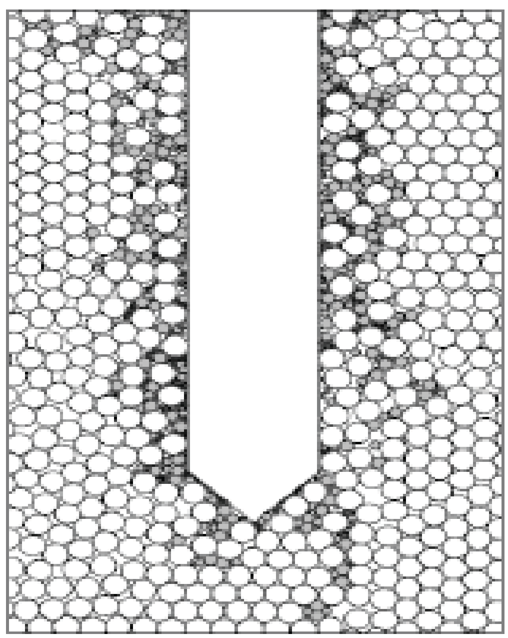

**Figure 6.4 Particle crushing around a cone penetration rod [Lobo-Guerrero and Vallejo 2006].**

A CPT analysis requires acknowledging that the cone must push soil aside in order to probe into the ground. Soil movement causes particle compression, which alters the data recorded by sensors. If compressive forces are high enough, the individual particles will crush into fragments. Figure 6.4 shows how particles close to the penetration rod crush in response to compression. The concentration of crushed particles decreases as distance from the rod increases, but the force is felt up to a distance of 20−50 cm away from the rod, depending on the density of the soil [Idriss and Boulanger 2008]. In order to understand the mechanics of particle crushing, the properties and behavior of fine and coarse grained soils must be explored.

### 6.2.3 Intermediate Soils

Engineers predict soil behavior by analyzing the properties known for soil and applying them to a model. Finding the input parameters for the model can be challenging when the soil composition changes, creating a more complex system compared with a pure sand or pure clay deposit. Heterogeneous mixtures, called intermediate soils, generally have a random structure because soil deposition occurs over time by many processes. Natural processes include rivers, rain flow, snow storms, wind, and other natural storms. These methods pick up soil from its native ground and carry it to new areas, often replacing it with foreign material. Unnatural processes include construction sites, excavation digs, etc., in which humans or mechanical equipment are the force behind soil movement. The resulting deposit is a combination of different soil types and particle sizes (see Figure 6.5). The composition of a deposit can change rapidly from one geographic region to another, or simply between locations in a construction site. Figure 6.1 underscores how soil properties can change rapidly, as the soil beneath the center building has liquefied, while the surrounding foundations remain intact.

Intermediate soils generally behave differently than homogeneous soils because varying particle size and mineralogy affects soil behavior. For example, sands are composed of coarse grains that lack inter-particle forces, resulting in cohesionless behavior. Water flows through the granular matrix unaffected, explaining why pure sands cannot retain shape when acted upon by an outside force. Clays, which are inherently fine grained soils, have significantly different properties than coarse grained soils. Clay particles have strong inter-particle forces that produce a very cohesive material that is able to retain shape when acted upon by an outside force. The nature of clays to bond together is a characteristic of plasticity.

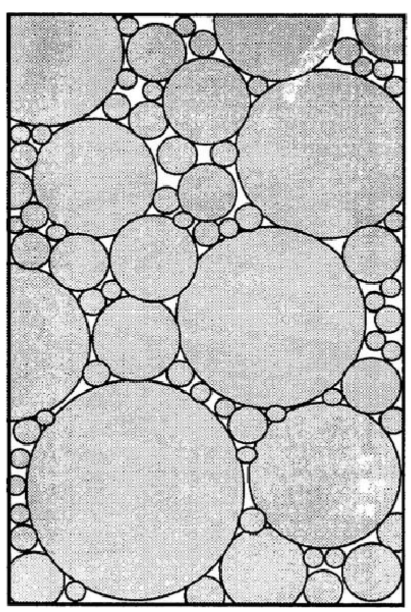

**Figure 6.5 Intermediate soil [Integrated Publishing].**

### 6.2.4 Plasticity

Plasticity is an index primarily associated with clays that describes the nature of soil under hydrated conditions. Negatively charged oxygen and hydroxyl molecules found on the surface of clay particles attract to positively charged hydrogen atoms in water, creating hydrogen bonds. An adsorbed water layer forms, attracting additional particles and creating strong inter-particle forces. Large water layers surrounding each particle lead to a large void ratio, so when compressive force is applied, there is significant displacement as this water is pushed out [Holtz et al. 1981]. Depending on the amount of water present in a clay sample, it can be classified as solid, semi-solid, plastic, semi-liquid, or liquid. The plastic limit (PL) is the water content defining the boundary between the semi-solid and plastic states. The liquid limit (LL) is the water content defining the boundary between the semi-liquid and plastic states. The range over which the soil behaves plastically is the plasticity index (PI), found by subtracting the plastic limit from the liquid limit (per ASTM D4318-10). A higher PI indicates a greater percentage of water that can be absorbed by the particles, and therefore a greater void ratio change during compression. Plasticity is not present in sands, suggesting that there is little void ratio change during compression.

### 6.2.5 Limiting Compression Curve

Plasticity is one of many soil properties that affects compressive behavior. This behavior is represented by a Limiting Compression Curve (LCC), which models the compressibility of soil when volumetric strain is governed by particle crushing [Pestana and Whittle 1995]. One-dimensional compression tests apply a force to soil samples to represent the pressure felt from a penetration rod. Soil initially compresses elastically as the particles deform and rearrange in response to the force. When all particles are in mutual contact, crushing occurs to facilitate continued contraction. Initial density affects the onset of crushing because high-density deposits have greater particle to particle contact, causing the stress to be distributed among more contacts, so the stress per contact is lower. A dense sample delays crushing while a loose sample, which has greater forces applied by fewer particles, crushes sooner [DeJong and Christoph 2004]. During the crushing process for intermediate soils, void ratio (or density) depends only on granular skeleton because high stress reduces the volume of voids, regardless of their initial state. Voids are forced out, and the curve at any initial void ratio converges to the same rate of crushing. Figure 6.6 shows the path of a soil prepared at different void ratios converging to the same LCC. Plastic soils, such as clays, have a gradually curving LCC while non-plastic soils, such as sands, have a yield point between non-plastic and plastic behavior. For this reason, the slope of the LCC for clays and sands is different, and the percentage of each within an intermediate soil affects the slope. The different curves are explained in detail in Section 6.4.2.

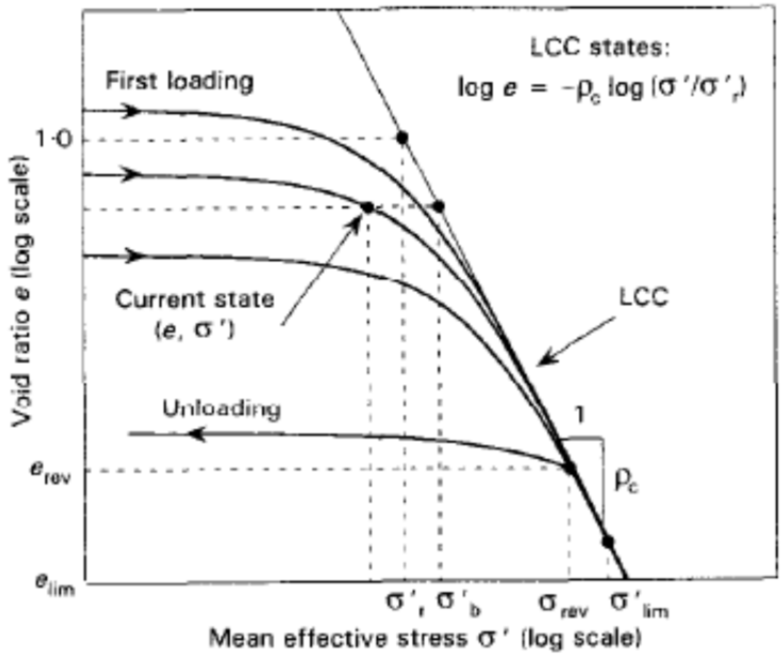


**Figure 6.6 Limiting Compression Curve [Pestana and Whittle 1995].**

### 6.2.6 Non-plastic, Cohesionless Soils

Extensive compression analysis has been performed on cohesionless, homogeneous soils. Pestana and Whittle [1995] created a model for freshly deposited, cohesionless soils in the LCC range based on formation density, mineralogy and structure, physical properties, applied boundary stress conditions, time dependent behavior, and interstitial fluids. The model illustrates the transition from elastic to plastic behavior that can be applied to all soil types. The cohesionless soils exhibit very little contraction at low stresses, thereby maintaining a relatively constant void ratio. Once stresses pass the point of non-plastic compression, particle crushing happens simultaneously throughout the sample, causing an increases rate of contraction [Pestana and Whittle 1995]. Initial particle size has very little influence on the slope of the LCC because particles crush into fine material, regardless of the initial size. Larger particles crush earlier because there are fewer contact points from surrounding particles, causing the forces applied at each contact to be larger. Large particles also have a greater chance of flaws, which provide unstable surfaces for fracture to occur.

### 6.2.7 Plastic, Cohesive Soils

Homogeneous fine grained soil is composed of particles less than 75 microns, (or those that pass the #200 sieve during a sieve test). Soil that falls into this description is fine material produced from crushed sand, which is non-plastic, and clay, which is plastic. Crushed sand has the same properties as its larger counterpart, so there is no effect on the slope of the LCC. Clays, however, follow a different LCC trend because of plasticity. Biscontin et al. [2007] performed compression tests on clays and found that the LCC has a smaller slope compared with that of sands and lacks a defined yield point. Clays are plastic because of a thick water layer held between each particle; when the sample is consolidated or compressed, that water is pushed out. Crushing happens gradually and there is no specific stress where crushing is concentrated. Bray and Sancio [2006], however, who studied the liquefaction potential of clays by performing cyclic tests, found that an increase in soil plasticity tends to indicate an increase in void ratio and that void ratio cannot independently characterize cyclic resistance because plasticity also has an influence. This supports LCC analysis in which initial void ratio only influences when crushing begins, while plasticity influences the slope.

### 6.2.8 LCC Analysis for Intermediate Soil

Biscontin et al. [2007] studied the compressibility of intermediate soils from the response of samples taken from the Venice Lagoon. One-dimensional compression tests showed that for clay contents between 20–70%, it was not clay content but mineralogy that affects the slope of the LCC [Biscontin et al 2007]. For samples with less than 20% clay contents, compressibility depends primarily on the granular material because clay particles are confined in the void space between the large grains. For samples with greater than 70% clay contents, compressibility depends primarily on the clay material because the large non-plastic grains essentially float in a clay matrix. The region between these extremes, where clay particles are neither confined to the granular voids nor enveloping the large grains, are therefore influenced by both soil properties [Biscontin et al. 2007]. When clay content is very low, the slope of the LCC is steeper than when clay content is high, leading to the conclusion that increasing the number of fines decreases the slope of the LCC.

## 6.3 PROCEDURE

### 6.3.1 Atterberg Limits

Ground silica silt and kaolin clay were chosen as the cohesionless and cohesive soil used for this project, respectively, because each exhibits typical characteristics of their soil type. Intermediate soils with 10, 20, 30, 40, and 50% dry weight kaolin were mixed with silica in preparation for finding PIs. The mixtures were brought to a water content slightly larger than the predicted liquid limit and then sat for 24 hours to allow maximum saturation throughout the sample. Atterberg limits tests were performed to find the liquid limit, plastic limit, and PI for each mixture. The liquid limit defines the boundary between the semi-liquid and plastic states. It measures the water content of a soil that, when placed in a brass cup and separated down the center by 2-mm line, closes a gap of 13 mm when dropped a given number of times. The plastic limit defines the boundary between the plastic and semi-solid states. It measures the water content of soil that, when repeatedly rolled into a 3.2-mm-diameter thread, cannot be reformed into an ellipsoidal mass from the broken thread pieces. The PI is the difference between the two, and therefore the range over which the soil behaves plastically; see ASTM D4318-10 [2010]. Examples of the liquid limit and plastic limit test are shown in Figure 6.7.

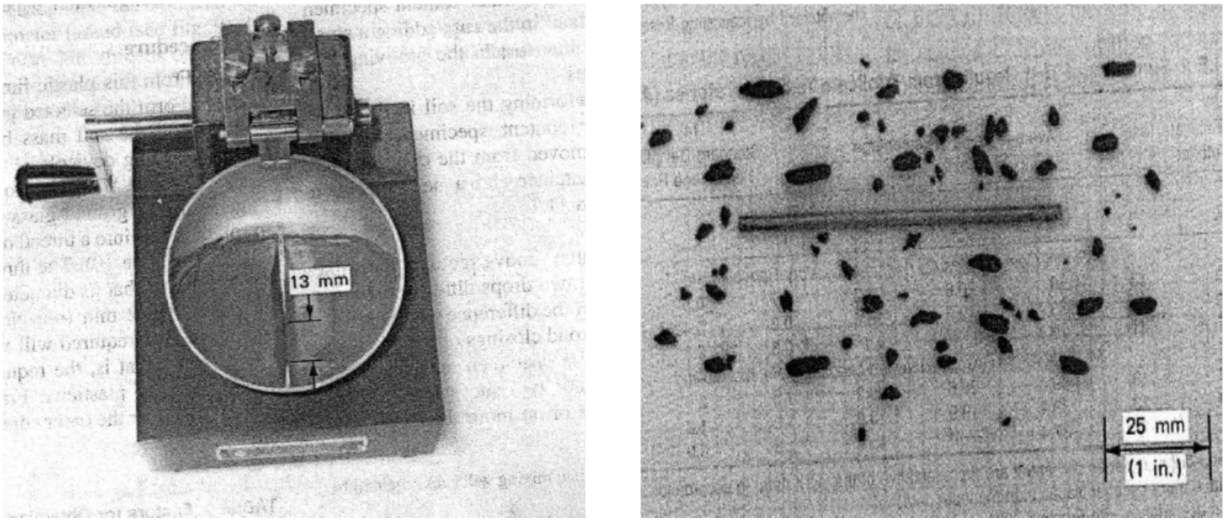


**Figure 6.7 Liquid Limit Test (left); Plastic Limit Test (right) [ASTM 2010].**

### 6.3.2 One-Dimensional Compression Test

A steel mold with an inside diameter of 63.42 mm was used to hold the soil during testing. Four screens were placed in the bottom of the mold, starting with a perforated metal screen, #30 screen, #200 screen, and #325 screen. Each consecutive screen had a smaller percent passing allowance so that only water could drain during compression. The sample was prepared at liquid limit and set aside overnight to allow for complete hydration. It was placed carefully over the #325 screen to avoid creating air pockets and four identical screens were placed on top, symmetric to the initial four, followed by the top cap (see Figure 6.8).

**Figure 6.8 Steel mold and screens (perforated, #30, #200, #325).**

A seating load of 100 kPa was applied to normalize initial height readings so that every test had an initial height and volume based on the same applied force. For pure silica samples, the seating load was applied by placing weights on the cap of the mold for approximately 30 minutes. All other samples contained kaolin and were loaded using a GeoJac consolidation device, which applied the load in increments of 25 kPa, 50 kPa, and 100 kPa every four hours. Initial height measurements were taken after consolidation had slowed to a negligible rate. The device was then placed onto the compression frame, as shown in Figure 6.9. To ensure drained loading, the bottom arm was set to move upward at a strain rate of .025 in./min for pure silica and .0007 in./min for samples with kaolin. A Linear Variable Differential Transformer (LVDT) measured the change in displacement during the test. The load applied was recorded and converted into MPa, which was used in conjunction with the displacement to find the height change, volume change, volumetric strain, and void ratio. Tests generally ran to a stress of about 10 MPa for pure kaolin samples and about 130 MPa for samples containing silica.

**Figure 6.9 One-dimensional compression test.**

## 6.4 RESULTS

### 6.4.1 Plasticity Indices

Plasticity tests on mixtures of 30, 40, 50, and 100% dry weight kaolin produced liquid limit, plastic limit, and PI values are listed in Table 6.1.

Table 6.1 Atterberg limit test results.

| Plasticity Indices | | | |
|---|---|---|---|
| 100% kaolin | 50% silica/50% kaolin | 60% silica/40% kaolin | 70% silica/30 kaolin |
| LL= 64% | LL= 33% | LL= 29% | LL= 27% |
| PL = 30% | PL = 19% | PL = 16% | PL = 18% |
| PI = 34% | PI = 15% | PI = 13% | PI = 10% |

Liquid limit tests on mixtures of 80% silica with 20% kaolin and 90% silica with 10% kaolin were attempted but could not be completed due to soil tearing in the Casagrande bowl when a groove was made down the center. As stated in ASTM standard D4318-10 [2010]. "If, after several trials at successively higher water contents, the soil pat continues to slide in the cup or if the blows required to close the grove is always less than 25, record that the liquid limit could not be determined, and report the soil as non-plastic without performing the plastic limit test." Soil compositions of 20% kaolin or less are therefore non-plastic. There are not enough clay particles to fill the voids between sand grains for the soil to behave cohesively.

The plasticity index changed significantly between the ranges of 100 to 50% clay. A 20% decrease was seen between pure kaolin and the composition of 50% kaolin, but only an additional 5% decrease from 50 to 30% kaolin. Once the clay content decreased enough that the sand grains were no longer isolated from one another in a clay matrix, the plastic nature of clay had a weaker influence on the plasticity. Figure 6.10 depicts the classification of soil as a function of liquid limit and plasticity index. 100% Kaolin is classified CH, or clay with high plasticity, while the intermediate soils are classified CL, or clay with low plasticity.

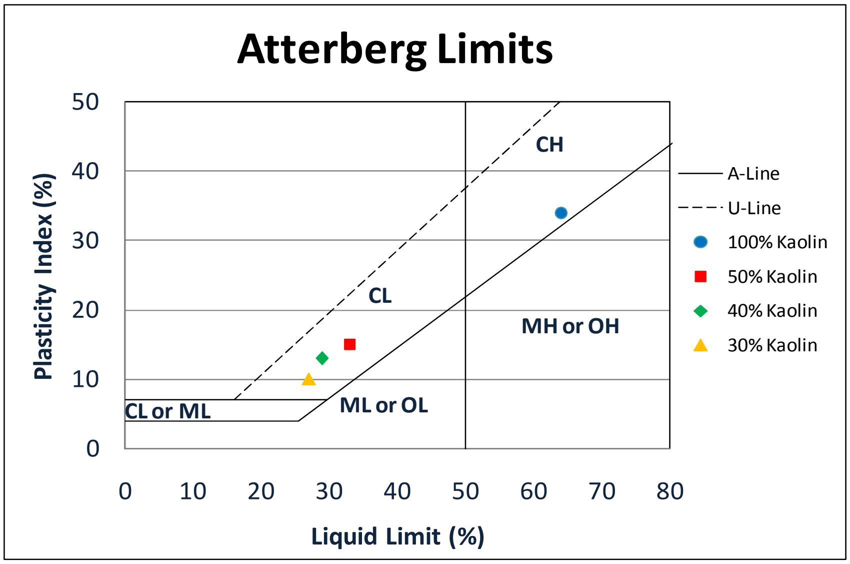


Figure 6.10 Soil classification based on Atterberg limits.

### 6.4.2 Limiting Compression Curves

The following compression curves were produced by processing data from one-dimensional compression tests on pure kaolin, pure silica, 50% kaolin with 50% silica, 40% kaolin with 60% silica, and 30% kaolin with 70% silica.

#### *6.4.2.1 Kaolin LCC*

Kaolin is a fine grained, cohesive soil with a high plasticity index. Significant drainage occurred as the load increased, leading to large changes in void ratio and minimal particle crushing. The LCC for three one-dimensional compression tests on kaolin are shown in Figure 6.11

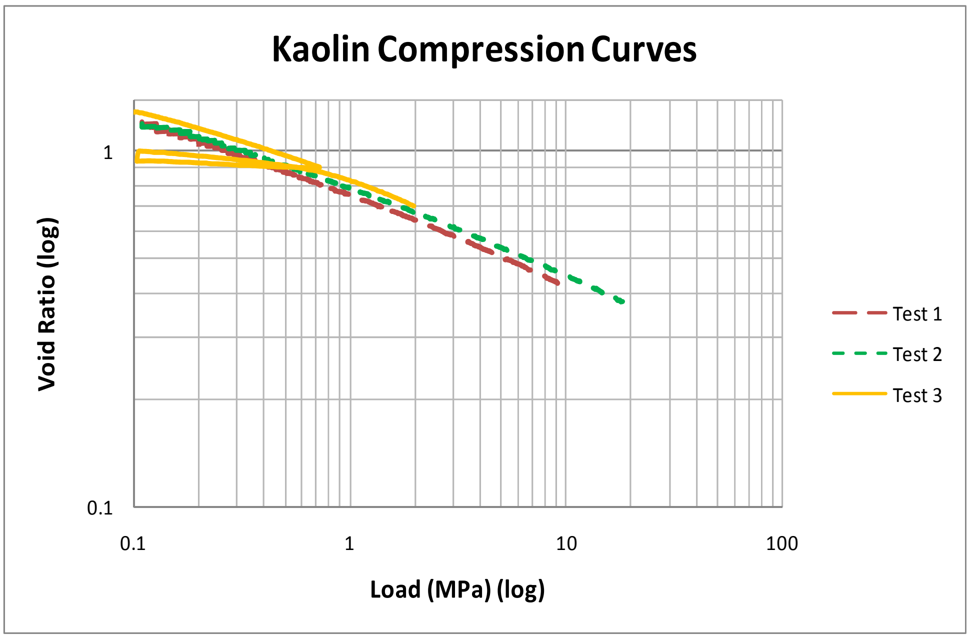


**Figure 6.11 Kaolin Compression Curves**

Two tests were performed with an MTS compression frame that had the ability to provide large forces. These tests displayed identical behavior confirming that the LCC is indeed a gradual curve. The final test was performed on a GeoJac consolidation device, which could not provide a force of equal magnitude as the MTS frame, but provided the opportunity to unload and reload the specimen. Unloading began just after a stress of 7 MPa and reloading began below .1 MPa. Reloading followed the unload line due to over-consolidation, but returned to the initial rate of contraction once normal consolidation resumed. There was no defined yield point where particle crushing began, but rather, the entire curve is the LCC. Due to their disk-like shape, clay particles lack contact points where strong forces can be applied that would induce particle crushing. Significant water drainage was observed during each test, confirming that water that once formed adsorbed water layers around each particle was forced out.

#### *6.4.2.2 Silica LCC*

The ground silica used for this project was identified as SIL-CO-SIL 250, taken from Ottawa, Illinois. It is a non-plastic, granular constituent of silica sand that had been crushed, removing most weak surfaces and creating particles with a mean diameter of 45 microns. Figure 6.12 shows results for five compression tests on pure silica.

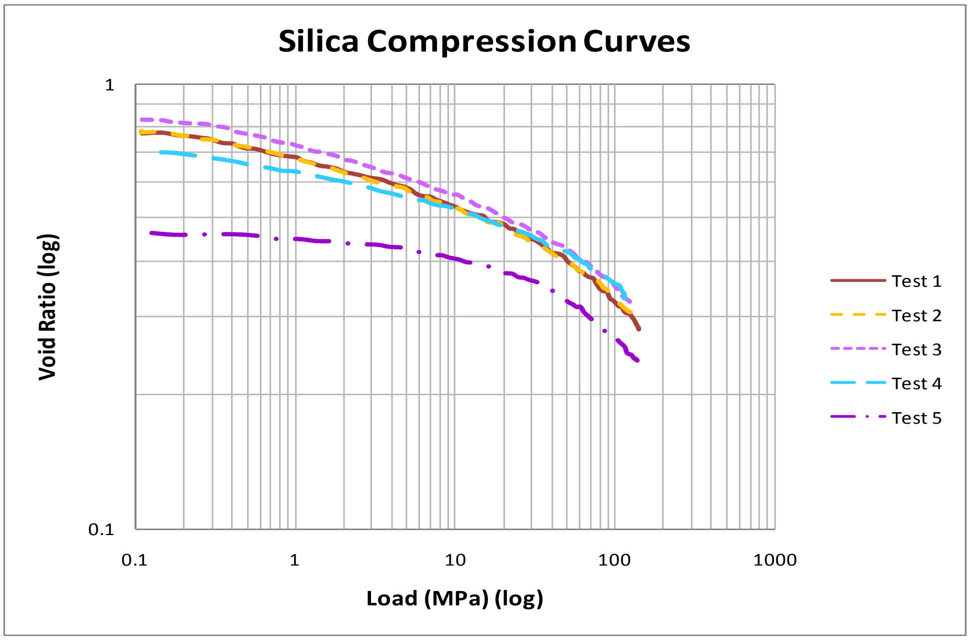


**Figure 6.12 Silica compression curves.**

Tests 1-4 were prepared by dry pluviation and vibrated until a desired initial void ratio was reached. There was a 30–40% void ratio change from the start of compression to the observed yield point, when the yield point is considered to be between .4 and .5 void ratio. Test 4 withstood greater forces before crushing because there were more contact points on each particle, causing less stress per contact. This behavior is shown by Test 4 crossing over Tests 1–3. A fifth test was prepared as a slurry to a water content of 23.5%; the greatest water content silica could hold without separation of sand and water layers. This preparation method was used to more accurately resemble the liquid limit preparation of the other samples. The sample was loaded into the mold and vibrated until a desired initial void ratio was reached. Compression yielded roughly 20% void ratio change (when the yield point is considered to occur at .33 void ratio), a much smaller change when compared to Tests 1–4. Vibrating Test 5 in the presence of water caused particles to rearrange into a very dense, strong packing, allowing large forces to be applied before any crushing was required to accommodate additional stress.

These tests were not able to provide complete results for the LCC because the compression frame used for this project had a maximum load capacity of 100 kips. This provided a maximum of 140.8 MPa, which was insuficient to decide if particle crushing was actually induced. Previous research has been done at UC Davis by Ian Maki on Nevada sand, a silica sand with greater mean diameter, producing compression curves that yielded at smaller stress values. Ground silica yielded later than the Nevada sand because angularities and weaker planes that may have been present on larger grains were already eliminated in order to make the ground material.

### *6.4.2.3 Intermediate Soil LCC*

The following compression curves were produced for mixtures of 50% silica with 50% kaolin (Figure 6.13), 60% silica with 40% kaolin (Figure 6.14), and 70% silica with 30% kaolin (Figure 6.15).

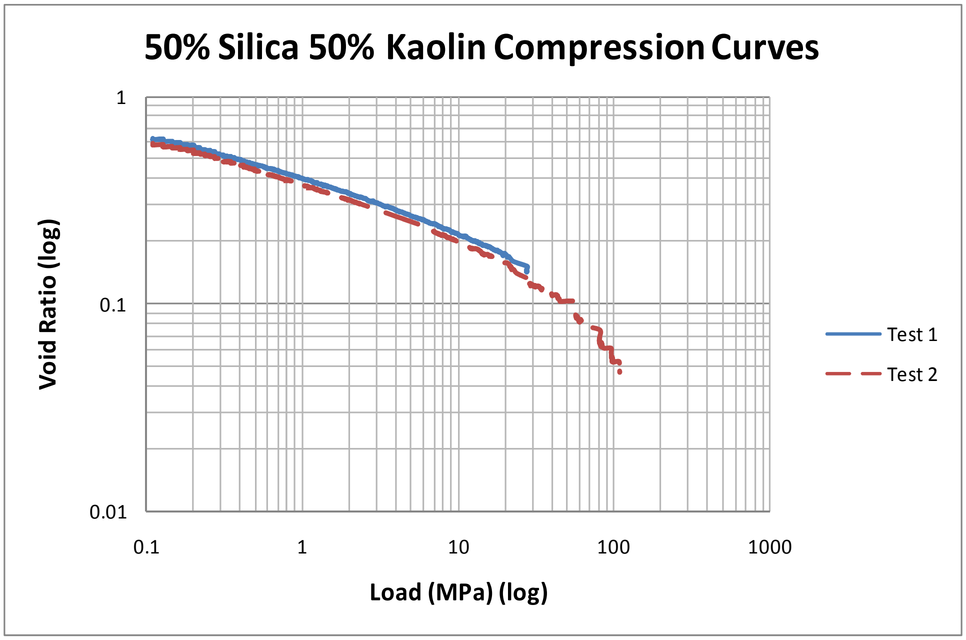


**Figure 6.13 50% Silica 50% Kaolin compression curves**

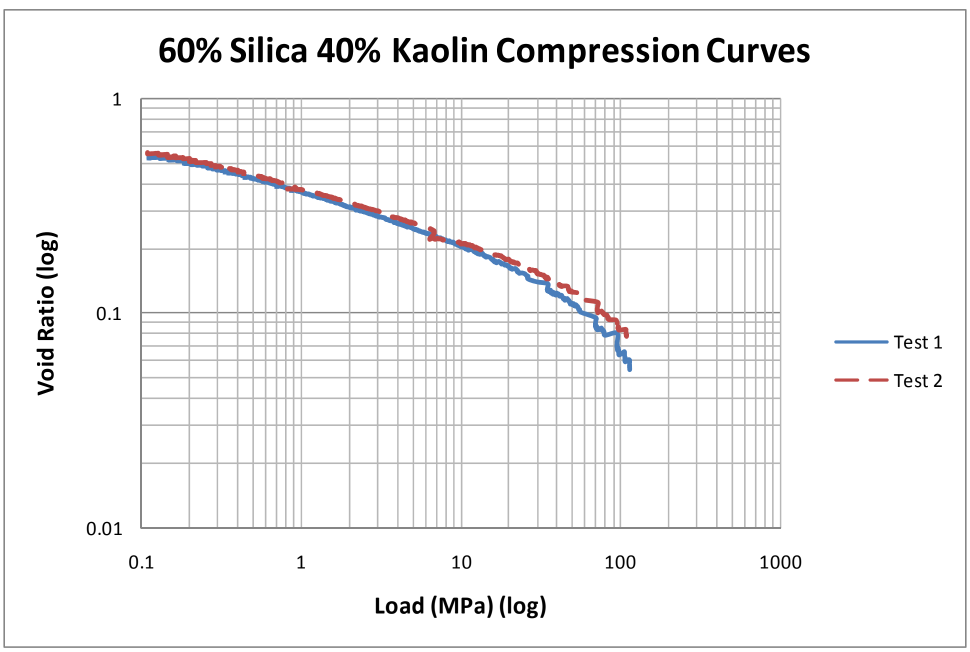


**Figure 6.14 60% Silica 40% Kaolin compression curves**

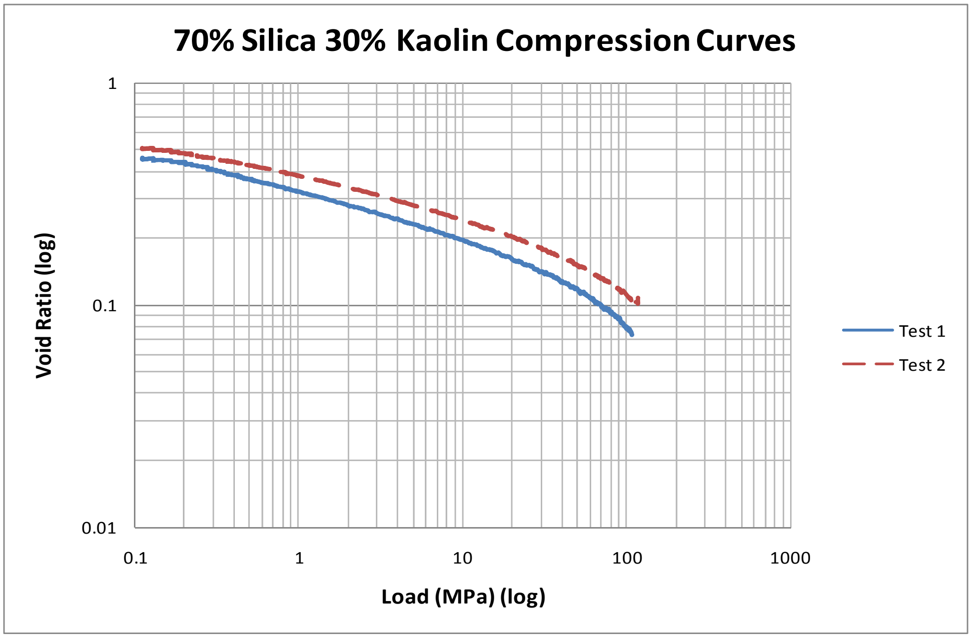


**Figure 6.15 70% Silica 30% Kaolin compression curves.**

### *6.4.2.4 Total Comparison*

The amount of plastic and non-plastic soil present in a mixture at a given stress state influences whether clay or sand behavior dominates. In the case of compressibility, five mixtures of various levels of ground silica and kaolin clay were of interest, with results shown in Figure 6.16.

Ground silica began with a smaller void ratio than kaolin clay because it was prepared at a lower water content than kaolin. The intermediate soils are a combination of silica and kaolin so it is expected that they begin at a void ratio between that of each constituent. As the clay content increased, the initial void ratio decreased because clay particles filled the voids created by the larger silica grains. Soil composed of 50% silica and 50% kaolin was the loosest of the three mixtures and therefore yielded with less stress. Next was the mixture of 60% silica with 40% kaolin, which began denser and crossed over the mixture with 50% silica in order to yield at a higher stress. The mixture of 70% silica with 30% kaolin was the densest and crossed over both previous curves to yield at a higher stress.

The compression curves for the intermediate soils had slopes almost identical to that of kaolin until stress reached approximately 20 MPa. Until this point, silica grains were suspended in a clay matrix. Clay filled the void space between silica grains, inhibiting mutual contact between all granular particles. The clay compressed during low stresses without significant movement of silica particles, therefore imitating the void ratio change of kaolin. When stress reached the yield point, the clay volume decreased to the point where sand grains formed an interconnected structure in which all particles were in contact. Particle crushing occurred to accommodate further stress and soil behavior became a function of granular skeleton. The LCC began after yielding and followed a slope identical to pure silica. This would be evident in Figure 6.16 if greater stresses could have been applied and the LCC for each soil had fully developed.

The data for mixtures of 50% silica with 50% kaolin and 60% silica with 40% kaolin appears distorted and missing values at high stresses. This has been determined not to be a result of soil properties, but instead a problem with the hydraulic pump used to apply the force. It is being discussed that applying large forces at very low rates caused the frame to slip. In response, larger loads than specified were applied in increments instead of smaller loads being applied continuously. It is unknown why this event only occurs at random.

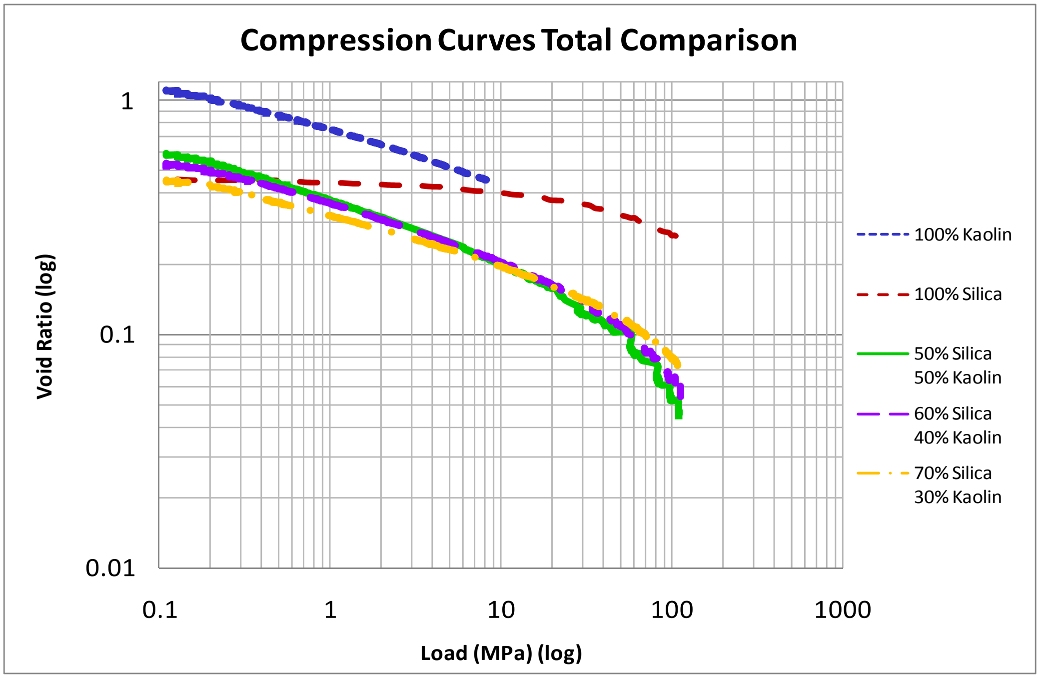


**Figure 6.16 Compression curve total comparison.**

## 6.5 CONCLUSIONS

Empirical relationships between ground conditions and soil strength allow the prediction of soil susceptibility to liquefaction. One soil property that affects the susceptibility is plasticity. One dimensional compression tests on soil composed of ground silica silt and kaolin clay prepared at different plasticity indices are an essential step in calibrating the model used to predict liquefaction.

Atterberg limits tests on soil composed of silica with 10, 20, 30, 40, and 50% kaolin yielded increasing plasticity indices, respectively, indicating that as clay content increases, soil plasticity increases. The atomic properties of clay produce an attraction between water molecules and the surface of each clay particle, allowing it to behave plastically. Therefore a soil with a larger plastic component exhibits greater plastic behavior.

The plastic nature of clays causes consolidation to occur throughout the compression process as the water that formed a thick layer around each particle is pushed out. Because clay particles have a disk-like shape, there is never a time when all particles in a sample are in mutual contact; therefore crushing and consolidation is simultaneous and gradual. The transition from elastic to plastic behavior is nonexistent. Silica exhibits a different trend because it is composed of non-plastic, granular particles. Particles compress until there is mutual contact and elastic compression can no longer be sustained, causing sudden crushing to occur. The ground silica yields at higher stresses than silica sand because weaker planes and angularities that would have crushed at the earliest have already been eliminated.

When kaolin clay is mixed with silica sand and compressed, the soil behaves similar to clay at low stresses and similar to sand at high stresses. Sand grains are suspended in a clay matrix until the clay volume has compressed to the point where sand particles inflict the greatest force on one another. At this point, soil behavior is dictated by granular crushing. Fines content does not define slope, but rather it is defined by granular skeleton. Before the yield point is reached, soil exhibits primarily elastic behavior. If unloaded, most of the void space would be recovered. Once crushing begins, plastic behavior prevails because the same structure cannot be recovered if unloaded.

These results support the results presented by Pestana and Whittle [1999], who state that particle mineralogy, size, grading and shape affect compressibility. Each of these properties affects either the location of the yield point or the slope of the LCC, which are used in the MIT-S1 model to simulate soil compression during a CPT.

## ACKNOWLEDGMENTS

This research was made possible by the Pacific Earthquake Engineering Research (PEER) Center under the direction of Heidi Tremayne, with funding from the National Science Foundation (NSF). I would specifically like to thank Dr. Ross Boulanger and Dr. Jason DeJong for their guidance and invaluable knowledge, and Adam Price for his generous instruction and patience. I am grateful to have had the opportunity to work with the entire geotechnical team at UC Davis. Lastly, I thank Bill Sluice and Daret Kehlet for their knowledge and instruction with lab equipment.

## REFERENCES

ASTM (2010). *Standard Test Methods for Liquid Limit, Plastic Limit, and Plasticity Index of Soils, ASTM D4318-10* American Society for Testing and Materials, West Conshohocken, PA.

Biscontin GM, S Cola, JM Pestana, and P Simonini (2007). Unified compression model for Venice Lagoon natural silts, *J. Geotech. Eng*., 133(8):932–942.

Boulanger RW, and IM Idriss (2008). *Soil Liquefaction during Earthquakes.* Earthquake Engineering Research Institute, Oakland, CA.

Bray JD, and RB Sancio (2006). Assessment of the liquefaction susceptibility of fine-grained soils, *J. Geotech. Eng.,* 132(9):1165–1177.

Chien-Hsun C, JC Hsein, and PW Mayne (2008), CPTu simplified stress-based model for evaluating soil liquefaction potential, *Soils and Foundations.* 48(6):755–770.

DeJong JT, and GG Christoph (2004). Relation of initial specimen state and particle properties to the breakage potential of granular soils, *Proc*., Geo-Quebec Conference, Quebec, City, 7 pgs., Canada.

Holtz RD, WD Kovacs, and TC Sheahan (1981). *An Introduction to Geotechnical Engineering.* Pearson. Education, Saddlebrook, New Jersey.

Integrated Publishing, *Structure of a Well-Graded Soil*, *http://armyengineer.tpub.com/En5341a/En5341a0111.htm.*

Lobo-Guerrero S, and LE Vallejo (2006). Degradation of a granular base under a flexible pavement: DEM simulation, *Inter. J. Geomech.*, 6(6):435–440.

Pestana JM, and AJ Whittle (1995). Compression Model for cohesionless soils, *Geotechnique*, 45(4):611–631.

USGS (2005). Implications for earthquake risk reduction in the United States from the Kocaeli, Turkey, earthquake of August 17, 1999, U.S. Geological Survey, *Circular 1193*, *http://pubs.usgs.gov/circ/2000/c1193/.*

# 7. Risk-Based Levee System Analysis with Multiple Failure Modes

PAUL SHIPMAN

## ABSTRACT

Most risk-based analysis of levee systems includes only one levee and only failure by overtopping. Using one failure mode overestimates the reliability of levees. Including multiple levee segments or reaches provides additional dimensions for design, which can lower costs, but also raise important policy challenges. Lowering levees in a critical region, called fail-safe levees, to safeguard other levees in the system may be optimal in some cases. The model in this paper simulates a two-reach levee system with one levee on each side of the river. The model finds optimal levee geometries: height, width, and setback separately for each side of the river. The intermediate failure modes of through-seepage, under-seepage, and erosion are included to give a more accurate representation of levee failure. A few important conclusions can be drawn from this work. First, when relative flood damage becomes significantly different on opposing sides of the river, it is more economical to not build a levee on the side with the least value. Secondly, designing the system with a fail-safe levee reduces construction costs overall and improves life safety. Third, the addition of intermediate failure-modes on levee system analysis drastically changes the optimal levee parameters. Widespread application of models such as the one presented in this paper could significantly contribute to efficiency and life safety by ensuring money is spent in the most ideal places to improve levee systems.

## 7.1 INTRODUCTION

Levee systems evolve over time with improvements typically following failure or near-failure events. Incremental infrastructure improvements may fix critical problems, but often lack the perspective needed to improve overall system reliability. Coordinated planning and design of levee systems can offer promising solutions missed by the historical piecemeal approach. An important approach to levee systems modeling is risk analysis. Risk analysis of levee systems requires estimating the probability of flood events and the consequences of levee failure. Risk analysis fits within a total cost framework where minimum overall cost is the primary planning and design goal. This is done by identifying failure modes, creating models for these modes to generate failure frequency curves, and finding the geometry of levees to minimize total expected annual damages and construction costs. Modeling multiple failure modes can be challenging because they are often poorly defined: “There is no single widely accepted analytical technique of performance function in common use for predicting internal erosion” [USACE 1999]. These individual levee models generally optimize levee height and width, however, levee setbacks are rarely considered. Levee systems analysis, on the other hand, will sometimes include levee setbacks but not optimize levee width as levee systems analysis generally consider overtopping alone and often excludes hydrologic uncertainties or simply apply additional safety factors instead. “In the design of flood levee systems there are many hydrologic and hydraulic design variables and parameters. Because the design variables and parameters have interdependent associated uncertainties, several of which are beyond man’s control, the risk of failure is difficult to analyze” [Tung 1981]. Systems models often ignore other failure modes to simplify the problem; however, this fails to reflect the actual mechanics of the problem, overestimates levee reliability, and may return inferior solutions. This paper investigates the potential effects of multiple failure modes on a system of levees to find optimal geometry in terms of levee height, width, and setback from a river.

The background section discusses levee failure modes, system modeling approaches, and solution algorithms for solving multi-decision problems. The methods section discusses the basic outline of what the model does, what it has the capability to do, what some of the equations running in the background are, and some limitations of the model. Model results identify the importance of fail-safe levees to protect other higher value areas and show the tradeoff between levee height, width, and setback for improving overall system reliability. The conclusion and future research sections discuss how the information and techniques in this paper could be applied in the future to work done on levee systems to improve reliability and further minimize total annual cost.

## 7.2 BACKGROUND

Risk-based analysis is important for planning and design of infrastructure. According to the Central Valley Flood Protection Plan (CVFPP), in California’s Central Valley alone about one million people and about $70 billion in assets are at risk in the event of a catastrophic flood control failure. As recently as 1997, over 120,000 people were evacuated and 9000 homes were destroyed, with over $1 billion in direct flood damages. Cumulative flood damages in 1983, 1986, 1995, and 1997 caused over $3 billion in flood damages [DWR 2012]. These statistics show why optimized evaluation and construction of levees is so important. Failure modes, levee systems research, and solution algorithms used in optimization problems are discussed.

### 7.2.1 Failure Modes

Several independent modes of failure are considered for this work. The first mode is overtopping. Overtopping occurs when water height exceeds channel capacity and can cause levee breaches. Erosion is another failure mode, caused by river currents and wave impacts on levees. Through-seepage is also addressed, defined as internal erosion through the main body of the levee. Through-seepage is caused by high exit gradients displacing particles and creating an internal flow path for water. It can be exacerbated by cracks from hydraulic fracturing, decayed vegetation, animal activity, or anything that creates a preferential seepage path [USACE 1999]. Under-seepage failure is similar to through-seepage except that it represents internal erosion occurring in the sub layers below the levee; it is also affected by cracks or preferential flow paths. Slope stability is also considered. Failure due to slope stability occurs when the resistive shear forces are overcome by gravitational forces, which often occurs with saturated levees. As soil becomes heavier and pore water pressure increases, the loading on the soil increases and the effective stress of the soil decreases. This increases the chance of a failure surface developing. The final failure mode considered is seismic vulnerabilities. Although the probability of a major flood event and an earthquake occurring at the same time is very low, there are many parts of the Sacramento-San Joaquin Delta where portions of the levees are saturated year-round due to tides, land subsidence, and other issues. Seismic vulnerabilities reflect the probability of liquefaction as well as the probability of cracks forming a preferential path for the flow of water through or under the levee. Figure 7.1 shows examples of failure modes on a cross section of a levee.

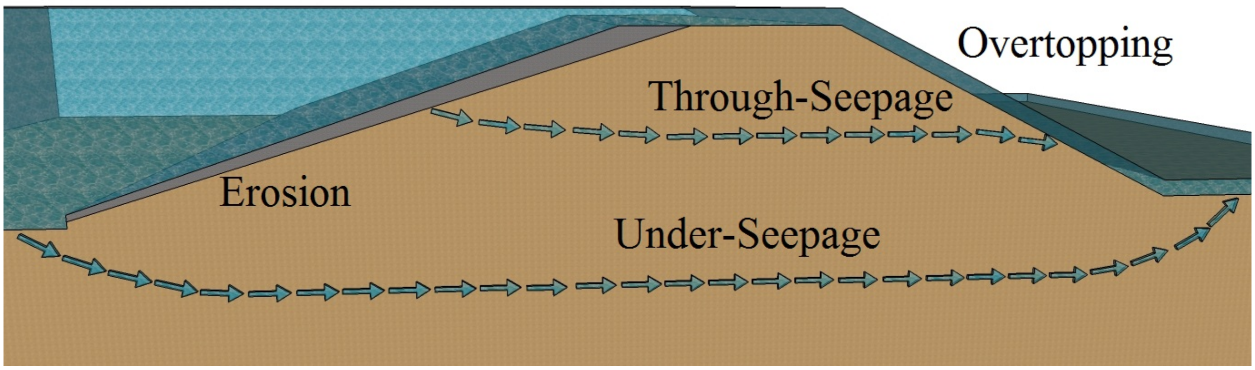


**Figure 7.1 Schematic of several failure modes.**

### 7.2.2 Levee Systems Models

Given that much of the Netherlands is below sea level, the Dutch have done extensive research on levee systems. Traditional levee design for levee systems often considers only overtopping failure. Per Dantzig [1956]: "When speaking about the 'height' of a dike, we do not mean the actual height of its crown, but the height of the 'critical sea level,' i.e., the sea level at which the dike may break (which can be lower than the height of the crown)." The determination of levee height based on past flood events and failures rather than analysis of the actual mechanics of potential failure modes was standard practice. Dantzig also points out, "… to every height there belongs a positive 'exceedance probability.' For this reason the expression 'flood *prevention*'…might be considered somewhat misleading." In risk-based optimization, the goal is not to minimize the chance of failure but rather the overall annualized cost as a function of flood damages and construction costs.

A more contemporary model is presented in Tung and May [1981] where they incorporate hydrologic and hydraulic uncertainties into a dynamic programing and discrete differential dynamic programing model. They attempt to optimize height and width of levees in a system of progressive levee reaches, such as those shown below in Figure 7.2.

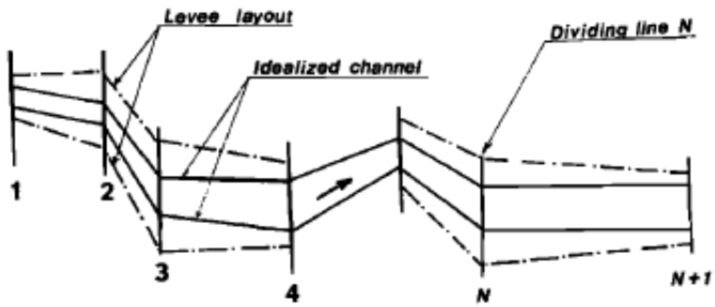


**Figure 7.2 Idealized channel reach configuration and levee layout [Tung and May 1981].**

A few limiting assumptions in this model makes it potentially difficult to apply. "The levees are symmetrical with respect to the center line of the straight channel, with equal height at all points in a reach." This is seen as a significant limitation as the system cannot model different resources (and associated damage costs) on either side of a levee within a single reach.

The U.S. Army Corps of Engineers *ETL 1110-2-556*, "Risk-Based Analysis in Geotechnical Engineering for Support of Planning Studies," deals extensively with analyzing levee failure modes. They include through-seepage, under-seepages, slope stability, and surface erosion. This is an important variation from the usual approach of only considering overtopping with a safety factor to optimize levee construction and could have significant insights into efficient levee geometry. A major limitation of this paper is the application to only an individual levee to create a performance curve, such as the one shown in Figure 7.3, as opposed to extending this to examine multiple levees in a system. These curves approximate performance functions for individual levees based on soil properties and levee geometry.

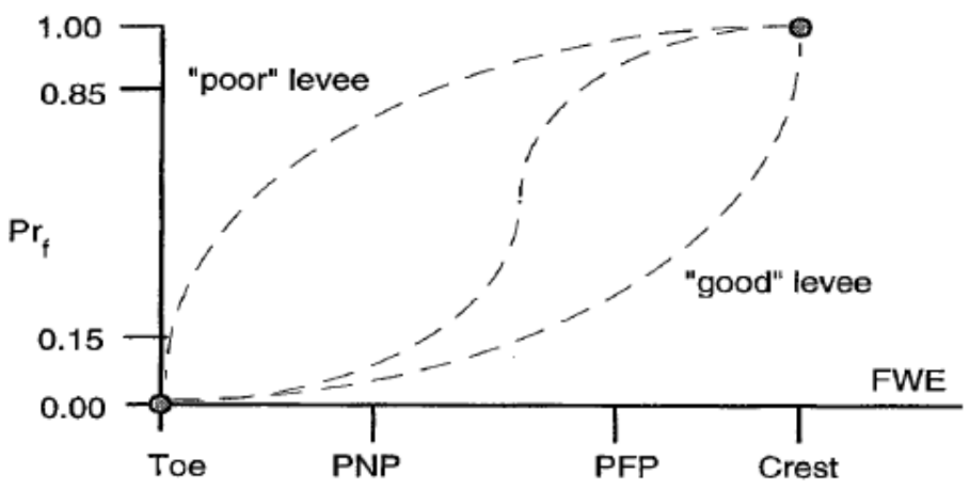


**Figure 7.3 Conceptual levee performance curves [USACE 1999].**

### 7.2.3 Solution Algorithms

Several solution algorithms are considered for solving a multi-decision levee systems model. A Monte Carlo simulation model generates many solutions; however, the approach does not focus on more optimal solutions. "Monte Carlo simulation performs risk analysis by building models of possible results by substituting a range of values—a probability distribution—for any factor that has inherent uncertainty. It then calculates results over and over, each time using a different set of random values from the probability functions" [Palisade 2012].

Another common solution algorithm is a grid search. A grid search checks every solution on a grid pattern over the feasible region and returns the global optimal solution. Finding the global solution can be difficult when the solution space has many dimensions and possibly numerous local maximums and minimums. Figure 7.4 is an example of a solution space where a grid search could be needed to identify the global minimum.

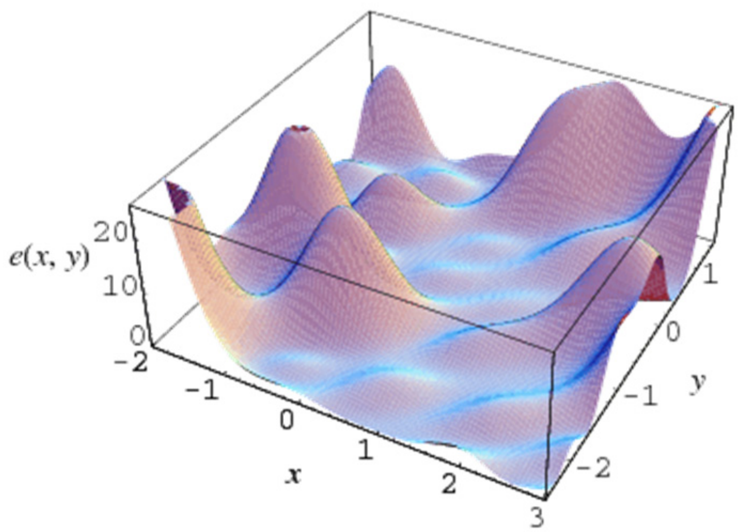


**Figure 7.4 Solution space with multiple maximums and minimums [Pintér 2012].**

Genetic algorithms, also called evolutionary algorithms, are an optimization approach that often reaches a solution more quickly than a grid search. Genetic algorithms use a set of trial values called chromosomes; chromosomes are randomly generated at the beginning of a genetic algorithm similar to Monte Carlo simulation. These trial solutions are then evaluated based on a fitness function and the more fit solutions are kept. Generally in optimization problems the fitness function is the equation that minimizes total cost. The algorithm then takes random properties from the more fit solutions and combines them to make the next generation of trial solutions. The algorithm will introduce mutations as well, which are new trial solutions not included in the initial randomization in case the global solution did not lie in the solution space bounded by the initial guess. This process of refining the solution set continues until a predetermined fitness level is reached or a set number of generations are searched. Microsoft Excel 2010 has a built-in evolutionary solver that utilizes a genetic algorithm to find the global solution to a problem with set bounds. Figure 7.5 outlines the process a genetic algorithm goes through to find a solution.

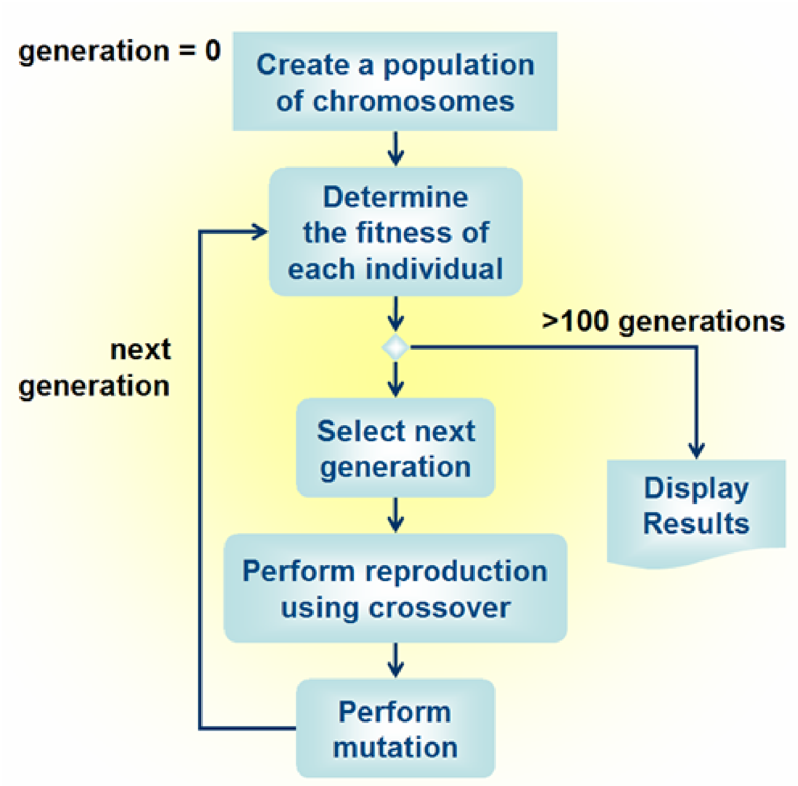


**Figure 7.5 Flowchart explaining the process of a genetic algorithm [Corbilla 2010].**

## 7.3 METHODS

Microsoft Excel and Visual Basic for Applications (VBA) are used to model a levee system. Levee and channel geometry, flood distribution parameters, and flood damage costs are input by the user. Designations "city," "town," or "field" change the associated damages values for levee failure and the cost of purchasing land to set the levee back from the river or increase the width of the levee. The model populates a list of water heights of a given flow that dynamically updates based on levee geometry and setbacks on both sides of the river. Failure modes are approximated and fit with an appropriate cumulative distribution to calculate potential damages. Construction and land acquisition costs are calculated based on levee geometry and dynamically update as setbacks vary on either side of the river. The program outputs optimal widths, heights, and setbacks for the conditions present in the model via either the Excel evolutionary solver or an incremental grid search. Figure 7.6 depicts the theoretical model set-up with decision variables.

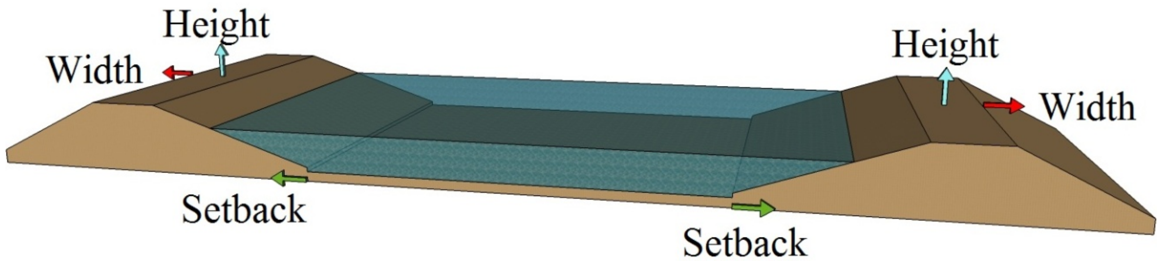


**Figure 7.6 System model showing decision variables.**

### 7.3.1 Flood Frequency Distribution

A Gumbel distribution represents peak flow frequencies. This distribution is used solely for demonstration purposes and can be replaced with another distribution. The Gumbel distribution and parameters—$\mu$ is the mean annual flood peak and $\sigma$ is the standard deviation of annual flood peaks—are given below in Equations (7.1) through (7.3).

$$F(Q) = e^{-e^{-a(Q-b)}} \tag{7.1}$$

$$a = \frac{\pi}{\sqrt{6}\sigma} \tag{7.2}$$

$$b = \mu - \frac{0.5772}{a} \tag{7.3}$$

Manning's equation, given in Equation (7.4), is used to determine flow capacities and height of water, where $Q$ is the flow rate in m/sec, $k$ is a conversion factor in $m^{1/3}$/sec, $n$ is Manning's number, $A$ is the area of the channel in $m^2$, $R$ is the hydraulic radius of the channel in m, and $S$ is the hydraulic slope.

$$Q = \frac{k}{n} A(R)_h^{2/3} S^{1/2} \tag{7.4}$$

### 7.3.2 Model Assumptions

- Levee construction cost is a function of levee volume (height and side slopes). The cost of other accessories such as interior ditches, gates, pumping facilities, cutoff walls, grouting, and sheet piles are not considered.
- Steady state hydraulics is assumed and flood duration effects are neglected.
- Each river reach is assumed to be straight.
- The cost of purchasing land is uniform along each levee reach.
- The hydraulic slope of the river is constant along each reach.
- Overtopping on one levee will prevent overtopping in adjacent or downstream levees of greater height.

### 7.3.3 Failure Mode Equations

Each failure mode considered has a performance function used to generate a probability of failure. The probabilities of failure are combined independently for simplicity. Although small amounts of overtopping do not always cause failure, for the purposes of this model any amount of water on the dry side of the levee is considered a failure. Fail-safe levees are allowed to fail in order to protect other levees; all other levees are given an extra 1 ft of freeboard to prevent failure. The performance function for under-seepage is based on the comparison of a critical exit gradient where internal erosion occurs to the exit gradient calculated from the levee geometry. Through-seepage has several possible equations; the one selected for this analysis is based on the USACE's Rock Island Division. This method determines if a toe berm is needed, specifying failure if a berm is required. The slope stability performance function is based on the factor of safety associated with each slope surface, which is calculated using The Simplified Bishop Method. The performance function for surface erosion is based off of the critical velocity at which surface erosion occurs divided by the actual velocity in the channel. Damages from each of the failure modes are calculated by multiplying the probability of failure by the probability of the water being at a specific height based on the flood distribution and then multiplied by the damages associated with that levee failing. If overtopping occurs, failure is assumed and all other probabilities of failure are set to zero. Figure 7.7 is an example of the probability of failure due to under-seepage with overtopping occurring at 47 ft.

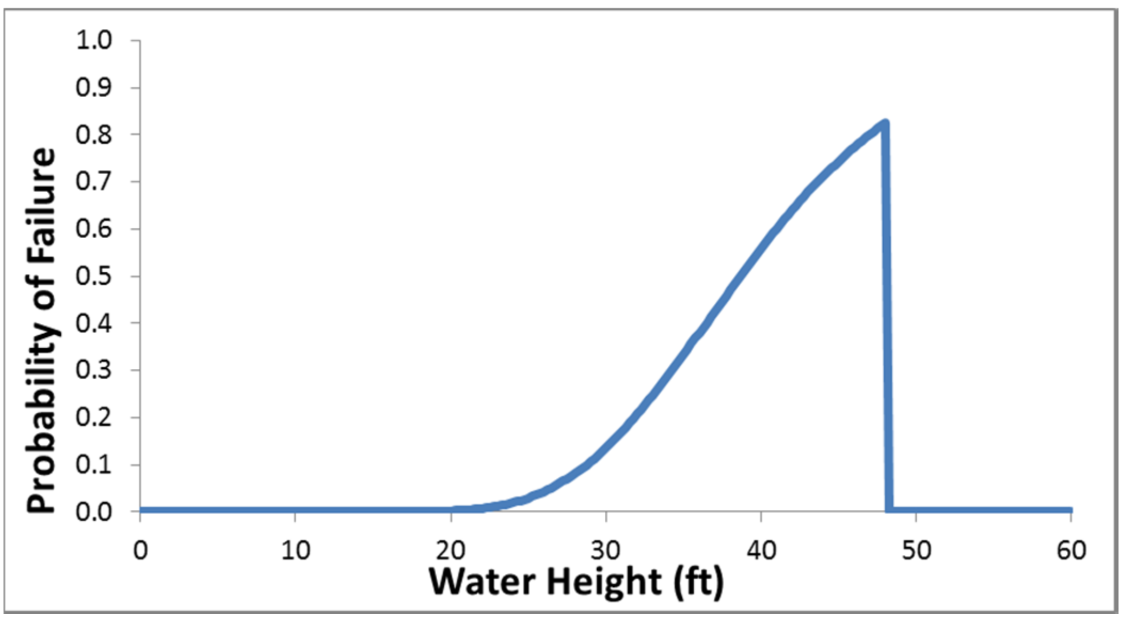


**Figure 7.7 Graph of probability of failure for one side of the river due to under-seepage.**

## 7.4 DISCUSSION OF MODEL

There were several interesting complications that came up while developing the model used in this paper. Initially the problem was set up using a Monte Carlo simulation model with basic nonlinear solver optimization; however, this algorithm was unable to find a reliable global solution due to the amount of variables in the solution. Due to time requirements as well as the complexity of the solution space having many maxima and minima, a genetic algorithm was determined to be the ideal solution method.

Another complication was determining the slope stability failure mode. Calculating slope stability requires an iterative process that is dependent on a safety factor. In addition, slope stability requires searching a large number of potential slip surfaces to find the worst factor of safety; this is usually done via a program such as UTEXAS. This model attempts to use solely Excel and VBA and, as such, having to search through numerous slip surfaces for each possible guess made the program take an impractically long amount of time to run. For this reason slope stability has been removed from the failure modes accounted for in the model. For an example of slope stability performance function, please see the companion paper in this volume by A. Sturm (Chapter 8), wherein the model develops a performance function for a single levee geometry.

The model for through-seepage also had some problems. As stated earlier, the Rock Island method works off of determining if a toe berm is needed by comparing the maximum erosion susceptibility to the relative erosion susceptibility. This provides results that match up with historical data of through seepage failures; however, it only works if the model allows the dry side slope to be 1/5 or greater. This is an issue since many levees, especially smaller agricultural levees, often have dry side slopes of 1/2 or even occasionally 1/1 in order to reduce construction costs. However, all the other methods considered—notably the Khilar method from the same report and another method that also worked off critical gradient, —were too sensitive to thermal fluctuations in the water temperature and would give back results that seemed highly unlikely varying from no chance to fail to a large failure probability by just changing the temperature of the water. Although the levees in this model do not have 1/5 dry side slope, the model uses 1/5 to check the through-seepage as this gives the most meaningful failure curve.

The model for erosion also does not really reflect the effects of erosion on the system. The model returns the likelihood of failure due to erosion as being very low, so low that the system could be considered to realistically never fail to erosion; this is because it is only considering steady state conditions without flood duration. If considered over the course of an entire flood season or even the course of several years, erosion could be a significant contributing factor to failure due to one of the other means such as through-seepage by lessening the over-all width of the levee. This interdependence is examined in the companion paper in this volume by A. Sturm (Chapter 8), where the model presented therein attempts to compare the reduction in width due to erosion to an increase in failure due to another failure mode.

## 7.5 RESULTS AND ANALYSIS

Results were generated comparing the effects of different land types on each side of the river. These results are summarized in Table 7.1, which includes the optimal geometries from the model as well as the total cost of the system and the probability of failure due to overtopping. The failure due to overtopping was included in the system to examine the effects of the fail-safe levee as well as to identify when the cost of building up the levee was prohibitively expensive and the point where it was more cost effective to not build any levee whatsoever.

Some interesting observations can be made from the table. First in the city/field case the overtopping probability of 99% indicates that the optimal solution was to allow the levee protecting a field to overtop most of the time in order to save money on levee construction and to not have to build as high of a levee on the city side. This solution assumes there is sufficient area in the fields for floodwaters to lessen the overall stage of the flood event. Another interesting observation is that in the city/city, town/town, and field/field cases the setback amount is set to the max (150 ft) amount and the overtopping probabilities are the lowest, which indicates that when relative values are equal on both sides of the river, levee construction should be substantially different than if property values are unequal. Lastly, the side with the least value is always built lower, signifying that if an extreme flood event were to occur, failure would happen there in order to protect the higher value area.

Additional information can be found in comparing the graphs of failure probability of levees generated by this model with traditional design. Table 7.2 shows predicted levee geometry using overtopping only compared to geometry predicted by including intermediate modes of failure (modeled here). Figures 7.8 and 7.9 show the effects of traditional design on levee geometries, Figures 7.10 and 7.11 show the effects of intermediate failure modes on levee design, and Figures 7.12 and 7.13 show the traditional design assuming multiple failure modes. From the graphs it is clear that the traditional design neglects a huge amount of failure probability and creates significantly less safe levees.

**Table 7.1 Summary of model results.**

| | Levee 1 | | | Levee 2 | | | | Overtopping Probability of Failure |
|---|---|---|---|---|---|---|---|---|
| Set up | Height (ft) | Width (ft) | Setback (ft) | Height (ft) | Width (ft) | Setback (ft) | Total Cost ($M/year) | |
| City/Field | 13.07 | 27.99 | 3.38 | 11.27 | 7.00 | 100.24 | 132.657 | 99% |
| City/Town | 42.00 | 72.85 | 98.83 | 41.74 | 83.66 | 148.27 | 273.787 | 4% |
| City/City | 47.18 | 32.42 | 148.84 | 47.41 | 33.27 | 149.50 | 352.443 | 1% |
| Town/Field | 40.50 | 97.79 | 60.43 | 39.63 | 100.34 | 150.00 | 123.817 | 8% |
| Town/Town | 44.80 | 44.95 | 149.95 | 44.95 | 24.55 | 149.95 | 200.586 | 1% |
| Field/Field | 42.00 | 72.30 | 149.66 | 41.92 | 108.96 | 149.07 | 55.782 | 3% |

**Table 7.2 Comparison of traditional design with the design presented in this model.**

| | Traditional | | Intermediate Failure | |
|---|---|---|---|---|
| | Levee 1 - Right Side | Levee 2 - Left Side | Levee 1 - Right Side | Levee 2 - Left Side |
| Height | 47.15 ft | 47.09 ft | 43.49 ft | 43.43 ft |
| Width | 7.01 ft | 7.20 ft | 67.47 ft | 53.48 ft |
| Setback | 0 ft | 105.00 ft | 97.38 ft | 149.68 ft |

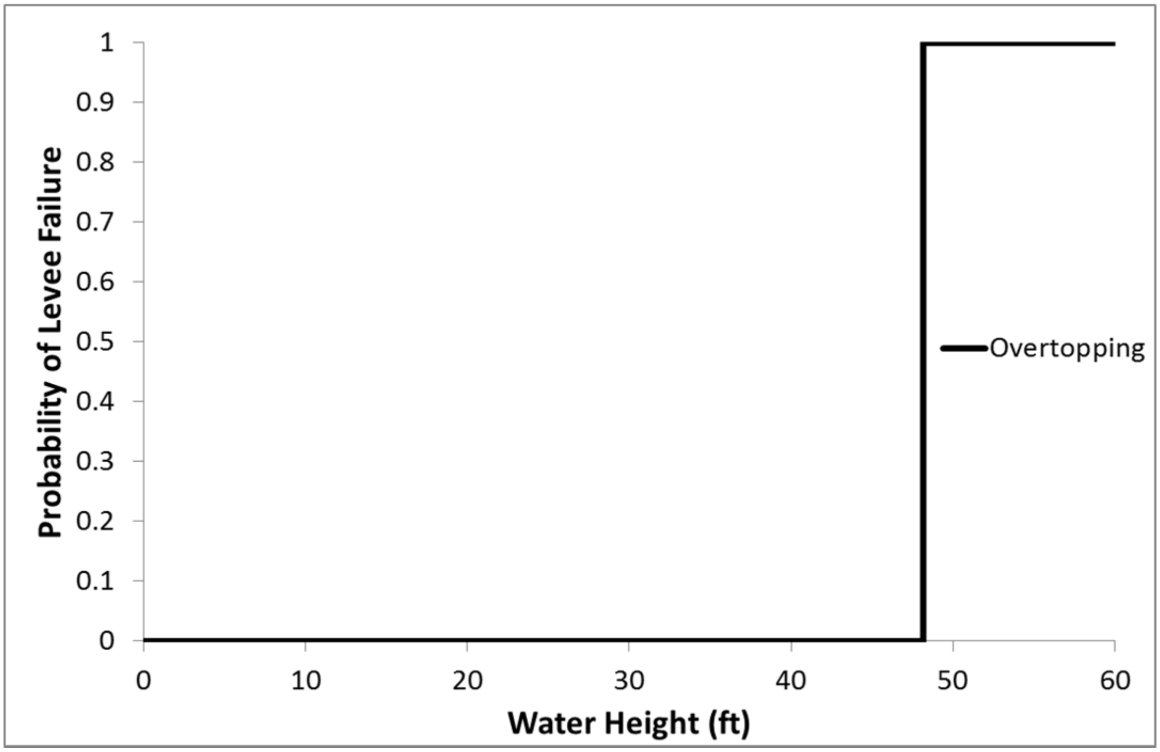


Figure 7.8 Traditional design considering only overtopping.

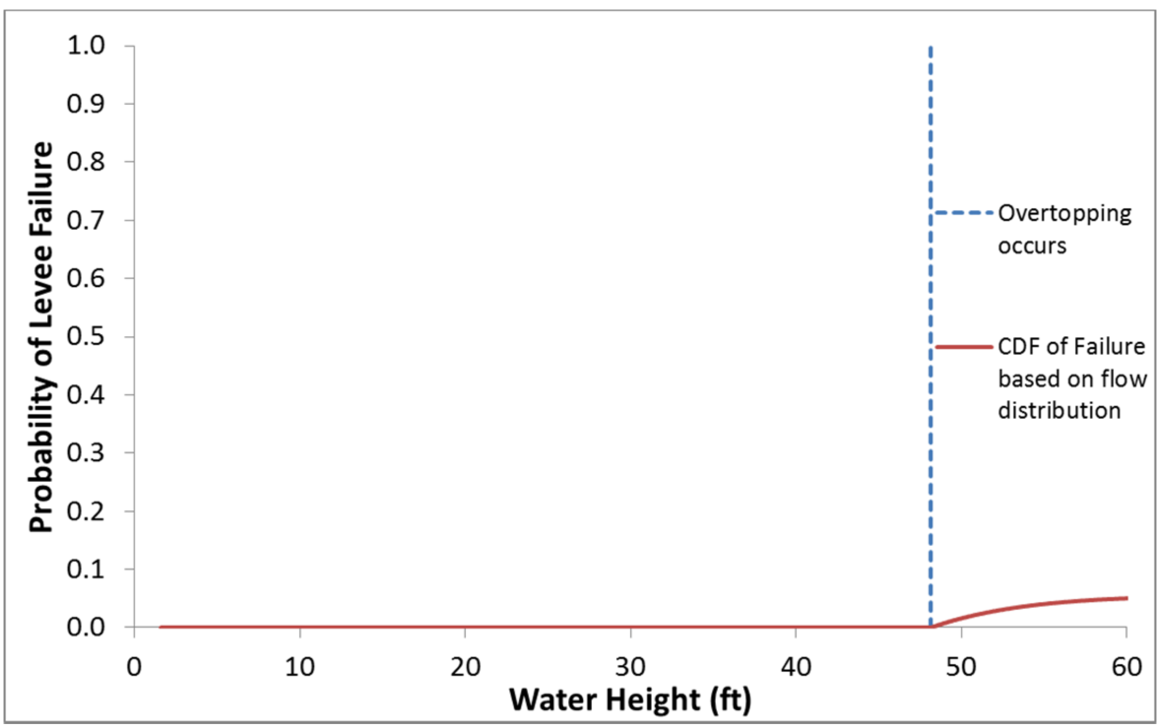


Figure 7.9 Cumulative failure probability based on flow distribution (see flood frequency section above) assuming only overtopping.

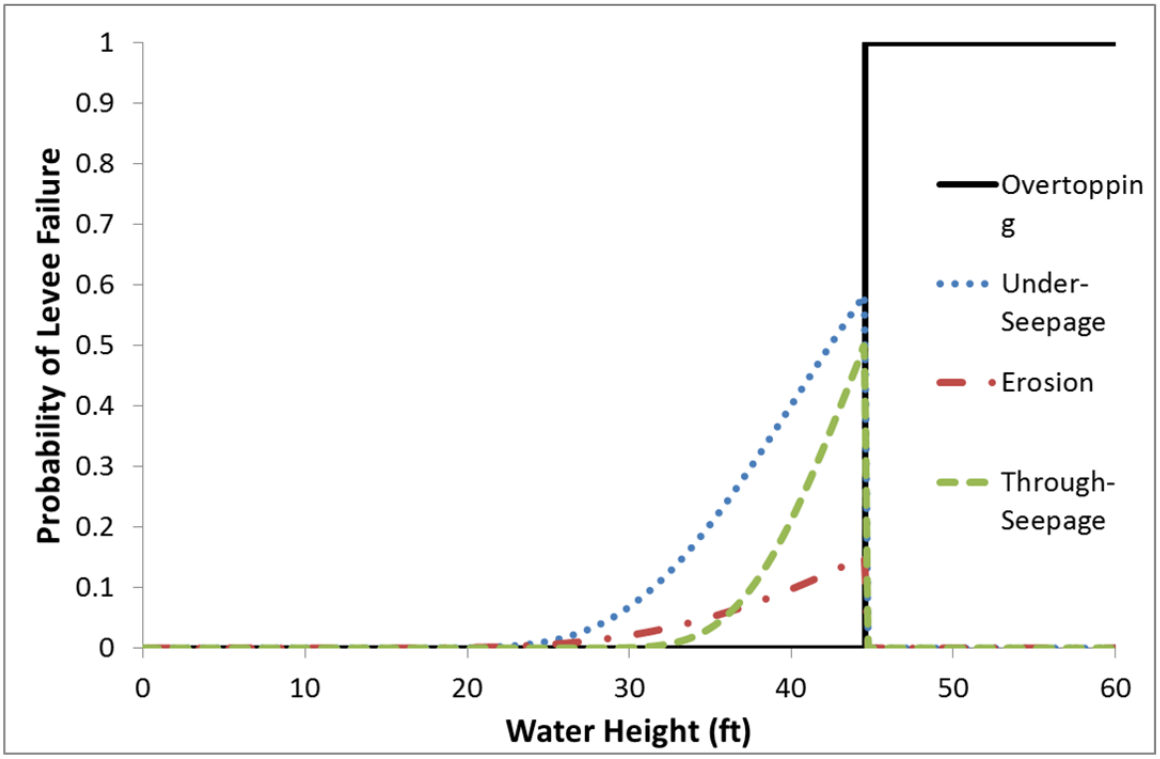


**Figure 7.10 Optimal design predicted by this model.**

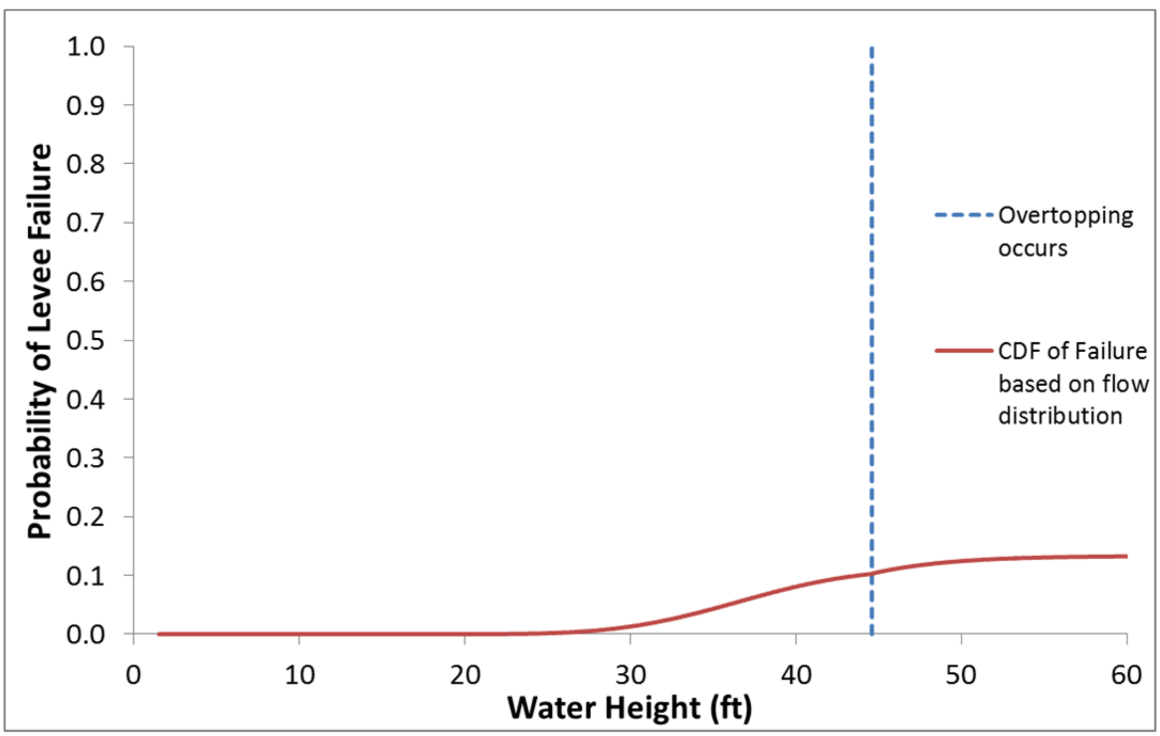


**Figure 7.11 Cumulative failure probability based on flow distribution predicted by this model.**

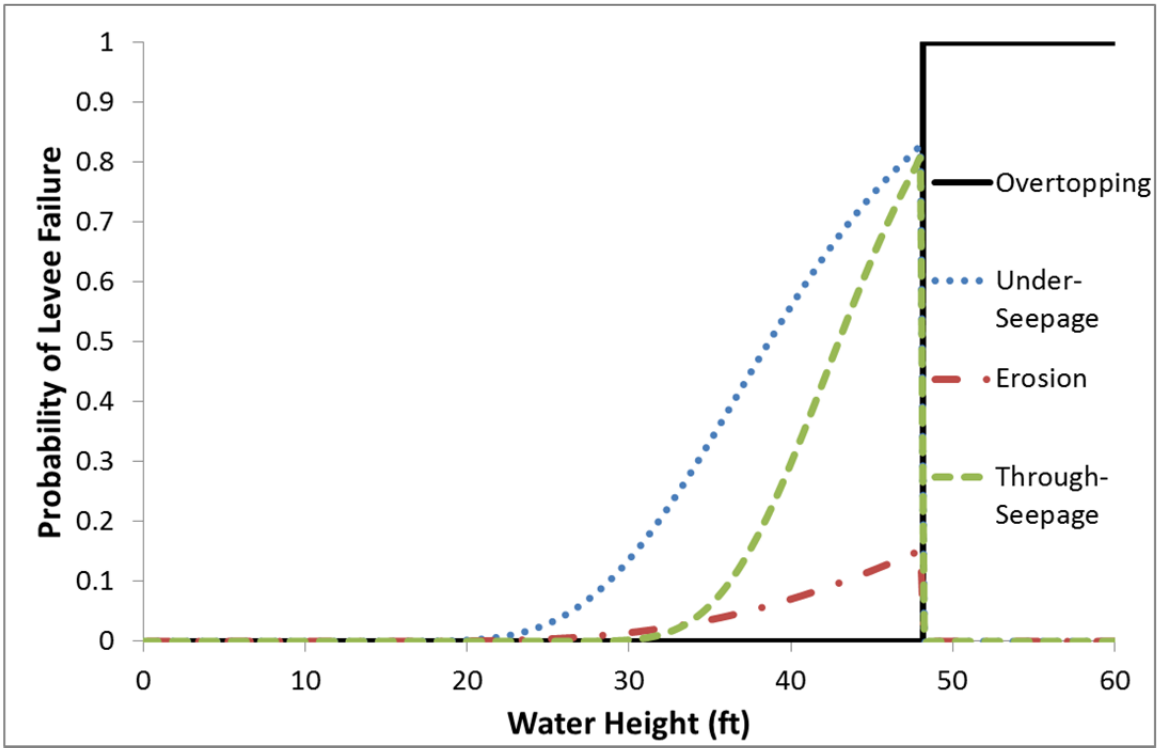


**Figure 7.12 Actual probability of failure based on geometries predicted by traditional design.**

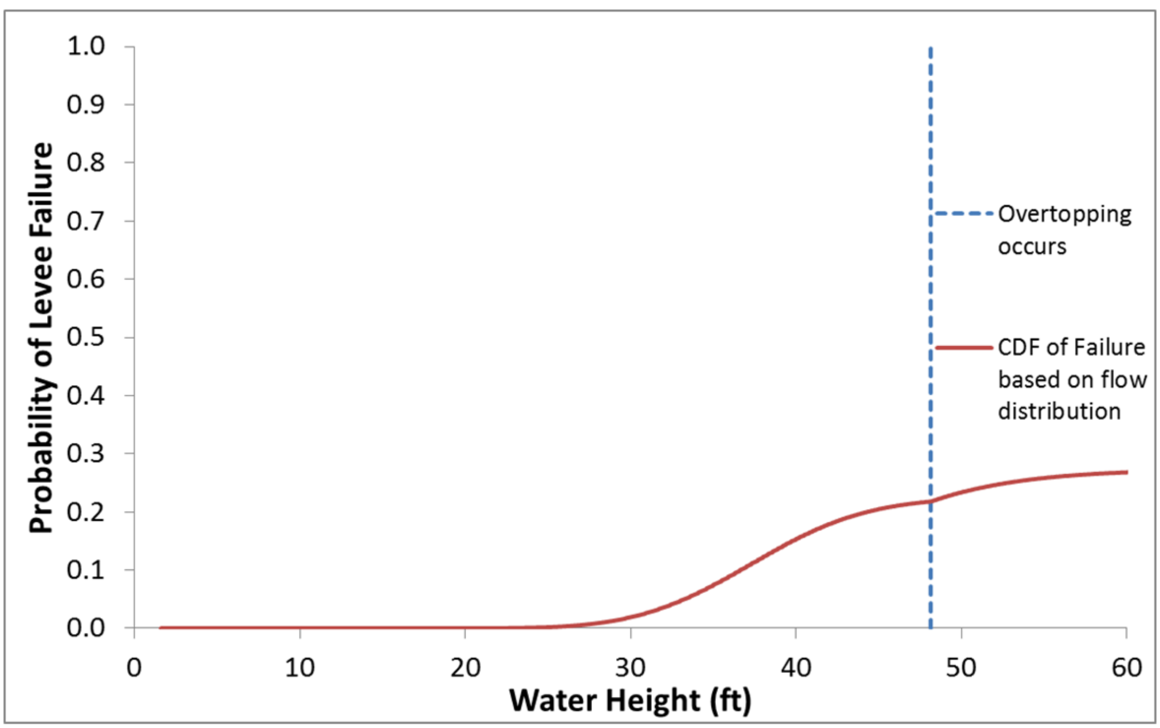


**Figure 7.13 Actual cumulative failure probability based on flow distribution assuming with traditional design geometries.**

## 7.6 CONCLUSIONS

In summary, there are several conclusions from this model. First, when relative flood damage is significantly different on opposing sides of the river, it is more economical to not build a levee on the side with the least value. Second, designing the system with a fail-safe levee reduces construction costs overall and improves life safety. Third, the addition of intermediate failure-modes on levee system analysis drastically changes the results of the optimization. Finally, there is a significant need for further research into levee failure modes to validate and improve current models. Little research has been done to validate the empirical equations used here for actual levee failures. In addition many of the methods used for predicting levee failure do not agree with each other; the U.S. Army Corps of Engineers acknowledge the two through-seepage models presented in their technical letter have drastically different outcomes for the same levee, one predicting a fairly high failure probability, the other predicting no probability of failure [USACE 1999]. Obtaining real data from scaled laboratory or field experiments could have a significant impact on increasing human safety and protection of property behind levees, as well as allowing for more efficient design and construction of levees in the future.

As mentioned previously this model takes methods developed in the CVFPP and PEER companion paper, *Multi-Mode Probability of Levee Failure Curves* [Sturm 2012], for evaluating single existing levees and modifies them for use in a levee systems analysis. While evaluating existing levees is an important goal, having a risk-based system analysis model to determine optimal heights, widths, and setbacks will save a significant amount of money and safeguard property and lives. This model shows that a comprehensive model including multiple failure modes is possible; with additional research and development it could be applied to any particular existing situation to create an optimal result. Considering the financial condition of the State of California and the huge importance of levees in the State, such a system would be critically important going forward and could help to protect our systems in the most efficient way possible.

## 7.7 FUTURE RESEARCH

In addition to field testing to calibrate failure models, there is room for further expansion of this model into a dynamic program with several sequential levees. A set up similar to that shown in Figure 7.14 could be used to examine the system effects of fail-safe levees. In theory, this could be done by approximating the combined failure modes using an equation form similar to Equation (7.5), where $h$ is the height of water, $H$ is the levee height, $a$ and $b$ are fitting parameters based off the performance functions, and $w$ is the crown width of the levee. This would allow for much faster solution space searching and would increase the number of potential reaches that could be incorporated into the model.

$$P_f(H, w, h) = \frac{b}{H}\left(\frac{h-a}{H}\right) e^{-k\omega} \; from \; a < h < H \tag{7.5}$$

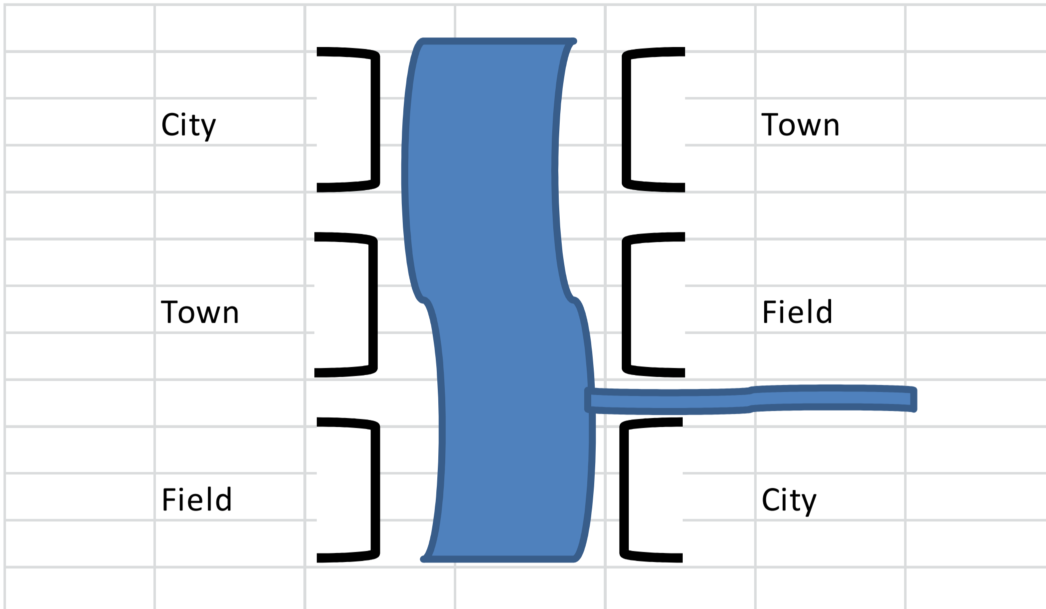


**Figure 7.14 Configuration of a more complex levee system.**

This model could also explore hydraulic impacts such as backwater effects and how much flow to pass downstream after a breach. Application of a model such as this on a large scale could significantly reduce construction costs and increase life safety by identifying a fail-safe levee in a large system of levees. Another further step would be to incorporate the cost associated with reservoir expansion, which could decrease the flow in the river and reduce pressure on levees. Eventually this model could represent a fully integrated flood prevention system that considered the costs of levees and other elements in flood prevention to optimize the entire flood control system.

## ACKNOWLEDGMENTS

This research was supervised and funded by the Pacific Earthquake Engineering Research Center and the National Science Foundation as part of the 2012 Summer PEER Internship Program. I would like to thank Nathan Burley and Dr. Jay Lund for advising and mentoring me during this research process, as well as fellow researcher Alex Strum for providing failure mode models. I would also like to thank Christy Jones and the Army Corps of Engineers for providing the *ETL 1110-2-556* on which much of this research is based. Any opinions, findings, and conclusions or recommendations in this material are those of the authors and do not necessarily reflect those of the sponsors.

## REFERENCES

Corbilla J (2010). *Random thoughts on coding & technology: Genetic Algorithms*. November 10, 2010, accessed July 23, 2012, *http://thundaxsoftware.blogspot.com/2010/11/genetic-algorithms-ga.html*.

Dantzig D. van (1956). Economic decision problems for flood prevention, *Econometrica*, 24(3):276–287.

DWR (2011). *2012 Central Valley Flood Protection Plan*, Department of Water Resources, State of California, Sacramento, CA.

Moss RES, and JM Eller (2007). Estimating the probability of failure and associated risk of the California Bay Delta levee system, *Proc.,* GeoDenver 2007 Probabilistic Applications in Geotechnical Engineering 170 (2007), accessed June 29, 2012, *http://ascelibrary.org/doi/abs/10.1061/40914(233)21*.

Palisade (2012). *Monte Carlo Simulation,* accessed July 25, 2012, *http://www.palisade.com/risk/monte_carlo_simulation.asp*.

Pintér J. (2012). *Global Optimization*, accessed July 23, 2012, *http://mathworld.wolfram.com/GlobalOptimization.html*.

Tung Y-K., and LW Mays (1981). Optimal risk-based design of flood levee systems, *Water Resources Research*, 17(4):843–852.

Tung Y-K (2005). Flood defense systems design by risk-based approaches, *Water International*, 30:50–57.

USACE (1990). Risk-based analysis in geotechnical engineering for support of planning studies, U.S. Army Corp of Engineers, Engineering and Design, *ETL 1110–2–556*, pp. 3–138.

# 8. Multi-Mode Probability of Levee Failure Curves

ALEX STURM


## ABSTRACT

Traditional risk analysis of riverine levees assumes overtopping as the only failure mode, despite the fact that multiple modes contribute to failure. This report follows existing methods of analysis that allow probability of levee failure to be calculated for failure modes of overtopping, erosion, under-seepage, though-seepage, slope stability and seismic vulnerabilities. When modes of failure other than overtopping are taken into account it is clear that traditional levee risk analysis underestimates probability of levee failure. These methods of analysis and their results are demonstrated using two simulated case study levees.


## 8.1 INTRODUCTION

Risk, from an engineering point of view, is the probability of failure multiplied by the damages of such a failure (Moss and Eller 2007). Damages are in monetary terms and represent costs of life loss, and damage to land and property. A common goal in flood control planning and design is to minimize risk, yet to minimize risk, food control improvements must be made, leading to higher construction costs. Thus, project cost often takes the form of an economic optimization problem in which the minimum total cost is sought. The total cost is taken to be the sum of risk and structural improvements costs. Risk analysis requires an accurate estimate of the probability of system failure. Without this, the risk of a system cannot accurately be characterized and the optimization problem cannot be properly solved.

Risk analyses are often performed by public agencies when deciding how to best allocate funds for improvements to existing infrastructure. Flood management is an example where risk analysis is performed. Flood management systems are composed of structural and non-structural measures that work in tandem to mitigate risk to life, land, and property posed by flood events. A major component of flood management systems is riverine levees. While riverine levees are vital to flood protection, they have many failure modes. Traditionally, levee risk analysis assumes overtopping as the only failure mode, an assumption, which greatly underestimates risk.

This paper develops a model capable of calculating probability of failure curves (PFCs) for levees of varying size, shape, and soil type. The PFCs calculate the probability of a levee failing at a given flood water height. The curves include four levee failure modes of overtopping, erosion, through-seepage, under-seepage. Additionally, the failure modes of slope stability and seismic vulnerabilities are also discussed qualitatively.

## 8.2 BACKGROUND

### 8.2.1 Probability of Failure Curves

Probability of failure curves (PFCs) are cumulative distribution functions that represent the likelihood of levee failure at varying floodwater heights. PFCs can model individual modes of levee failure as well as combinations of failure modes.

Previous studies have developed PFCs. In California, the California Valley Flood Protection Plan, CVFPP, developed individual failure mode levee PFCs and combined them to yield a single PFC. They assumed that the different failure modes operate independently, meaning that an increased likelihood of failure due to one mode does not affect the probability of failure of other modes. The report acknowledges that this assumption, while not ideal, does provide an estimate of the actual PFC [DWR 2012].

The CVFPP developed their PFCs by following the methods laid out in United States Army Corps of Engineers (USACE) Engineering Technical Letter (ETL) *1110-2-556*. This technical letter, which provides the basis for this report, expired in June of 2004 [USACE 1999]. The USACE has not preplaced or updated the ETL.

### 8.2.2 Levee Failure Modes

Levee failure modes describe the various mechanisms that can cause failure. Failure in this report is defined as any event that results in substantial water entering the protected floodplain. This report focuses on six modes of levee failure: overtopping, erosion, through-seepage, under-seepage, slope stability, and seismic vulnerabilities.

#### *8.2.2.1 Overtopping*

Overtopping (Figure 8.1) of a levee occurs when floodwater height exceeds levee height. This failure mode does not always result in a complete levee breach. If the levee is sufficiently strong and/or the period of overtopping is short, overtopping may simply mean that the excess water is passed onto the protected floodplain. However, if the levee is structurally weak or if the period of overtopping is sufficiently long, the levee may be breached, resulting in a more catastrophic collapse and failure [Ellis and Groves 2008].

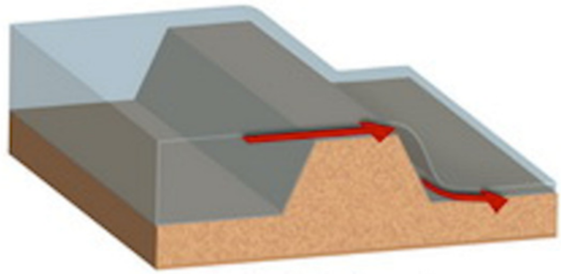

**Figure 8.1 Schematic of levee overtopping (courtesy of Deretsky).**

### *8.2.2.2 Erosion*

Erosion (Figure 8.2) is the loss of levee material due to current scour and/or wave attack. Current scour is the removal of levee soils due to shear stress parallel to the levee. Wave attack removes material through stress perpendicular to the levee. Erosion depends on the duration of a flood. Erosion can be mitigated with vegetation and/or rock armor [Shewbridge et al. 2010].

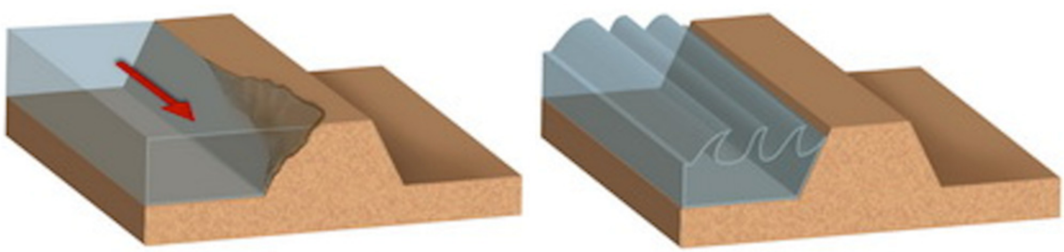

**Figure 8.2 Schematics of current scour (left) and wave attack (right) (courtesy of Deretsky).**

### *8.2.2.3 Through-Seepage*

Through-seepage (Figure 8.3) describes water movement through the bulk of a levee, caused by excess hydrostatic pressure on the wetted side. Poorly-engineered, sandy levees are highly susceptible to through-seepage. While well-engineered clay levees are considered safer, their integrity can be jeopardized by cracks and or animal burrows, which can act as flow paths. Furthermore, sandy levees can be improved with the addition of a clay core to hinder water movement [Ellis and Groves 2008]. This mode of levee failure lacks a definitive method for analysis. The USACE presents two different methods for estimating the effects of through-seepage: the Rock Island Method and Khilar's equation.

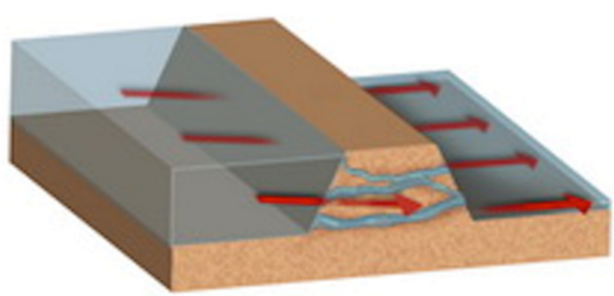

**Figure 8.3 Schematic of levee through-seepage (courtesy of Deretsky).**

The Rock Island method (RIM) is used to determine if a toe berm is necessary to combat erosion. Due to the correlation between erosion and through-seepage, which is essentially internal levee erosion, the Corps proposes that this model can be adapted to predict through-seepage. This method takes the boundary between needing and not needing a toe berm as the limit state where through-seepage occurs [USACE 1999].

Khilar's equation was originally developed to predict whether clays would allow or prevent water flow through internal channels. Movement of water through internal channels is known as piping, a synonym for through-seepage. The USACE states Khilar's equation can be used to predict a critical exit gradient that will initiate though-seepage [USACE 1999].

### *8.2.2.4 Under-Seepage*

For under-seepage (Figure 8.4), hydrostatic pressure on the wet side of the levee causes water to flow under the bulk of the levee. The difference between this failure mode and through-seepage is the water's flow path. Flow path is governed by the soil properties of the levee as well as the soil profile beneath the levee. In *ETL 1110-2-556* the USACE proposes two distinct soil layers: the upper blanket and underlying substratum. The blanket layer is generally composed of more impermeable organic soils while the substratum is comprised of more porous soils. Under-seepage is governed by a combination of levee characteristics and soil profile characteristics [USACE 1999].

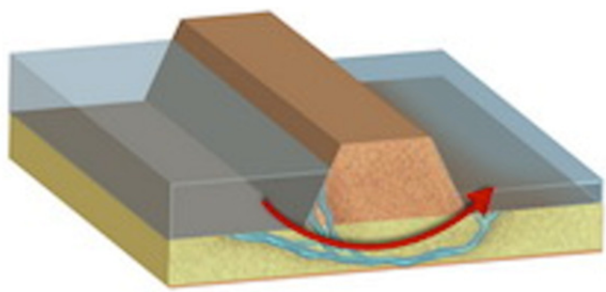

**Figure 8.4 Schematic of levee under-seepage (courtesy of Deretsky).**

### *8.2.2.5 Slope Stability*

Slope stability analysis aims to find the slip surface most likely to fail due to sliding (Figure 8.5). The critical surface is defined as the one with the lowest factor of safety (FS). For this reason a FS must be calculated for many trial slip surfaces. The USACE describes several methods used to calculate slope stability factors of safety.

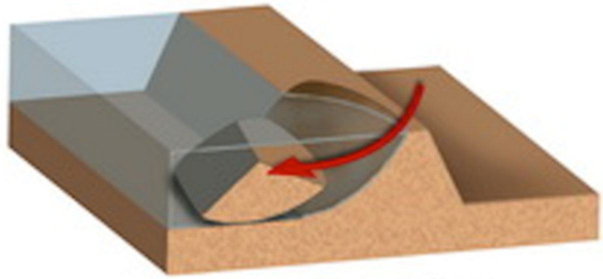

**Figure 8.5 Schematic of levee slope failure (courtesy of Deretsky).**

The Ordinary Method of Slices (OMS) uses circular slip surfaces for which a center point and radius must be defined. Once a trial slip surface has been drawn, it is then divided into slices, as shown in Figure 8.6. The OMS sums forces in the vertical direction while neglecting the forces on the sides of each slice. Vertical forces include the upward normal and pore water pressure forces, and the downward forces from soil and water. Once the forces are calculated, the moments of each slice are summed about the center of the circular slip surface. The FS is then taken as the ratio between the moments inducing sliding and those resisting sliding. Acknowledged as the simplest method presented by the USACE for slope stability analysis, the OMS is known to result in errors as large as 20% when compared to more rigorously computed values; therefore, the USACE recommends usage for estimation only [USACE 2003].

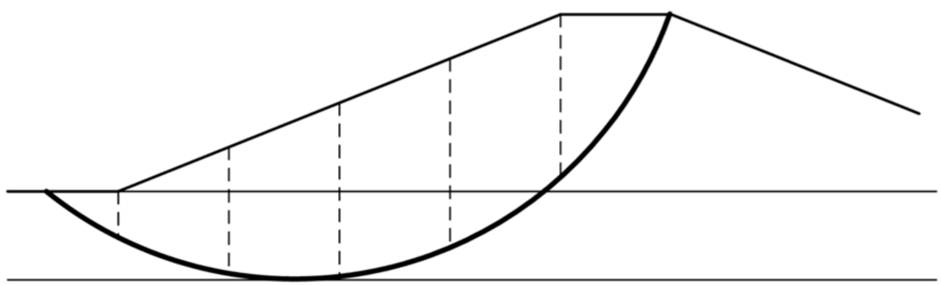

**Figure 8.6 Typical circular slip surface divided into slices [USACE 2003].**

The Simplified Bishop Method is another approach known to compare well with more rigorous methods while still allowing hand calculations. This method assumes a circular slip surface divided into slices. The forces between slices are strictly horizontal and the combination of static force equilibrium with the Mohr-Coulomb equation is used to calculate the FS. One drawback of this method is the equation used to calculate the FS is dependent on the FS. This means that an iterative process is required in which trial factors of safety are guessed and used to calculate actual factors of safety until the two converge.

More complex methods such as the Modified Swedish Method and Spencer's Method increase the accuracy of computation; however, they greatly increase the difficulty level. For this reason slope stability analyses using these methods are often carried out using computer programs such as UTEXAS or Slope/W [USACE 2003].

### *8.2.2.6 Seismic Vulnerabilities*

Seismic events are not often discussed in tandem with riverine levee failure due the almost nil probability of a high flood event coinciding with a large magnitude earthquake. If there is no flood, a levee failure due to earthquake presents no flooding risk and thus is not a concern in flood risk management. Yet, it is possible for an earthquake to cause liquefaction, slope failure, and or cracking that if not repaired would greatly increase the risk of flooding during later high water events [Ellis and Groves 2008]. Earthquakes also pose a substantial risk to areas below sea level.

Liquefaction occurs when cyclic shaking causes soil particles to rearrange and transfer effective soil stress to pore water between the soil particles, creating a large reduction in the strength of soil; see Figure 8.7. It only occurs in saturated soils and is more typical of smaller-grained, less-compacted soils such as sands and silts [Idriss and Boulanger 2008]. The FS against liquefaction is the ratio of the cyclic resistance ratio (CRR) to the cyclic stress ratio (CSR). These values are highly dependent on the site's soil properties and characteristics of ground motion [Seed et al. 2003].

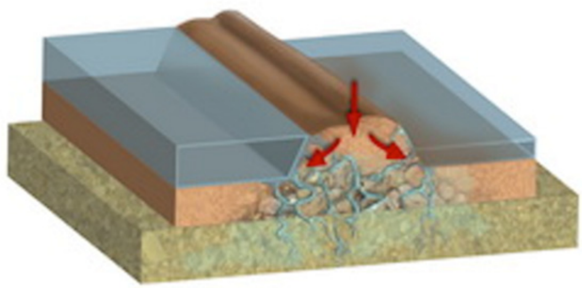

**Figure 8.7 Schematic of levee liquefaction (Deretsky).**

Slope failure can be induced through cyclic shaking if the peak ground acceleration exceeds yield acceleration of the slope. Peak ground acceleration is dependent on the size and location of the earthquake, while the yield acceleration is dependent on the characteristics of the slope. Yield acceleration can be calculated by rearranging the FS equations that correspond to each slope stability analysis method [Kim and Sitar 2004]. Various slope stability methods have their strengths and weaknesses.

## 8.3 METHODS

### 8.3.1 Probability of Failure Curves

Four individual probability of failure curves (PFCs) are developed following the methods laid out in USACE's *ETL 1110-2-556*. The steps are summarized here [USACE 1999]. For definitions and descriptions of relevant probabilistic terms refer to the Appendix.

1. Define a performance function (PF) and limit state.

   PFs govern each mode of levee failure. All PFs must have limit states. An example of a PF is the factor of safety or ratio of capacity to demand. The limit state is reached when the FS equals one or when capacity equals demand.

2. Define the random variables (RVs) and characterize them by their expected values, standard deviations, and coefficients of variance.

   Once a PF and limit state are defined for the levee failure mode of interest, it must be decided which parameters within the function have the most inherent uncertainty. These parameters are called RVs. They are characterized by their expected values, standard deviations, and correlated coefficients. For a detailed description of these and other relevant probabilistic terms refer to the Appendix.

3. Calculate the expected value, variance, standard deviation, and correlated coefficient of the PF.

   RVs are used to calculate the expected value, standard deviation, variance, and correlated coefficient of the PF. While many methods can be used to calculate these values, this study relied on the Taylor's series method.

   In the Taylor's series method, the expected value of the PF is calculated by evaluating the PF at the RV's expected values:

$$E[PF] = PF(E[RV_1], E[RV_2]...E[RV_n]) \tag{8.1}$$

   The variance is calculated via numerically approximated derivatives:

$$Var[PF] = \left( \frac{PF(RV_{1+}) - PF(RV_{1-})}{2\sigma_{RV_1}} \right)^2 \sigma^2_{RV_1} + \left( \frac{PF(RV_{2+}) - PF(RV_{2-})}{2\sigma_{RV_2}} \right)^2 \sigma^2_{RV_2} \tag{8.2}$$

   Where $PF(RV_{1+})$ is the PF evaluated at the expected value of the RV plus one standard deviation:

$$PF(RV_{1+}) = E[RV_1] + \sigma_{RV_1} \tag{8.3}$$

   Subsequently $PF(RV_{1-})$ is:

$$PF(RV_{1-}) = E[RV_1] - \sigma_{RV_1} \tag{8.4}$$

   The standard deviation of the PF is taken to be the square root of the variance, i.e.,:

$$\sigma_{PF} = \sqrt{Var(PF)} \tag{8.5}$$

   Finally, the coefficient of variation is:

$$V_{PF} = \frac{\sigma_{PF}}{E[PF]} \tag{8.6}$$

4. Calculate the reliability index, $\beta$.

   The reliability index depends on two factors: the assumed distribution and the form of the PF.

   a) If a normal distribution is assumed and the PF is in the form of a ratio, i.e., capacity over demand, then the reliability index is calculated using:

   $$\beta = \frac{E[C-D]}{\sqrt{\sigma_C^2 + \sigma_D^2}} \tag{8.7}$$

   b) However, if a normal distribution is assumed and the PF does not appear as a ratio, or if the terms in the ratio cannot be explicitly separated (such as a FS), then the reliability index is:

   $$\beta = \frac{E[FS]}{\sqrt{\sigma_{FS}^2}} \tag{8.8}$$

   c) For a lognormal distribution and a PF in ratio form, beta is:

   $$\beta = \frac{\ln\left[\dfrac{E[C]\sqrt{1+V_D^2}}{E[D]\sqrt{1+V_C^2}}\right]}{\sqrt{\ln[1+V_C^2] + \ln[1+V_D^2]}} \tag{8.9}$$

   d) Finally, for lognormal distribution and a PF that cannot be separated, beta is calculated by:

   $$\beta = \frac{\ln\left[\dfrac{E[FS]}{\sqrt{1+V_{FS}^2}}\right]}{\sqrt{\ln(1+V_{FS}^2)}} \tag{8.10}$$

5. Calculate the probability of failure.

   The probability of failure is calculated by evaluating the cumulative distribution function of the standard normal distribution at the negative of the reliability index, or:

   $$P_f = \Psi(-\beta) \tag{8.11}$$

### 8.3.2 Geotechnical Parameters

This report requires representative values for effective cohesion, permeability, bulk/saturated densities, critical tractive stresses, and effective friction angles. Numerous journal articles were consulted to obtain reasonable values of these parameters for four main soil types: gravel, clay, sand and silt. From these four main soil types intermediate soil mixture values were obtained via averaging. These values are presented in Table A.1 of the Appendix.

### 8.3.3 Failure Modes

The PFs, limit states, and RVs used to develop PFCs for each of the four levee failure modes considered in this report are described below. Methods of qualitative analysis for the remaining two failure modes are also discussed.

#### *8.3.3.1 Overtopping*

Failure from overtopping is defined as any situation that results in water entering the protected floodplain because floodwater height exceeds levee height, i.e.,:

$$H > h \tag{8.12}$$

where $H$ = floodwater height (ft) and $h$ = levee height (ft). Taking this as the overtopping PF, the limit state is reached when the ratio of the two heights equals 1.

No RVs are defined for overtopping because floodwater height and levee height are considered to have minimal uncertainty. With no RVs being defined, the probability of failure for levee overtopping is simply:

$$P_f = \begin{cases} 0 & if \quad H < h \\ 1 & \quad\;\; H > h \end{cases} \tag{8.13}$$

This equation governs the overtopping PFC.

#### *8.3.3.2 Erosion*

In this report, erosion is assumed to act uniformly across the entire levee embankment under the waterline. Erosion within the river channel was not calculated because, relative to embankment erosion, it would not greatly reduce levee safety. The effects of wave attack were also neglected because rivers usually have shorter fetch lengths; therefore damaging waves are less of a concern [Shewbridge et al. 2010].

For these reasons the erosion PF chosen uses a ratio of critical velocity to floodwater velocity. Critical velocity is dependent on levee soil and armor. Floodwater velocity is calculated using Manning's equation:

$$V = \frac{1.4859}{n} \cdot R_h^{2/3} \cdot S^{1/2} \tag{8.14}$$

where $n$ = Manning's n (unit less), $R_h$ = hydraulic radius (ft), and $S$ = energy slope (ft/ft). The limit state taken to be:

$$\frac{V_{crit}}{V} = 1 \tag{8.15}$$

To calculate an erosion PFC, Manning's n; the energy slope, S; and the critical velocity are defined as RVs. Following the USACE's example, the coefficients of variation of each RV are presented in Table A.2 of the Appendix. Beta is calculated using Equation (8.9) [USACE 1999].

#### *8.3.3.3 Under-Seepage*

To analyze under-seepage, the landside exit gradient is calculated and compared with a critical exit gradient. The limit state of this PF is reached when the critical exit gradient equals the actual exit gradient. The critical exit gradient is assumed to be 0.85, the same value used in *ETL 1110-2-556*.

To calculate the landside exit gradient, the proper blanket length, thickness and permeability, as well as the substratum thickness and permeability, are chosen based on levee type. After these values are selected, the effective seepage exit distance, $x_3$, is calculated as follows:

$$x_3 = \sqrt{\frac{k_f}{k_b} \cdot z \cdot q} \tag{8.16}$$

Where $k_f$ = substratum permeability (ft/sec), $k_b$ =blanket permeability (ft/sec), $z$ = blanket thickness (ft), and $q$ = substratum thickness (ft). The distance from the landside toe to the effective source of seepage entrance, $s$, is taken to be:

$$s = x_1 + x_2 \tag{8.17}$$

where $x_1$ = blanket length (ft) and $x_2$ = embankment width (ft).

Next, the net residual head is calculated [where $H$ = floodwater height (ft)]:

$$h_0 = \frac{H \cdot x_3}{s + x_3} \tag{8.18}$$

Finally, the landside exit gradient is [USACE 1999]:

$$i = \frac{h_0}{z} \text{(ft/ft)} \tag{8.19}$$

The RVs assumed for under-seepage analysis are $k_f$, $k_b$, $z$, and $q$. The associated coefficients of variation used can be found in Table A.3 of the Appendix. Beta is calculated using Equation (8.9) [USACE 1999].

### *8.3.3.4 Through-Seepage*

The two methods presented by the USACE the Rock Island method (RIM) and Khilar's equation are not without flaws. The RIM's biggest limitation is that numerical errors occur for dry slopes steeper than 1V:5H [USACE 1999]. Dry slopes this shallow are seldom seen in practice. The alternative, Khilar's equation is used to calculate a critical exit gradient [USACE 1999]:

$$i_{crit} = \frac{\tau_c}{2.878 \cdot \rho}\left(\frac{n_0}{k_0}\right)^{1/2} \tag{8.20}$$

where $\tau_c$ = critical shear stress (lb/ft$^2$), $\rho$ = density of water (lb/ft$^3$), $n_0$ = initial porosity (%), and $K_0$ = initial intrinsic permeability (ft$^2$).

The limitation of this method is that the initial intrinsic permeability, $K_0$, is highly sensitive to the viscosity of water, which depends on water temperature. This high variability brings the validity of the method into question. In addition, the method was originally developed for clay levees and is acknowledged by the USACE to under predict the contribution of through-seepage to levee failure. While neither method is perfect the lack of a definitive PF for through-seepage means that one must be selected. The RIM is used to model though-seepage here.

As described earlier, the RIM was adapted from an equation used to predict the necessity of a levee toe berm. A toe berm was deemed necessary when the maximum erosion susceptibility, *M*, and the relative erosion susceptibility, *R*, fell above the shaded region, shown in Figure 8.8. To simplify calculations the shaded regions are represented with the linear approximation [USACE 1999]:

$$M + 14.4R - 13.0 = 0 \tag{8.21}$$

Maximum erosion susceptibility, *M,* is calculated as:

$$M = \frac{\lambda_2 y_e^{0.6}}{\lambda_1 \tau_c} \tag{8.22}$$

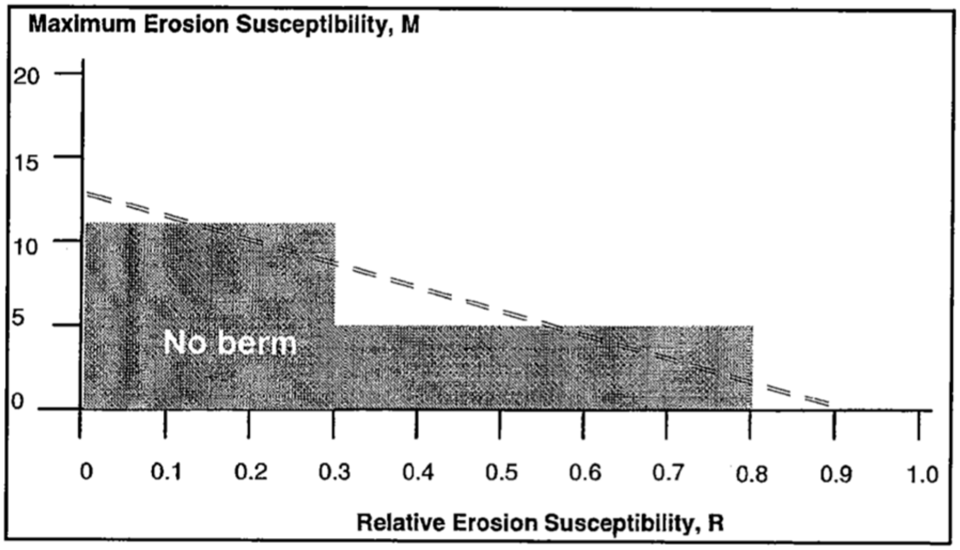


**Figure 8.8 Rock Island Method toe berm necessity and linear approximation [USACE 1999].**

where $\tau_c$ = critical tractive stress (lb/ft$^2$). While relative erosion susceptibility, *R,* is calculated as:

$$R = \frac{y_e - \left(\frac{\lambda_1 \tau_c}{\lambda_2}\right)^{1.67}}{H} \tag{8.23}$$

where $H$ = floodwater height (ft).

The two parameters $\lambda_1$ and $\lambda_2$, which appear in the above equations, are calculated as:

$$\lambda_1 = \cos(\alpha) - \frac{\gamma_w}{\gamma_{sub}}\sin(\alpha)\tan(\alpha - \delta) - \frac{\gamma_{sat}}{\gamma_{sub}}\frac{\sin(\alpha)}{\tan(\phi')} \tag{8.24}$$

$$\lambda_2 = \gamma_w \sin^{0.7}(\alpha)\left(\frac{n}{1.49}\right)^{0.6}\left[k\tan(\alpha - \delta)\right]^{0.6} \tag{8.25}$$

where $\alpha$= downstream slope angle, $\gamma_w$= density of water, $\gamma_{sub}$= submerged effective density of the soil (lb/ft$^3$), $\delta$ = taken as zero for a horizontal exit gradient, $\gamma_{sat}$= saturated density of the soil (lb/ft$^3$), $\phi'$ = effective friction angle, $n$ = manning's n (unitless), and $k$ = permeability (ft/sec). The parameter $y_e$ is taken to be the vertical distance of the water's exit point on the dry slope as found by Casagrande's parabola (see Figure 8.9) and is calculated as follows [USACE 1986]:

$$y_e = a\sin(\alpha) \tag{8.26}$$

The variable $a$ is the distance from the levee toe to the exit point as measured along the dry slope. Following Casagrande's method for $\alpha \leq 90°$, $a$ is calculated as follows:

$$a = s_0 - \sqrt{s_0^2 - \frac{h^2}{\sin^2(\alpha)}} \tag{8.27}$$

With $s_0$ being:

$$s_0 = \sqrt{d^2 + H^2} \tag{8.28}$$

where $d$ = distance from levee toe to point A (ft) (Figure 8.9) and $H$ = floodwater height (ft).

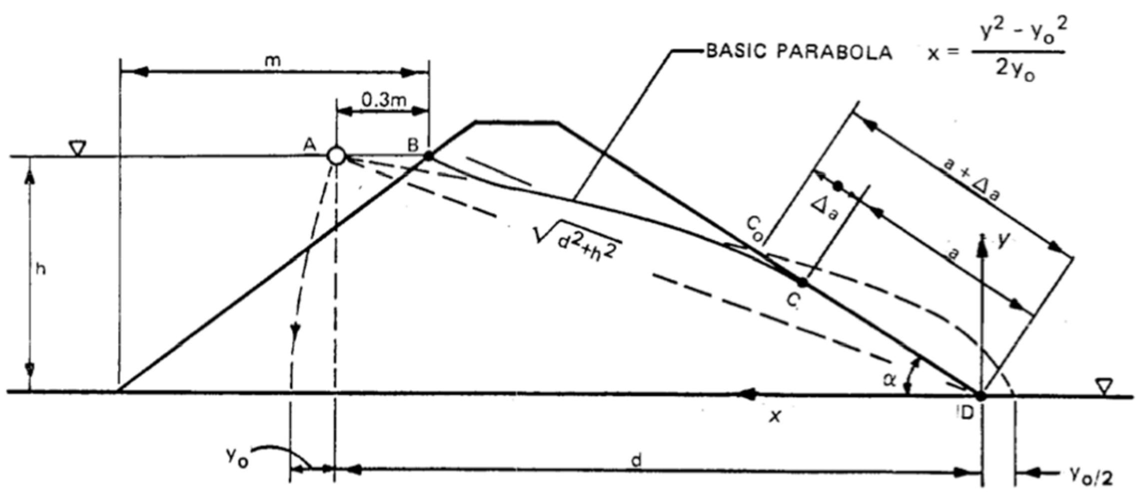


**Figure 8.9 Casagrande's parabola (USACE 1986).**

To progress from the PF to a through-seepage PFC Manning's $n$, $\gamma_{sat}$, $\phi$, $k$, and $\tau_c$ are considered RVs. Their coefficients of variation are presented in Table 8.4. To calculate beta, a normal distribution is assumed and Equation (8.8) is used [USACE 1999].

### *8.3.3.5 Slope Stability*

For this report both the OMS and the Simplified Bishop Method are used. While the final results presented are those found using the Simplified Bishop Method, the OMS is used to verify the factors of safety calculated by the more rigorous method. For both methods of analysis the floodwater is treated as an external hydrostatic load on each slice. The equation used to calculate the FS associated with the OMS is as follows [USACE 2003]; see Figure 8.10:

$$FS = \frac{\sum\left\{c'\Delta x + \left[W\cos(\Omega) + P\cos(\Omega-\theta) - u\Delta x\cos^2(\Omega)\right]\tan(\phi')\right\}}{\sum W\sin(\Omega) - \frac{\sum M_P}{r}} \tag{8.29}$$

where $c'$= cohesion intercept of effective stress Mohr-Coulomb diagram (lb/ft$^2$), $\Delta x$= width of each slice (ft), $W$= weight of each slice (lb), $\Omega$ = inclination from horizontal to the bottom of the slice (radians), $P$= force of the water acting perpendicular to top of each slice (lb), $\theta$= inclination from horizontal of the top of the slice (radians), $u$= pore water pressure (lb/ft$^2$), $\phi'$= friction angle of effective stress Mohr-Coulomb diagram (radians), and $r$ = radius of the circular slip surface (ft).

The moment about the center of the circle due to force of the floodwater, $M_P$, is calculated as:

$$M_P = P\left\lfloor d_v\sin(\theta) + d_h\cos(\theta)\right\rfloor \tag{8.30}$$

where $d_v$ = vertical distance from midpoint of each slice top to center of circle (ft) and $d_h$= horizontal distance from midpoint of each slice top to center of circle (ft).

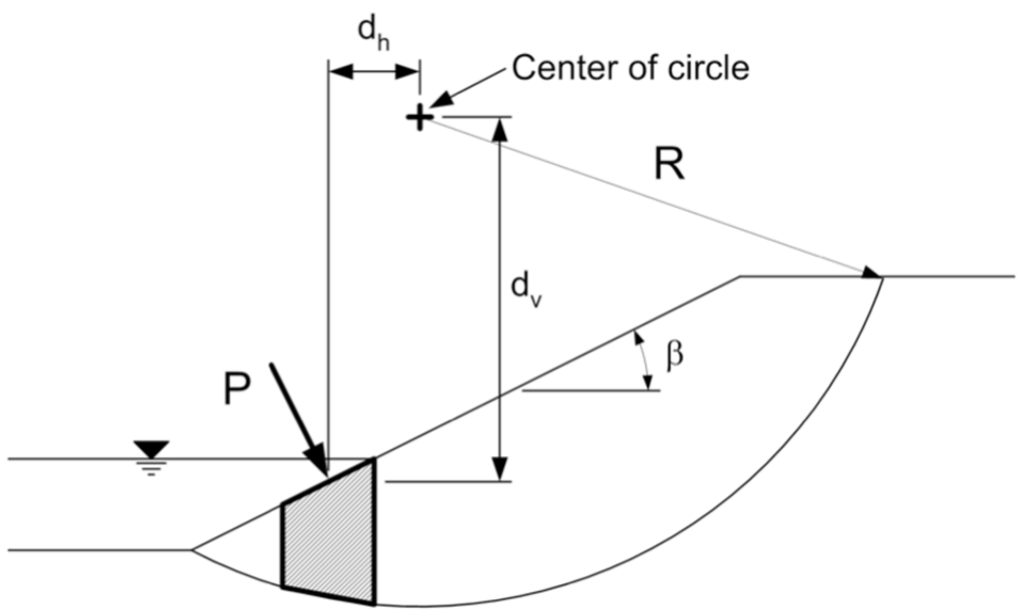


**Figure 8.10 Diagram showing positive sign convention for $d_v$ and $d_h$ [USACE 2003].**

The Simplified Bishop Method uses the following equation to calculate a FS (USACE 2003):

$$FS = \frac{\sum\left[\frac{c'\Delta x + (W + P\cos(\theta) - u\Delta x\sec(\Omega))\tan(\phi')}{m_{\Omega}}\right]}{\sum W\sin(\Omega) - \frac{\sum M_P}{r}} \tag{8.31}$$

where $m_{\varphi}$ is defined by the following formula:

$$m_{\Omega} = \cos(\Omega) + \frac{\sin(\Omega)\tan(\phi')}{FS} \tag{8.32}$$

It is $m_{\Omega}$'s dependence on the FS that makes the Simplified Bishop Method an iterative process. To expedite the guess and check process in the method, 1000 guessed factors of safety between 0 and 10 are used to estimate the actual FS. The values are graphed (Figure 8.11) and the inverse tangent of the ratio between subsequent guessed FS's and calculated FS's is taken. The inverse tangent calculates the angle of the line formed between the two values. The guessed and calculated FS that corresponding to a 45°angle, or a 1:1 ratio is selected as the true FS [USACE 2003].

In order to locate the critical slip surface, or the one having the lowest FS, many trial slip surfaces must be assumed; for this a search scheme is used. The search scheme is summarized here (GEO-SLOPE). As noted earlier, circular slip surfaces are assumed, and are therefore defined by a center point and radius.

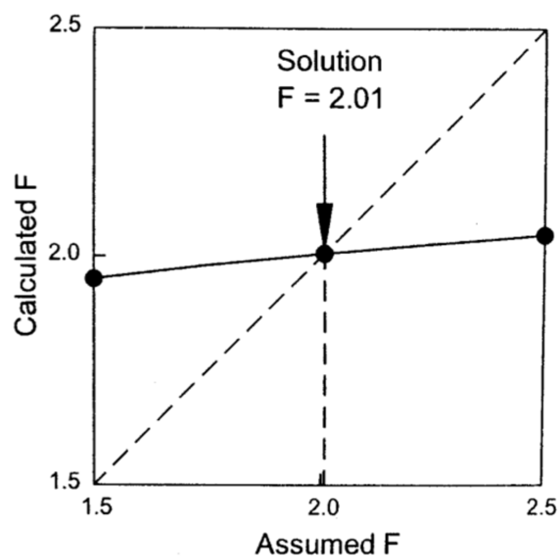


**Figure 8.11 Graph of guessed FS versus calculated FS [USACE 2003].**

1. A grid of potential center points is specified. The grid is located above the levee's crown and over its wet slope.
2. Numerous tangent lines are specified. The tangent lines are located within the levee and parallel to its wet slope.
3. The radius of each trial slip surface is calculated as the perpendicular distance between each center point and the selected tangent line.
4. The first tangent line is selected and held constant as the center varies through all the points in the specified grid.
5. After a complete cycle through the grid, the next tangent line is selected, and held constant, while the center varies once again.
6. A FS is calculated and recorded for each iteration.
7. Once every specified tangent line has been selected, with the center varying for each, the floodwater height is increased.
8. This process is repeated for every floodwater height where a critical slip surface is sought.
9. Finally, after the search scheme has run the recorded factors of safety are sorted to locate the critical slip surface associated with each floodwater height.

It is important to note that increasing the size of the search scheme, by adding tangent lines or increasing the grid size, will increase accuracy, it will also require more time. For the purposes of this report 5 tangent lines were defined for a 6-by-6 grid. The spacing and location of the grid and tangent lines is dependent on the size of the levee being analyzed. Floodwater height is varied from 0 feet to just before overtopping in 1-foot increments.

A probabilistic analysis is performed on the critical slip surface of each floodwater height in order to arrive at a probability of failure. These individual probabilities of failure are used to graph a PFC for slope stability. In order to perform the probabilistic analysis $c'$ and $\phi'$ are taken as RVs whose coefficients of variation are presented in Table A.5 of the Appendix. A lognormal distribution is assumed; therefore, beta is calculated via Equation (8.10) [USACE 1999].

#### *8.3.3.6 Seismic Vulnerabilities*

The two discussed methods for evaluating a levee's seismic vulnerability rely on a FS. The first method defined the FS as the ratio between the CRR and the CSR [Seed et al. 2003]. This method does not depend on floodwater height. This lack of dependence means this method does not generate PFC's of the same nature as those developed for other failure modes. For this reason the first method was not used to model a levee's seismic vulnerability.

The second method calculates a FS as the ratio between the yield acceleration and the peak ground acceleration. The yield acceleration is calculated by rearranging the equations used in slope stability analyses. In order to stay consistent, the yield acceleration is calculated using the Simplified Bishop Method [Kim and Sitar 2004]:

$$a_{yield} = \frac{1}{\sum W \frac{a}{r}} \left\{ \sum \left[ \frac{\{c'\Delta x + (W - u\Delta x)\tan(\phi')\}\sec(\Omega)}{1 + \tan(\Omega)\tan(\phi')} \right] - \sum W \sin(\Omega) \right\} \tag{8.33}$$

where $a$ = vertical distance between a slice's centroid and slip surface center (ft).

The peak ground acceleration is dependent on the earthquake size and location as well as the distance between the earthquake's epicenter and the levee in question. For this reason the peak ground acceleration is not calculated but rather assumed based on the desired test earthquake intensity.

### 8.3.4 Combination of Failure Mechanisms

The combined probability of failure, at any floodwater height, is calculated as follows:

$$Pf = 1 - (1 - P_O)(1 - P_E)(1 - P_{US})(1 - P_{TS}) \tag{8.34}$$

where $P_O$ = probability of failure due to overtopping, $P_E$ = probability of failure due to erosion, $P_{US}$ = probability of failure due to under-seepage, and $P_{TS}$ = probability of failure due to through-seepage. The above equation is used to generate combined PFC's based on individual failure mode PFCs [USACE 1999].

### 8.3.5 Case Studies

In this report two case studies are defined: an urban levee and an agricultural levee. The two levee cross sections are representative of levees found along the Sacramento River in California's Central Valley.

#### *8.3.5.1 Agricultural Levee*

The agricultural levee represents an un-engineered levee that might protect farmland. The parameters that define the agricultural levee cross section are estimates based on existing levees. The agricultural levee parameters are presented in Table 8.1.

Ideally, the wet and dry slopes of the agricultural levee would both be set to 1V:1H or 1V:2H on the landside yet, the limitations of the RIM, used to predict through-seepage, require a shallower dry slope. The channel depth and width are arbitrarily set to 10 and 100 ft, respectively, to simulate a real world scenario. Being that the floodwater heights are assumed, the channel parameters have very little bearing on the performance of either case study levee. Agricultural levee are often made out of the soils at hand (a non-ideal sandy clay in this case). Finally, the blanket and substratum thicknesses; critical velocity; and critical exit gradient were assumed to be the same as those used in *ETL 1110-2-556*.

**Table 8.1 Agricultural levee parameters.**

| | |
|---|---|
| Levee Height | 50 ft |
| Crown Width | 15 ft |
| Wet Slope | 1V:1H |
| Dry Slope | 1V:5H |
| Channel Depth | 10 ft |
| Channel Width | 100 ft |
| Manning's n | 0.03 |
| Energy Slope | 0.0001 |
| Levee Soil | Sandy Clay |
| Blanket Soil | Clayey Sand |
| Substratum Soil | Silty Sand |
| Blanket Thickness | 8 ft |
| Substratum Thickness | 80 ft |
| Critical Velocity | 5 ft/sec |
| Critical Exit Gradient | 0.85 |

#### *8.3.5.2 Urban Levee*

The urban levee represents an engineered levee that would protect a metropolitan area. The parameters chosen are estimated based on existing levees in California's Central Valley. Those parameters are presented in Table 8.2.

Consistent with engineered levees along the Sacramento River, the crown width and side slopes are increased from those of the agricultural levee. It was assumed that engineered levees would be constructed out of lower permeability soils (a clayey sand in this study). In practice the USACE can inject bentonite slurry or other seepage barrier into the soils underlying the levee, which decreases the permeability and mitigates under-seepage. For this reason the top blanket thickness of the urban levee was increased by four ft. Finally the critical velocity of the urban levee is increased by 1 ft/sec to account for vegetation and/or armor that are common of engineered levees.

**Table 8.2 Urban levee parameters.**

| | |
|---|---|
| Levee Height | 50 ft |
| Crown Width | 60 ft |
| Wet Slope | 1V:3H |
| Dry Slope | 1V:5H |
| Channel Depth | 10 ft |
| Channel Width | 100 ft |
| Manning's n | 0.03 |
| Energy Slope | 0.0001 |
| Levee Soil | Clayey Sand |
| Blanket Soil | Clayey Sand |
| Substratum Soil | Silty Sand |
| Blanket Thickness | 12 ft |
| Substratum Thickness | 80 ft |
| Critical Velocity | 6 ft/sec |
| Critical Exit Gradient | 0.85 |

## 8.4 RESULTS

The methods presented allow for the calculation of individual PFCs for the failure modes of overtopping, erosion, under-seepage, and through-seepage. These individual PFCs were combined to create a single PFC, which was done for both case studies.

Slope stability analysis resulted in PFCs that predicted increasing probabilities of failure with increasing floodwater height, up until floodwater height reached approximately two-thirds of the levee height, at which point the probability of failure began to decrease. Because the slope stability analysis presented in USACE *ETL 1110-2-556* showed no signs of this behavior, it is considered to be an error. Despite numerous attempts to resolve and/or explain this behavior, it persisted. For this reason, no PFC is presented for slope stability. Additionally, the errors in slope stability mean that no PFC could be presented for seismic vulnerabilities because calculation of yield acceleration relies on an accurate slope stability analysis.

### 8.4.1 Agricultural Levee

Individual PFCs were generated for the agricultural levee (Figure 8.12) and combined into a single PFC (Figure 8.13). Under-seepage is the failure mode that controls the probability of agricultural levee failure. Erosion is the second largest threat to the agricultural levee, followed by through-seepage. Overtopping presents no threat to the levee as long as floodwater height remains below levee height, yet, when floodwater height exceeds levee height, failure due to overtopping is guaranteed. The threat posed by any individual failure mode is low when floodwater height is below 20 ft. However, when floodwater height surpasses 20 ft the individual failure modes start to pose a larger threat to the agricultural levee.

Despite the combination of failure modes, the levee still has a relatively low probability of failure for floodwater height less than 20 ft. As with the individual modes the agricultural levee becomes much less safe when floodwater height exceeds 20 ft. When the individual modes of failure are combined the agricultural levee has a 100% chance of failure before the point of overtopping is reached.

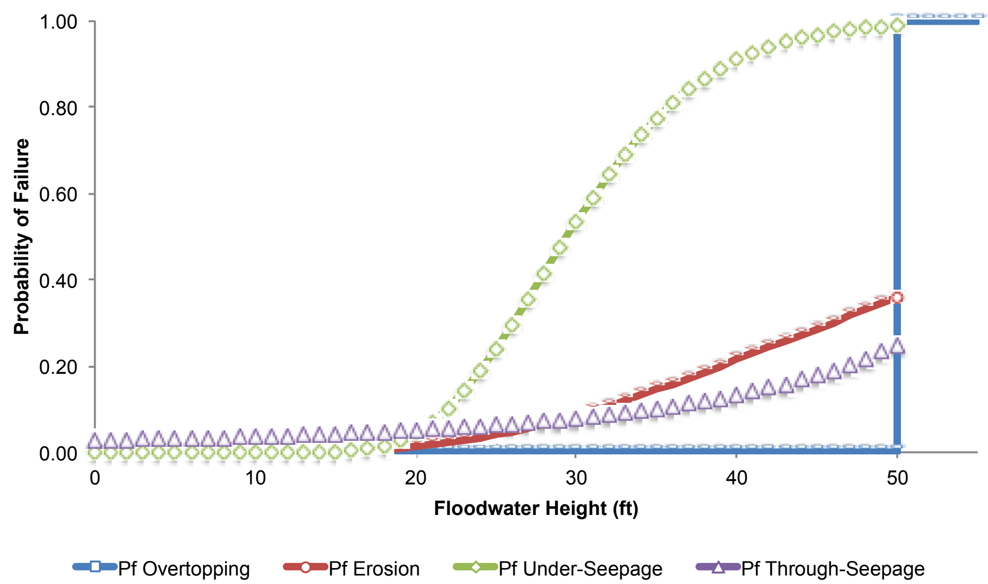


**Figure 8.12 Agricultural levee: individual modes.**

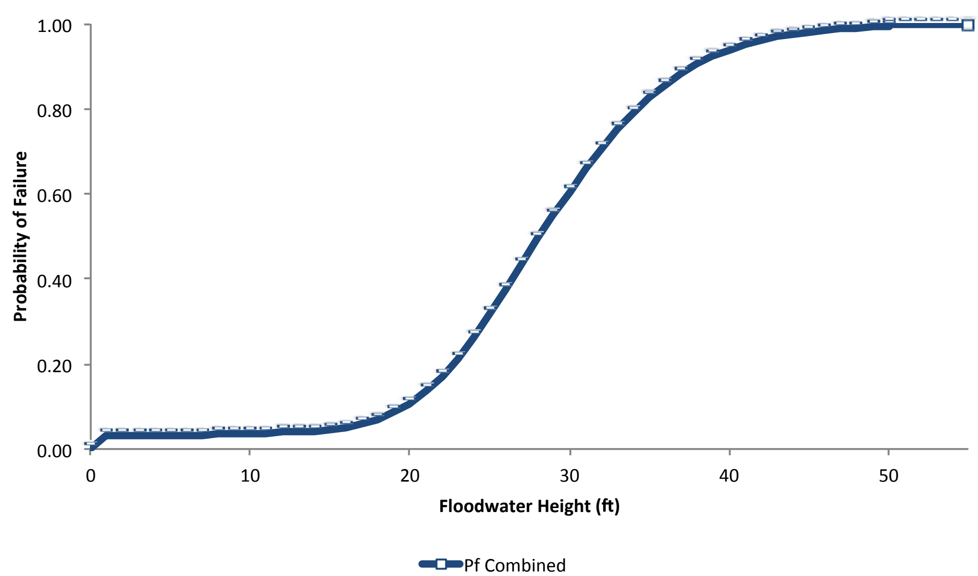


**Figure 8.13 Agricultural levee: combined modes.**

### 8.4.2 Urban Levee

Individual PFCs were also generated for the urban levee (Figure 8.14) and combined into a single PFC (Figure 8.15). As with the agricultural levee, under-seepage is the failure mode that most contributes to urban levee failure, followed once again by erosion and then through-seepage. However, the probabilities of failure due to the individual mode are much smaller for the urban levee than they were for the agricultural levee. When floodwater height is at a maximum of 50 ft there is less than 20% probability of failure due to either erosion or through-seepage. Similarly, when floodwater elevation is 50 ft the probability of failure due to the most threatening failure mode, under-seepage, is less than 60%. In addition, the individual failure modes do not begin to significantly threaten the urban levee until after floodwater height has surpasses 30 ft, compared to 20 ft for the agricultural levee.

When the individual modes are combined, the probability of urban levee failure does not reach 100% until the point of overtopping. Comparing this to the agricultural levee, which had guaranteed failure before overtopping, it is evident that the urban levee is safer. When floodwater height is below 30 ft the urban levee has a relatively low probability of failure. This is consistent with the low threat posed by the individual modes at the same floodwater elevations.

In both the agricultural and urban levees there is a tipping point where the probability of failure begins to drastically increase. This transition point takes place at a floodwater height of 20 ft for the agricultural levee and at 30 ft for the urban levee. These points are important for understanding the trends in the failure analysis and may be included in design alternatives for system improvements.

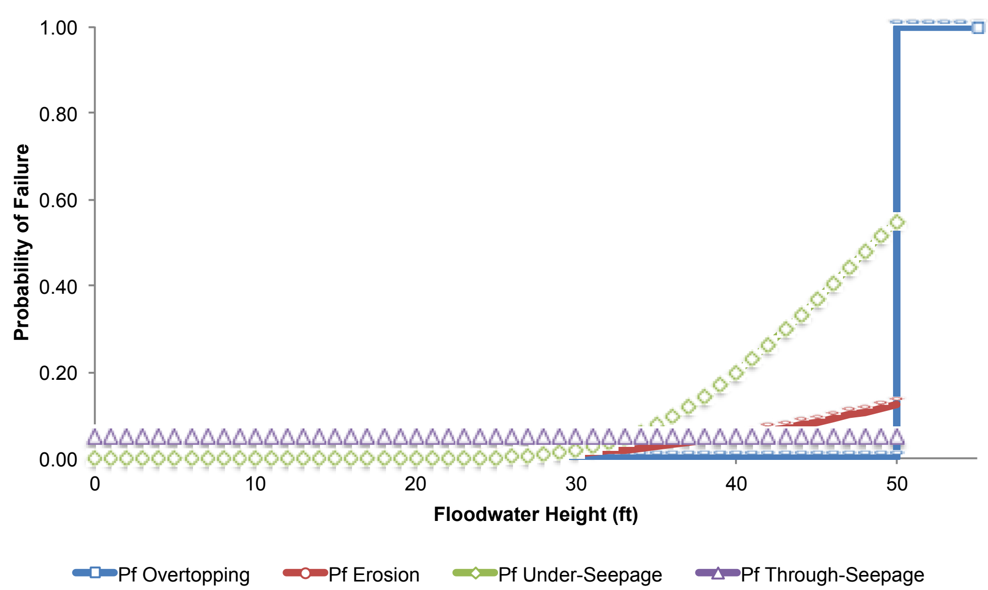


**Figure 8.14 Urban levee: individual modes.**

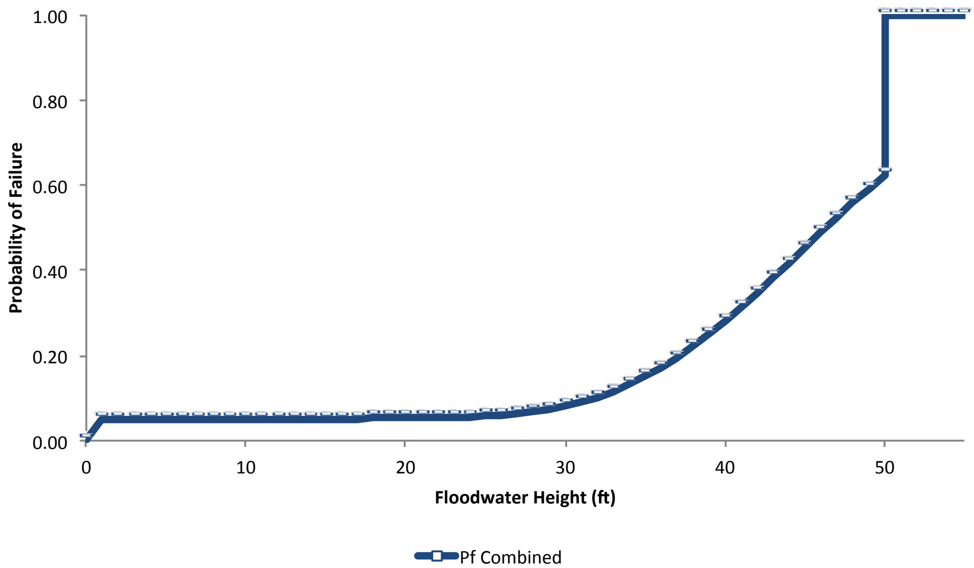


**Figure 8.14 Urban levee: individual modes.**

## 8.5 CONCLUSIONS

Typical risk analysis assumes overtopping as the only mode of levee failure, yet when multiple failure modes are taken into account the probability of levee failure is greatly increased. This trend can be seen in both the agricultural and urban case study levees. Therefore, overall probability of levee failure is underestimated by assuming overtopping as the only failure mode. This underestimation may influence risk analysis, which relies on accurate estimates of probability of system failure. In turn, altered risk calculations can affect decisions being made in riverine levee planning and construction, which is a vital component of overall flood management. For these reasons this report concludes that an effort needs to be made to include multiple modes of failure into risk analyses to achieve optimal system design.

This report finds that under-seepage is the most substantial threat to the case study levees during flood stage not large enough to induce overtopping. However, this finding is specific to the case study levees and cannot be generalized to all levees. The real benefit of this method of analysis is that it allows the most threatening failure mode to be pinpointed for any levee in question. The case study levees provide examples of real-world levees to demonstrate the methods ability to determine which failure mode the levee is most susceptible. If a different levee were analyzed, any of the failure modes may present itself as the most threatening. The benefits of knowing which mode most threatens a particular levee are that levees may be improved to combat their biggest weaknesses. As seen in the two case study levees, under-seepage is the most threatening while erosion and through-seepage are substantially less threatening. If the threat of under-seepage could be reduced through planning and design, then the overall result would be a much safer levee.

These methods of analyses also highlighted key areas that, if improved, would greatly reduce the probability of failure due to individual failure modes. The most beneficial method was to reduce failure due to erosion. This could be done through the addition of vegetation and or rock armor. Through-seepage is most influenced by levee geometry; therefore, increasing the width of the levee is most beneficial in mitigating through-seepage failure. Finally, the PF used to predict under-seepage is highly sensitive to the thicknesses and permeability of the blanket and substratum soil layers. Therefore, if the top blanket is made thicker, such as with the injection of a bentonite slurry, under-seepage can be mitigated.

## ACKNOWLEDGMENTS

This research would not have been possible without the funding provided by PEER and NSF. I thank both organizations for this invaluable learning opportunity. Additional thanks to my graduate mentor, Nate Burley, for all of his guidance this summer. I am grateful to my faculty advisor, Professor Jay Lund, for his time and encouragement. Thank you to the entire staff of the Center for Watershed Sciences for making me feel like a part of the team. Robbie Pires deserves thanks for reading and editing the numerous drafts of this report. And finally I thank my fellow interns, especially my colleague Paul Shipman.

## REFERENCES

Deretsky Z., Modes of Levee Failure. National Science Foundation.

DWR (2012). *Attachment 8E: Levee Performance Curves*, Department of Water Reseources, The State of California, Sacramento, CA.

DWR (2012). *California Velley Flood Protection Plan*." Department of Water Resources, State of California, Sacramento, CA.

Ellis H, CB Groves, and GR Fischer (2008). Rapid levee assessment for reliability and risk analysis, *Proc*., ASCE, GeoCongress, pp. 170−177, New Orleans, LA.

GEO-SLOPE International Ltd. Grid and Radius. Geo-Slope, Calgary: Geo-Slope.

Geotechnical Properties of Soils. April 29, 2011, accessed August 9, 2012, *http://www.geotechdata.info/parameter.*,

Idriss IM., and RW Boulanger (2008). *Soil Liquefaction During Earthquakes*, Earthquake Engineering Research Institute, Oakland, CA.

Kim J, and N Sitar (2004).Direct estimation of yield accelaration in slope stability analysis, ASCE, *J. Geotech. Geoenviro. Eng.*, 130(1):111−115.

Kulhawy FH., and PW Mayne (1990). Manual on estimating soil properties for foundation design, *EL-6800, Geotechnical Enginering Group*, Cornell University, Ithaca, NY.

Moss RES, and JM Eller (2007). Estimating the probability of failure and associated risk of the California Bay delta levee system, *Proc.*, ASCE, -Denver 2007, Denver, CO.

NRCS (2012). General Guide for Estimating Moist Bulk Density. National Resources Conservation Service. June 13, 2012, accessed August 9, 2012, *http://www.mo10.nrcs.usda.gov/references/guides/properties/moistbulkdensity.html*.

Seed RB. et al. (2003). Recent advances in soil liquefaation engineering: a unified and consistent framework, *Proc.*, 26th Annual ASCE Los Angeles Geotechnical Spring Seminar, Long Beach, CA, 72 pgs. Earthquake Engineering Research Center, University of California, Berkeley, Berkeley, 2003.

Shewbridge S. et al. (2010). Levee erosion prediction equations calibrated with laboratory testing,, S.E. Burns, S.K. Ghatia, C.M.C. Avila, and B.E. Hunt, eds, *Proc*., 5th Inter. Conf. on Scour and Erosion, San Francisco, CA. Scour and Erosion (*ASCE Geotechnical Special Publication No. 210*).

Tiwari B. (2008). Constant head and falling head permeability test, Cal State Fullerton, March 17, 2008, accessed August 9, 2012, *http://faculty.fullerton.edu/btiwari/geotech_Lab/mainpage_files/other/Permeability.pdf.*

USACE (1986). Engineering and design-seepage analysis and control for dams, *EM 1110-2-1901*, U.S. Army Corp of Engineers, Washington D.C.

USACE (2003). Engineering and design: Slope stability, *EM 1110-2-1902*, U.S. Army Corp of Engineers, Washington D.C.

USACE (1999). Risk-based analysis in geotechnical engineering for support of planning studies, *ETL 1110-2-556*, United States Army Corps of Engineers , Washington D.C.

## 8.6 APPENDIX

### 8.6.1 Review of Probabilistic Moments

#### Mean Value

The mean value, $\mu_X$, of $N$ sample values is calculated by summing the $X$ values and dividing by $N$ [USACE 1999].

$$\mu_X = \frac{\sum_{i=1}^{N} X_i}{N} \tag{8.35}$$

#### Expected Value

The expected value, $E[X]$, represents the mean value that would be calculated if all values of the RVs are multiplied by their probability of occurrence and summed [USACE 1999].

$$E[X] = \mu_X = \int Xf(X)dx \approx \sum Xp(X_i) \tag{8.36}$$

#### Variance

Variance, $Var[X]$, is a measure of the expected value of the squared difference between the RV and mean value (USACE 1999).

$$Var[X] = E[(X-\mu_x)^2] = \int (X-\mu_x)^2 f(X)dX = \frac{\sum[(X_i-\mu_x)^2]}{N} \tag{8.37}$$

#### Standard Deviation

The standard deviation, $\sigma_X$, quantifies the dispersion of a RV about its expected value. It is defined to be the square root of the variance [USACE 1999].

$$\sigma_X = \sqrt{Var[X]} \tag{8.38}$$

#### Coefficient of Variation

The coefficient of variation, $V_X$, provides a convenient representation of the inherent uncertainty of a given RV; it is calculated by dividing the standard deviation by the expected value and multiplying by 100 to obtain a percentage [USACE 1999].

$$V_X = \frac{\sigma_X}{E[X]} \times 100\% \tag{8.39}$$

### 8.6.2 Geotechnical Parameters

**Table A.1 Geotechnical parameters.**

| Soil Type | $c'$ (lb/ft$^2$) | $k$ (ft/sec) | $\gamma_b$ (lb/ft$^3$) | $\gamma_{sat}$ (lb/ft$^3$) | $\tau_{crit}$ (lb/ft$^2$) | $\phi'$ (radians) |
|---|---|---|---|---|---|---|
| **Gravel** | 0.00 | 3.05E-02 | 123.90 | 140.50 | 1.06 | 0.70 |
| *Clayey Gravel* | 0.00 | 3.05E-08 | 107.99 | 129.64 | - | 0.59 |
| *Sandy Gravel* | 0.00 | 9.64E-04 | 109.86 | 122.32 | - | 0.66 |
| *Silty Gravel* | 0.00 | 3.05E-07 | 98.26 | 123.64 | - | 0.63 |
| **Clay** | 208.85 | 3.05E-10 | 97.39 | 122.40 | 0.09 | 0.38 |
| *Gravely Clay* | - | 3.05E-04 | 113.30 | 133.26 | - | - |
| *Sandy Clay* | - | 3.05E-05 | 99.26 | 115.08 | - | 0.47 |
| *Silty Clay* | - | 3.05E-09 | 87.65 | 116.40 | - | 0.44 |
| **Sand** | 0.00 | 3.05E-04 | 100.50 | 110.20 | 0.01 | 0.59 |
| *Gravely Sand* | 0.00 | 9.64E-03 | 114.54 | 128.38 | - | 0.66 |
| *Clayey Sand* | 0.00 | 3.05E-09 | 98.63 | 117.52 | - | 0.56 |
| *Silty Sand* | 0.00 | 9.64E-08 | 88.90 | 111.52 | - | 0.59 |
| **Silt** | 208.85 | 3.05E-08 | 81.16 | 112.40 | 0.00 | 0.44 |
| *Gravely Silt* | - | 3.05E-03 | 106.80 | 129.26 | - | - |
| *Clayey Silt* | - | 9.64E-10 | 90.90 | 118.40 | - | - |
| *Sandy Silt* | - | 9.64E-05 | 92.76 | 111.08 | - | - |

**(Geotechnical Properties of Soils [2011]; Kulhawy and Mayne [2003]; NRCS [2012]; Shewbridge et al. [2010]; Tiwari [2008])**

### 8.6.3 Probabilistic Moments Used for Analysis

**Table A.2 Probabilistic moments used in erosion models.**

| | Variable | Coefficient of Variation |
|---|---|---|
| **Urban Levee** | $n$ | 10% |
| | $S$ | 10% |
| | $V_{crit}$ | 20% |
| **Agricultural Levee** | $n$ | 10% |
| | $S$ | 10% |
| | $V_{crit}$ | 20% |

**[USACE 1999]**

**Table A.3 Probabilistic moments used in under-seepage model.**

| | Variable | Coefficient of Variation |
|---|---|---|
| **Urban Levee** | $k_f$ | 25% |
| | $k_b$ | 25% |
| | $z$ | 25% |
| | $q$ | 6.25% |
| **Agricultural Levee** | $k_f$ | 25% |
| | $k_b$ | 25% |
| | $z$ | 25% |
| | $q$ | 6.25% |

**[USACE 1999]**

**Table A.4 Probabilistic moments used in through-seepage model.**

| | Variable | Coefficient of Variation |
|---|---|---|
| **Urban Levee** | $n$ | 10% |
| | $\gamma_{sat}$ | 6% |
| | $\phi'$ | 8.8% |
| | $k$ | 25% |
| | $\tau_{crit}$ | 10% |
| **Agricultural Levee** | $n$ | 10% |
| | $\gamma_{sat}$ | 6% |
| | $\phi'$ | 6.5% |
| | $k$ | 25% |
| | $\tau_{crit}$ | 10% |

**[USACE 1999]**

**Table A.5 Probabilistic moments used in slope stability analysis.**

| | Variable | Coefficient of Variation |
|---|---|---|
| **Urban Levee** | $c'$ | 40% |
| | $\phi'$ | 8.8% |
| **Agricultural Levee** | $c'$ | 40% |
| | $\phi'$ | 6.5% |

**[USACE 1999]**

## 8.7 GLOSSARY OF TERMS

CRR = cyclic resistance ratio
CSR = cyclic stress ratio
CVFPP = California Valley Flood Protection Plan
ETL = Engineering Technical Letter
$FS$ = Factor of Safety
OMS = Ordinary Method of Slices
PF = performance function
PFC = probability of failure curve
RIM = Rock Island method
RV = random variable
USACE = United States Army Corps of Engineers
$a$ = vertical distance between slice centroid and slip surface center (ft)
$a_{yield}$ = yield acceleration (ft/sec$^2$)
$c'$ = effective cohesion intercept (lb/ft$^2$)
$d$ = distance from levee toe to point A (Figure 8.9) (ft)
$d_h$ = horizontal moment arm (ft)
$d_v$ = vertical moment arm (ft)
$E[X]$ = expected value of random variable X
$f_c$ = current friction factor (unitless)
$g$ = acceleration due to gravity (ft/sec$^2$)
$H$ = height of floodwater (ft)
$h$ = height of levee (ft)
$h_0$ = net residual head (ft)
$i$ = exit gradient (ft/ft)
$i_{crit}$ = critical exit gradient (ft/ft)
$K$ = errodability coefficient (ft$^3$/lb-hr)
$k$ = permeability (ft/sec)
$k_b$ = blanket permeability (ft/sec)
$k_f$ = substratum permeability (ft/sec)
$k_0$ = initial intrinsic permeability
$M$ = maximum erosion susceptibility
$M_P$ = moment about center of circle due to floodwater force (lb-ft)
$n$ = manning's n (unitless)
$n_0$ = initial porosity (%)
$P$ = force of the water acting perpendicular to top of each slice (lb)
$P_f$ = probability of failure
$q$ = substratum thickness (ft)
R = relative erosion susceptibility

| | |
|---|---|
| $R_h$ | = hydraulic radius (ft) |
| $r$ | = radius of circular slip surface (ft) |
| $S$ | = energy slope (unitless) |
| $s$ | = distance from landside toe to effective source of seepage (ft) |
| $u$ | = pore water pressure (lb/$^2$) |
| $V$ | = velocity (ft/sec) |
| $V_{crit}$ | = critical velocity (ft/sec) |
| $V_X$ | = coefficient of variation of random variable X |
| $Var[X]$ | = variance of the random variable X |
| W | = weight of each slice (lb) |
| $x_1$ | = blanket length (ft) |
| $x_2$ | = embankment width (ft) |
| $x_3$ | = effective seepage exit distance (ft) |
| $y_e$ | = vertical distance of the water's exit point (ft) |
| $z$ | = blanket thickness (ft) |
| $\alpha$ | = downstream slope angle (radians) |
| $\beta$ | = reliability index |
| $\gamma_{sub}$ | = submerged effective density of the soil (lb/ft$^3$) |
| $\gamma_{sat}$ | = wet bulk density of soil (lb/ft$^3$) |
| $\Delta x$ | = width of each slice (ft) |
| $\varepsilon$ | = erosion rate (ft/hour) |
| $\varepsilon_{crit}$ | = critical erosion rate (ft/hour) |
| $\theta$ | = inclination from horizontal of the top of the slice (radians) |
| $\mu_X$ | = mean value of random variable X |
| $\rho$ | = density of water (lb/ft$^3$) |
| $\tau$ | = effective hydraulic stress (lb/ft$^2$) |
| $\tau_{crit}$ | = critical shear stress (lb/ft$^2$) |
| $\tau_s$ | = shear stress due to current scour (lb/ft$^2$) |
| $\phi'$ | = effective friction angle (radians) |
| $\Omega$ | = inclination from horizontal to bottom of slice (radians) |

# 9. Exploration of Earthquake Intensity Measure Relationships with Pore Pressure and Liquefaction

MICHAEL ERCEG


## ABSTRACT

Investigations were made into the reliability of six earthquake intensity measures; PGA, PGV, PGD, CAV, $I_a$, and $PGA_M$ for use in liquefaction hazard evaluation. The reliability of each intensity measure incorporates both the predictability of the intensity measure itself using empirical ground motion models and the efficiency of each intensity measure in determining peak pore pressure ratio. The efficiency of each intensity measure was quantified using a correlation coefficient for data generated using equivalent linear analyses and using a standard deviation of residuals for the nonlinear analyses. The correlation coefficient was used to evaluate the linear relationship between the intensity measure and the pore pressure ratio, which was observed to be applicable only at shallow depths. In order to capture the nonlinear relationship between the intensity measures and the peak pore pressure ratio, standard deviation of residuals were evaluated using a Butterworth function, which proved to be a more appropriate fit to the data. The uncertainty in both the predictability of the intensity measure, and the efficiency of the intensity measure to evaluate the peak pore pressure ratio were combined into a single parameter, referred to herein as the total uncertainty index. The calculated total uncertainty indices showed that cumulative absolute velocity is the most reliable intensity measure among the six addressed for use in liquefaction hazard analysis.


## 9.1 INTRODUCTION

Among the many hazards associated with earthquakes, liquefaction poses a great threat to the integrity of man-made structures. Soil liquefaction has caused buildings to topple, dams to fail, and bridges to collapse. Dynamic site response analysis methods can be used to determine various intensity measures at a site given the soil conditions of the site and an input earthquake motion. An intensity measure is a means of quantifying the level of shaking produced by an earthquake, and can be as simple as the peak (absolute) value from an accelerogram (PGA), or as complex as the cumulative integral of the absolute value of the entire acceleration time history (CAV). Looking at a variety of motions applied to a diverse set of soil profiles can provide insight into the relationships between different intensity measures (IM) and the performance of a given soil deposit. Specifically, we investigated how each IM relates to peak shear strain and pore pressure generation, key indicators of the presence of liquefaction. The strength or efficiency of each IM in determining the excess pore water pressure was investigated using two measures; the correlation coefficient and the standard deviation of residuals using a Butterworth function regression. The efficiency of each IM was then combined with the predictability of each IM using empirical ground motion models to create a total uncertainty index. This index was used to determine which IM is the most reliable with respect to liquefaction hazard evaluation.

## 9.2 BACKGROUND

### 9.2.1 Liquefaction

Liquefaction is a phenomenon that occurs in mainly loose sandy soils subjected to cyclic earthquake loading. The liquefaction of soils occurs when the strain of the soil membrane causes a buildup of pore water pressure. When the pore water pressure increases to or beyond the level of total stress in the soil matrix, the effective stress between soil particles is reduced. When the effective stress approaches or reaches zero, the water in the soil membrane takes on the entire load of the soil itself and any structures that induce loading at the surface. At this point there are no normal forces between the individual soil particles, so the soil matrix behaves as a liquid and the normal shear strength of the soil is lost. There are two general types of liquefaction: flow liquefaction and cyclic mobility [Kramer 1996].

Flow liquefaction occurs when the shear stress resisted by a soil under static conditions exceeds the reduced shear strength of the soil after triggering of liquefaction. The effective stress between soil particles can drop significantly upon triggering. In this state, the static shear stress acting on the soil must be resisted to maintain equilibrium, which can produce drastic displacements. In cyclic mobility, the second form of liquefaction, the static shear stress does not exceed the shear strength of the soil. Instead, as the soil is cyclically loaded, the shear strength of the soil is exceeded by the imposed shear stress in short increments at the peak of each cycle of loading. The physical effects of cyclic loading are usually observed as vertical cracks in the soil perpendicular to the primary direction of the cyclic displacements. This is known as lateral spreading and usually is found in stretches of gently sloping land or in steeper areas near river banks.

The most common evaluation method for liquefaction potential today is the cyclic stress method [Mayfield 2007]. The cyclic stress method uses a factor of safety to quantitatively describe a soil's resistance to liquefaction in terms of shear stresses; for a factor of safety greater than one, the soil is expected not to liquefy. Although there is a certain amount of uncertainty in the calculation of this factor of safety, the cyclic stress method has proven to be "comfortably conservative." Far fewer instances of liquefaction with a factor of safety greater than one have occurred than instances of no liquefaction with a factor of safety less than one. In the simpler form, the factor of safety against liquefaction, $FS_{L,}$ is calculated in Equation (9.1) as the ratio of resistance to liquefaction to the loading.

$$FS_L = \frac{CRR}{CSR} \tag{9.1}$$

The cyclic demand experienced by a soil is quantified using a factor called the cyclic stress ratio (CSR), which is calculated in Equation (9.2) as the ratio of the cyclic shear stress to the vertical effective overburden stress. Because the cyclic shear stress is not naturally uniform in an earthquake event, it is approximated using the ratio of total to effective vertical overburden stress, the peak acceleration normalized with respect to gravity, and a depth reduction coefficient.

$$CSR = \frac{\tau_{cyc}}{\sigma'_{vo}} \approx 0.65 \frac{a_{max}}{g} \frac{\sigma_{vo}}{\sigma'_{vo}} r_d \tag{9.2}$$

The coefficient of 0.65 is used to convert the irregular amplitude of an earthquake to equivalent uniform amplitude for harmonic cycles. The depth reduction coefficient $r_d$ makes it possible to estimate the acceleration at some depth based on the acceleration history at the surface. Figure 9.1 shows a graph of the depth reduction coefficient proposed by Seed and Idriss [1971], which was determined based on results from numerical site response analyses. The graph contains a range of $r_d$ values for different soil profiles as well as an average curve for estimating the depth reduction coefficient. Liao and Whitman [1986] provide equations [Equations (9.3) and (9.4) to estimate the value of $r_d$ with depth.

$$r_d = 1.0 - 0.00765z \quad for\ z \leq 9.15 \tag{9.3}$$

$$r_d = 1.174 - 0.0267z \quad for\ 9.15\ m\ < z\ \leq 23\ m \tag{9.4}$$

The soil's resistance to liquefaction can be quantified using the cyclic resistance ratio (CRR). The accepted method of determining the CRR comes from empirical relationships involving the corrected standard penetration test blow count $(N_1)_{60}$ and the fines content of the soil. Equation (9.5) is an example of one of those relationships, proposed by Idriss and Boulanger [2004]. These relationships are based on logistic regression of case history data from post-earthquake reconnaissance from sites that did or did not liquefy. An example of this is shown in Figure 9.2, from Youd et al. [2001].

$$CRR = exp\left\{\frac{(N_1)_{60cs}}{14.1} + \left(\frac{(N_1)_{60cs}}{126}\right)^2 - \left(\frac{(N_1)_{60cs}}{23.6}\right)^3 + \left(\frac{(N_1)_{60cs}}{25.4}\right)^4 - 2.8\right\} \tag{9.5}$$

$(N_1)_{60cs}$ is calculated using $(N_1)_{60}$, the SPT blow count that has already been corrected to an equivalent 60% hammer efficiency and one atmosphere of vertical effective stress. First, $(N)_{60}$ is corrected for energy ratio by Equation (9.6),

$$N_{60} = N\frac{ER}{60} \tag{9.6}$$

where *ER* is the actual energy delivered in percent. Then $N_{60}$ is corrected to the equivalent of one atmosphere of vertical overburden stress using an iterative process with the following three equations.

$$(N_1)_{60} = C_N(N)_{60} \tag{9.7}$$

$$C_N = \left(\frac{P_a}{\sigma'_{vo}}\right)^{\alpha} \leq 1.7 \tag{9.8}$$

$$\alpha = 0.784 - 0.0768\sqrt{(N_1)_{60}} \tag{9.9}$$

The final correction accounts for shifts in the SPT CRR curve with the fines content of the soil, which can be seen in Figure 9.2. It can be calculated by adding a value of $\Delta(N_1)_{60}$, which is calculated from the fines content FC using the following two equations:

$$(N_1)_{60cs} = (N_1)_{60} + \Delta(N_1)_{60} \tag{9.10}$$

$$\Delta(N_1)_{60} = \exp\left\{1.63 + \frac{9.7}{FC} - \left(\frac{15.7}{FC}\right)^2\right\} \tag{9.11}$$

These corrected SPT blow counts can then be used in Equation (9.5) to calculate CRR. The factor of safety against liquefaction can then be found using CSR and CRR in Equation (9.1). Uncertainty in the calculation of the resistance and loading of the soil can lead to uncertainty in the factor of safety against liquefaction.

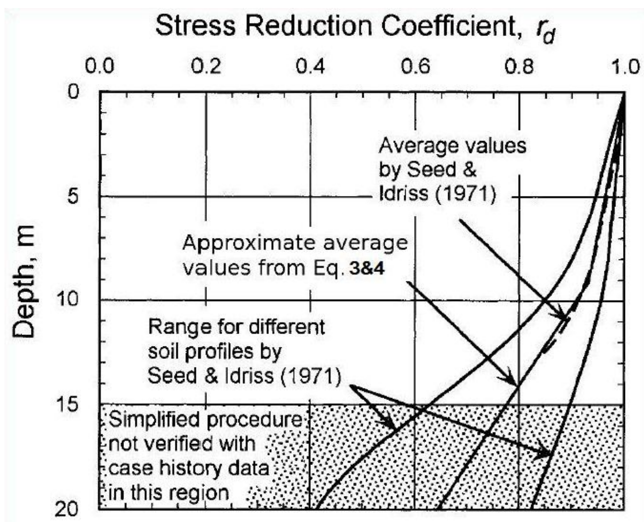


**Figure 9.1** **Stress reduction coefficient curve from Youd et al. [2001].**

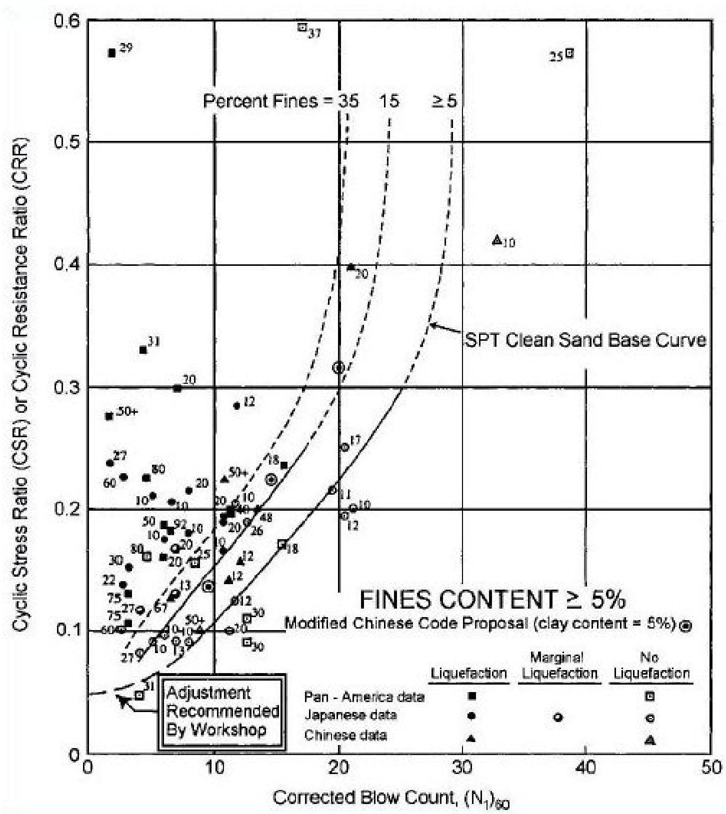


**Figure 9.2 CRR versus $(N_1)_{60}$ curve from Youd et al. [2001].**

### 9.2.2 Quantifying Liquefaction

As mentioned previously, liquefaction is a result of excess pore pressure generation in a soil and is most commonly associated with earthquake loading. The pore pressure ratio is a parameter that can be used as an indicator of liquefaction is occurrence in a soil. At a point in time, the pore pressure ratio, $r_u$, is calculated as

$$r_u = \frac{u}{\sigma'_{vo}} \tag{9.12}$$

where $u$ is the pore water pressure and $\sigma'_{vo}$ is the initial vertical effective overburden stress. The pore pressure ratio can range from values of zero to one, with zero representing no pore water pressure at all and one representing pore water pressure fully overtaking and replacing the effective overburden stress. As the pore pressure ratio increases and approaches one, liquefaction will begin to occur. The predictability of $r_u$ from the earthquake intensity measures described in Section 9.2 will be determined in this paper. However, pore water pressure is only explicitly calculated in nonlinear analysis programs and cannot be determined using an equivalent linear approach, which is the most predominant site response analysis method currently used in practice. As a result, an alternative parameter—peak shear strain—will be used for evaluating the efficiency of a given IM for the equivalent linear results. As described in the following paragraphs previous research has shown that shear strain is closely related to excess pore pressure generation.

Dobry et al. [1982] first introduced the cyclic strain approach for evaluating liquefaction potential, which uses the cyclic shear strain induced by an earthquake and the expected number of shear cycles. Dobry et al. [1982] conducted strain-controlled cyclic triaxial tests on reconstituted laboratory specimens. The tests showed a strong relationship between cyclic shear strain and pore pressure generation. These findings were reaffirmed with further testing on reconstituted samples [Hazirbaba and Rathje 2004], which were compared to Dobry's findings as well as *in situ* results from Chang [2002], shown in Figure 9.3. Strong relationships were exhibited by all between cyclic shear strain and pore pressure. The effective overburden stress also has a strong influence in the shape of the relationship, showing that pore water pressures were lower for greater values of $\sigma'_v$ (Figure 9.4).

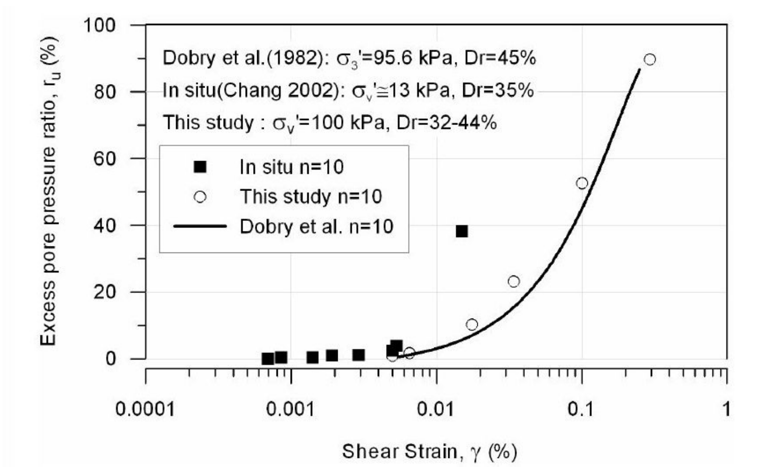


**Figure 9.3 Comparison of past strain-controlled pore pressure ratio tests from Hazirbaba and Rathje [2004].**

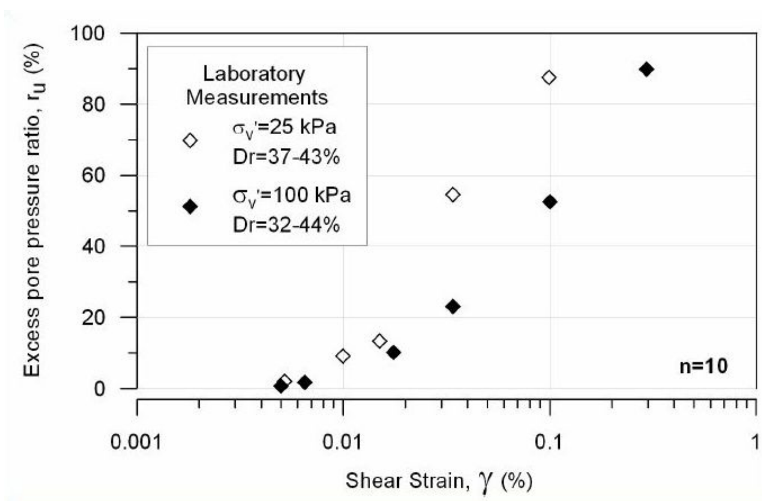


**Figure 9.4 Laboratory-measured pore pressure generation from Hazirbaba and Rathje [2004].**

## 9.3 EARTHQUAKE INTENSITY MEASURES

This study assessed the relationships between various earthquake IMs. The IMs compared were scalar, making it simple to compare measures from many different earthquakes against one another at different depths. The scalar IMs range in complexity from simple peak values to the results of integrals.

The peak measures are the most easily obtained scalar IMs. The peak ground acceleration (PGA), velocity (PGV), and displacement (PGD) are simply measured as the greatest value of the acceleration, velocity, and displacement time histories of the response. The naming convention is used loosely in this paper as it also describes the peak values at various depths in the soil profiles, rather than just at the ground surface.

The cumulative absolute velocity (CAV) is defined as the integral of the absolute value of the acceleration series for the duration of a motion [Campbell and Bozorgnia 2010]. The term "cumulative absolute velocity" comes from recognition that $v(t) = \int a(t)dt$. It can be thought of as the summation of incremental velocities in the time series.

$$CAV = \int_0^{t_{max}} |a(t)|dt \tag{9.13}$$

Arias Intensity ($I_A$) is another integral earthquake intensity measure [Travasarou et al. 2003], which has become increasingly popular as an index of earthquake damage since its proposal by Arias in 1970. It is a measure of the energy absorbed per unit weight for an infinite set of SDOF oscillators with uniformly distributed fundamental frequencies ranging from zero to infinity. The units of $I_A$ are length per time along a particular axis. Arias Intensity can be calculated using the following equation [Equation (9.4)], where *a*(*t*) is the acceleration history of the site along a particular axis in units of *g*, and where *g* is the acceleration due to gravity. Both CAV and Arias Intensity reflect the amplitude, frequency content, and duration of the earthquake.

$$I_A = \frac{\pi}{2g}\int_0^{t_{max}} a(t)^2 dt \tag{9.14}$$

The magnitude-corrected peak ground acceleration ($PGA_M$) takes into account both the simple peak acceleration of PGA and the duration of the earthquake using a magnitude scaling factor MSF. Seed and Idriss [1971] first introduced the concept of the MSF, as they realized that the maximum acceleration cannot account for the duration or frequency content of the earthquake. As more research has been conducted since the original inception of the MSF, several adjustments have been proposed [Mayfield 2007]. To obtain $PGA_M$, the PGA is scaled by the MSF according to Equation (9.15).

$$PGA_M = \frac{PGA}{MSF} \tag{9.15}$$

The magnitude scaling factor used for $PGA_M$ calculations in this experiment was calculated using the cycle-counting procedure outlined by Liu et al. [2001]. The magnitude scaling factor is found based on *N*, the number of equivalent cycles in an earthquake with uniform amplitude 0.65 times the PGA. For a detailed description of this process see Liu et al. [2001].

Empirical ground motion models have been developed for various intensity measures by Campbell and Bozorgnia [2008, 2010] and Travasarou et al. [2003]. The studies by Campbell and Bozorgnia focused on PGA, PGV, and PGD in 2008 followed by a study of CAV in 2010, using the PEER strong-motion database. Campbell and Bozorgnia found the standard deviations for CAV to be the smallest among any IM they had previously investigated. The relationships determined in the peak parameter study were determined to be valid for magnitudes from 4.0 to 7.5−8.5 and distances from 0−200 km. The relationship for CAV is considered to be valid for magnitudes from 0.5 to 7.5–8.5 and distances from 0–200 km as well. A compatible group of motions was used from the PEER database for this experiment, with magnitudes ranging from 5.9 to 7.9 and Joyner-Boore distances ranging from 10 to 80 km. A similar investigation of Arias Intensity for slope deformation problems by Travasarou et al. [2003] was based on 1208 recorded ground motions from 75 earthquakes. The standard deviation of predictability for $PGA_M$ will be assumed to be the same as that for PGA due to the direct correlation between the two. The standard deviations of predictability from literature are summarized in Table 9.1.

**Table 9.1 Standard deviations of predictability for each intensity measure.**

| IM | Predictive Uncertainty $\sigma_{IM}$ | Reference |
|---|---|---|
| PGA | 0.526 | Campbell & Bozorgnia [2008] |
| PGV | 0.525 | Campbell & Bozorgnia [2008] |
| PGD | 0.825 | Campbell & Bozorgnia [2008] |
| CAV | 0.420 | Campbell & Bozorgnia [2010] |
| Ia | 0.870 | Travasarou et al. [2003] |
| PGAm | 0.526 | |

### 9.3.1 Objectives of Work

The primary objective of this research is to determine a range of ground motion parameters from a wide variety of earthquake motions applied to several soil profiles using both equivalent linear and nonlinear site response analysis techniques, and explore the relationships between the various IMs and parameters that describe the response of the soil deposit with respect to liquefaction. In particular, efficiency of each intensity measure to predict peak shear strain (equivalent linear analysis) and pore pressure ratio (nonlinear analysis) will be investigated. The predictability of each intensity measure as described in literature will be combined with the efficiency found here to determine an index that incorporates both the predictability and efficiency. The final objective is to identify those ground motion parameters that are both predictable and efficient in the determination of pore water pressure for liquefaction hazard analysis.

## 9.4 METHODS

### 9.4.1 Selection of Soil Profiles and Earthquake Motions

Soil profiles were selected from a suite of 35 actual soil profiles which were known to have experienced liquefaction during previous earthquakes. The thirty-five profiles considered are based on an investigation described in the doctoral dissertations of Mayfield [2007] and Çetin's [2000], who used them to develop depth reduction factors. Further descriptions of all 35 profiles can be seen in Çetin [2000]. Among the thirty-five profiles, the six that best represented the range of shear wave velocities of the entire batch were selected. Average shear wave velocity curves were generated, as well as lower and upper boundary curves based on plus or minus one standard deviation from the mean, at which point six curves were visually selected. Two profiles were selected for each of the mean and plus or minus standard deviation curves; one that closely matched the curves and one that was irregular but which approximately followed the shape of the curves. This provided a total of six soil profiles ranging from soft to stiff for analysis of the relations between IMs at depth. Brief descriptions of the selected soil profiles can be found in Table 9.2.

A total of 45 earthquake motions were selected from the 3551 motions archived in PEER's Next Generation Attenuation Relationships (NGA) database based on the summary information provided in the Flatfile. The Flatfile was used to filter the entire spread of motions based on the average shear wave velocity of the top 30 m of the point of recording ($V_{s30}$) as well as the Joyner-Boore distance ($R_{jb}$) and the magnitude (M) of the earthquake. All of the motions were first filtered using a minimum $V_{s30}$ of 600 m/sec. From here the motions were separated into nine "bins" with combinations of three categories of $R_{jb}$ and magnitude. Five motions were to be selected from each bin to create a batch of earthquakes that evenly represents the range of earthquake conditions that are likely to induce liquefaction. The specific criteria for each bin are described in Table 9.3. Some of the bins did not contain at least five motions at first with the filters applied to them. Also, some of the motions described in the Flatfile are not available for download from the PEER Strong Motion Database. Because of these limitations, the minimum $V_{s30}$ filter was lowered for those particular bins. The minimum $V_{s30}$ used for each bin is provided in Table 9.3.

**Table 9.2 Soil profiles selected for analysis.**

| Profile | Stiffness | Fit | Depth |
|---|---|---|---|
| Heber Road A2 | Stiff | Irregular | 69.6 ft |
| Marine Lab B2 | Medium | Irregular | 181.4 ft |
| Miller Farm | Stiff | Smooth | 37.3 ft |
| Treasure Island | Soft | Irregular | 107.2 ft |
| Wildlife Site | Soft | Smooth | 270.8 ft |
| Wynne Avenue | Medium | Smooth | 90.2 ft |

Table 9.3 Earthquake motion bins and criteria.

| Bin | Min $V_{s30}$ (m/sec) | Magnitude | $R_{jb}$ (km) | Motions in Bin | Selected Motions |
|---|---|---|---|---|---|
| 1 | 600 | M<6.5 | 10<R<20 | 15 | 5 |
| 2 | 600 | M<6.5 | 20<R<40 | 24 | 5 |
| 3 | 600 | M<6.5 | 40<R<80 | 18 | 5 |
| 4 | 600 | 6.5<M<7.5 | 10<R<20 | 15 | 5 |
| 5 | 600 | 6.5<M<7.5 | 20<R<40 | 16 | 5 |
| 6 | 600 | 6.5<M<7.5 | 40<R<80 | 28 | 5 |
| 7 | 493 | 7.5<M | 10<R<20 | 6 | 5 |
| 8 | 550 | 7.5<M | 20<R<40 | 11 | 5 |
| 9 | 580 | 7.5<M | 40<R<80 | 5 | 5 |

The five motions selected from each bin were chosen graphically using the response spectra. The spectra for all of the motions in the bin were plotted on the same graph along with a mean spectra curve. Five motions were then selected visually such that they each had varying frequency contents but that their average response spectrum for the five selected motions would come close to the mean curve for the entire bin. This ensured that the five selected motions were an appropriate representative sample of all motions in the bin. An example of this response spectrum curve matching can be found in Figures 9.5 and 9.6 for Bin 5. The entire bin of response spectra and the mean spectrum, in bold red, are shown in Figure 9.5. Figure 9.6 shows the five selected spectra, the mean of the bin (bold red), and the mean of the five selected (bold blue). The complete list of earthquake motions selected for these analyses can be found in Appendix A, Section 9.8.

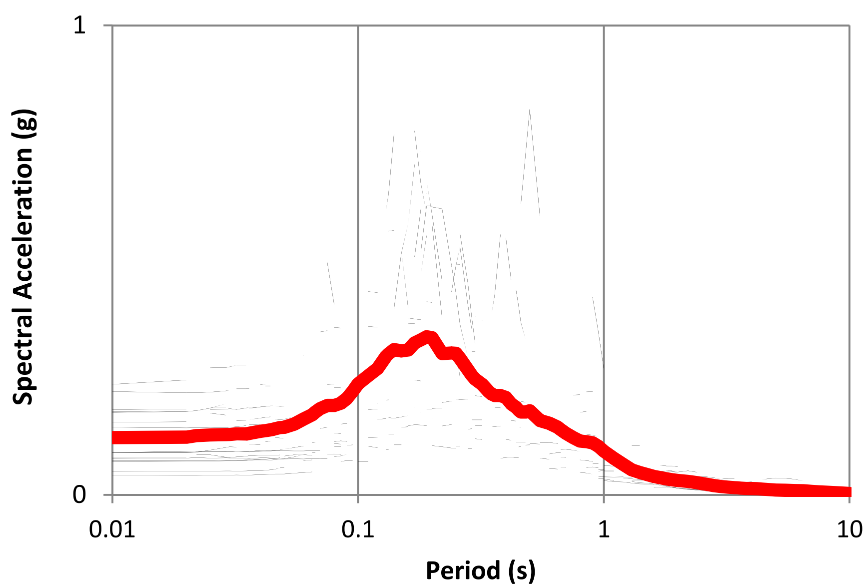


Figure 9.5 All response spectra of Bin 5; mean spectrum in bold red.

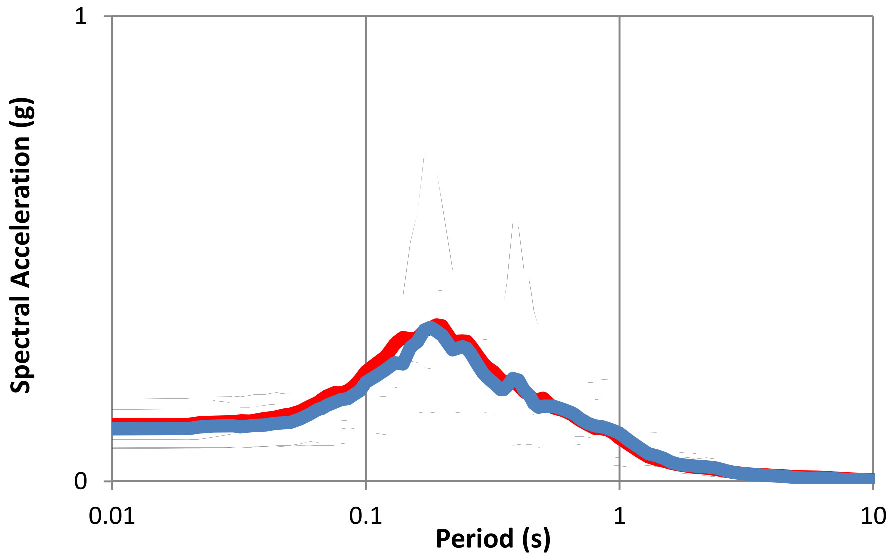


**Figure 9.6** **Selected response spectra for Bin 5; mean of bin in bold red, mean of five selected motions in bold blue.**

### 9.4.2 Site Response Analyses

Site response analysis can take the properties of the ground at a certain site and the input strong motion at the base to compute an acceleration-time history at the middle of each soil layer specified by the user. One-dimensional site response analysis assumes that the boundaries between layers are all perfectly horizontal and each soil layer extends infinitely. It also assumes that vertically propagating shear waves originating at the bedrock control the soil's response [Sideras 2011].

Three software packages were used to conduct site response analyses of the six profiles. Equivalent linear analysis was performed using ProSHAKE, a modern evolved form of SHAKE. Equivalent linear modeling does not account for liquefaction or the material softening that is induced by the greater pore water pressures and smaller effective stresses. For this reason the IMs calculated from the output acceleration time history at each soil layer can only be compared to the peak shear strain output for the equivalent linear analyses. The comparisons to pore water pressure ratio are made in the nonlinear analyses.

The nonlinear analyses were performed using D-MOD2000 and PSNL. D-MOD2000 is a commercially available program distributed by GeoMotions, LLC. The interface allows the user to input each soil layer (up to 200 layers) and its corresponding properties, as well as select earthquake ground motions to apply to the soil profiles. Modulus reduction curves and damping curves can be specified, as well as other properties, for each soil type that are included in the soil profiles. The output of the program includes the acceleration time histories of each layer in the profile as well as maximum pore pressure ratios generated during the motion.

The PSNL is currently being developed by Dr. Steven Kramer at the University of Washington. It is currently an executable file and uses text files for input. It uses the same .EQ input motion files as ProSHAKE. In contrast to D-MOD2000, modulus reduction and damping curves are selected from a library of predefined soil types. One key difference between the ways each nonlinear program models liquefaction is that PSNL accounts for the increase in soil stiffness due to dilatancy at high strains after the onset of liquefaction. The PSNL outputs the acceleration time history as well as the effective overburden stress time history from which the maximum pore water pressure ratio can be calculated.

### 9.4.3 Intensity Measure Efficiency

For the results of the equivalent linear analyses in ProSHAKE, a simple correlation coefficient was taken using Microsoft Excel between each IM and the peak shear strain during the motion for each layer of the soil profile. The correlation was found between the natural logarithms of each set of data in an attempt to linearize the data. The correlation coefficients were plotted versus the depth of the midpoint of each layer for each IM up to a depth of 20 m. A depth of 20 m was used because below this depth the excess pore pressure generation was negligible in comparison with that generated above 20 m. The correlation coefficient shows the relative strength or weakness of the linear relationship each intensity measure shares with the peak shear strain. However, because not all intensity IMs share a linear relationship with pore pressure generation, another measure of the correlation was used for the more advanced nonlinear analyses.

In the case of the nonlinear analyses, a standard deviation of residuals was used to quantify the efficiency of each IM with respect to predicting pore pressure ratio. Standard deviations were calculated at three points in each soil profile; an upper, middle, and lower layer in the primary liquefiable region of the profile. For each IM, the values for each input motion were plotted against the corresponding values of pore pressure ratio. A Butterworth function of the form shown in Equation (9.16) was used to determine a best-fit nonlinear regression for each set of data at critical liquefying layers.

$$y = \frac{1}{\sqrt{1+(a/x)^b}} \tag{9.16}$$

The standard deviation was taken of the residuals (difference between experimental and predicted value of pore pressure ratio) for each data set. This value will be used to quantify the efficiency of each IM. Higher standard deviation values ($\sigma_{ru}$) represent a less efficient IM. This choice of measure of efficiency is comparable to the measures of predictability that have been specified in literature (and presented in Table 9.1). The standard deviation of the residuals is calculated using Equation (9.17); $N$ is the sample size, $\varepsilon_i$ is each value of the residual between the actual pore pressure value and the expected from the Butterworth function, and $\bar{\varepsilon}$ is the average of all the residuals.

$$\sigma_{ru} = \sqrt{\frac{1}{N}\sum_{i=1}^{N}(\varepsilon_i - \bar{\varepsilon})^2} \tag{9.17}$$

### 9.4.4 Total Uncertainty Index

In order to rank the IMs by their combined predictability and efficiency a new index called the Total Uncertainty Index (TUI) is used. The standard deviations of the predictability and efficiency of the IMs are combined using a standard deviation of sum of squares (SRSS) per Equation (9.18).

$$TUI = \sqrt{\sigma_{IM}^2 + \sigma_{r_u}^2} \tag{9.18}$$

The TUI is intended to be used as an index for the relative reliability of each IM with respect to the others for use in determining pore pressure. It does not have any real statistical meaning and as such should not be used in any calculations.

## 9.5 RESULTS

### 9.5.1 Equivalent Linear Analysis

Correlation coefficients between IMs and peak shear strain from the ProSHAKE analysis show the strengths of linear relationships with peak shear strain, see Figure 9.7, as a function of depth. From this data it is clear that among the six IMs, PGD has the weakest linear relationship with peak shear strain. There is little difference between correlations of the remaining intensity measures, especially at depths beyond 5 m. However, it appears that PGA, PGAM, and Arias Intensity share the best linear relationships with peak shear strain, which is known to be closely correlated with pore water pressure buildup. Initially PGV and CAV have lower coefficients than PGA, $PGA_M$, and $I_A$ until approximately 5 m, at which point all five converge to closer values and some correlation curves cross each other.

Because the Wildlife Site is well known and thoroughly investigated by previous researchers [Bennett et al. 1984; Zeghal and Elgamal 2007; Ziotopoulou 2010], its results were selected to illustrate results in the main body of this report. The order of correlation coefficients of the six IMs is consistent throughout all six soil profiles at shallow depths. The graphs of IM correlation with depth for all soil profiles can be found in Appendix B, Section 9.9. Because the correlation coefficient measures the strength of a linear relationship and nothing guarantees the linearity of relationships between the natural logarithms of the IMs and shear strain, the results of this equivalent linear analysis cannot completely describe the relationships being investigated. In addition the pore pressure cannot be determined using ProSHAKE. Finally, the relative order of the uncertainty for the IMs tends to change with depth, as indicated by some of the data shown in Figure 9.7 crossing each other at depths below 5 m. As previously noted, while shear strain is a good indicator of pore pressure, a direct comparison between the IMs and pore pressure is needed.

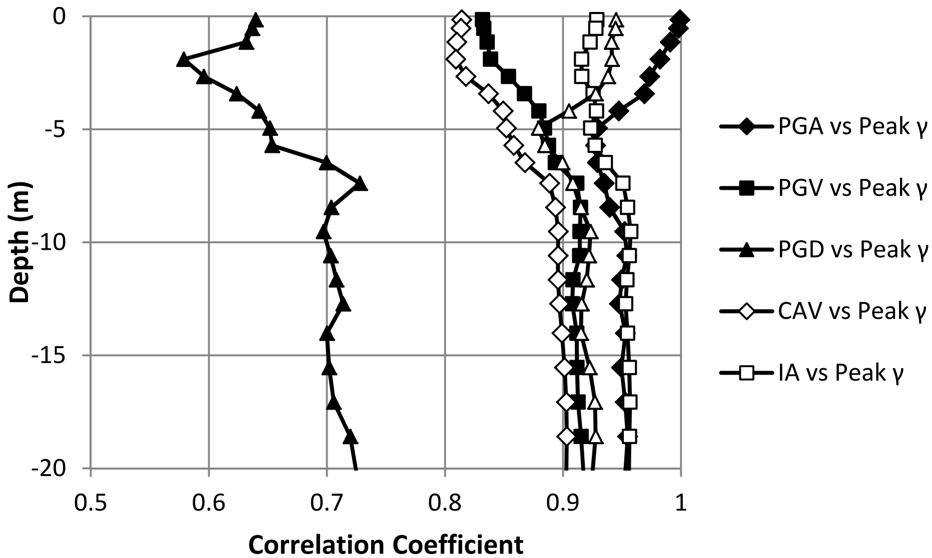


**Figure 9.7 Intensity measure correlations from equivalent linear analysis using ProSHAKE at the Wildlife Site.**

### 9.5.2 Nonlinear Analysis

For the nonlinear analyses, standard deviations of residuals were calculated based on regressions of plots between the IMs and pore pressure ratio using a Butterworth function. An iterative process was used to define the best fit Butterworth function by minimizing the standard deviation of residuals. Data points with pore pressure values less than 0.1 were eliminated unless that lowered the sample size an unreasonable amount. This was done to avoid the high uncertainty in low pore pressure predictions from contributing to the standard deviation [Kramer, personal communication]. These standard deviations served as index values for the relative efficiency of each IM in the prediction of pore pressure. An example of this curve-fitting process using PGA is shown below in Figure 9.8. Diamonds represent the data points from the nonlinear analyses and the red curve represents the predicted pore pressure ratio using the Butterworth function.

After calculating the efficiency of each IM at each layer of each profile for both nonlinear analysis programs, the results from PSNL and D-MOD2000 were compared. It was first observed that the results from both programs gave a different result in terms of the relative ranking of each of the six IMs. The standard deviations of residuals for the D-MOD2000 data were higher across the board than the values for the PSNL data. Standard deviations of the value of $\sigma_{ru}$ found for each layer were also calculated. Along with higher values overall, the standard deviations of efficiency also were much more variable for the D-MOD2000 data than those for the PSNL data. The standard deviations of $\sigma_{ru}$ for the D-MOD2000 data approached and sometimes exceeded twice that of those for the PSNL data. The difference likely results from the way each program models liquefaction.

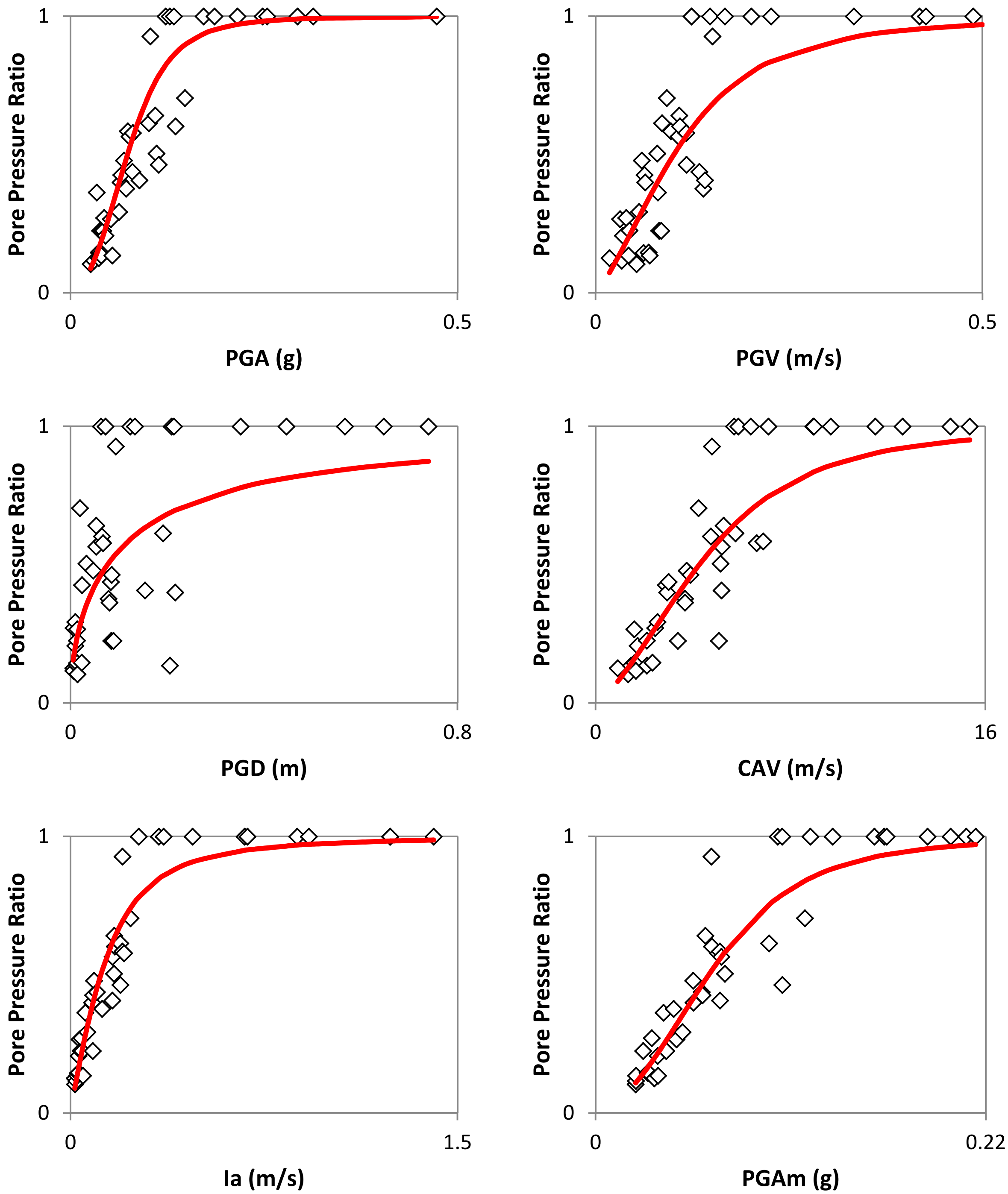


**Figure 9.8** **Example Butterworth function fits for the Wildlife Site (middle layer).**

Table 9.4 Comparison of results for D-MOD2000 and PSNL.

| | D-MOD2000 $\sigma_{ru}$ | | PSNL $\sigma_{ru}$ | |
|---|---|---|---|---|
| **IM** | **Average** | **Standard Deviation** | **Average** | **Standard Deviation** |
| PGA | 0.360 | 0.117 | 0.327 | 0.103 |
| PGV | 0.526 | 0.206 | 0.395 | 0.115 |
| PGD | 0.536 | 0.216 | 0.503 | 0.135 |
| CAV | 0.554 | 0.197 | 0.331 | 0.099 |
| Ia | 0.471 | 0.175 | 0.247 | 0.071 |
| PGAm | 0.408 | 0.164 | 0.272 | 0.091 |

Table 9.5 Standard deviation of efficiency for each profile from PSNL.

| IM | Heber Road A2 | Marine Lab B2 | Miller Farm | Treasure Island | Wildlife Site | Wynne Avenue | Global Average |
|---|---|---|---|---|---|---|---|
| PGA | 0.323 | 0.306 | 0.381 | 0.319 | 0.319 | 0.312 | 0.327 |
| PGV | 0.488 | 0.388 | 0.334 | 0.340 | 0.439 | 0.379 | 0.395 |
| PGD | 0.598 | 0.484 | 0.481 | 0.438 | 0.489 | 0.530 | 0.503 |
| CAV | 0.402 | 0.340 | 0.262 | 0.314 | 0.348 | 0.320 | 0.331 |
| Ia | 0.298 | 0.240 | 0.236 | 0.222 | 0.248 | 0.239 | 0.247 |
| PGAm | 0.282 | 0.173 | 0.330 | 0.260 | 0.279 | 0.308 | 0.272 |

Due to the large differences in results from the two programs, it would not be appropriate to combine the two data sets using an average or some other method. As such, the more consistent values from the PSNL analysis were selected for use in calculating the TUI. Table 9.4 compares the average values of $\sigma_{ru}$ as well as their standard deviations for each analysis program for comparison.

For the full set of standard deviation of efficiency results for PSNL and D-MOD2000, see Appendix C, Section 9.10. These tables contain the standard deviation of the residuals (efficiency) at each layer of each soil profile for each IM. The average and standard deviation of the three values are also included in each block. The standard deviations of efficiency from PSNL are presented for each soil profile along with the global average in Table 9.5. This table further illustrates the consistency of results from PSNL.

The standard deviations of efficiency from PSNL were combined with the standard deviations of predictability from literature using Equation (9.18) to generate the TUI for each IM. The TUI calculation is outlined in Table 9.6 showing both standard deviations and the resulting total uncertainty indices. The final results are graphically presented in Figure 9.9 with the IMs in order of ascending TUI. These results offer an index for the relative reliability of each IM.

**Table 9.6** **TUI calculation from standard deviations of predictability and efficiency.**

| IM | Predictive Uncertainty $\sigma_{IM}$ | Efficient Uncertainty $\sigma_{ru}$ | TUI |
|---|---|---|---|
| PGA | 0.526 | 0.327 | 0.619 |
| PGV | 0.525 | 0.395 | 0.657 |
| PGD | 0.825 | 0.503 | 0.966 |
| CAV | 0.420 | 0.331 | 0.535 |
| Ia | 0.870 | 0.247 | 0.904 |
| PGAm | 0.526 | 0.272 | 0.592 |

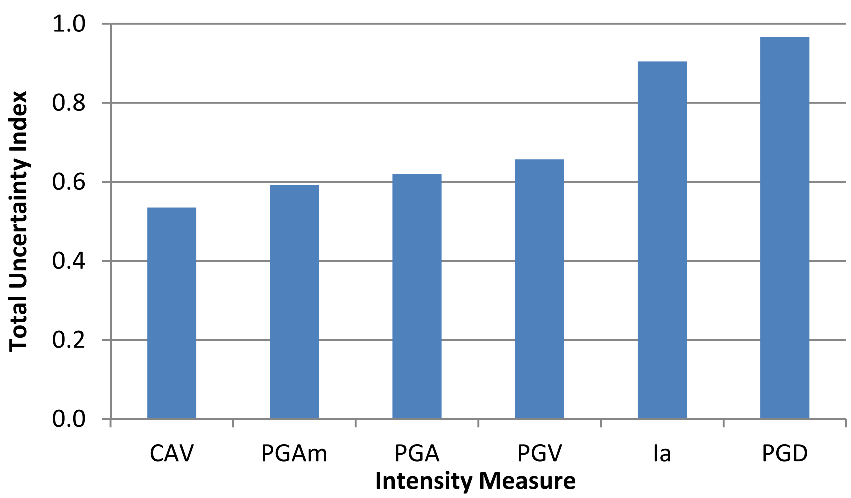


**Figure 9.9** **Total Uncertainty Indices of the six intensity measure**

These final results represent a measure of the total reliability, or combined efficiency and predictability, of each IM. Although CAV had only the fourth-best efficiency, its superior predictability made it the most reliable IM of the six. Conversely, the Arias Intensity was the most efficient IM, but its poor predictability made it the second-least reliable IM; $PGA_M$ scored slightly better than PGA. Although the two had the same predictability, the PSNL analyses revealed that the magnitude-corrected PGA had a greater efficiency in determining pore pressure. This demonstrates the power of the magnitude scaling factor in increasing the precision of PGA. Among the peak intensity values (PGA, PGV, PGD), PGA and $PGA_M$ performed best with PGD performing the worst of all six IMs.

## 9.6 CONCLUSIONS

This study investigated a variety of motions applied to a diverse set of soil profiles in order to provide insight into the relationships between different intensity measures (IMs) and the performance of a given soil deposit with respect to liquefaction. Specifically, the way each IM relates to peak shear strain and pore pressure generation was analyzed. The efficiency of each IM in determining the excess pore water pressure was investigated using two measures: the correlation coefficient and the standard deviation of residuals using a Butterworth function regression. The efficiency of each IM was then combined with the predictability of each IM found using empirical ground motion models to create a total uncertainty index, which was used to compare the reliability of six IMs for the purpose of liquefaction hazard evaluation.

It was determined that the correlation coefficient, which measures the strength of a linear relationship between two variables, was not an effective measure of the relationship between the IMs and strain, or with pore pressure. The relative order of coefficients for each IM changed with depth, inconsistently between different soil profiles. This was not the case for the standard deviation of residuals using a Butterworth function regression, which showed to be a higher quality measure of efficiency. The PSNL, a program in development, provided consistent results for each IM and pore pressure ratio.

The results of this experiment give a relative scale of the reliability, or combined predictability and efficiency, of six intensity measures for use in determining pore pressure ratio at a site. The initial efficiency of each IM showed strength in PGA and $I_A$. However, after adding the effects of predictability and calculating the TUI, CAV overcame all the five other IMs to be the most reliable of the six. Variations of CAV such as $CAV_5$ [Kramer and Mitchell 2006] have been introduced, whose reliabilities would also be interesting to determine. This study highlights the importance of using an intensity measure that is both predicable and efficient for liquefaction hazard analysis.

## 9.7 FUTURE WORK

Although a wide range of soil sites and earthquake motions were considered in this investigation, there are still many other combinations that can be tested to contribute to global uncertainties in efficiency of each IM. It would also be useful to explore whether there are site-specific factors that influence the total reliability of individual locations, or whether a global average is most appropriate. Because CAV was found to be the most reliable, further investigation into the reliability of $CAV_5$ would be useful. Finally, the determination of a more statistically significant measure of uncertainty than the TUI would allow application of these uncertainties in design using an appropriate factor of safety.

## ACKNOWLEDGMENTS

I would like to first thank Professor Steve Kramer and Sam Sideras, my faculty advisor and graduate mentor for my work this summer. They offered me guidance and their full attention whenever possible to help my personal learning process and the development of this project. Thanks to Heidi Tremayne for her work in organizing this internship program. This project would not have been possible without the generous funding of the National Science Foundation. Finally thank you to my fellow interns at the University of Washington, for striving and standing by my side this summer.

# REFERENCES


Bennett MJ, PV McLaughlin, JS Sarmiento, and TL Youd (1984). Geotechnical investigation of liquefaction sites, Imperial Valley, California. *USFS OFL 84–252.*

Campbell KW, and Y Bozorgnia (2008). NGA ground motion model for the geometric mean horizontal component of PGA, PGV, PGD and 5% damped linear elastic response spectra for periods ranging from 0.01 to 10 s, *Earthq. Spectra*, 24(1):139−171.

Campbell KW, and Y Bozorgnia (2010). A ground motion prediction equation for the horizontal component of cumulative absolute velocity (CAV) based on the PEER-NGA strong motion database, *Earthq. Spectra*, 26(3):635–650.

Çetin KÖ (2000). Rel*iability-Based Assessment of Seismic Soil Liquefaction Initiation Hazard*, PhD dissertation, Dept. of Civil and Enviro. Eng., University of California, Berkeley, California.

Dobry R, RS Ladd, FY Yokel, RM Chung, and D Powell (1982). Prediction of pore water pressure buildup and liquefaction of sands during earthquakes by the cyclic strain method, *National Bureau of Standards Building Science*, Series 138, Washington, D.C.

Idriss IM, and RW Boulanger (2004). Semi-empirical procedures for evaluating liquefaction potential during earthquakes, *Soil Dyn. Earthq. Eng.*, 26(2-4):115−130.

Kramer SL (1996). *Geotechnical Earthquake Engineering*, New Jersey: Prentice Hall.

Kramer SL, and RA Mitchell (2006). Ground motion intensity measures for liquefaction hazard analysis, *Earthq. Spectra*, 22(2):413–438.

Liao SSC, and V Whitman (1986). Catalogue of liquefaction and non-liquefaction occurrences during earthquakes, *Res. Rep.*, Dept. of Civ. Eng., Massachusetts Institute of Technology, Cambridge, MA.

Liu AH, JP Stewart, NA Abrahamson, and Y Moriwaki (2001). Equivalent number of uniform stress cycles for soil liquefaction analysis, ASCE, *J. Geotech. Eng.*, 127(12):1017−1026.

Mayfield RT (2007). *The Return Period of Soil Liquefaction*., PhD dissertation, Dept. of Civil and Enviro. Eng., University of Washington, Seattle, Washington.

Seed HB, and IM Idriss (1971). Simplified procedure for evaluating soil liquefaction potential, ASCE, *J. Geotech. Eng.,* 97(9):1249−1273

Sideras SS (2011). *Response of Liquefiable Soil Deposits to Earthquake Loading*, Master's Thesis, Dept. of Civil and Enviro. Eng., University of Washington, Seattle, WA.

Travasarou T, JD Bray, and NA Abrahamson (2003). Empirical attenuation relationship for Arias Intensity, *Earthq. Eng. Struct. Dyn.*, 32:1133−1155.

Youd TL et al. (2001). Liquefaction resistance of soils: summary report from the 1996 NCEER and 1998 NCEER/NSF workshops on evaluation of liquefaction resistance of soils, ASCE, *J. Geotech. Eng.*, 127(10):817–833.

Zeghal M, and A. Algamal (1994). Analysis of soil liquefaction using earthquake records, ASCE, *J. Geotech. Eng.*, 127(10): 996−1017.

Ziotopoulou K (2010). *Evaluating Model Uncertainty against Strong Motion Records at Liquefiable Sites*, Master's Thesis, Dept. of Civil and Enviro. Eng., University of California, Davis, CA.

## 9.8 APPENDIX A: SELECTED EARTHQUAKE MOTIONS

| Bin | Record Sequence Number | Earthquake Name | YEAR | Station Name | Mw | Joyner-Boore Dist. (km) | Preferred Vs30 (m/s) |
|---|---|---|---|---|---|---|---|
| 1 | 2622 | Chi-Chi, Taiwan-03 | 1999 | TCU071 | 6.20 | 15.04 | 624.9 |
| 1 | 265 | Victoria, Mexico | 1980 | Cerro Prieto | 6.33 | 13.80 | 659.6 |
| 1 | 296 | Irpinia, Italy-02 | 1980 | Bagnoli Irpinio | 6.20 | 17.79 | 1000.0 |
| 1 | 297 | Irpinia, Italy-02 | 1980 | Bisaccia | 6.20 | 14.73 | 1000.0 |
| 1 | 455 | Morgan Hill | 1984 | Gilroy Array #1 | 6.19 | 14.90 | 1428.0 |
| 2 | 2427 | Chi-Chi, Taiwan-02 | 1999 | TCU138 | 5.90 | 36.72 | 652.9 |
| 2 | 295 | Irpinia, Italy-02 | 1980 | Auletta | 6.20 | 28.69 | 1000.0 |
| 2 | 303 | Irpinia, Italy-02 | 1980 | Sturno | 6.20 | 20.38 | 1000.0 |
| 2 | 3472 | Chi-Chi, Taiwan-06 | 1999 | TCU076 | 6.30 | 23.84 | 615.0 |
| 2 | 3507 | Chi-Chi, Taiwan-06 | 1999 | TCU129 | 6.30 | 22.69 | 664.4 |
| 3 | 2601 | Chi-Chi, Taiwan-03 | 1999 | TCU045 | 6.20 | 76.90 | 704.6 |
| 3 | 3202 | Chi-Chi, Taiwan-05 | 1999 | TCU102 | 6.20 | 49.66 | 714.3 |
| 3 | 476 | Morgan Hill | 1984 | UCSC Lick Observatory | 6.19 | 45.47 | 714.0 |
| 3 | 525 | N. Palm Springs | 1986 | Lake Mathews Dike Toe | 6.06 | 66.59 | 684.9 |
| 3 | 657 | Whittier Narrows-01 | 1987 | Malibu - Las Flores Canyon | 5.99 | 46.43 | 622.9 |
| 4 | 289 | Irpinia, Italy-01 | 1980 | Calitri | 6.90 | 13.34 | 600.0 |
| 4 | 71 | San Fernando | 1971 | Lake Hughes #12 | 6.61 | 13.99 | 602.1 |
| 4 | 801 | Loma Prieta | 1989 | San Jose - Santa Teresa Hills | 6.93 | 14.18 | 671.8 |
| 4 | 809 | Loma Prieta | 1989 | UCSC | 6.93 | 12.15 | 714.0 |
| 4 | 957 | Northridge-01 | 1994 | Burbank - Howard Rd. | 6.69 | 15.87 | 821.7 |
| 5 | 1023 | Northridge-01 | 1994 | Lake Hughes #9 | 6.69 | 24.86 | 670.8 |
| 5 | 1091 | Northridge-01 | 1994 | Vasquez Rocks Park | 6.69 | 23.10 | 996.4 |
| 5 | 63 | San Fernando | 1971 | Fairmont Dam | 6.61 | 25.58 | 684.9 |
| 5 | 782 | Loma Prieta | 1989 | Monterey City Hall | 6.93 | 39.69 | 684.9 |
| 5 | 791 | Loma Prieta | 1989 | SAGO South - Surface | 6.93 | 33.94 | 684.9 |
| 6 | 1074 | Northridge-01 | 1994 | Sandberg - Bald Mtn | 6.69 | 41.26 | 821.7 |
| 6 | 1096 | Northridge-01 | 1994 | Wrightwood - Jackson Flat | 6.69 | 64.46 | 821.7 |
| 6 | 1795 | Hector Mine | 1999 | Joshua Tree N.M. - Keys View | 7.13 | 50.42 | 684.9 |
| 6 | 283 | Irpinia, Italy-01 | 1980 | Arienzo | 6.90 | 52.93 | 1000.0 |
| 6 | 946 | Northridge-01 | 1994 | Antelope Buttes | 6.69 | 46.65 | 821.7 |
| 7 | 1148 | Kocaeli, Turkey | 1999 | Arcelik | 7.51 | 10.56 | 523.0 |
| 7 | 1198 | Chi-Chi, Taiwan | 1999 | CHY029 | 7.62 | 10.97 | 544.7 |
| 7 | 1482 | Chi-Chi, Taiwan | 1999 | TCU039 | 7.62 | 19.90 | 540.7 |
| 7 | 1541 | Chi-Chi, Taiwan | 1999 | TCU116 | 7.62 | 12.40 | 493.1 |
| 7 | 1548 | Chi-Chi, Taiwan | 1999 | TCU128 | 7.62 | 13.15 | 599.6 |
| 8 | 1234 | Chi-Chi, Taiwan | 1999 | CHY086 | 7.62 | 27.57 | 553.4 |
| 8 | 1245 | Chi-Chi, Taiwan | 1999 | CHY102 | 7.62 | 36.06 | 553.4 |
| 8 | 1350 | Chi-Chi, Taiwan | 1999 | ILA067 | 7.62 | 33.28 | 553.4 |
| 8 | 1594 | Chi-Chi, Taiwan | 1999 | TTN051 | 7.62 | 30.77 | 553.4 |
| 8 | 1626 | Sitka, Alaska | 1972 | Sitka Observatory | 7.68 | 34.61 | 659.6 |
| 9 | 1154 | Kocaeli, Turkey | 1999 | Bursa Sivil | 7.51 | 65.53 | 659.6 |
| 9 | 1169 | Kocaeli, Turkey | 1999 | Maslak | 7.51 | 52.96 | 659.6 |
| 9 | 1523 | Chi-Chi, Taiwan | 1999 | TCU094 | 7.62 | 54.50 | 589.9 |
| 9 | 2107 | Denali, Alaska | 2002 | Carlo (temp) | 7.90 | 49.94 | 963.9 |
| 9 | 2111 | Denali, Alaska | 2002 | R109 (temp) | 7.90 | 42.99 | 963.9 |

## 9.9 APPENDIX B: CORRELATION COEFFICIENT CHARTS

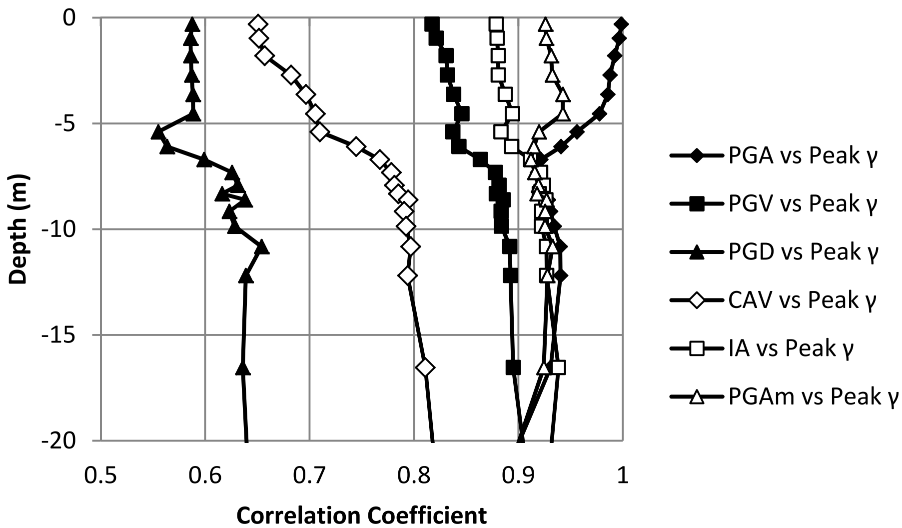


**Figure B.1 Heber Road A2.**

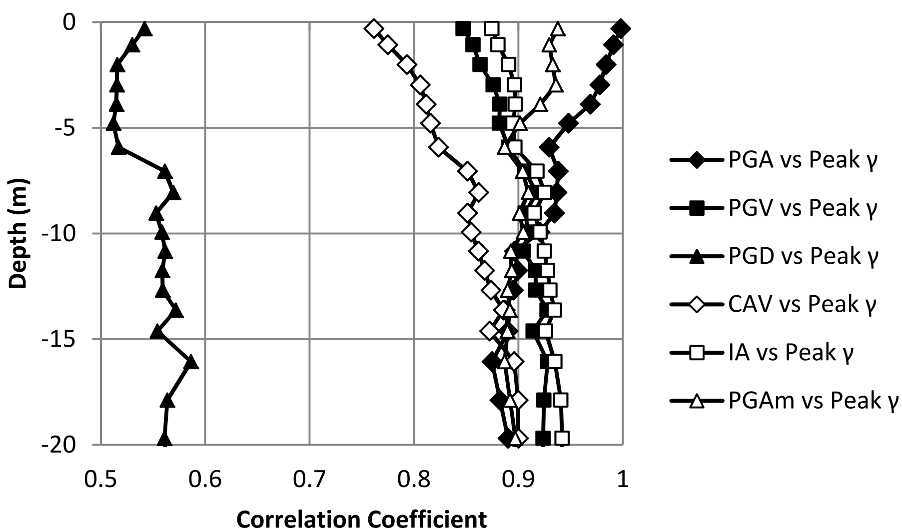


**Figure B.2 Marine Lab B2.**

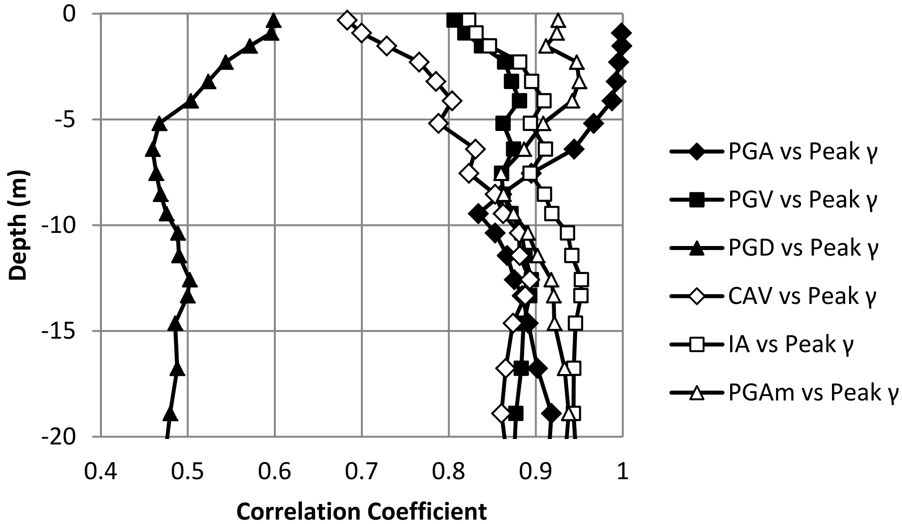


**Figure B.4 Miller Farm.**

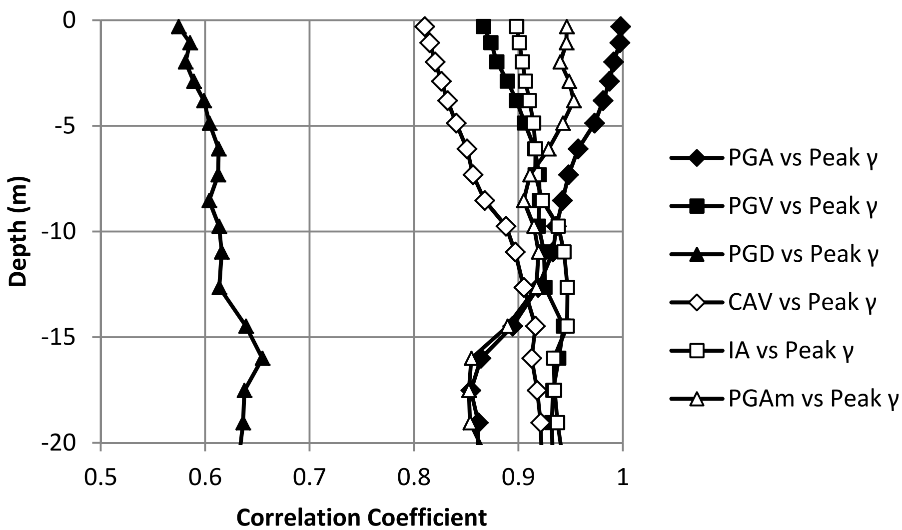


**Figure B.5 Treasure Island.**

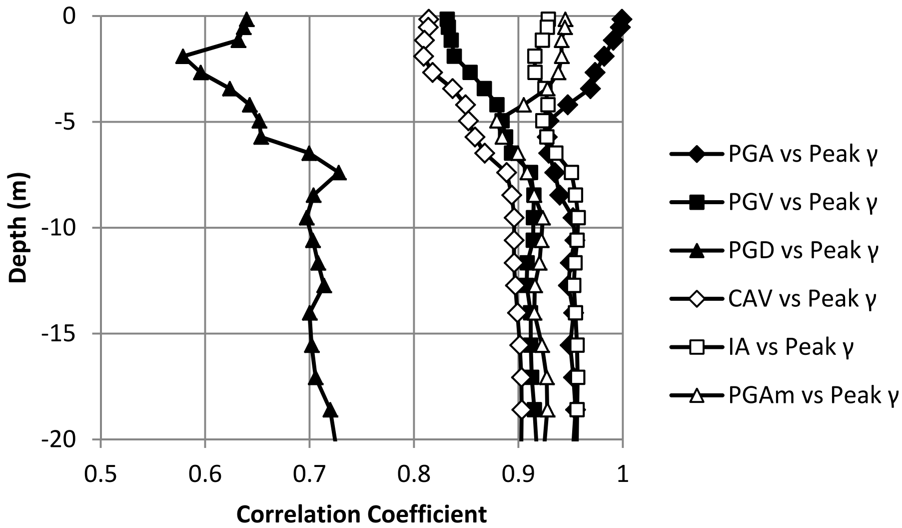


**Figure B.6 Wildlife Site.**

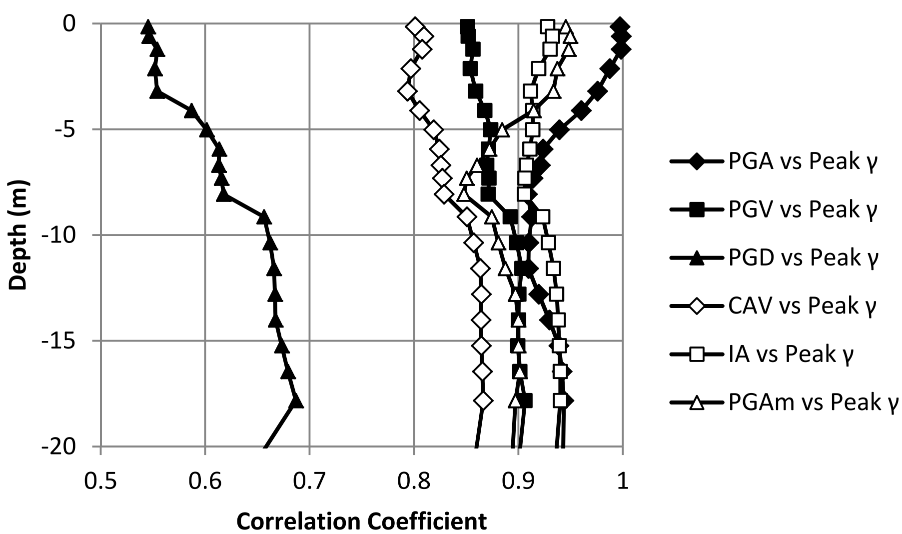


**Figure B.7 Wynne Avenue.**

## 9.10 APPENDIX C: STANDARD DEVIATIONS OF EFFICIENCY

**PSNL**

| IM | Layer | Heber Road A2 | | Marine Lab B2 | | Miller Farm | | Treasure Island | | Wildlife Site | | Wynne Avenue | | Global |
|---|---|---|---|---|---|---|---|---|---|---|---|---|---|---|
| PGA | Upper | 0.442 | μ=0.323 | 0.267 | μ=0.306 | 0.370 | μ=0.381 | 0.247 | μ=0.319 | 0.370 | μ=0.319 | 0.367 | μ=0.312 | μ=0.327 |
| | Middle | 0.205 | | 0.372 | | 0.466 | | 0.357 | | 0.286 | | 0.202 | | |
| | Lower | 0.321 | σ=0.119 | 0.280 | σ=0.057 | 0.307 | σ=0.080 | 0.352 | σ=0.063 | 0.301 | σ=0.045 | 0.368 | σ=0.095 | σ=0.103 |
| PGV | Upper | 0.562 | μ=0.488 | 0.361 | μ=0.388 | 0.391 | μ=0.334 | 0.295 | μ=0.340 | 0.436 | μ=0.439 | 0.434 | μ=0.379 | μ=0.395 |
| | Middle | 0.505 | | 0.398 | | 0.346 | | 0.391 | | 0.427 | | 0.300 | | |
| | Lower | 0.397 | σ=0.084 | 0.406 | σ=0.024 | 0.265 | σ=0.064 | 0.334 | σ=0.048 | 0.454 | σ=0.014 | 0.405 | σ=0.070 | σ=0.115 |
| PGD | Upper | 0.657 | μ=0.598 | 0.441 | μ=0.484 | 0.528 | μ=0.481 | 0.328 | μ=0.438 | 0.467 | μ=0.489 | 0.537 | μ=0.530 | μ=0.503 |
| | Middle | 0.624 | | 0.482 | | 0.438 | | 0.502 | | 0.519 | | 0.483 | | |
| | Lower | 0.513 | σ=0.076 | 0.529 | σ=0.044 | 0.479 | σ=0.045 | 0.484 | σ=0.096 | 0.480 | σ=0.027 | 0.570 | σ=0.044 | σ=0.135 |
| CAV | Upper | 0.507 | μ=0.402 | 0.325 | μ=0.340 | 0.296 | μ=0.262 | 0.358 | μ=0.314 | 0.406 | μ=0.348 | 0.352 | μ=0.320 | μ=0.331 |
| | Middle | 0.389 | | 0.356 | | 0.229 | | 0.349 | | 0.317 | | 0.284 | | |
| | Lower | 0.309 | σ=0.100 | 0.341 | σ=0.016 | 0.260 | σ=0.033 | 0.234 | σ=0.069 | 0.323 | σ=0.050 | 0.325 | σ=0.034 | σ=0.099 |
| Ia | Upper | 0.376 | μ=0.298 | 0.243 | μ=0.240 | 0.194 | μ=0.236 | 0.226 | μ=0.222 | 0.301 | μ=0.248 | 0.269 | μ=0.239 | μ=0.247 |
| | Middle | 0.286 | | 0.244 | | 0.229 | | 0.246 | | 0.219 | | 0.194 | | |
| | Lower | 0.232 | σ=0.073 | 0.231 | σ=0.007 | 0.285 | σ=0.046 | 0.192 | σ=0.027 | 0.224 | σ=0.046 | 0.254 | σ=0.040 | σ=0.071 |
| PGAm | Upper | 0.332 | μ=0.282 | 0.137 | μ=0.173 | 0.294 | μ=0.330 | 0.189 | μ=0.260 | 0.300 | μ=0.279 | 0.360 | μ=0.308 | μ=0.272 |
| | Middle | 0.284 | | 0.177 | | 0.363 | | 0.276 | | 0.239 | | 0.217 | | |
| | Lower | 0.231 | σ=0.051 | 0.205 | σ=0.034 | 0.332 | σ=0.035 | 0.315 | σ=0.065 | 0.298 | σ=0.035 | 0.347 | σ=0.079 | σ=0.091 |

## D-MOD2000

| IM | Layer | Heber Road A2 | | Marine Lab B2 | | Miller Farm | | Treasure Island | | Wildlife Site | | Wynne Avenue | | Global |
|---|---|---|---|---|---|---|---|---|---|---|---|---|---|---|
| PGA | Upper | 0.459 | μ=0.421 | 0.481 | μ=0.417 | 0.386 | μ=0.358 | 0.427 | μ=0.213 | 0.326 | μ=0.414 | 0.274 | μ=0.334 | μ=0.360 |
| | Middle | 0.390 | | 0.451 | | 0.321 | | 0.086 | | 0.351 | | 0.307 | | |
| | Lower | 0.413 | σ=0.035 | 0.320 | σ=0.086 | 0.368 | σ=0.033 | 0.125 | σ=0.187 | 0.566 | σ=0.132 | 0.421 | σ=0.077 | σ=0.117 |
| PGV | Upper | 0.841 | μ=0.817 | 0.734 | μ=0.668 | 0.591 | μ=0.535 | 0.417 | μ=0.252 | 0.425 | μ=0.421 | 0.424 | μ=0.463 | μ=0.526 |
| | Middle | 0.810 | | 0.544 | | 0.338 | | 0.099 | | 0.433 | | 0.456 | | |
| | Lower | 0.799 | σ=0.022 | 0.725 | σ=0.107 | 0.675 | σ=0.176 | 0.239 | σ=0.159 | 0.405 | σ=0.015 | 0.509 | σ=0.043 | σ=0.206 |
| PGD | Upper | 0.876 | μ=0.847 | 0.782 | μ=0.669 | 0.537 | μ=0.510 | 0.448 | μ=0.269 | 0.396 | μ=0.453 | 0.433 | μ=0.470 | μ=0.536 |
| | Middle | 0.860 | | 0.456 | | 0.334 | | 0.100 | | 0.509 | | 0.458 | | |
| | Lower | 0.806 | σ=0.037 | 0.768 | σ=0.184 | 0.660 | σ=0.164 | 0.257 | σ=0.174 | 0.455 | σ=0.057 | 0.519 | σ=0.045 | σ=0.216 |
| CAV | Upper | 0.793 | μ=0.807 | 0.761 | μ=0.698 | 0.616 | μ=0.524 | 0.455 | μ=0.271 | 0.455 | μ=0.529 | 0.439 | μ=0.495 | μ=0.554 |
| | Middle | 0.818 | | 0.579 | | 0.340 | | 0.099 | | 0.585 | | 0.484 | | |
| | Lower | 0.810 | σ=0.013 | 0.753 | σ=0.103 | 0.615 | σ=0.159 | 0.259 | σ=0.178 | 0.549 | σ=0.067 | 0.563 | σ=0.063 | σ=0.197 |
| Ia | Upper | 0.737 | μ=0.704 | 0.695 | μ=0.594 | 0.591 | μ=0.430 | 0.439 | μ=0.244 | 0.406 | μ=0.413 | 0.398 | μ=0.441 | μ=0.471 |
| | Middle | 0.689 | | 0.471 | | 0.332 | | 0.098 | | 0.445 | | 0.416 | | |
| | Lower | 0.685 | σ=0.029 | 0.616 | σ=0.113 | 0.366 | σ=0.141 | 0.195 | σ=0.175 | 0.388 | σ=0.029 | 0.509 | σ=0.060 | σ=0.175 |
| PGAm | Upper | 0.628 | μ=0.623 | 0.595 | μ=0.491 | 0.398 | μ=0.312 | 0.417 | μ=0.233 | 0.327 | μ=0.431 | 0.259 | μ=0.358 | μ=0.408 |
| | Middle | 0.575 | | 0.427 | | 0.153 | | 0.095 | | 0.408 | | 0.325 | | |
| | Lower | 0.665 | σ=0.045 | 0.452 | σ=0.091 | 0.384 | σ=0.137 | 0.186 | σ=0.166 | 0.559 | σ=0.118 | 0.491 | σ=0.119 | σ=0.164 |

# 10. Stainless Steel Reinforcement in Unbonded, Pre-Tensioned Bridge Bent System

## CARLOS ESPARZA

### ABSTRACT

At the University of Washington, high-performance materials will be used in a bridge-bent system to improve seismic performance, durability, and sustainability. One of these materials includes stainless steel longitudinal reinforcement. The physical properties of stainless steel compared to carbon steel are needed to evaluate whether the higher costs associated with using stainless steel for reinforcement are justified. The study concentrated on two types of steel: 2205 Duplex stainless steel and A706 G60 carbon steel. Monotonic and low-cycle fatigue testing were planned to obtain typical tension test properties, such as modulus of elasticity, yield strength, and ultimate strength, as well as cyclic-test properties, such as fatigue life. A buckling-restrained-brace (BRB) system that can be used in columns was also designed in hopes of improving low-cycle fatigue performance. Monotonic tests were conducted but no conclusive data was obtained due to errors in experimental procedures. Low-cycle fatigue tests were not conducted. Issues with time and equipment resulted in no data being obtained. The bar designed for BRB testing was not possible to machine, according to various machine shops, leading the BRB tests to be put on hold until alternate systems are designed. Future recommendations for these tests were obtained as a result of all the problems encountered throughout the summer. These recommendations include: using a different strain/displacement reader for low-cycle fatigue tests, using different equipment to automate strain limits applied to specimens, and creating a new BRB system that can be easily constructed.

### 10.1 INTRODUCTION

Research at the University of Washington is being conducted to address three key aspects of reinforced concrete bridge design for seismic regions. These aspects include seismic damage resiliency, speed of construction, and extended bridge life span. Reinforced concrete bridge columns undergo structural damage and residual displacements after a seismic event that lead to bridge closure for inspections and repairs. By making the system more resilient to the seismic damage, the economic and social costs associated with these bridge closures can be minimized. Economic and environmental costs associated with traffic delays caused by slow construction of the bridge structure can be decreased by using pre-cast concrete members in lieu of cast-in-place concrete. Finally, in order for a bridge to be economical and sustainable, its life span must be extended.

A new bridge system is being developed to address these three areas by implementing four new strategies. Unbonded, pre-tensioned strands in the columns will be used to provide an elastic re-centering force, which will decrease residual displacements. Precast columns and beams will accelerate construction and provide high quality, more durable members due to strict quality control in place at precast plants. Socket column-to-footing connections developed at the University of Washington accelerate on-site construction processes. Finally, high-performance materials such as hybrid reinforced concrete, epoxy coated pre-stressing strands, and stainless steel bar reinforcement improves seismic performance, durability, and sustainability. A detailed analysis of stainless steel bar reinforcement and its effect on the new bridge bent system was conducted at the University of Washington this summer and is presented in the following report.

## 10.2 BACKGROUND

Three of the four strategies have already been tested successfully in scaled-size models (42%) of the bridge bent system. Unbonded, pre-tensioned strands in columns have been shown to provide a re-centering force that returned the column to 1% of original vertical position up to 10% drift [Davis et al. 2011]. A simple column-to-footing socket connection was capable of resisting large, inelastic moment reversals that occur in the plastic hinge region in columns subjected to seismic loads [Haraldsson et al. 2011]. The RC version of the socket connection has been implemented in the field during the construction of US 12 over I-5. Although the previously tested specimens were able to re-center after going to 10% drift, the columns experienced bar buckling, bar fracture, and concrete spalling at much lower drift ratios than in the RC system [Davis et al. 2011]. The bar buckling, concrete buckling, and concrete fracture in a test specimen is shown in Figure 10.1.

**Figure 10.1 Failure initiated by bar buckling and bar fracture [Davis et al. 2011].**

The use of high-performance materials, specifically Hybrid-Fiber reinforced concrete, can help delay these failures and make the system more ductile. The use of epoxy-coated strands will be used to increase bond strength and durability. Finally, another high-performance material that will help the overall performance of the system is stainless steel reinforcement. In place of black steel used in previous systems, stainless steel will be used as longitudinal reinforcement. Stainless steel has greater energy dissipation and ductility than its carbon steel counterpart. Its chemical composition also makes it more resistant to corrosion, promoting durability. Two 42% scale columns will be tested at the University of Washington to test the performance of high-performance materials, as seen in Figure 10.2. A thorough investigation on the properties of stainless steel bar reinforcement was done to ensure the added cost of this high-performance material is justified.

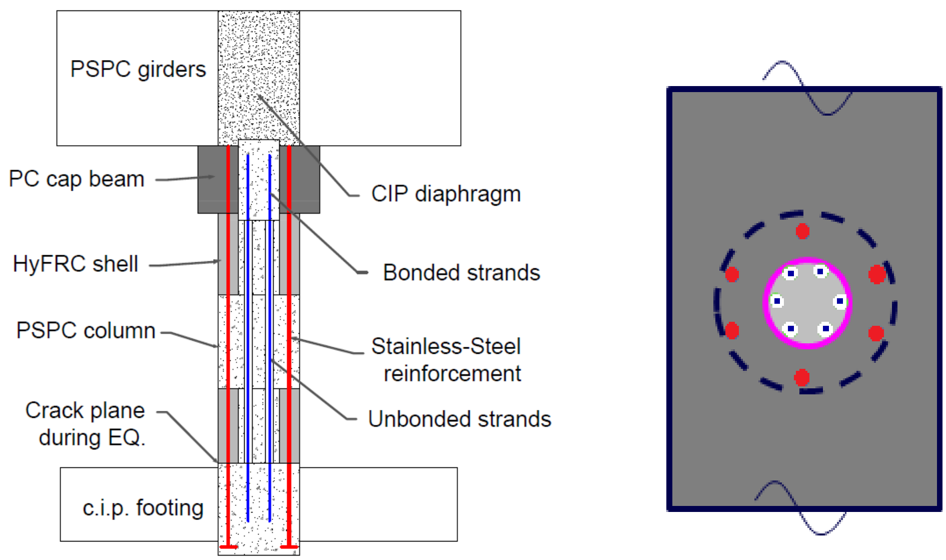


**Figure 10.2 Proposed Bridge Bent System.**

### 10.2.1 Grades of Stainless Steel Reinforcement

Three different grades of stainless steel rebar (2205 Duplex, 316 LN, and EnduraMet 32) are typically used in the industry. Salit Specialty Rebar recommends the use of 2205 Duplex (UNS# S31803) to obtain the twin objectives of cost saving and the best protection against corrosion. It is also the most easily available in a variety of sizes. Table 10.1 shows the chemical makeup of a few commonly used stainless steel alloys [ASTM 2004].

Although ASTM A955 classifies stainless steel as an alloy with a minimum of 11% chromium, typical stainless steel used in the industry has chromium levels in the 20% range [ASTM 2004]. Higher chromium percentages in stainless steel help with corrosion issues but also make the rebar more expensive.

**Table 10.1 Chemical composition of stainless steel alloys [ASTM 2004].**

| Alloy | C | P | Si | Ni | Mo | Mn | S | Cr | N |
|---|---|---|---|---|---|---|---|---|---|
| Type 304LN | 0.030 | 0.045 | 1.00 | 8.0-11.0 | | 2.00 | 0.030 | 18.0-20.0 | 0.10-0.16 |
| Type 316LN | 0.030 | 0.045 | 1.00 | 10.0-13.0 | 2.00-3.00 | 2.00 | 0.030 | 16.0-18.0 | 0.10-0.16 |
| Alloy 2205 | 0.030 | 0.030 | 1.00 | 4.5-6.5 | 2.5-3.5 | 2.00 | 0.020 | 21.0-23.0 | 0.08-0.20 |
| EnduraMet 33 | 0.08 | 0.060 | 1.00 | 2.3-3.7 | | 11.5-14.5 | 0.030 | 17.0-19.0 | 0.20-0.40 |
| EnduraMet 32 | 0.15 | 0.045 | 1.00 | 0.50–2.50 | | 11.0-14.5 | 0.030 | 16.5-19.0 | 0.20-0.45 |

### 10.2.2 Corrosion

Durability of new structures is key when addressing the issue of sustainability. Corrosion in steel reinforcement contributes to premature failure of highway bridge decks, columns, and superstructures. Corrosion is caused by either chloride attack from deicing salts and weather or carbonation of concrete due to carbonic acid from carbon dioxide [Zhou et al. 2010]. Stainless steel reinforcement has superior corrosion resistance compared to carbon steel and surface treated steel such as epoxy coated reinforcement, stainless clad rebar, and galvanized rebar [Schnell and Bergmann 2007].

### 10.2.3 Mechanical Properties

Although corrosion protection is important in any reinforced concrete member, the mechanical properties are of more importance in the bridge bent system proposed by the University of Washington. Stainless steel is being used mainly to provide greater energy dissipation and ductility to the system. Monotonic and low-cycle fatigue tests have been conducted on various stainless steel alloys to see how their mechanical properties compare with black steel.

The University of Buffalo conducted tests on three different types of stainless steel rebar alloys (316 LN, 2205 Duplex and EnduraMet 32) and compared the results with A706 carbon steel and MMFX II [Zhou et al. 2008]. Monotonic test results show that all three stainless steel rebar's had higher Young's modulus, higher ultimate strengths, and elongated to a higher percent. Therefore, the stainless steel reinforcement tested was more ductile than the carbon steel under identical tests. More ductility results in greater energy dissipation needed in areas with seismic activity. Table 10.2 summarizes the monotonic test results.

Fatigue loading tests with constant strain amplitude were also conducted to investigate the low-cycle fatigue behavior of the five different steels. Constant strain amplitude was limited to avoid buckling of the specimens. Results show that in the large plastic strain amplitude region, the three stainless steel rebar's had higher fatigue lives than carbon steel [Zhou et al. 2008]. Under cyclic loading, stainless steel rebar reinforcement will perform better than carbon steel.

**Table 10.2 University of Buffalo monotonic test results [Zhou et al. 2008].**

| | E (ksi) | Specified $\sigma_y$ (ksi) | Actual $\sigma_{y1}$ (ksi) | Actual $\sigma_{y2}$ (ksi) | Actual $\sigma_u$ (ksi) | $\frac{\sigma_u}{\sigma_{y2}}$ | Elongation (%) |
|---|---|---|---|---|---|---|---|
| **Enduramet 32** | 29848 | 75 | 84.17 | 83.52 | 136.25 | 1.63 | 58.66 |
| **316LN** | 28981 | 75 | 77.14 | 77.75 | 116.34 | 1.50 | 52.82 |
| **2205 Duplex** | 27705 | 75 | 94.06 | 96.97 | 130.53 | 1.35 | 38.74 |
| **A706 G60** | 30244 | 60 | 73.67 | 72.59 | 106.02 | 1.46 | 26.5 |
| **MMFX II** | 31533 | 100 | 137.88 | 100.73 | 179.43 | 1.78 | 17.51 |

$\sigma_{y1}$ is determined by 0.2% offset method according to ASTM E 8 (ASTM, 2004).

$\sigma_{y2}$ is defined as the stress corresponding to a strain of 0.35 percent (ACI 318-05, 2005).

### 10.2.4 Strength Degradation and Energy Dissipation

Zhang et al. [2011] investigated the difference in strength degradation and energy dissipation between three specimens with ribbed stainless steel and one with ribbed carbon steel. The chemical makeup of 1.4362 duplex stainless steel rebar used in the tests closely resembles the 2205 duplex alloy that will be used in the unbonded, pre-stressed bridge bent system being constructed at the University of Washington. Tests performed by Zhang et al. [2011] show that reinforced concrete columns with stainless steel rebar damaged to a lesser extent than those with carbon steel. The columns with stainless steel reinforcement also showed good ductility and greater energy dissipation and bearing capacity than carbon steel reinforced columns.

### 10.2.5 Buckling-Restrained-Brace

In typical steel braced-frame buildings, buckling-restrained-braces are used to take full advantage of the compressive strength of steel. A sleeve that can be made of steel, concrete or a composite material encases a steel core that supports lateral forces. The steel core and sleeve are de-bonded to ensure the steel core resists only axial stresses while the sleeve resists flexural buckling stresses [Sabelli et al. 2003]. The slender core can develop high compressive stresses without failing due to buckling. The major components of a typical buckling-restrained-brace (BRB) are show in Figure 10.3.

This system can achieve high ductility and energy dissipation. The benefits of buckling-restrained-braces gained in steel structures would also increase the performance of concrete columns subjected to seismic loads. Prevention of bar buckling, increased ductility, and better energy dissipation are properties that are wanted in the bridge bent system being developed. If the same system that is used in steel frames can be modified and used in the columns being tested, the entire system would perform better under cyclic loading.

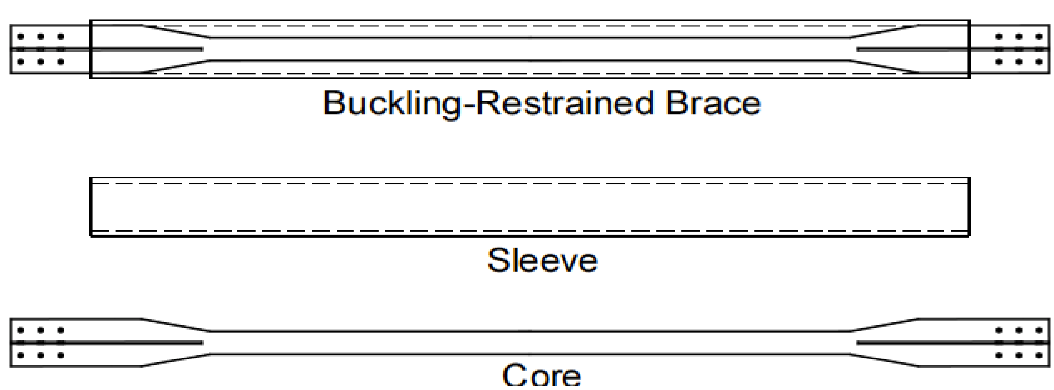


**Figure 10.3 BRB Components [Sabelli et al. 2003].**

## 10.3 BAR TYPES AND CONFIGURATIONS CONSIDERED

Monotonic tension and low-cycle fatigue tests were performed to investigate the properties of stainless steel reinforcement and compare them with carbon reinforcement that is typically used. The following section details the types of bars that were tested and their configurations.

### 10.3.1 Stainless Steel Bars

The use of stainless steel reinforcement in columns subjected to high seismic activity requires an investigation on the properties of stainless steel. After discussions with rebar providers, it was determined that 2205 Duplex stainless steel is the most widely available in many sizes. Although No. 4 rebar will be used in the scaled models, larger sizes must be used in real-world applications. For this reason, a stainless steel alloy that is available in many sizes was required and 2205 Duplex was chosen. Of the two columns being tested, one will use regular A706 G60 carbon steel and the other 2205 Duplex stainless steel. The monotonic and low-cycle fatigue tests conducted were focused on these two rebar types. The University of Buffalo conducted monotonic cyclic tests on stainless steel rebar to obtain tension test and low-cycle fatigue properties of various common carbon and stainless steel alloys, including 2205 Duplex and A706 G60. For monotonic tests, the University of Buffalo followed ASTM E8 [ASTM 2004] specifications for coupon dimensions, shown in Figure 10.4.

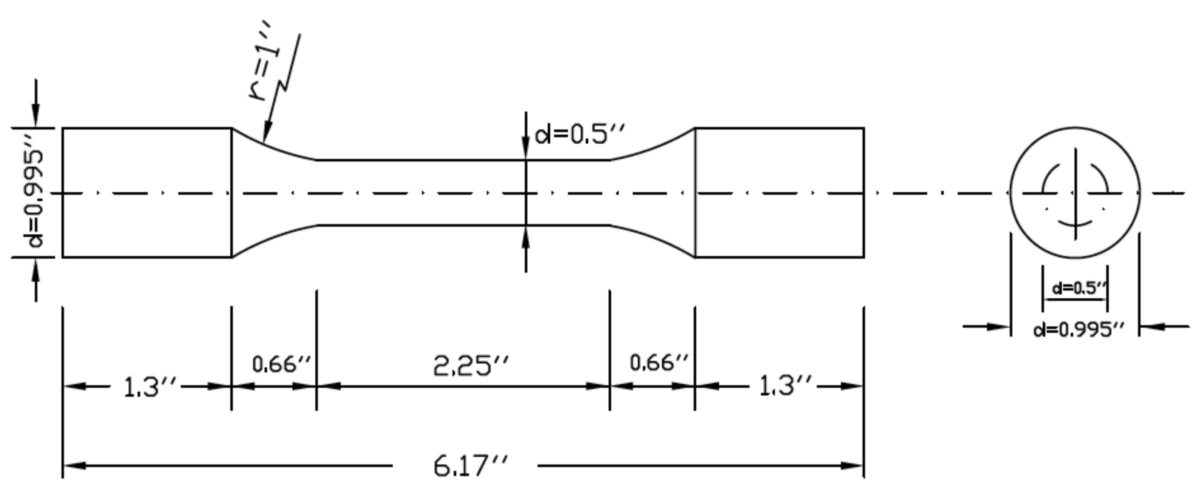


**Figure 10.4 University of Buffalo monotonic test coupons [Zhou et al. 2008].**

For testing conducted at the University of Washington, a different approach was taken. The No. 4 rebar being used was not machined. Instead, a 24-in.-long piece of rebar was cut. It was divided into 3 parts, each 8 in. long. The middle portion was used as the gauge length, as required by ASTM, and the outer portions were used to grip the specimen in the tension machine. Longer grip lengths ensured no slipping occurred during tension tests.

Low-cycle fatigue tests were also conducted at the University of Buffalo for 2205 Duplex stainless steel and A707 G60 carbon steel. These tests were performed using coupons with dimensions designed according to ASTM E606 [ASTM 2004]. Coupons used for testing at Buffalo were machined from No. 8 bars. In order to compare results to previous research done at the University of Buffalo, specimens were machined to identical proportions. The rebar being tested in this stainless steel study is from the same batch that will be used for columns being constructed to test high-performance material at the University of Washington. All bars used for these columns were No. 4 size. Therefore, the dimensions used for low-cycle fatigue coupons were half of what was used at the University of Buffalo. These dimensions are shown in Figure 10.5. The 3 in. provided on each side were used to grip the specimen into the testing machine.

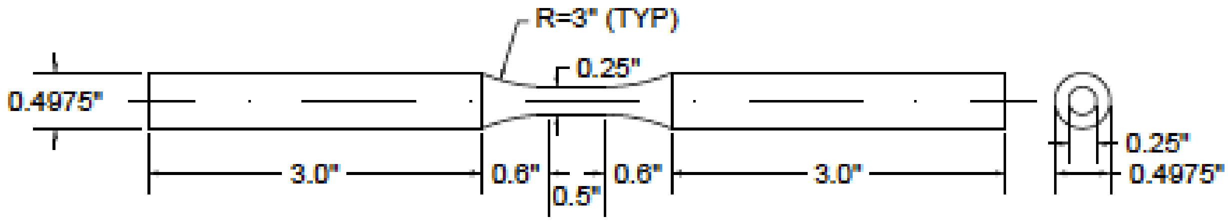


**Figure 10.5 Low-cycle fatigue test coupon dimensions.**

### 10.3.2 Buckling-Restrained-Brace Bars

In order to prevent buckling of the steel reinforcement and increase ductility/energy dissipation, a BRB system was designed. A machined bar would be encased by a steel sleeve to model BRB systems used in steel frames. The ridges on a No. 4 rebar were to be machined off to remove any space between the steel sleeves that would surround the reinforcement. The middle section was to be machined down to an area that would ensure the reduced cross section would fracture before the larger cross-section yielded. The required thickness of the sleeve was calculated to ensure no buckling occurred. Sample calculations are shown below.

*Reduced cross-section calculations:*

$$\text{Assuming } \sigma_y=95 \text{ ksi and } \sigma_u=130 \text{ ksi (stainless steel)}$$

$$\#4 \text{ Rebar: } A=0.20 \text{ in}^2 \text{ and } d=0.5 \text{ in}$$

$$A \times \sigma_y > A_{reduced} \times \sigma_u$$

$$(0.2 \text{ in}^2)(95\text{ksi}) > A_{reduced}(130 \text{ ksi})$$

$$A_{reduced}=0.14 \text{ in}^2 \text{ yielding a } d_{reduced}=0.422 \text{ in.}$$

*For steel tube sleeve thickness:*

$$P_{applied}=A_{reduced}\ \sigma_u=(0.14 \text{ in}^2)(130 \text{ ksi})= 18.2 \text{ kip}$$

$$P_{cr}>P_{applied}$$

$$P_{cr}=\pi^2 EI/L^2$$

$$18.2 = \pi^2(29{,}000 \text{ ksi})I/20^2$$

$$I = .0252\ in^4$$

$$For\ D_i = 0.5\ in,\ D_o = 0.866\ in.$$

$$Thickness\ of\ tube = 0.25\ in.$$

Possible configurations of the BRB system are shown in Figure 10.6. The lengths of all of the steel tubes were based off the diameter of the column where the system would be integrated. The 42% scaled columns had diameters of 20 in. The length of the sleeve was given a size of 1 diameter or 0.75 diameter. The length of the bar with a larger cross-sectional area was given dimensions 3 and 6 times the cross-section area of the bar (0.5 in.$^2$). The transition zone from 0.5 in.$^2$ to the reduced cross-sectional area was left arbitrary. For the planned tests, a length of 1 in. was assumed.

The sleeve and the rebar would be de-bonded using saran wrap and grease to ensure the rebar resisted only axial stresses and the sleeve resisted flexural buckling stresses. The space between the reduced cross section and the sleeve would be filled using hydrostone. Any other material would most likely be too large to fit into the small gap that needed to be filled. For testing purposes, system number 3 (with steel tube length of 15 in.) from Figure 10.6 was picked. The final dimensions of the specimen that needed to be machined are shown in Figure 10.7. The transition length shown in question mark was assumed to be 1 in.

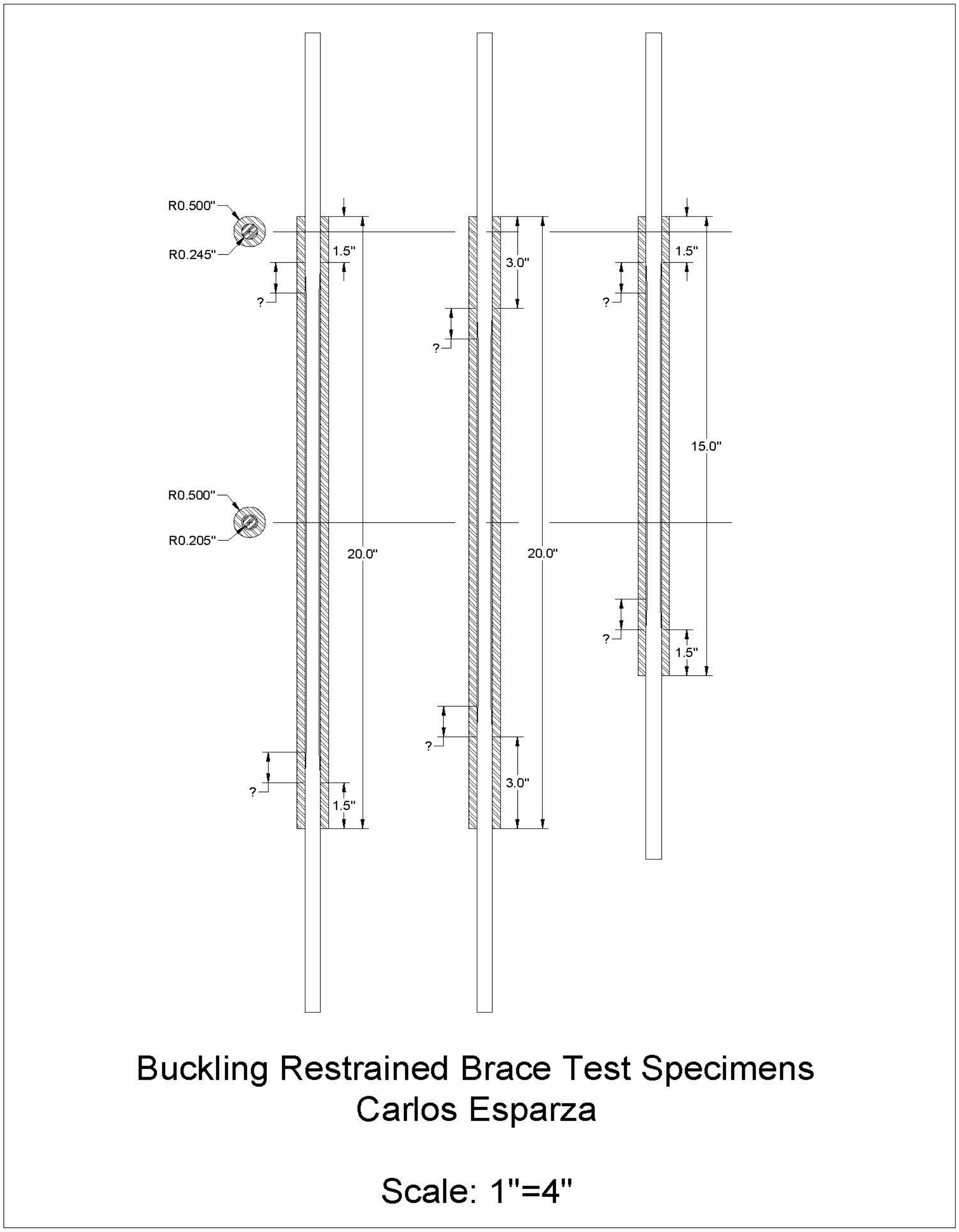


**Figure 10.6 Possible BRB system configurations.**

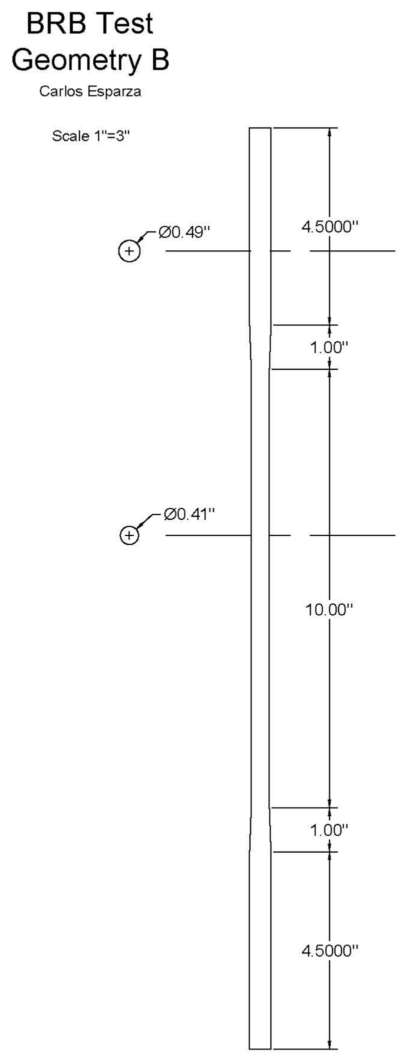


**Figure 10.7 Dimensions of Bar in BRB system**

## 10.4 TEST PROGRAM

### 10.4.1 Planned Tests

Future research will involve construction of two columns with high-performance materials. One column will use 2205 Duplex stainless steel and the other will have ordinary carbon steel for comparison purposes. For each type of steel reinforcement (A706 G60 carbon steel and 2205 Duplex steel) monotonic, low-cycle fatigue, and BRB tests were planned to compare the physical properties under different loading of each steel type. The monotonic and low-cycle fatigue tests were designed to obtain results that could be compared to the University of Buffalo's findings.

### 10.4.1.1 Monotonic Tests

A total of four monotonic tests were planned to compare the mechanical properties of A706 G60 carbon steel and 2205 Duplex alloy stainless steel under tension. Two of the specimens were to be carbon steel and the remaining two would be stainless steel. All coupons tested were No. 4 bars with nominal diameter and cross-sectional areas of 0.50 in. and 0.20 square in. respectively. Each coupon was to be 24 in. long with gauge lengths of 8 in. as required by ASTM [ASTM, 2004]. Each steel type was tested twice to ensure accurate data was obtained.

### 10.4.1.2 Low-Cycle Fatigue Tests

A total of six low-cycle fatigue tests were planned for this research. Four 2205 Duplex stainless steel coupons and two A706 G60 carbon steel coupons were machined for testing. The tensile and compressive strain limits that were to be examined were based off data from research performed at the University of Buffalo. Although the research that was done there fit the definition of low cycle fatigue (< $10^5$ cycles), the number of cycles were too high to accurately represent what is happening in the UW column-to-foundation system. Higher strain values would be needed to model expected performance. On the other hand, due to the small diameter of the coupons that were to be tested, strain values needed to be limited to avoid buckling. Table 10.3 summarizes the strain values that were to be used for each steel coupon.

Test number 1, 4 and 5 use the same strain rates as tests performed by the University of Buffalo [Zhou et al, 2008]. Data obtained from these tests would be used to compare and confirm the results of tests performed at Buffalo. Comparing the results of test 2 to 3 and 4 to 5 would show the difference between carbon steel and stainless steel in cyclic tests. By limiting the maximum compressive strain to 1.33%, the coupons were less likely to buckle. Although the compressive strain was limited considerably, it is an accurate representation of what would actually happen in the column-foundation system. The compressive strains would be lower than the tensile strains due to the surrounding concrete taking a part of the compressive stresses that would be present in that region.

**Table 10.3 Strain limits.**

| Test No. | Specimen | Max. Tensile Strain (%) | Max Compressive Strain (%) | Range (%) |
|---|---|---|---|---|
| 1 | S.S. 1 | 1 | -1 | 2 |
| 2 | S.S. 2 | 1.33 | -0.667 | 2 |
| 3 | B.S.1 | 1.33 | -0.667 | 2 |
| 4 | S.S. 3 | 2 | -1 | 3 |
| 5 | B.S. 2 | 2 | -1 | 3 |
| 6 | S.S. 4 | 2.667 | -1.33 | 4 |

### *10.4.1.3 BRB Bar Tests*

Buckling-restrained-brace bar tests were to be conducted using the same maximum tensile and compressive strain rates as low-cycle fatigue tests. Four tests would be performed on 2205 Duplex stainless steel coupons and 2 tests would perform on A706 G60 carbon steel. In the low-cycle fatigue tests, buckling of the coupons was prevented by geometry. For a particular geometry of those coupons, a maximum compressive strain was established to prevent buckling. For BRB tests, the geometry of the coupons was to be altered. The coupons were to be machined longer and with a smaller diameter. Buckling in this system was to be prevented by the outer sleeve that would resist the lateral buckling forces. If the low-cycle fatigue performance of the BRB system was determined to be the same as the unsupported, geometrically restrained tests, it would show that incorporating BRB systems into columns would help with the problem of bar buckling without having to limit the maximum compressive strain or geometry.

## 10.4.2 Tests Conducted

Due to time, fabrication, and instrumentation issues that arose during experimental process, not all planned tests were performed. A detailed discussion of the tests that were conducted and the problems that impeded the others from taking place follow.

### *10.4.2.1 Monotonic Testing*

All four planned monotonic tests were conducted. One pair of two-wire strain gauges was placed in the middle of each coupon's gage length to measure strain values. The coupons were subjected to tensile loading using a 300-kip-capacity Baldwin machine. Figure 10.8 shows the initial set up of a specimen.

**Figure 10.8 Initial test set up.**

The Baldwin machine used for testing required the load rate to be adjusted manually. This was achieved by controlling the hydraulics using a turn-knob. The coupons were stressed in tension using as constant of a load rate as possible until they fractured. The strains and corresponding forces were recorded using LabView and used for data analysis.

#### *10.4.2.2 Low-Cycle Fatigue Testing*

A 110-kip MTS machine was used to conduct low cycle fatigue tests on the steel coupons. A laser extensometer was used to record the displacement that occurred throughout the gauge length during testing. This setup is shown in Figure 10.9.

Strain gages were not used due to the fact that the strain levels used during testing exceeded the reading capacity of the strain gages that were available. Instead, two pieces of special tape were attached to the ends of the 0 0.5-in. gauge length. The laser would then read the relative displacement between the two tapes. A snapshot of this process can be seen in Figure 10.10.

Practice runs using rods of steel similar in size to the steel coupons that were to be tested showed errors in the data. Straining the specimens past the yield point led to messy graphs that did not depict what was actually happening in the specimen gage length. To simplify the troubleshooting, strains applied to the practice specimens were kept low to keep the specimen in the elastic range. Figure 10.11 shows the data obtained from the first run.

The strains plotted on the previous graph are calculated using the displacement recorded from the laser extensometer divided by the overall gage length. Three errors are immediately evident from the curve. The initial jump in stress to 20 ksi does not seem reasonable. At the top and bottom of the loop, the graph indicates the strain continues to increase although the stress is decreasing. Finally, although the strain levels were kept low enough to keep the practice sample in the elastic range, the graph shows a hysteresis loop. Hysteresis loops typically only appear when a steel specimen is stressed past the yield point under cyclic loads. Additional practice tests were needed to determine if the MTS machine or the laser extensometer were causing these problems.

After the first practice run, a strain gage was added to the next practice sample as an alternate way to measure strain. The sample was again kept in the elastic range. Figure 10.12 shows the stress-strain diagram graphed using the data collected from the strain gage. The graph shows linear-elastic behavior of the practice sample, as was expected.

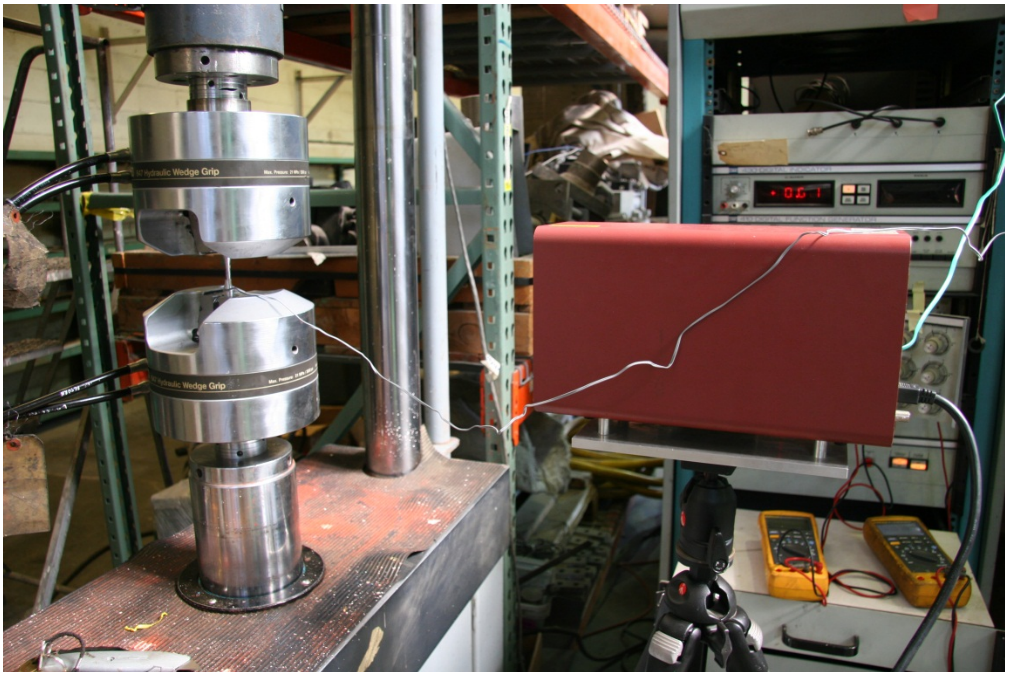

**Figure 10.9 Low-cycle fatigue test set up.**

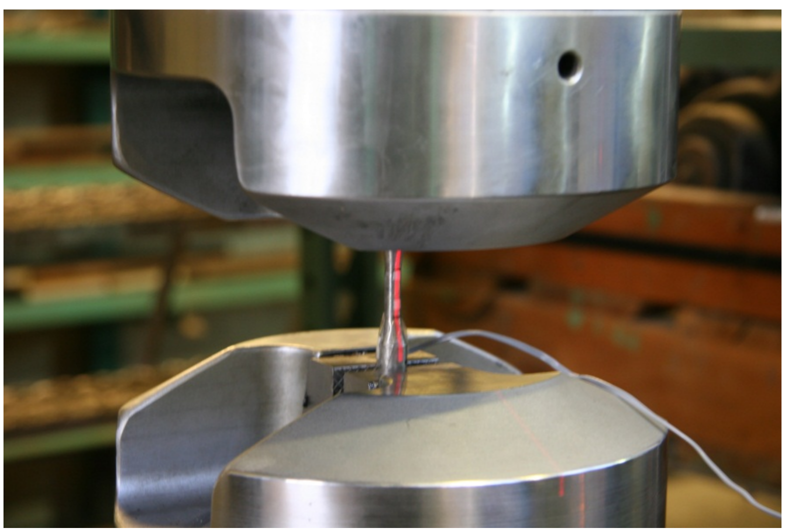

**Figure 10.10 Laser extensometer displacement reading.**

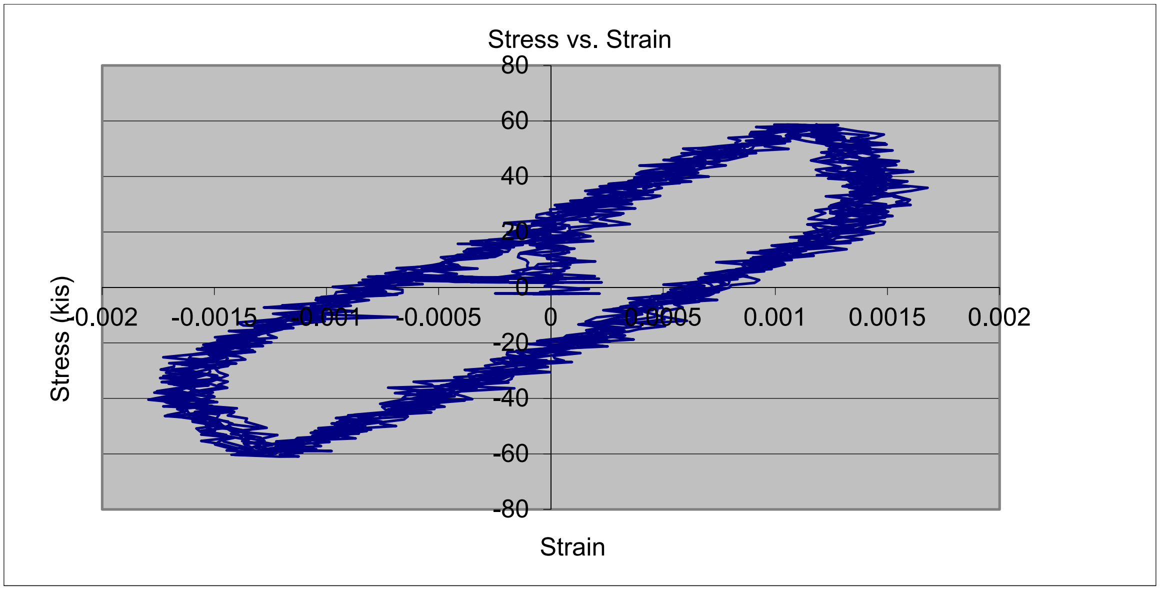


**Figure 10.11 Stress-strain diagram from laser extensometer- Trial #1.**

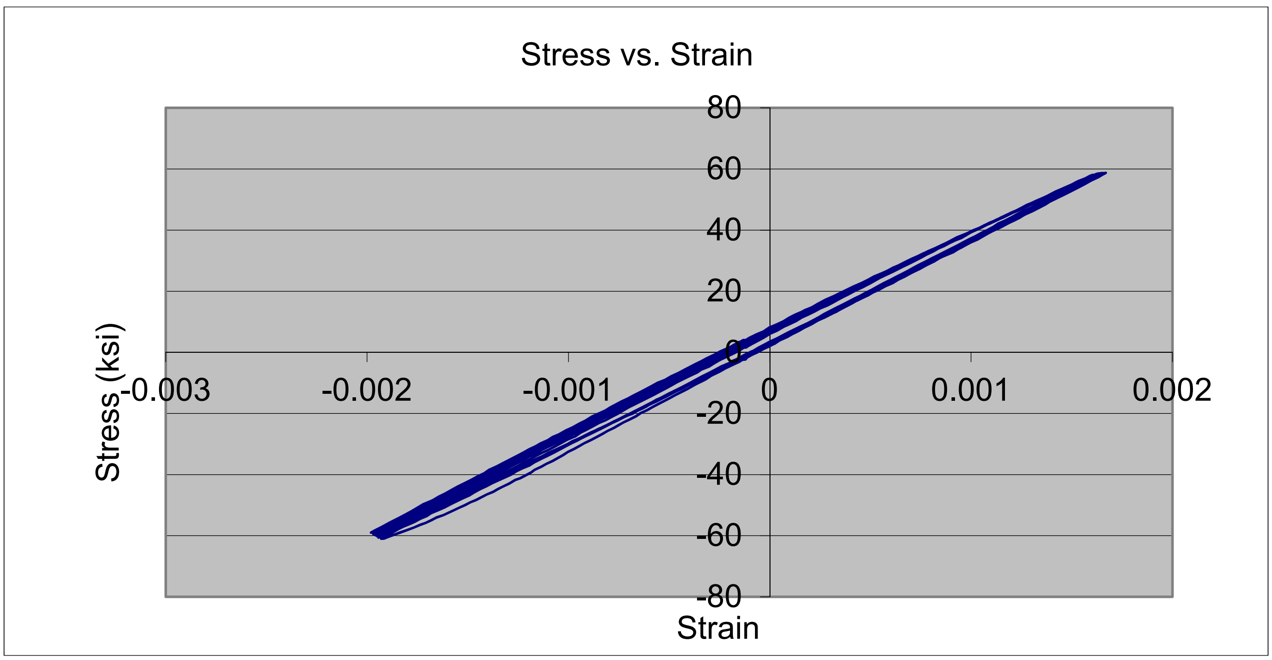


**Figure 10.12 Stress-strain diagram using strain gage data- Trial #2.**

The initial errors showed in Figure 10.11 were due to an error in the displacement readings from the laser extensometer, not the loading set up or test procedures. Comparing the strain readings from the laser extensometer and the strain gage plotted against data points collected reveals why the laser extensometer shows an initial jump in stress and a hysteresis loop. As seen in Figure 10.13, there is an initial lag that causes the upper and lower strain limits in the laser extensometer curve to be offset, when compared with the strain gage readings.

The initial lag is removed by aligning the points where the strains calculated using displacements from the laser extensometer pass zero strain and the points where strain readings from the strain gage pass zero strain. Plotting the stress-strain diagram using the laser extensometer data with the initial lag removed shows the same results that were seen after graphing the strain gage data, as seen in Figure 10.14.

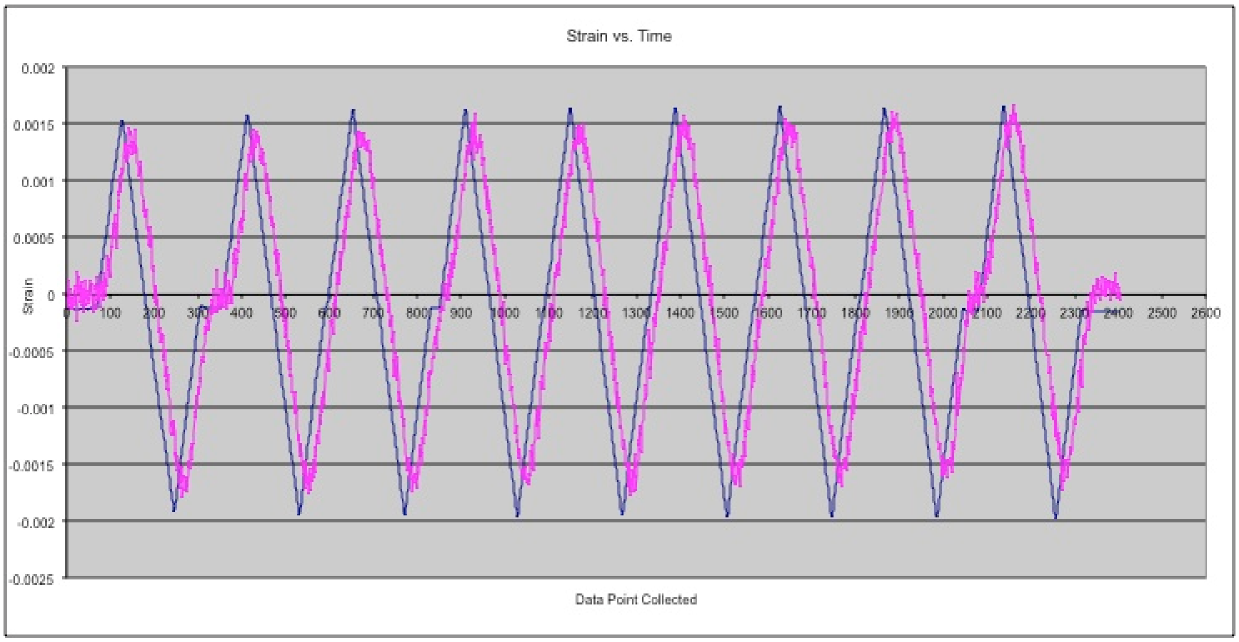


**Figure 10.13 Comparison of strains using laser extensometer and strain gage.**

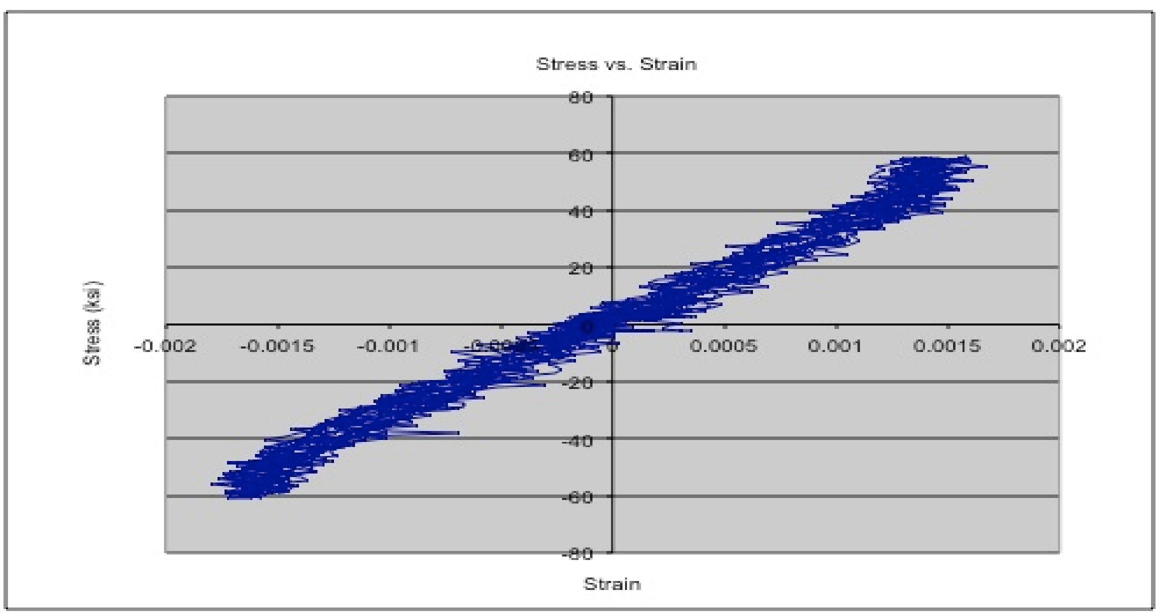


**Figure 10.14 Stress-Strain diagram using laser extensometer after lag is removed.**

The reason for the initial lag that is seen in the laser extensometer readings is unknown and was not fixable within the time allotted. In order to solve this issue for the actual A706 G60 and 2205 Duplex specimens that were to be tested, a strain gage was attached, in addition to the laser extensometer tape, to the specimens. Strains before the strain gage limit is reached would be plotted and the laser extensometer readings would be calibrated using this data. Once the laser extensometer data is calibrated, strain readings after the strain gage breaks would come from the laser extensometer.

Controlling the strain limits each specimen was stressed to would need to be done manually. A slow enough strain rate was used to give the tester enough time to stop the MTS machine at the required strain. The MTS machine was in use most of the summer and after installing the needed grips and calibrating the load cell, only a limited time for testing was remaining. By the time all the issues with the laser extensometer were resolved, only one test was partially completed. The need to manually control the strain limits further lengthened the time needed to complete one test. In the end, only 100 cycles of a stainless steel coupon strained to 1% and -1% tensile and compressive strains were completed.

### 10.4.3 Buckling-Restrained-Brace Testing

No testing was completed on the designed BRB system. Some issues that need to be addressed for future testing were encountered. The primary issue was machining the rebar to obtain the required reduced cross-sectional area. Two different shops were contacted to see if it was possible and both replied that it was not. A diameter of .41 in. for a length of 10 in. is difficult to obtain using a lathe machine. Another issue that was encountered was finding a steel pipe that fit snuggly onto the rebar. There must be minimal gap between the sleeve and the rebar to minimize hydrostone leaks and failure outside of the reduced area. After confirmation that the BRB specimens would not be fabricated, no time was remaining to consider and implement alternatives.

## 10.5 TEST RESULTS

### 10.5.1 Monotonic Test Results

The results of the 4 monotonic tests performed are shown in Figure 10.15. From this graph, important properties were obtained. These properties include modulus of elasticity (E), yield strength ($\sigma_y$), and ultimate strength ($\sigma_u$). Yield strength was defined as the stress corresponding to a strain of 0.35% (ACI 318-05, 2005). The results are summarized in Table 10.4.

A706 carbon steel showed an average modulus of elasticity of 26,055 ksi. It was higher than the average 2205 Duplex stainless steel modulus that was 20,663 ksi. The yield stresses calculated indicate yield stresses that varied as much as 9 ksi for both steel types. Ultimate stresses exhibited by 2205 Duplex S.S. were approximately 20 ksi larger than A706 carbon steel.

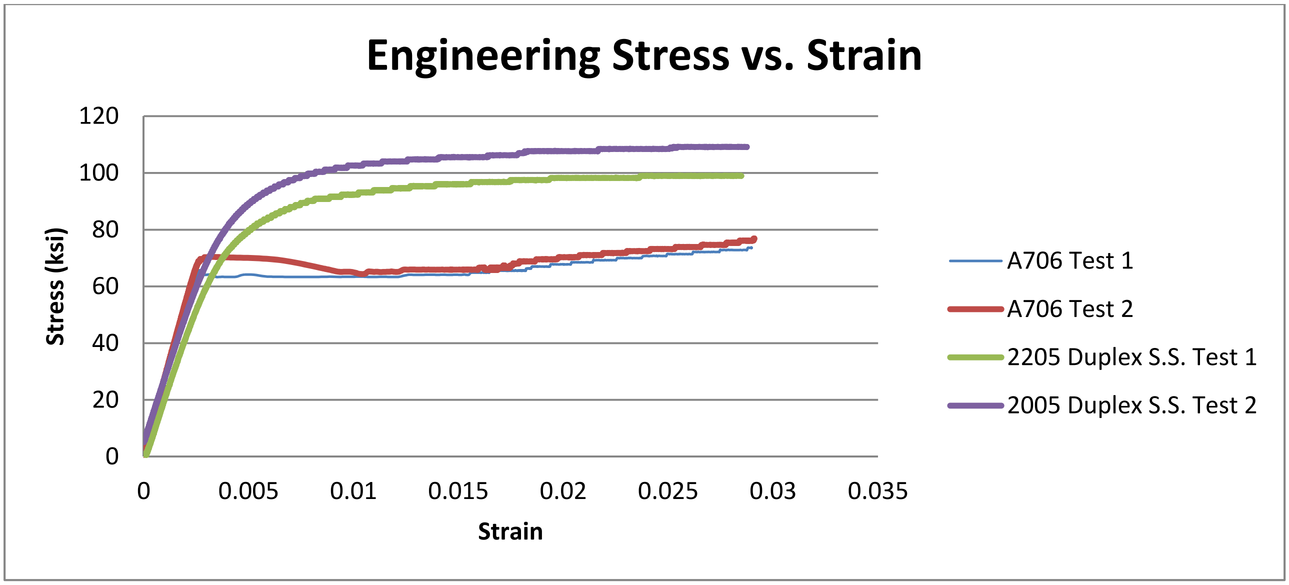


**Figure 10.15 Results of monotonic tests**

**Table 10.4 Monotonic test results.**

| Test | Young's Modulus (ksi) | $\sigma_y$ (ksi) | $\sigma_u$ (ksi) |
|---|---|---|---|
| A706 #1 | 25817.22 | 63.35 | 89.18 |
| A706 #2 | 26293.03 | 70.35 | 90.89 |
| 2205 S.S. #1 | 20272.03 | 66.71 | 110.1 |
| 2205 S.S.# 2 | 21054.57 | 75.48 | 109.26 |

### 10.5.2 Low-Cycle Fatigue Test Results

The only specimen to be tested was a 2205 Duplex stainless steel coupon. The maximum tensile and compressive strains the coupon was subjected to were 1% and -1% respectively. After discussing the test setup with the University of Washington Structures Lab director, it was determined that the best way to reach the maximum and minimum strain limits was to lower the strain rate and manually stop the MTS machine at 1% tensile strain, reverse the loading and stop it again at -1% compressive strain. For similar strain rates, the University of Buffalo reached fatigue lives of 750–1000 cycles. After 3 hours of manually loading and unloading the specimen (approx. 150 cycles), the following results were obtained (Figure 10.16). The strains shown in this figure correspond to those obtained from the strain gauge readings. The data obtained from the laser extensometer was also graphed. Figure 10.17 shows the strain-stress graph using displacement data from the extensometer. Although the data obtained from both displacement readers should be exactly the same, the stress-strain diagram from the laser extensometer was completely different. It appears to be shifting to the left as the experiment progresses.

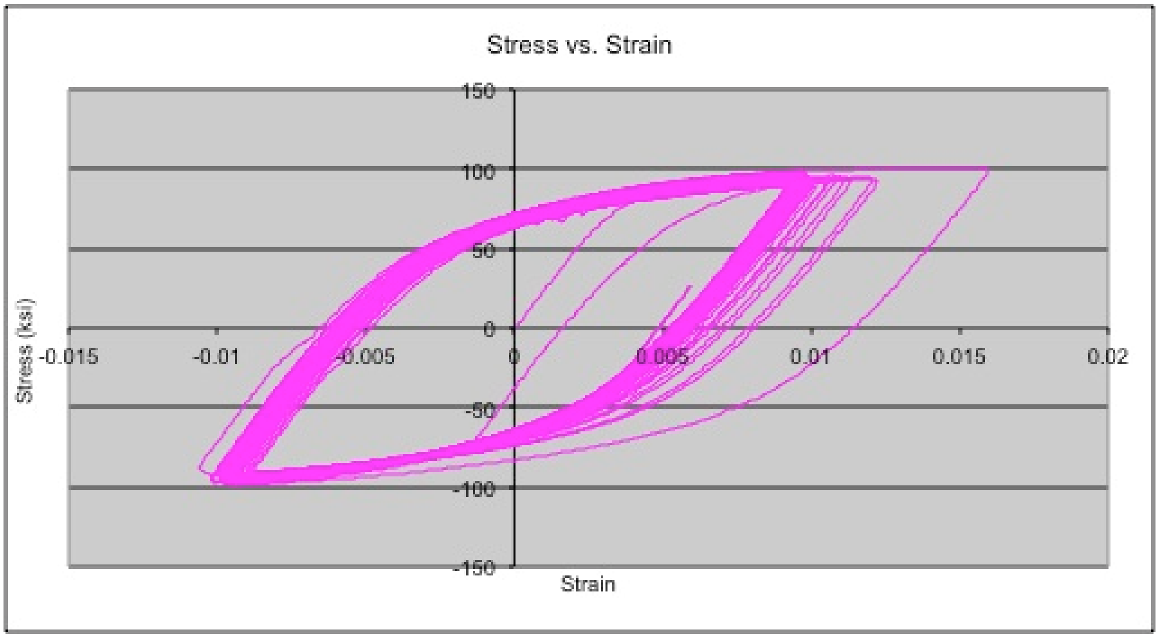


**Figure 10.16 2205 Duplex S.S. low-cycle fatigue test using strain gauge.**

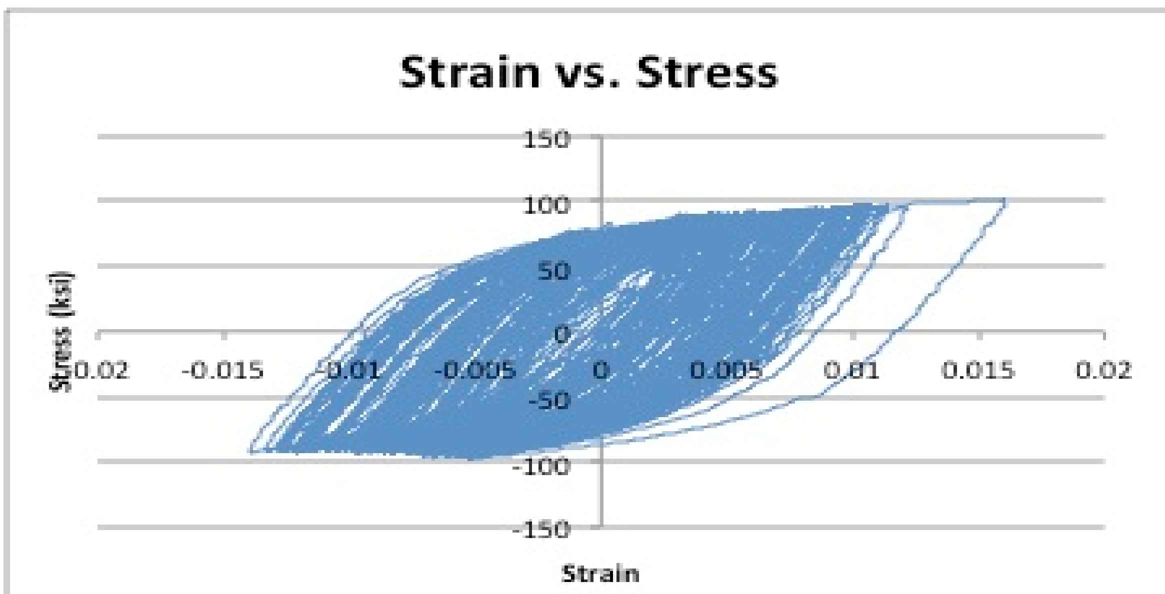


**Figure 10.17 2205 Duplex S.S. stress-strain diagram using laser extensometer readings.**

## 10.6 ANALYSIS OF RESULTS

### 10.6.1 Monotonic Tests

Comparison of the values obtained in our experiment with those obtained at the University of Buffalo shows a large variance in results. The University of Buffalo obtained modulus of elasticity's of 27,7705 and 30,244 ksi for 2205 Duplex stainless steel and A706 carbon steel respectively [Zhou et al. 2008]. These are much higher than the 20,663 ksi and 26,055 ksi modulus's for stainless and carbon steel respectively obtained in Washington. The results in Buffalo show a clear difference between the yield strengths of stainless steel and A706. The two strengths varied by 24 ksi, with stainless steel having the larger one. The data obtained at the University of Washington does not show a definitive difference in the two steels in terms of yield strength. One trial for stainless steel resulted in a yield strength of 66 ksi while the other showed a larger strength of 75 ksi. Carbon steel results show a similar pattern. One specimen had a yield strength of 63 ksi and the other a strength of 70 ksi. These large jumps and unpredictable patterns indicate the results obtained in the monotonic test of A706 and 2205 Duplex steel are not reliable.

Possible sources of error could have occurred in the way the specimens were prepared for testing. Because the ridges in the rebar where not machined, the location where the strain gages were placed had to be sanded down to provide a flat surface. If too much of the steel were removed, the cross-sectional area would be smaller than the specified 0.20 square in. The stresses in the steel would be much higher than those calculated using the assumed cross section. The University of Buffalo avoided this problem by measuring strain using an extensometer, which did not require sanding of the specimen. Another possible error could have occurred during the test. If the load were applied to quickly, the properties obtained from the stress-strain diagrams would be incorrect. Because the load rate was controlled manually, human error is always a concern.

### 10.6.2 Low-Cycle Fatigue Test

Although the majority of the hysteresis loops stop near the 1% and -1% strains, manually controlling the MTS machine can lead to errors. This can be seen in the graph where one cycle was allowed to reach 1.5%. Apart from the inherent error involved in human control, time was also a constraint. After 3 hours, only 150 cycles were completed. In order to reach the high number of cycles needed, a more efficient and accurate way to control the strain limits will need to be developed.

Analyzing the data from the laser extensometer shows that a new problem came up during the test. After the initial lag was removed, the stress-strain diagram graphed using data from the laser extensometer did not match the stress-strain diagram graphed from the strain gage data. Although the range from maximum tensile to maximum compressive strain remained constant for all loops (2%), the graph shifted towards the left as the test progressed. Figure 10.17 shows this shift. The previous idea of calibrating the data to use the laser extensometer for high strain rates would need to be adjusted. It is clear there are more problems with using the laser extensometer as a displacement measurement tool than anticipated.

## 10.7 SUMMARY, CONCLUSIONS, AND RECOMMENDATIONS

### 10.7.1 Summary

The monotonic and low-cycle fatigue properties of 2205 Duplex stainless steel and A706 G60 carbon steel were the primary concern of this research. Specimens that would be tested to determine these properties were designed and machined. A BRB system that could be used to improve low-cycle fatigue performance was also designed. Monotonic tests were conducted as planned. Low-cycle fatigue tests encountered difficulties that made it difficult to conduct the tests and obtain results. These difficulties included: obtaining use of the testing machine in time, determining the errors in data obtained from the laser extensometer, and having to manually control strain limits. BRB tests were also not performed due to problems in machining the specimens. The dimensions of the BRB bars (small cross-section, long length) made them difficult to machine without buckling occurring. Monotonic properties such as modulus of elasticity, yield strength, and ultimate strength were determined from the tension tests performed.

### 10.7.2 Conclusions

The following conclusions can be made from the testing conducted on stainless and carbon steel:

1. Monotonic test results can be dramatically altered by load rate and sanding of rebar for strain gauge placement.
2. Low-cycle fatigue tests using a laser extensometer to measure gage displacement is unreliable.
3. Low-cycle fatigue tests where the strain rates are manually controlled are prone to errors and are not time efficient.
4. BRB bars are not easily machined due to their slenderness.
5. Construction of BRB system (machining of bars, finding proper size sleeve, inserting hydrostone) is a difficult process.

### 10.7.3 Recommendations

Due to inconsistent results obtained from the tests that were conducted and the difficulties that arose that caused other planned tests to be put on hold, it is difficult to provide recommendations for implementing the results obtained in these experiments. Recommendations for future research can be made to help obtain more conclusive results that could be implemented.

For monotonic testing, it is important that the load rate be as controlled as possible. The Baldwin machine used for monotonic tests used a hydraulic system that required the tester to manually adjust load rates. If not done properly, the load rate could be too high and the data obtained would be inaccurate. Also, when sanding the rebar to obtain a flat surface for strain gage placement, it is crucial that the cross-section not be reduced greatly.

For low-cycle fatigue tests, an improvement needs to be made in the way the strain is measured. Strain gages work well until their strain limit is reached, but it high strains are desired an extensometer will need to be used. The size of the specimens makes this difficult because extensometers of that size are not available in the University of Washington lab. Either the specimens would need to be machined larger, or a special extensometer would need to be found. It is recommended that the laser extensometer not be used. It would be hard to trust data from a laser extensometer for this type of research after all the problems encountered. It is also recommended that an automated method of applying the required strains be developed. Manually controlling the strains leads to human errors that are easily made. It also makes the testing extremely long. The longer a researcher has to control the loads by hand, the more likelihood errors will occur.

Buckling-Restrained-Brace testing is recommended for future research. In order to complete this testing, a method of machining slender bars must be developed. If the bars dimensions are not feasible, alternate systems should be considered.

## ACKNOWLEDGMENTS

First and foremost, I would like to thank my faculty advisors, Marc O. Eberhard and John Stanton, and my mentor Olafur Haraldsson for all the guidance they provided me with throughout the summer. Although many problems came up throughout the research process, they always encouraged me and helped me find solutions. I would also like to thank Gunnsteinn Finnsson and Spencer Livermore for their daily help in the lab. Thank you to Heidi Tremayne who helped the PEER Summer Research program run smoothly all summer. This research experience would not have been possible without the funding of the National Science Foundation and I am extremely grateful. Last, but certainly not least, I would like to thank my fellow summer interns. Without their support day in and day out, this summer would not have been the rewarding, satisfying experience it turned out to be.

## REFERENCES

ACI Committee 318–05. (2005). *Building Code Requirements for Structural Concrete (ACI 318-05) and Commentary,* Amerian Concrete Institute, Farmington Hills, MI: American Concrete Institute.

ASTM International. (2004). *ASTM Annual Book,* American Society for Testing and Materials, West Conshohocken, PA.

ASTM International. (2010). *Standard Specification for Stainless Steel Bars and Shapes,* American Society for Testing and Materials, West Conshohocken, PA.

Davis PM, T Janes, MP Eberhard, and JF Stanton (2011). Unbonded pre-tensioned columns for bridges in seismic regions, *PEER Report No. 2012/04*, Pacific Earthquake Engineering Research Center, Berkeley, CA.

Haraldsson O, MO Eberhard, and JF Stanton (2011). *Spread Footing Socket Connections for Precast Columns*, Master's Thesis, University of Washington, Seattle, WA.

Sabelli, R, S. Mahin, and C. Chang (2003). Seismic demands on steel braced frame buildings with buckling restrained braces, *Eng. Struct*., 25:655–666.

Schnell RE, and MP Bergmann (2007). Improving tomorrow's infrastructure: Extending the life of concrete structures with solid stainless steel reinforcing bar, *Proceedings*, Bridge Engineering Conference, NY, NY.

Zhang G, C. Wang, and Z Zhang (2011). Strength degradation and energy dissipation of stainless steel reinforced concrete columns, *Appl. Mech. Mat.,* 90–93:1614–1617.

Zhou Y, Y-C Ou, GC Lee, and JS O'Connor (2008). *A Pilot Experimental Study on the Low Cycle Fatigue Behavior of Stainless Steel Rebars for Earthquake Engineering Applications*. University of Buffalo, Buffalo, NY.

# 11. Bond Capacity of Steel Epoxy-Coated and Uncoated Pre-Stressing Strands

## JOSE G. JIMENEZ, JR.

### ABSTRACT

A precast, pre-tensioned concrete bridge bent system developed at the University of Washington (UW) aims to accelerate bridge construction, extend the bridge's life-span, and increase the bridge's earthquake resiliency. One aspect of this research focuses on the column's unbonded, pre-tensioned, epoxy coated strands, which are designed to restore the column to its original position after a seismic event. It is essential to study the epoxy coated strand's bond characteristics in order to determine how its benefits compare to the benefits of using traditional carbon (black) strand in the re-centering system. Data collected from strand bond tests conducted at UW were analyzed to compare both strands' ability to resist a pull-out force. In order to normalize the test results, averages were calculated from compiling data for the strands at their respective embedment lengths in grout. In this research, there were three main questions: (1) which type of strand has a higher bond stress capacity, the black carbon or the epoxy strand?; (2) what is the effect of the strand's diameter and embedment length on its bond stress capacity?; and (3) what effect does the grout mix's compressive strength have on the strand's bond stress capacity? The results from this research will enable bridge engineers to choose the optimal design for the unbonded strands in the column in terms of the type of strand and the required anchorage length.

### 11.1 INTRODUCTION

Researchers at the University of Washington (UW) have developed a precast concrete bridge bent system to accelerate highway bridge construction. The project has been ongoing for some time now, and the Washington State Department of Transportation (WSDOT) has implemented a version of the concrete bridge bent system in a few of their highway bridge construction projects.

The UW researchers are now developing a more advanced version of the bent system. The new concrete bridge bent system for Accelerated Bridge Construction (ABC) features stainless-steel reinforcement, pre-tensioned, epoxy coated strands, and two sections of hybrid fiber reinforced concrete (HyFRC) shells in its plastic hinge regions. Its column to cap-beam connection and unbonded section of epoxy coated strands are two critical aspects of this system that ensure the column's rapid constructability and earthquake resiliency [Davis et al. 2011].

### 11.1.1 Background

The proposed bridge bent system is show in Figure 11.1. At the column-to-footing connection, the pre-fabricated concrete column is first set in position and then a spread footing is cast in place around it. The embedded portion of the column has a roughened surface that maximizes the load transfer between the column and footing. The column's cap beam connection requires that the column's bars be grouted into the corrugated metal ducts that are precast in the cap beam. The number of bars was reduced from that used in conventional columns. Larger diameter bars facilitate column assembly compared to attempting to align a large number of smaller diameter bars into the ducts in the cap beam. This method of construction saves time and money due to the fact that it reduces onsite casting. Around the column's center there are two cylindrical concrete shells that encase the top and bottom sections of the six pre-stressed, epoxy-coated strands. This forms the inner wall for the HyFRC shell in which the top and bottom sections of the stainless steel rebar are cast. The strands are aligned hexagonally around the column's center and extend throughout the entire length of the column. The stainless steel rebar surround the shells and extend from the cap beam to the footing connections. Concrete is cast inside the shell and in the remaining sections of the beam [Davis et al. 2011].

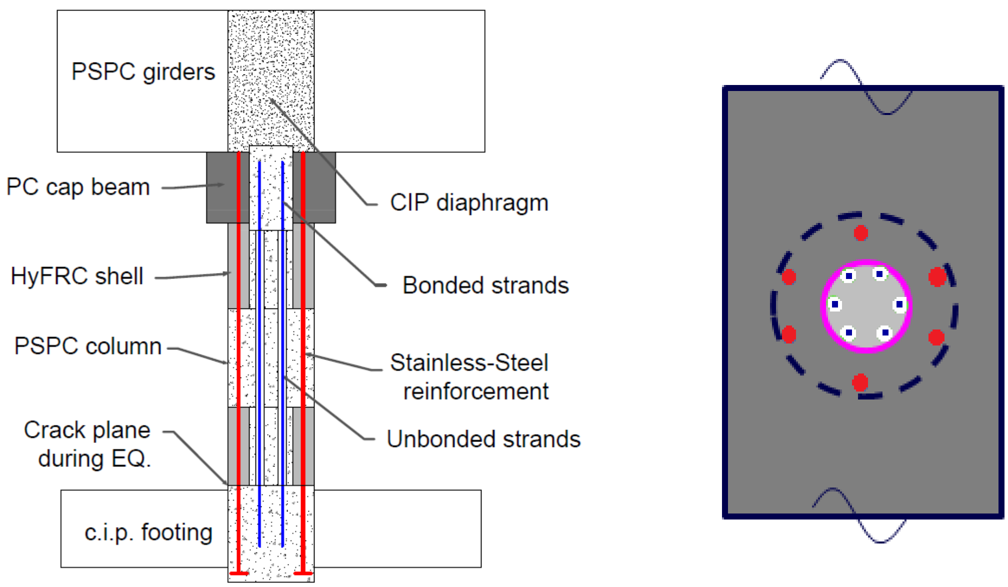


**Figure 11.1 Precast bridge bent system with unbonded epoxy coated strands and stainless steel reinforcement.**

To maintain their tension, these strands are bonded to the concrete at the column-to-footing and column-to-cap-beam connections. In contrast, over the clear height of the precast column, the strands are encased in slender PVC pipes, which ensure that this region of the strands remains unbonded. This arrangement minimizes the change in strain (and stress) in the strand when the column deflects laterally, because the strand's elongation is distributed throughout the unbonded region [Davis et al. 2011]. This system of bonded and unbonded strands provides a re-centering force that can restore the column back to its original plumb position after a seismic event. As shown in Figure 11.2, as a lateral force is applied and initiates the column's horizontal movement to the right, the pre-stressed strands restore the column to its original position.

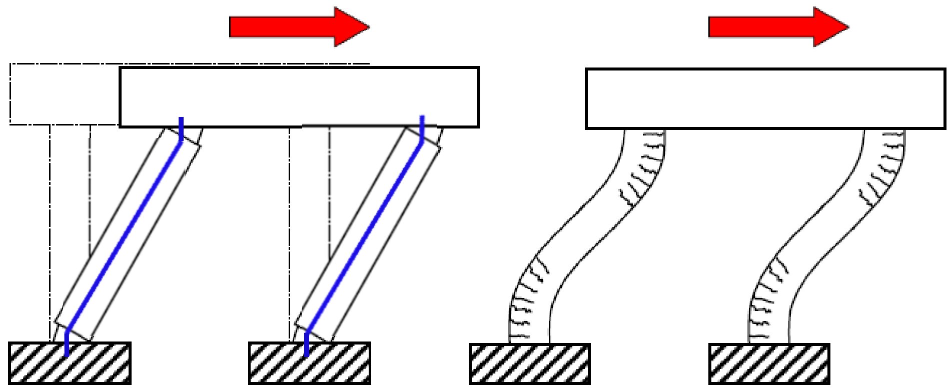

**Figure 11.2** **Behavior of precast (left) and cast-in-place (right) bridge bents [Steuck et al. 2008].**

The system's re-centering system relies heavily on the strand's bond with the concrete. As the column shifts from side to side during an earthquake, the strand would eventually slip out of the concrete foundation or beam if it were not bonded over a sufficient length. To minimize the stress increase in strand caused by lateral displacements, the unbonded region must be as long as possible in order to distribute the strain throughout the strand [Davis et al. 2011]. Since the column's length is fixed, the bonded region must therefore be as short as possible. However, it must be long enough to ensure sufficiently stable bond with a minimal amount of slippage. The purpose of this research is to investigate the differences between the bond properties of epoxy coated strand and regular "black" strand in order to design the strand anchorage in the precast concrete bridge bent system.

## 11.2 LITERATURE REVIEW

The first two sections of this report summarize the relevant background information and conclusions found from strand bond tests conducted prior to UW's strand bond tests. The third section of this chapter gives the background information regarding UW's strand bond tests, the results of which are analyzed in the subsequent chapters.

### 11.2.1 Epoxy-Coated Strand's Bond Strength's Dependence on Temperature

LeClaire and Shaikh [1996] investigated the effects of temperature on the epoxy-coated strand's bond strength at the University of Wisconsin-Milwaukee (UWM). They claimed that "freshly placed concrete [can] reach 120 to 140°F (48 to 60°C) as a result of heat of hydration of concrete alone." In addition, steam curing of precast members can raise the concrete's internal temperature to a range of 150 to 180°F (66 to 82°C) in order to increase its rate of hydration. This prompted the need for their study of epoxy-coated strand's bond with concrete at high temperatures.

Twenty-four test specimens of 1/2-in. diameter epoxy coated and uncoated black strands were implemented in UWM's test configuration, which was also used by Florida Wire and Cable Company, Inc. (FWC) in their 1988 pull-out strength study. As shown in Figure 11.3, the test specimens consisted of an 18-in.-long seven-wire strand embedded 3 in. deep into an 8-in. concrete cube. The reaction member that counteracted the pullout force consisted of a threaded rod cast in line with the strand. A small section of PVC pipe aligned the strand and the rod along the same axis. The nuts and washer served as a reaction member that held the rod in place. The MTS loading frame applied a tensile force to each specimen creating a constant grip displacement as a load cell and a mounted LVDT measured the load and grip displacement respectively [LeClaire and Shaikh 1996].

Each specimen had two thermocouples. One was attached to the surface of the threaded rod and another was attached to the interior wall of the environmental control chamber (Figure 11.4) that encased each specimen. Room temperature was marked as 70°F (21°C) and each specimen was tested at different 25°F (14°C) increments. The control group of specimens consisted of uncoated strand at 70 and 200°F (21 and 93°C) in order to compare their data with the data from the epoxy-coated strands.

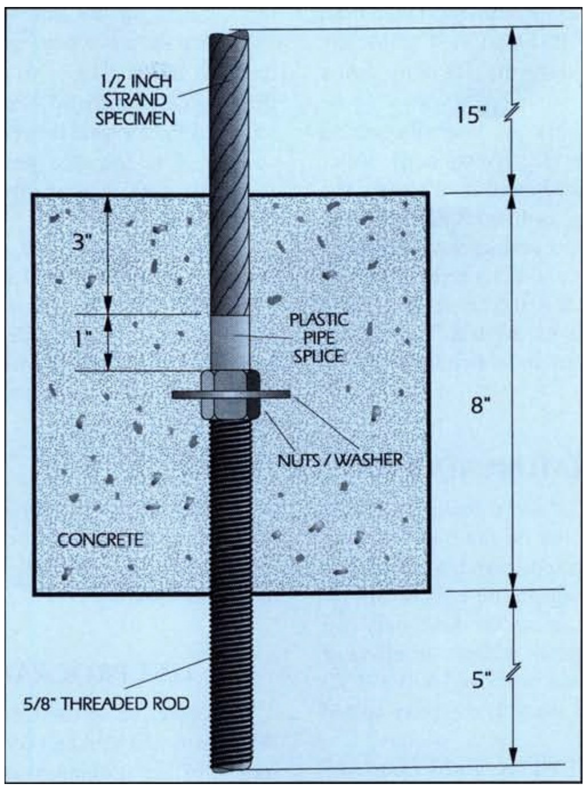


**Figure 11.3 Schematic diagram of test specimen [LeClaire and Shaikh 1996].**

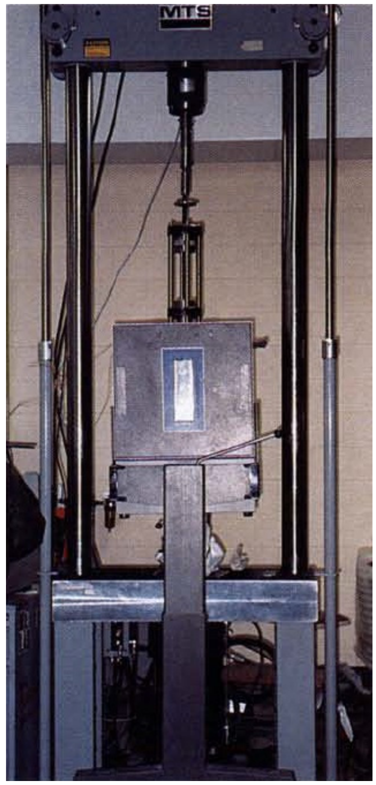


**Figure 11.4 Loading frame with environmental control chamber [LeClaire and Shaikh 1996].**

Based on the results from the bond tests, LeClaire and Shaikh [1996] found that epoxy-coated strand's bonding capabilities diminishes at a temperature of 125°F (52°C), and it experiences severe bond loss at temperatures between 160 and 175°F (71 and 79°C). At temperatures below 100°F (38 °C) the epoxy coating bonds well to the steel strand, and under a pull-out force bond failure occurs between the outer surface of the epoxy and the concrete. At temperatures between 100 and 160°F (38 and 71°C), the decrease in bond capacity is the result of the "shear displacement" between the coating and the concrete as well as the weakening of the bond between the epoxy coating and the steel strands. By strand temperatures of 175°F (79°C), the degradation of the bond interface between the epoxy coating and the steel strand is the primary agent in the strand's debonding from the concrete. Finally, it was recommended that the internal temperature of the concrete should not exceed 160°F (71°C) when de-tensioning the epoxy-coated strands in the process of making pre-stressed concrete [LeClaire and Shaikh 1996].

### 11.2.2 Pull-out Bond tests of Epoxy Coated Pre-stressing Strand

A series of strand bond test were conducted at North Carolina State University by Brearley and Johnston [1990]. Their primary objective was to find the grit density's effect on the epoxy-coated strand's bond with concrete. At the time of the pull-out tests, Florida Wire and Cable Company produced several types of epoxy strands that had a variety of grit densities on its surface. The impregnated grit coating is meant to increase the epoxy strand's bonding capabilities [Brearley and Johnston 1990].

Fifty-two pull-out tests were conducted to test 270-ksi seven-wire strand in concrete. The specimens consisted of 3/8-in.-, 1/2-in.-, and 0.6-in.-diameter strands. The types of strands that were tested consisted of uncoated black strand and four types of epoxy coated strand that differed in grit densities ranging from no grit, low-grit density, medium-grit density, and high-grit density. Each strand was cast in an 8-in. × 8-in. × 12-in. concrete prism, in the center along the 12-in. axis, as shown in Figure 11.5. The strand's bonded region was 12 in. and a hydraulic ram, shown in Figure 11.6, was used to pull each strand in tension [Brearley and Johnston 1990].

A dial gage, attached to "each collar arm end with contact directly on the prism face," was implemented in the test apparatus and was intended to average out the strand's movement as a result of its "natural curvature." The bond capacity of a given strand was normalized by dividing the bond stress by the square root of the concrete compressive strength [Brearley Jr. and Johnston 1990].

As a result of the pull-out tests, Brearley and Johnston found that the epoxy coated strand with medium density grit has a larger stress capacity after initial failure than did the uncoated strand. This was attributed to the increase in friction between the strand's exterior grit coating and the concrete. With respect to strand size, the 3/8-in. black strand had the largest bond stress capacity followed by the 1/2-in. black strand, and the 0.6-in. black strand. On the other hand, of the epoxy coated strand with medium density grit, the 1/2-in. strand had a slightly larger bond stress capacity than the 3/8-in. strand, and the 0.6-in. strand's bond stress strands "well below these values." Upon visual inspection, it was noted that the 0.6-in. epoxy strand with a coated medium grit density had a "lower [grit] density" than its 3/8-in. and 1/2-in. counterparts even though they had asked the manufacturer to supply them with strands that had the same grit density. In addition, the 3/8-in. and 1/2-in. epoxy strands had a very similar grit density, which explains why they had a similar bond stress capacity. It also explains why the 0.6-in. strand had such a comparatively low bond stress capacity [Brearley and Johnston 1990].

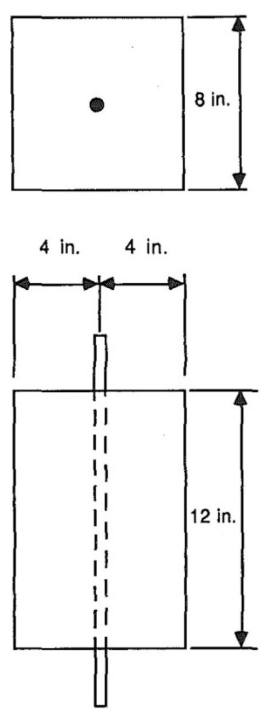


**Figure 11.5 Pull-out specimen [Brearley Jr. and Johnston 1990]**

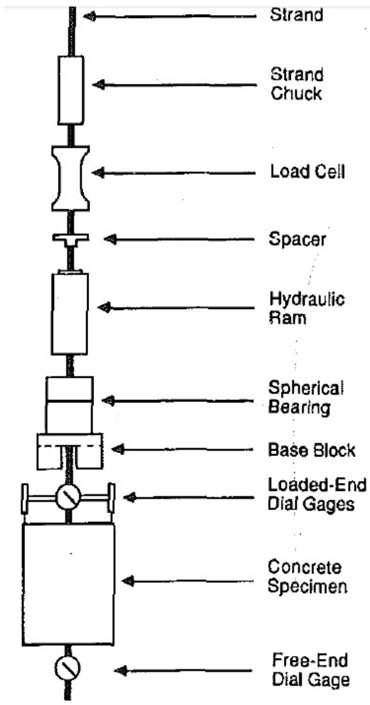


**Figure 11.6 Components of testing apparatus [Brearley Jr. and Johnston 1990].**

Further visual inspection of the epoxy strands revealed that the high density grit and medium density grit strands had “little difference in grit density,” which explains why they had similar bond stress capacities. Ultimately, the high density grit strand had the highest bond stress capacity, followed by the medium density grit, the low density grit, the black strand, and finally the epoxy coated strand without any grit. Among the most important conclusions was that the coated strand without grit had almost no bond strength and that the “variability in the grit density along the epoxy strand signifies that the pull-out test on a single random portion of strand will not give a truly representative sampling of the bond strength capacity of the entire batch” [Brearley Jr. and Johnston 1990].

### 11.2.3 Black and Epoxy Strand Pull-Out Tests

In 2011, Matthias Henry, an intern from France, conducted 65 strand bond pull-out tests at the UW to determine whether the epoxy coated strand had a larger bond stress capacity than conventional black carbon strand. The test results were meant to improve the precast bridge bent system’s design of its unbonded strand re-centering component. Since it was not possible to determine which of the three types of epoxy strands tested by Brearley and Johnston was comparable to the epoxy coated strand tested by Henry, these pull-out tests became necessary. The 3/8-in. and 1/2-in. diameter strands for both carbon black and epoxy coated strand were used in the pull-out tests. The epoxy coated strand tested was manufactured to one grit density, and the strands were all cast in grout. The specimens were prepared following the guidelines specified by the North American Strand Producers (NASP). The large number of specimens required the preparation of eleven grout mixes. Each strand was cast in a solid cylinder of grout within a hollow steel cylinder, as shown in Figure 11.7. A PVC pipe around part of the strand’s length determined its embedded length because it encased the top end of the strand allowing the remaining part of the strand to bond with the grout. The strands were tested at various embedded lengths, such as 3 in., 4 in., 9 in., 12 in., and 16 in.

The strands were in all cases unstressed at the time of casting. For each pull-out test, the specimen's top surface (see Figure 11.7) was placed on the 120-kip Baldwin's top plate; see Figure 11.8. The long end of the strand was pulled through the Baldwin's two test heads and anchored at its end by a strand chuck at the bottom of the second one. A displacement transducer was attached to strand at the bottom surface of the specimen to measure the strand's movement at the end of the unbonded region. Two additional displacement transducers were also attached to the strand at the top surface of the specimen to measure the strand's initial slip as the strand was pulled out. The remaining sections of this report outline the compilation and analyses of the data from these tests.

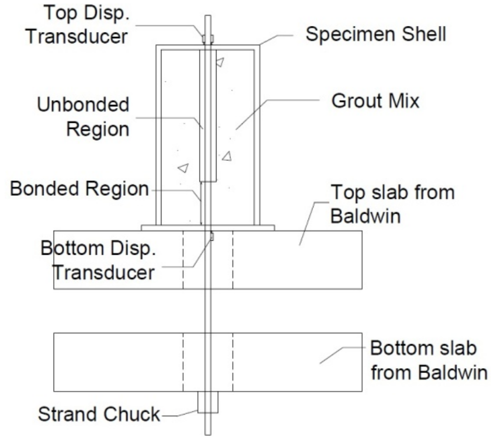


**Figure 11.7 Matthias Henry's test specimen and set up.**

**Figure 11.8 Baldwin 120-kip hydraulic testing machine.**

## 11.3 METHODS

The testing procedure was followed by organizing the information obtained from the sixty five strand bond tests, which led to several conclusions about how a strand's diameter, its embedded length in the grout, and coating type (epoxy or none) effects its bond stress capacity. This chapter outlines the data-processing techniques. Note that the statistics in Section 11.3.2 refer to non-normalized bond stresses, as opposed to the normalized bond stresses used to determine the effects of grout strength in a strand's bond stress reported in a later section of this report.

### 11.3.1 Spreadsheet Generation

To calculate the key information critical to this research, data was gathered from the strand bond tests and an Excel spreadsheet was created for each pull-out test. An example of a strand bond test spreadsheet of a 3/8-in.-diameter black carbon strand that was embedded three in. into Grout Mix A is depicted in Figure 11.9. Each spreadsheet graphically represents the Baldwin's load reading versus the strand's slip reading collected from the displacement transducers. The seven yellow columns at the bottom left of the figure contain the raw test data that was gathered for each pull-out test. Above this section is the maximum/minimum load from the test, as well as the maximum/minimum displacement readings from all of the transducers. At the top left of the spreadsheet is the strand's elastic modulus (E.str), the value for the distance between the center of the bottom transducer to the top of the shell (L.free), its diameter (d.str), area (A.str), embedment length (L.embed), and the two critical slip displacements (Slip 1 and Slip 2 refer to 0.02-in. and 0.1-in. pull-out displacements, respectively). The green table calculates the displacement, load, and average bond stress at the test's peak load, 0.02-in. slip displacement, and 0.1-in. slip displacement.

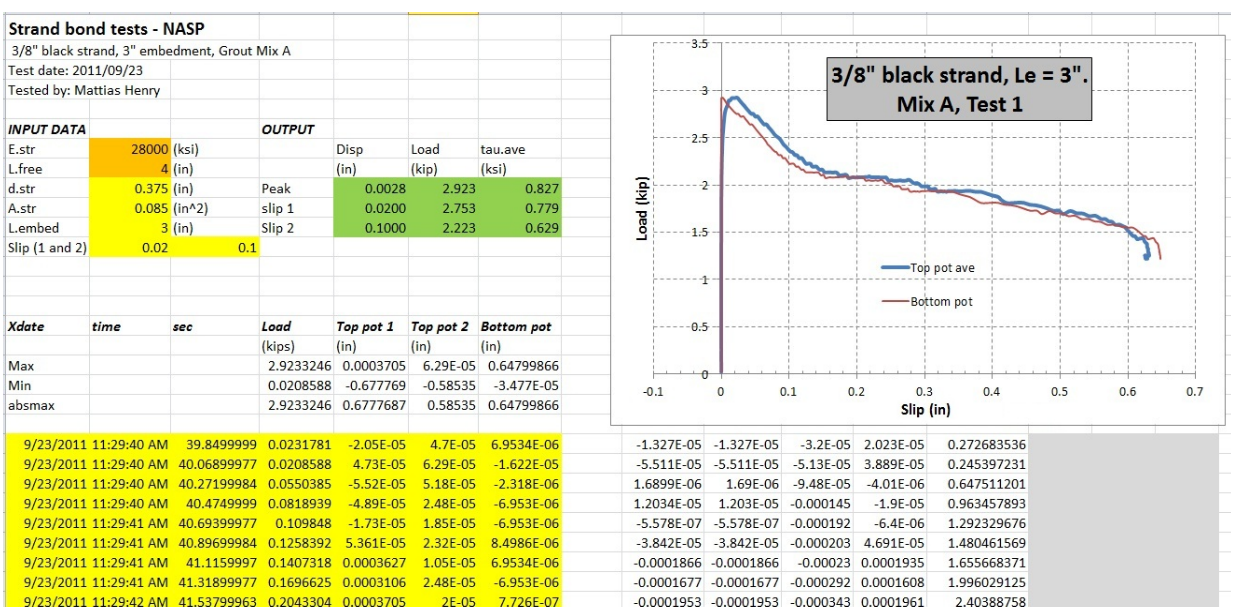


**Strand bond tests - NASP**
3/8" black strand, 3" embedment, Grout Mix A
Test date: 2011/09/23
Tested by: Mattias Henry

| INPUT DATA | | | OUTPUT | | | |
|---|---|---|---|---|---|---|
| E.str | 28000 | (ksi) | | Disp | Load | tau.ave |
| L.free | 4 | (in) | | (in) | (kip) | (ksi) |
| d.str | 0.375 | (in) | Peak | 0.0028 | 2.923 | 0.827 |
| A.str | 0.085 | (in^2) | slip 1 | 0.0200 | 2.753 | 0.779 |
| L.embed | 3 | (in) | Slip 2 | 0.1000 | 2.223 | 0.629 |
| Slip (1 and 2) | 0.02 | 0.1 | | | | |

| Xdate | time | sec | Load | Top pot 1 | Top pot 2 | Bottom pot |
|---|---|---|---|---|---|---|
| | | | (kips) | (in) | (in) | (in) |
| Max | | | 2.9233246 | 0.0003705 | 6.29E-05 | 0.64799866 |
| Min | | | 0.0208588 | -0.677769 | -0.58535 | -3.477E-05 |
| absmax | | | 2.9233246 | 0.6777687 | 0.58535 | 0.64799866 |
| 9/23/2011 11:29:40 AM | | 39.8499999 | 0.0231781 | -2.05E-05 | 4.7E-05 | 6.9534E-06 |
| 9/23/2011 11:29:40 AM | | 40.06899977 | 0.0208588 | 4.73E-05 | 6.29E-05 | -1.622E-05 |
| 9/23/2011 11:29:40 AM | | 40.27199984 | 0.0550385 | -5.52E-05 | 5.18E-05 | -2.318E-06 |
| 9/23/2011 11:29:40 AM | | 40.4749999 | 0.0818939 | -4.89E-05 | 2.48E-05 | -6.953E-06 |
| 9/23/2011 11:29:41 AM | | 40.69399977 | 0.109848 | -1.73E-05 | 1.85E-05 | -6.953E-06 |
| 9/23/2011 11:29:41 AM | | 40.89699984 | 0.1258392 | 5.361E-05 | 2.32E-05 | 8.4986E-06 |
| 9/23/2011 11:29:41 AM | | 41.1159997 | 0.1407318 | 0.0003627 | 1.05E-05 | 6.9534E-06 |
| 9/23/2011 11:29:41 AM | | 41.31899977 | 0.1696625 | 0.0003106 | 2.48E-05 | -6.953E-06 |
| 9/23/2011 11:29:42 AM | | 41.53799963 | 0.2043304 | 0.0003705 | 2E-05 | 7.726E-07 |

| | | | | |
|---|---|---|---|---|
| -1.327E-05 | -1.327E-05 | -3.2E-05 | 2.023E-05 | 0.272683536 |
| -5.511E-05 | -5.511E-05 | -5.13E-05 | 3.889E-05 | 0.245397231 |
| 1.6899E-06 | 1.69E-06 | -9.48E-05 | -4.01E-06 | 0.647511201 |
| 1.2034E-05 | 1.203E-05 | -0.000145 | -1.9E-05 | 0.963457893 |
| -5.578E-07 | -5.578E-07 | -0.000192 | -6.4E-06 | 1.292329676 |
| -3.842E-05 | -3.842E-05 | -0.000203 | 4.691E-05 | 1.480461569 |
| -0.0001866 | -0.0001866 | -0.00023 | 0.0001935 | 1.655668371 |
| -0.0001677 | -0.0001677 | -0.000292 | 0.0001608 | 1.996029125 |
| -0.0001953 | -0.0001953 | -0.000343 | 0.0001961 | 2.40388758 |

**Figure 11.9 Strand bond test Excel profile.**

The graph in Figure 11.9 shows that the average displacement calculated from the two top transducers is similar to the readings from the bottom displacement transducer. This result suggests that as the strand was pulled out, the strand experienced little elongation in the region closest to where the pull out force was applied. Thus, the bond stress is the same throughout the strand up until the strand slips more than 0.02 in. The strand's slip displacement was calculated by subtracting the elongation in the strand's L.free length from the slip recorded by the bottom displacement transducer. Once the strand reached the required slip displacement, such as 0.02 in. or 0.1 in., the bond stress was calculated by dividing the strand's pull-out force at this instant by the area of its diameter. Following this process, profiles were created for each of the sixty five strand bond tests. This includes tests for the 3/8-in.-diameter strand at anchorage lengths of 3 in., 9 in., and 12 in. for both the black carbon and epoxy coated type strand. This also includes tests for the 1/2-in.-diameter strand at anchorage lengths of 4 in. and 12 in. and for the black carbon type strand and at anchorage lengths of 4 in., 12 in., and 16 in. for the epoxy coated type strand.

### 11.3.2 Statistics

Once the spreadsheet generation was complete, all of the data from the spreadsheets were compiled into a table to calculate average values for all of the samples for each condition. Since eleven batches of grout mix were made in order to make all of the specimens, the spreadsheets were organized by grout mix type as shown in Table 11.1. Three of the sixty five tests were rejected because the data was unreliable. (For example, the displacement sensors were not working properly.) As shown by Table 11.1, six specimens of the same strand type and size were made from each mix in order to test any given strand at several embedment lengths. Slip 1 and Slip 2 refer to the 0.02 in. slip displacement and 0.1 in. slip displacement, respectively. The loads, bond stresses, diameter, and embedment length was gathered from each strand bond test spreadsheet.

Table 11.2 shows the averages and standard deviations taken from the test profiles in Table 11.1. For each of the four types of strand, (3/8-in.-diameter and 1/2-in.-diameter, uncoated and epoxy-coated strands), the profiles were gathered from the tests done in different grout mixes in order to find the average values for the strand's bonding characteristics. The information included for each strand type and given embedment length is the non-normalized stress at the two slip displacements, 0.02 in. and 0.1 in. noted as "Non-Norm. Tau at Slip 1" and "Non-Norm. Tau at Slip 2", respectively, as well as the maximum normalized bond stress, "Max Non-Norm Tau". These values represent averages from the several test spreadsheets' non-normalized bond stresses. The standard deviation is given for each non-normalized bond stress in order to calculate the coefficient of variation. Lastly, the last column of the table reports the average coefficient of variation from the three coefficients of variation given by the three bond stresses.

## Table 11.1 Strand bond test profile summary.

| Date | D.str (in.) | Typ.str | Mix | L.embed (in.) | Load @ Slip 1 (kips) | Load @ Slip 2 (kips) | Max load (kips) | Stress @ Slip 1 (ksi) | Stress @ Slip 2 (ksi) | Max Stress (ksi) |
|---|---|---|---|---|---|---|---|---|---|---|
| 09/23/11 | 3/8 | bl. | A | 12 | 13.065 | 12.957 | 13.099 | 0.924 | 0.917 | 0.927 |
| 09/23/11 | 3/8 | bl. | A | 12 | 12.347 | 11.695 | 12.575 | 0.873 | 0.827 | 0.890 |
| 09/23/11 | 3/8 | bl. | A | 9 | 9.048 | 9.200 | 9.200 | 0.853 | 0.868 | 0.868 |
| 09/23/11 | 3/8 | bl. | A | 9 | 8.005 | 8.408 | 8.999 | 0.755 | 0.793 | 0.849 |
| 09/23/11 | 3/8 | bl. | A | 3 | 2.753 | 2.223 | 2.923 | 0.779 | 0.629 | 0.827 |
| 09/23/11 | 3/8 | bl. | A | 3 | 2.635 | 2.257 | 2.750 | 0.746 | 0.639 | 0.778 |
| 09/23/11 | 3/8 | bl. | B | 12 | 5.654 | 11.051 | 13.571 | 0.400 | 0.782 | 0.960 |
| 09/23/11 | 3/8 | bl. | B | 12 | 12.170 | 12.174 | 12.251 | 0.861 | 0.861 | 0.867 |
| 09/23/11 | 3/8 | bl. | B | 9 | 7.515 | 7.209 | 7.521 | 0.709 | 0.680 | 0.709 |
| 09/23/11 | 3/8 | bl. | B | 9 | 6.650 | 6.916 | 8.289 | 0.627 | 0.652 | 0.782 |
| 09/23/11 | 3/8 | bl. | B | 3 | 1.981 | 1.747 | 2.376 | 0.560 | 0.494 | 0.672 |
| 09/23/11 | 3/8 | bl. | B | 3 | 1.937 | 1.724 | 1.996 | 0.548 | 0.488 | 0.565 |
| 09/23/11 | 3/8 | bl. | C | 12 | 7.747 | 9.264 | 11.352 | 0.548 | 0.655 | 0.803 |
| 09/23/11 | 3/8 | bl. | C | 12 | 6.759 | 10.633 | 12.306 | 0.478 | 0.752 | 0.870 |
| 09/23/11 | 3/8 | bl. | C | 9 | 7.050 | 6.359 | 7.276 | 0.665 | 0.600 | 0.686 |
| 09/23/11 | 3/8 | bl. | C | 9 | 7.005 | 6.200 | 7.209 | 0.661 | 0.585 | 0.680 |
| 09/23/11 | 3/8 | bl. | C | 3 | 2.396 | 2.251 | 2.547 | 0.678 | 0.637 | 0.721 |
| 09/23/11 | 3/8 | bl. | C | 3 | 2.186 | 2.227 | 2.788 | 0.618 | 0.630 | 0.789 |
| 09/27/11 | 3/8 | ep. | D | 12 | 7.507 | 8.448 | 16.826 | 0.531 | 0.598 | 1.190 |
| 09/27/11 | 3/8 | ep. | D | 12 | 5.684 | 6.796 | 16.383 | 0.402 | 0.481 | 1.159 |
| 09/27/11 | 3/8 | ep. | D | 9 | 4.153 | 3.552 | 9.153 | 0.392 | 0.335 | 0.863 |
| 09/27/11 | 3/8 | ep. | D | 9 | 4.963 | 2.588 | 5.055 | 0.468 | 0.244 | 0.477 |
| 09/27/11 | 3/8 | ep. | D | 3 | 2.402 | 2.435 | 4.735 | 0.680 | 0.689 | 1.340 |
| 09/27/11 | 3/8 | ep. | D | 3 | 1.459 | 1.901 | 4.690 | 0.413 | 0.538 | 1.327 |
| 09/28/11 | 3/8 | ep. | E | 12 | 4.596 | 6.970 | 15.531 | 0.325 | 0.493 | 1.099 |
| 09/28/11 | 3/8 | ep. | E | 12 | 5.418 | 6.588 | 16.442 | 0.383 | 0.466 | 1.163 |
| 09/28/11 | 3/8 | ep. | E | 9 | 3.072 | 5.121 | 13.221 | 0.290 | 0.483 | 1.247 |
| 09/28/11 | 3/8 | ep. | E | 9 | 2.985 | 4.794 | 13.012 | 0.281 | 0.452 | 1.227 |
| 09/28/11 | 3/8 | ep. | E | 3 | 1.230 | 2.166 | 5.069 | 0.348 | 0.613 | 1.434 |
| 09/28/11 | 3/8 | ep. | E | 3 | 1.141 | 1.952 | 5.129 | 0.323 | 0.552 | 1.451 |
| 09/29/11 | 3/8 | ep. | F | 12 | 6.856 | 9.954 | 18.221 | 0.485 | 0.704 | 1.289 |
| 09/29/11 | 3/8 | ep. | F | 12 | 7.050 | 9.917 | 19.036 | 0.499 | 0.702 | 1.346 |
| 09/29/11 | 3/8 | ep. | F | 9 | 5.219 | 6.827 | 12.461 | 0.492 | 0.644 | 1.175 |
| 09/29/11 | 3/8 | ep. | F | 9 | 5.846 | 8.396 | 14.853 | 0.551 | 0.792 | 1.401 |
| 09/29/11 | 3/8 | ep. | F | 3 | 1.579 | 2.574 | 6.158 | 0.447 | 0.728 | 1.742 |
| 09/29/11 | 3/8 | ep. | F | 3 | 1.635 | 2.695 | 5.366 | 0.463 | 0.763 | 1.518 |
| 09/30/11 | 1/2 | bl. | G | 12 | 15.576 | 16.635 | 16.660 | 0.826 | 0.882 | 0.884 |
| 09/30/11 | 1/2 | bl. | G | 12 | 14.871 | 14.506 | 14.889 | 0.789 | 0.770 | 0.790 |
| 09/30/11 | 1/2 | bl. | G | 12 | 13.315 | 15.271 | 15.721 | 0.706 | 0.810 | 0.834 |
| 09/30/11 | 1/2 | bl. | G | 4 | 2.603 | 3.841 | 4.167 | 0.414 | 0.611 | 0.663 |
| 09/30/11 | 1/2 | bl. | G | 4 | 3.564 | 4.416 | 5.063 | 0.567 | 0.703 | 0.806 |
| 09/30/11 | 1/2 | bl. | G | 4 | 3.869 | 3.603 | 4.111 | 0.616 | 0.573 | 0.654 |
| 10/05/11 | 1/2 | bl. | H | 12 | 14.717 | 16.711 | 16.975 | 0.781 | 0.887 | 0.901 |
| 10/05/11 | 1/2 | bl. | H | 12 | 13.128 | 14.566 | 15.243 | 0.696 | 0.773 | 0.809 |
| 10/05/11 | 1/2 | bl. | H | 12 | 14.042 | 15.763 | 18.019 | 0.745 | 0.836 | 0.956 |
| 10/05/11 | 1/2 | bl. | H | 4 | 2.579 | 4.485 | 4.690 | 0.410 | 0.714 | 0.746 |
| 10/05/11 | 1/2 | bl. | H | 4 | 2.671 | 4.946 | 5.130 | 0.425 | 0.787 | 0.816 |
| 10/05/11 | 1/2 | bl. | H | 4 | 3.886 | 4.571 | 6.044 | 0.618 | 0.727 | 0.962 |
| 10/06/11 | 1/2 | ep. | I | 12 | 10.322 | 8.353 | 17.358 | 0.548 | 0.443 | 0.921 |
| 10/06/11 | 1/2 | ep. | I | 12 | 11.286 | 9.445 | 12.527 | 0.599 | 0.501 | 0.665 |
| 10/06/11 | 1/2 | ep. | I | 4 | 6.153 | 5.532 | 8.237 | 0.979 | 0.880 | 1.311 |
| 10/06/11 | 1/2 | ep. | I | 4 | 4.042 | 3.363 | 5.161 | 0.643 | 0.535 | 0.821 |
| 10/07/11 | 1/2 | ep. | J | 16 | 13.947 | 13.947 | 14.081 | 0.555 | 0.555 | 0.560 |
| 10/07/11 | 1/2 | ep. | J | 16 | 10.524 | 8.173 | 14.390 | 0.419 | 0.325 | 0.573 |
| 10/07/11 | 1/2 | ep. | J | 12 | 7.927 | 7.599 | 12.527 | 0.421 | 0.403 | 0.665 |
| 10/07/11 | 1/2 | ep. | J | 4 | 2.541 | 3.125 | 6.059 | 0.404 | 0.497 | 0.964 |
| 10/07/11 | 1/2 | ep. | J | 4 | 2.955 | 3.070 | 7.041 | 0.470 | 0.489 | 1.121 |
| 10/11/11 | 1/2 | ep. | K | 16 | 17.393 | 17.393 | 17.568 | 0.692 | 0.692 | 0.699 |
| 10/11/11 | 1/2 | ep. | K | 12 | 14.128 | 13.660 | 14.659 | 0.750 | 0.725 | 0.778 |
| 10/11/11 | 1/2 | ep. | K | 12 | 8.821 | 9.540 | 11.812 | 0.468 | 0.506 | 0.627 |
| 10/11/11 | 1/2 | ep. | K | 4 | 2.408 | 2.844 | 4.780 | 0.383 | 0.457 | 0.761 |
| 10/11/11 | 1/2 | ep. | K | 4 | 2.950 | 2.959 | 4.867 | 0.469 | 0.471 | 0.775 |

**Table 11.2 Averages calculated from the profile summary for each strand at its different embedment lengths.**

| D.str (in.) | Type Str. | L.embed (in.) | Non-Norm. Tau At Slip 1 (ksi) | ST.DEV (ksi) | Coeff. VAR. | Non-Norm. Tau At Slip 2 (ksi) | ST.DEV (ksi) | Coeff. VAR. | Max Non-Norm. Tau (ksi) | ST.DEV (ksi) | Coeff. VAR. | Avg. Coeff. VAR. |
|---|---|---|---|---|---|---|---|---|---|---|---|---|
| 3/8 | bl. | 3 | 0.655 | 0.096 | 0.146 | 0.586 | 0.074 | 0.126 | 0.725 | 0.096 | 0.132 | 0.135 |
| 3/8 | bl. | 9 | 0.712 | 0.082 | 0.116 | 0.696 | 0.112 | 0.161 | 0.762 | 0.083 | 0.109 | 0.128 |
| 3/8 | bl. | 12 | 0.681 | 0.231 | 0.339 | 0.799 | 0.091 | 0.114 | 0.886 | 0.054 | 0.061 | 0.171 |
| 1/2 | bl. | 4 | 0.509 | 0.102 | 0.202 | 0.686 | 0.079 | 0.115 | 0.775 | 0.114 | 0.148 | 0.155 |
| 1/2 | bl. | 12 | 0.757 | 0.051 | 0.067 | 0.826 | 0.051 | 0.062 | 0.862 | 0.063 | 0.073 | 0.067 |
| 3/8 | ep. | 3 | 0.445 | 0.127 | 0.285 | 0.647 | 0.094 | 0.145 | 1.469 | 0.152 | 0.104 | 0.178 |
| 3/8 | ep. | 9 | 0.412 | 0.111 | 0.269 | 0.492 | 0.200 | 0.408 | 1.065 | 0.338 | 0.317 | 0.331 |
| 3/8 | ep. | 12 | 0.438 | 0.079 | 0.182 | 0.574 | 0.110 | 0.192 | 1.208 | 0.092 | 0.076 | 0.150 |
| 1/2 | ep. | 4 | 0.558 | 0.226 | 0.404 | 0.554 | 0.162 | 0.293 | 0.959 | 0.220 | 0.230 | 0.309 |
| 1/2 | ep. | 12 | 0.557 | 0.128 | 0.230 | 0.516 | 0.124 | 0.241 | 0.731 | 0.120 | 0.165 | 0.212 |

## 11.4 RESULTS

Based on the compiled data from the sixty-two strand bond tests, conclusions were developed on what type of strand has the largest bond stress capacity as well as the effects on stress capacity of a strand's diameter, embedment length, and grout mix's compressive strength. The following sections describe the findings derived from the strand bond test analyses.

### 11.4.1 Effect of Epoxy Coating on a Strand's Bond Stress Capacity

This section focuses on the effect of the grit-impregnated epoxy coating on the strand's bond stress for the 3/8-in.- and 1/2-in.-diameter strands. Figures 11.9 to 11.14 compares the three slip levels for the 3/8-in.- and 1/2-in.-diameter black strands with the 3/8-in.- and1/2- in-diameter epoxy-coated strands, respectively. In order to allow bond stress comparisons across strand embedment lengths, their embedment lengths were divided by their respective strand's diameter.

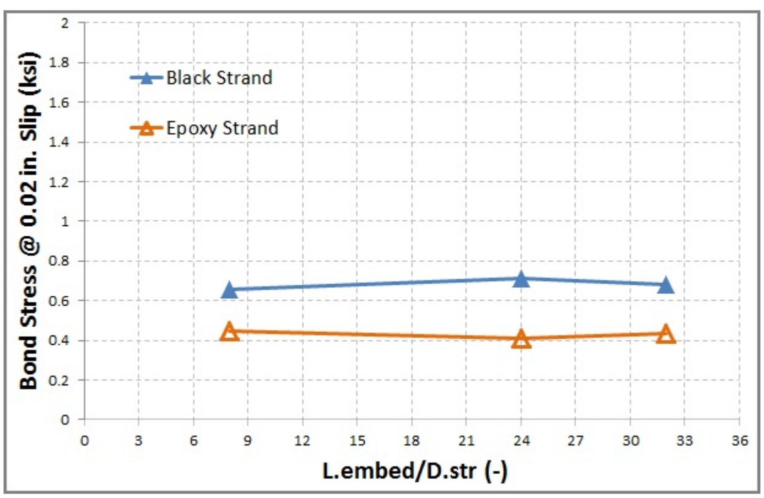


**Figure 11.9 Bond stresses at 0.02 in. slip: 3/8-in. black versus 3/8-in. epoxy strand.**

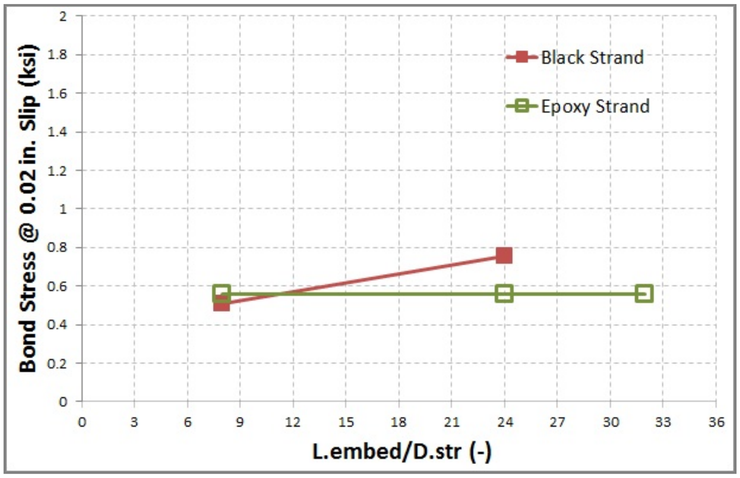


Figure 11.10 Bond stresses at 0.02 in. slip: 1/2-in. black versus 1/2-in. epoxy strand.

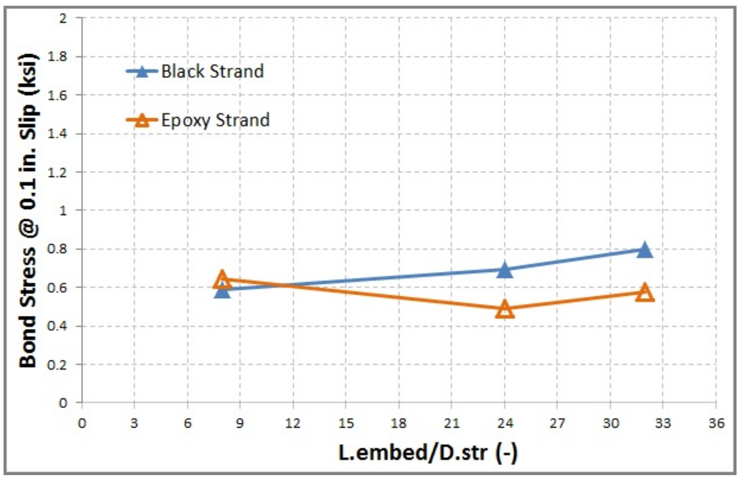


Figure 11.11 Bond stresses at 0.1 in. slip: 3/8-in. black versus 3/8-in. epoxy strand.

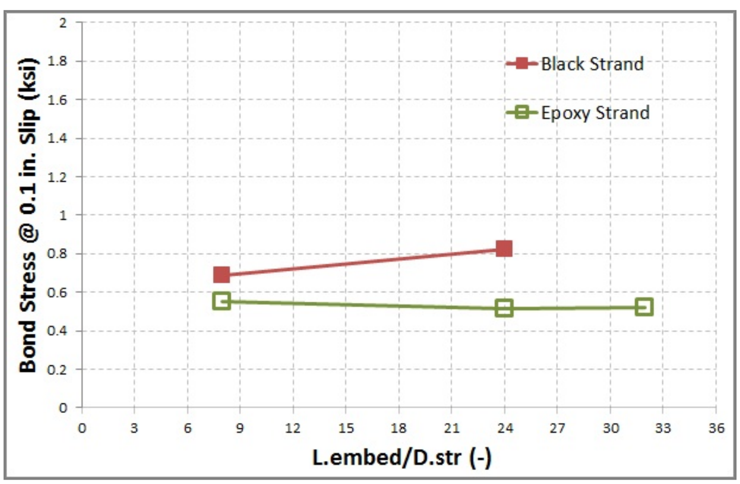


Figure 11.12 Bond stresses at 0.1 in. slip: 1/2-in. black versus 1/2-in. epoxy strand.

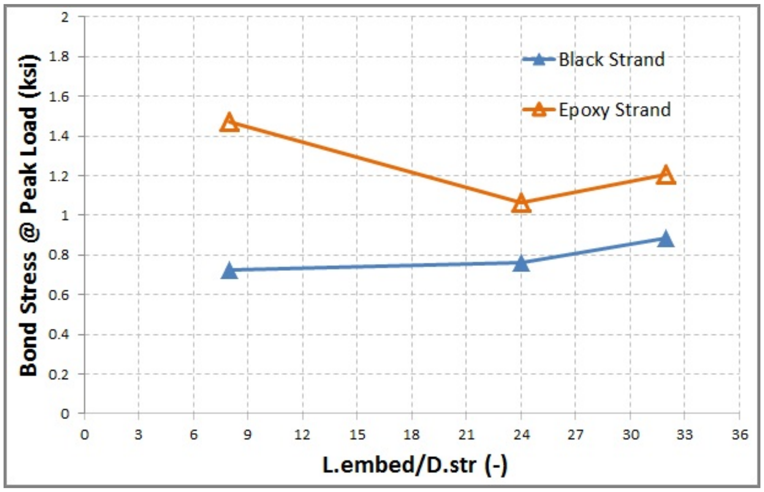


**Figure 11.13** Bond stresses at the peak load: 3/8-in. black versus 3/8-in. epoxy strand.

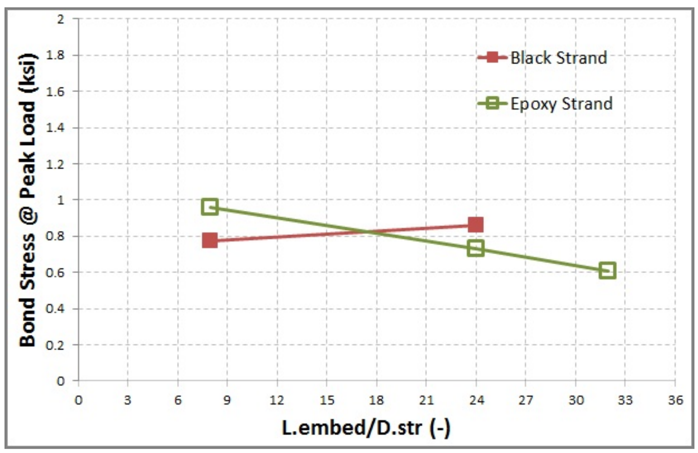


**Figure 11.14** Bond stresses at the peak load: 1/2-in. black versus 1/2-in. epoxy strand.

At lower slip displacements the black strand, on average across all of its embedment lengths, yields a larger bond stress than the epoxy strand for both the 3/8-in. and 1/2-in. case. However in the larger slip displacement, which occurs at the strand's peak load capacity, the 3/8-in. black strand has a larger bond stress than its epoxy counterpart. For the 1/2-in. case this is not as clear because the black and epoxy yielded very similar average bond stresses at its peak load across all of their embedment lengths; see Figure 11.14.

In this study, the effect of only one type of grit coating for the epoxy strand was investigated. Since no visual inspection of the epoxy coated strands was made, there is no conclusive reason why the 1/2-in. black and epoxy strands have similar average bond stresses across their embedment lengths at their peak load.

### 11.4.2 Effect of Diameter and Embedment Length on a Strand's Bond Stress Capacity

A strand's diameter and embedment length are two other factors considered in analyzing the carbon black and epoxy strand's bond stresses. Figures 11.15 to 11.20 compare the 3/8-in. carbon black and epoxy strand's bond stress capacity with the 1/2-in. carbon black and epoxy strand's bond stress capacity, respectively. The average bond stress and coefficient of variation included in each graph refer to the data points from all of the bond stresses in the graph. For instance, Figure 11.15 displays five data points that represent bond stresses, three bond stresses from the 3/8-in. strand and two bond stresses from the ½-in. strand. The average bond stress and coefficient of variation in Figure 11.15 refers to the five bond stress values mentioned. In the same manner, the average bond stress and coefficient of variation was found and displayed for each graph.

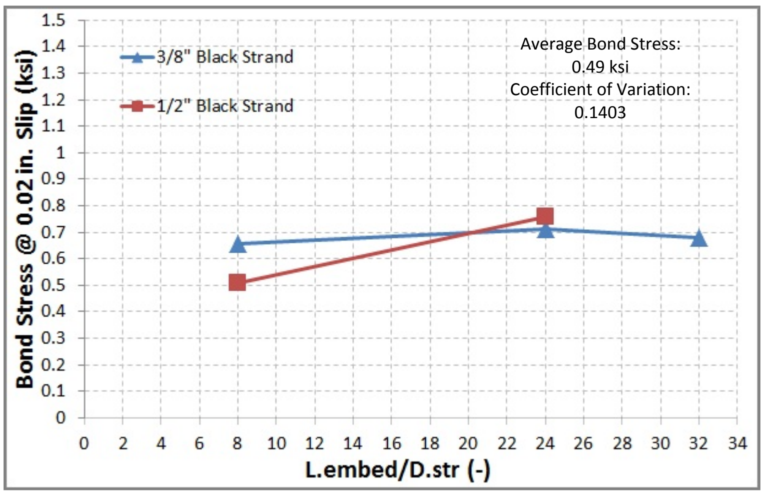


**Figure 11.15 Bond stresses at 0.02 in. slip: 3/8-in. black versus 1/2-in. black strand.**

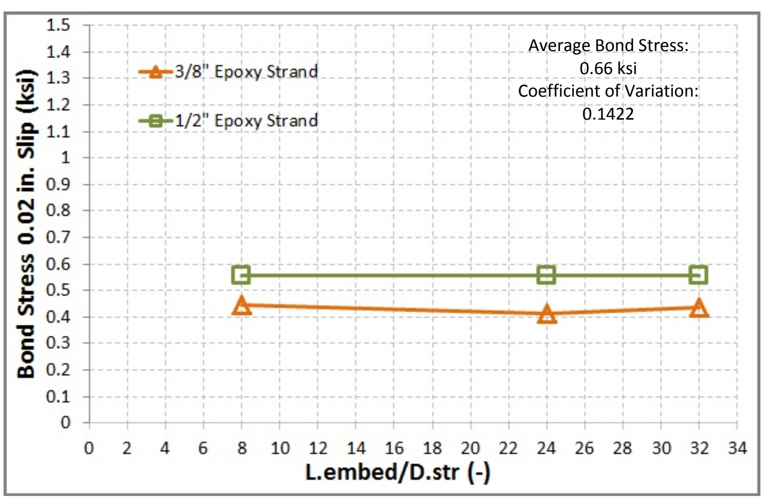


**Figure 11.16 Bond stresses at 0.02 in. slip: 3/8-in. epoxy versus 1/2-in. epoxy strand.**

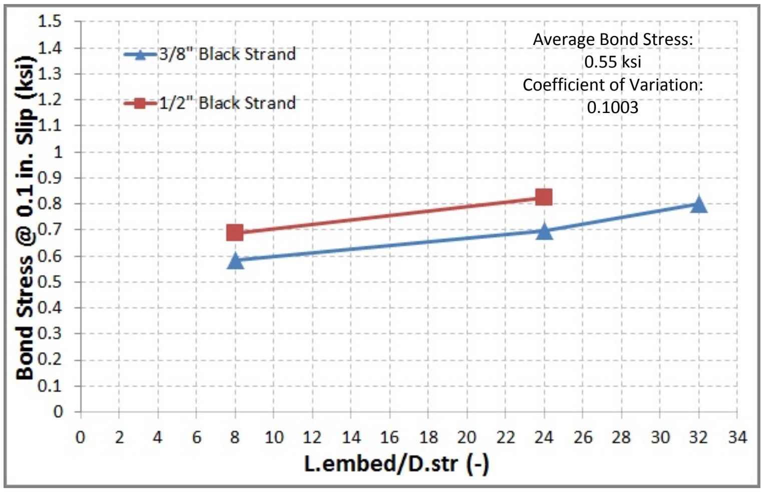


**Figure 11.17 Bond stresses at 0.1 in. slip: 3/8-in. black versus 1/2-in. black strand.**

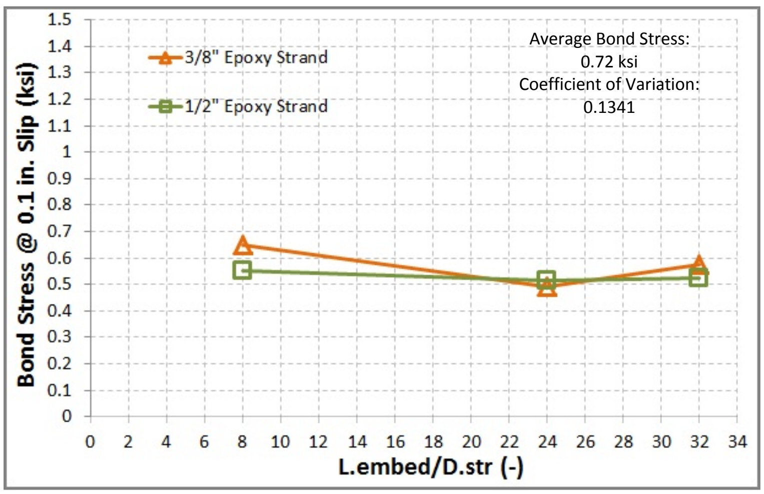


**Figure 11.18 Bond stresses at 0.1 in. slip: 3/8-in. epoxy versus 1/2-in. epoxy strand.**

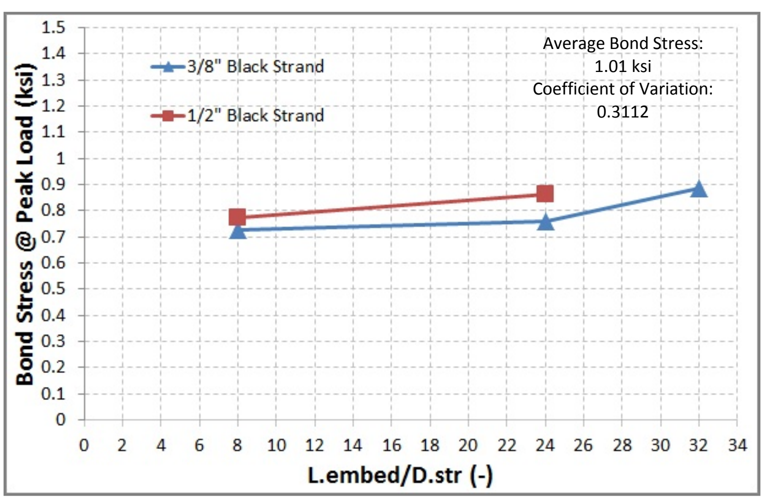


**Figure 11.19 Bond stresses at the peak load: 3/8-in. black versus 1/2-in. black strand.**

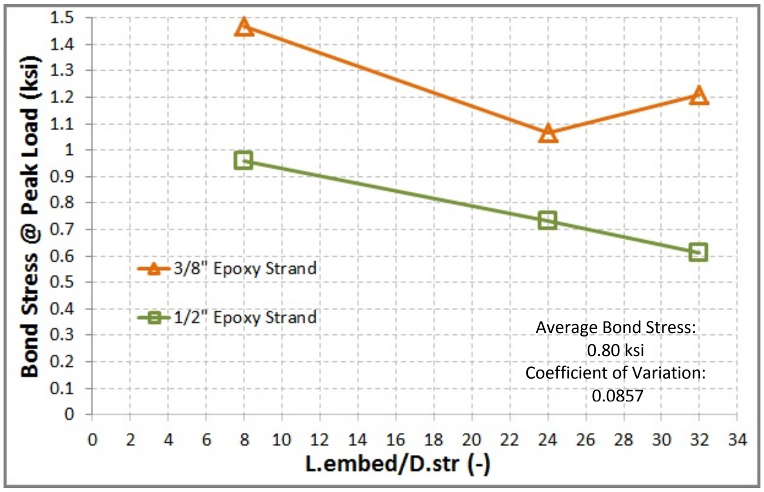


**Figure 11.20 Bond stresses at the peak load: 3/8-in. epoxy vs. 1/2-in. epoxy strand.**

Since there is little variability among the bond stresses for the 3/8-in. black and epoxy strands that are averaged with the 1/2-in. black and epoxy strand's bond stresses at all of its embedment lengths, respectively, the strand's diameter has no significant effect on both strands' bond stress capacity. This conclusion is suggested by the low coefficients of variability shown in Figures 11.15 to 11.20. Figure 11.20, however, which compares the 3/8-in. and 1/2-in. epoxy strand's peak bond stresses and has a coefficient of variability of 0.31, the remaining graphs have a consistently low and similar coefficient of variation. The high amount of variability shown in Figure 11.20 may be the result of testing error.

In order to determine if the strand's embedment length affects its average bond stress, the variability in bond stresses among the black and epoxy strand's various embedment lengths was analyzed. Table 11.3 shows the summary of comparing these bond stresses. The average coefficient of variability was calculated by averaging all of the coefficients of variability taken from the two slip displacements and peak load. The last column of this table, which shows consistently low average coefficients of variability, suggests that a strand's embedment length does not affect its average bond stress.

**Table 11.3 Summary of the average bond stress for all respective embedment lengths for the 3/8 in. and 1/2 in. black and epoxy strands.**

| D.str (in.) | Type Str. | Avg. Tau @ 0.02 in. Slip (ksi) | ST.DEV (ksi) | Coeff. VAR. | Avg. Tau @ 0.1 in. Slip (ksi) | ST.DEV (ksi) | Coeff. VAR. | Avg. Tau @ Peak Load (ksi) | ST.DEV (ksi) | Coeff. VAR. | Avg. Coeff. VAR. |
|---|---|---|---|---|---|---|---|---|---|---|---|
| 3/8 | bl. | 0.682 | 0.028 | 0.042 | 0.694 | 0.106 | 0.153 | 0.791 | 0.084 | 0.106 | 0.100 |
| 1/2 | bl. | 0.633 | 0.176 | 0.278 | 0.756 | 0.099 | 0.131 | 0.818 | 0.062 | 0.076 | 0.162 |
| 3/8 | ep. | 0.432 | 0.017 | 0.040 | 0.571 | 0.078 | 0.136 | 1.247 | 0.205 | 0.164 | 0.113 |
| 1/2 | ep. | 0.557 | 0.002 | 0.003 | 0.531 | 0.020 | 0.038 | 0.767 | 0.177 | 0.231 | 0.091 |

Since it is determined that a given strand's diameter and embedment length have little effect in its bond stress capacity, the black strand's average bond stresses at its two slip displacements and peak load can be compared to the epoxy strand's average bond stresses. Figure 11.21 compares the black and epoxy strand's average bond stresses shown in Figures 11.15 to 11.20. By averaging the black strand's percent change in bond stresses from its epoxy counterpart at a 0.02-in. and 0.1-in. slip displacement, as well as the peak load, it is determined that the black strand has about a 15% larger average bond stress than the epoxy coated strand.

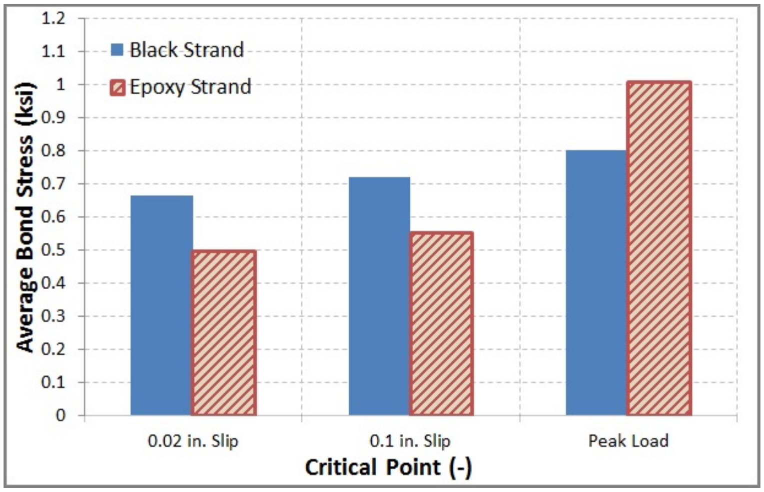


**Figure 11.21** **Average bond stresses at the two slip displacements and peak load: black versus epoxy strand.**

### 11.4.3 Effect of the Grout's Compressive Strength on a Strand's Bond Stress

The strand bond test results were normalized to determine how the grout's compressive strength affects the strand's bond. The bond stresses in Table 11.1 were normalized by dividing them by the square root of their respective mix's compressive strength shown in Table 11.4, with the exception of grout mix K (whose compressive strength was not recorded). The summary of all the averages is shown in Table 11.5.

**Table 11.4** **Grout mix data.**

| Grout Mix | Compressive Strength (psi) |
|---|---|
| A | 5938 |
| B | 5242 |
| C | 4563 |
| D | 4863 |
| E | 4688 |
| F | 6444 |
| G | 5175 |
| H | 5363 |
| I | 5013 |
| J | 4688 |
| K | N/A |

**Table 11.5 Summary of the average normalized bond stress for all respective embedment lengths for the 3/8-in. and 1/2-in. black and epoxy strands.**

| D.str (in.) | Type Str. | L.embed (in.) | Norm. Tau At Slip 1 | ST. DEV. | Coeff. VAR. | Norm. Tau At Slip 2 | ST. DEV. | Coeff. VAR. | Max Norm. Tau | ST. DEV. | Coeff. VAR. | Avg. Coeff. VAR. |
|---|---|---|---|---|---|---|---|---|---|---|---|---|
| 3/8 | bl. | 3 | 9.048 | 1.132 | 0.125 | 8.129 | 1.166 | 0.143 | 10.044 | 1.353 | 0.135 | 0.134 |
| 3/8 | bl. | 9 | 9.825 | 0.764 | 0.078 | 9.581 | 1.004 | 0.105 | 10.516 | 0.588 | 0.056 | 0.079 |
| 3/8 | bl. | 12 | 9.322 | 2.782 | 0.298 | 11.026 | 0.826 | 0.075 | 12.262 | 0.661 | 0.054 | 0.142 |
| 1/2 | bl. | 4 | 7.010 | 1.430 | 0.204 | 9.445 | 1.020 | 0.108 | 10.665 | 1.510 | 0.142 | 0.151 |
| 1/2 | bl. | 12 | 10.437 | 0.741 | 0.071 | 11.384 | 0.704 | 0.062 | 11.876 | 0.814 | 0.069 | 0.067 |
| 3/8 | ep. | 3 | 6.132 | 1.825 | 0.298 | 8.864 | 0.830 | 0.094 | 20.168 | 1.250 | 0.062 | 0.151 |
| 3/8 | ep. | 9 | 5.612 | 1.202 | 0.214 | 6.641 | 2.268 | 0.341 | 14.574 | 4.414 | 0.303 | 0.286 |
| 3/8 | ep. | 12 | 5.997 | 0.942 | 0.157 | 7.830 | 0.957 | 0.122 | 16.592 | 0.448 | 0.027 | 0.102 |
| 1/2 | ep. | 4 | 8.924 | 3.533 | 0.396 | 8.600 | 2.564 | 0.298 | 15.142 | 2.974 | 0.196 | 0.297 |
| 1/2 | ep. | 12 | 7.445 | 1.184 | 0.159 | 6.408 | 0.608 | 0.095 | 10.700 | 2.004 | 0.187 | 0.147 |

Table 11.5 also shows the standard deviations from the test data collected for the normalized bond stress at each slip displacement and maximum bond stress. The last column shows the average coefficient of variation among all of the variation in the bond stresses for each slip displacement and maximum bond stress. Figures 11.22 to 11.26 were created from Table 11.5 in order to show the differences in normalized bond stress between the 3/8-in. and 1/2-in. black strand and 3/8-in. and 1/2-in. epoxy-coated strands, respectively.

A side-by-side comparison of Tables 11.2 and 11.5 reveals that normalizing the bond stresses for each strand bond test profile decreased the average coefficient of variation. A lower coefficient of variation means that there is less variability in the data from the strand bond tests. For these strand bond tests this reduction in variability was small as there was little variability in the grout's compressive strength among the samples used for the strand bond tests. However, this normalization is still important in order to determine which type of strand yields a higher bond stress regardless of the grout's compressive strength. Figures 11.22 to 11.27 compare the normalized bond stresses between the black and epoxy strand for its two diameter lengths, 3/8 in. and 1/2 in., at the two critical slip displacements and peak load for all its embedment lengths.

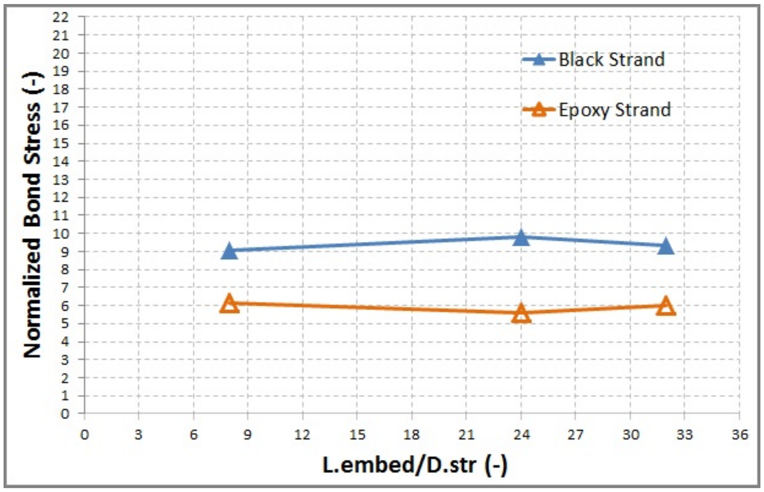


**Figure 11.22 Normalized bond stresses at 0.02 in. slip: 3/8-in. black versus 3/8-in. epoxy strand.**

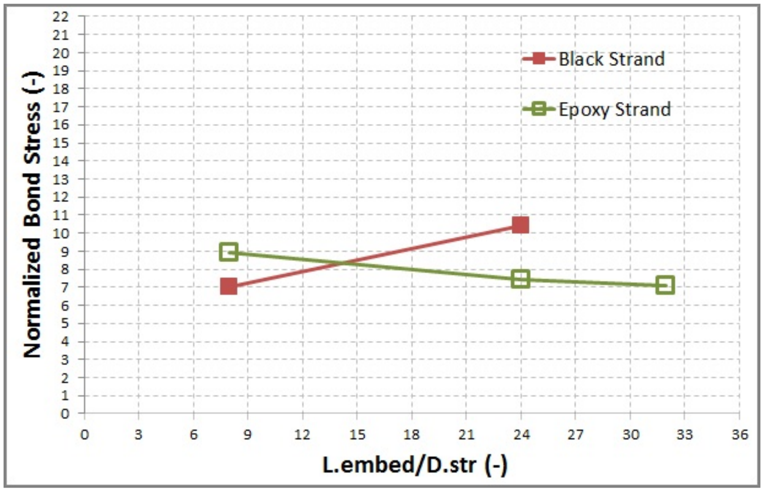


**Figure 11.23 Normalized bond stresses at 0.02 in. slip: 1/2-in. black versus 1/2-in. epoxy strand.**

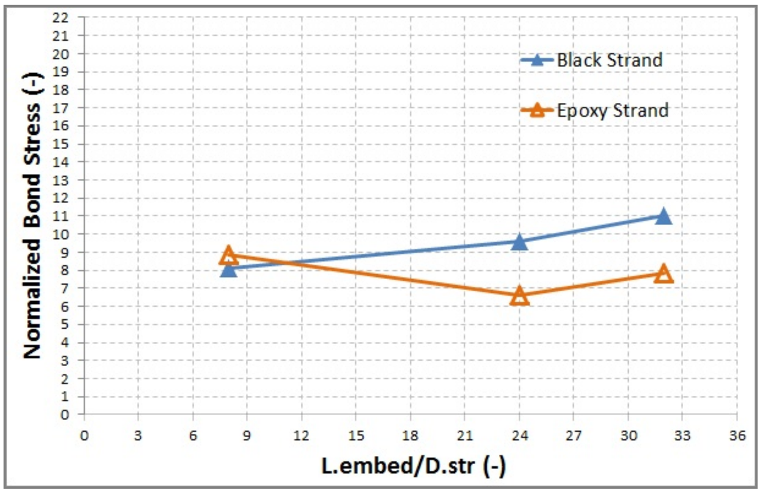


**Figure 11.24 Normalized bond stresses at 0.1 in. slip: 3/8-in. black versus 3/8-in. epoxy strand.**

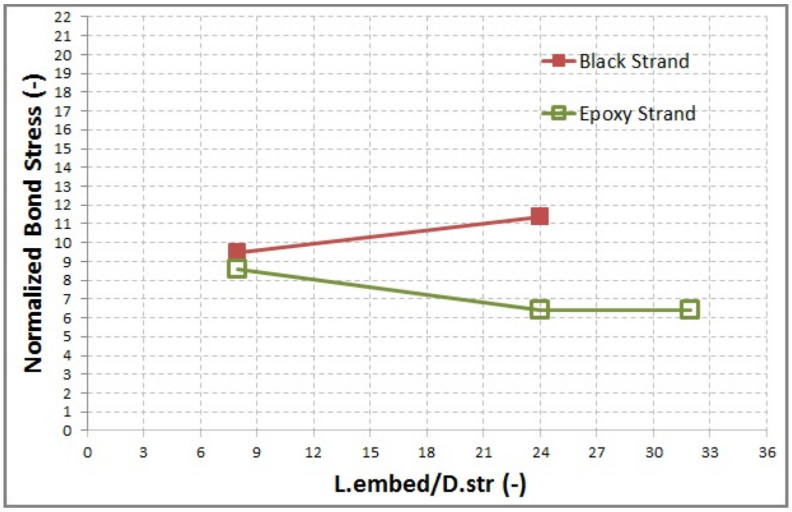


**Figure 11.25** Normalized bond stresses at 0.1 in. slip: 1/2-in. black versus 1/2-in. epoxy strand.

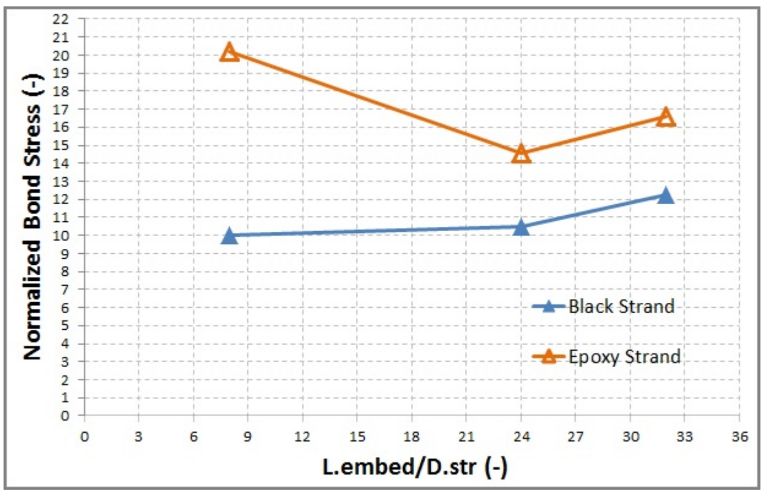


**Figure 11.26** Normalized bond stresses at the peak load: 3/8-in. black versus 3/8-in. epoxy strand.

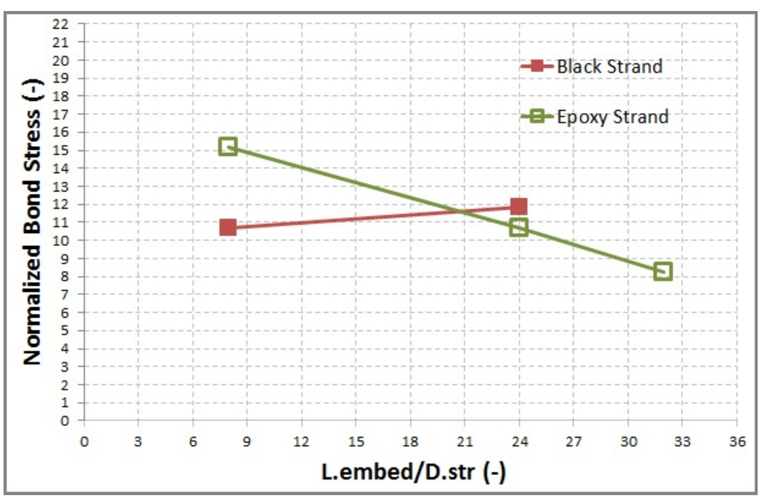


**Figure 11.27** Normalized bond stresses at the peak load: 1/2-in. Black versus 1/2-in. epoxy strand.

Lastly, Figures 11.28 to 11.33 compare the normalized bond stresses of the 3/8-in. black strand and 1/2-in. black strand, as well as the differences in normalized bond stresses between the 3/8-in. epoxy and 1/2-in. epoxy strands. The average bond stress included in each graph represents the average from all of the data points in the graph that represent bond stresses. These values were calculated in the same way as for Figures 11.15 to 11.20. Similarly, the average bond stress and coefficient of variation are shown for each graph. Each figure has a low coefficient of variability. Therefore, since there is little variability in the normalized bond stresses between the 3/8-in. and1/2-in. black strands as well as between the 3/8-in. and 1/2-in. epoxy-coated strands, it is clear that a strand's diameter has no effect on both strands' normalized bond stress capacity.

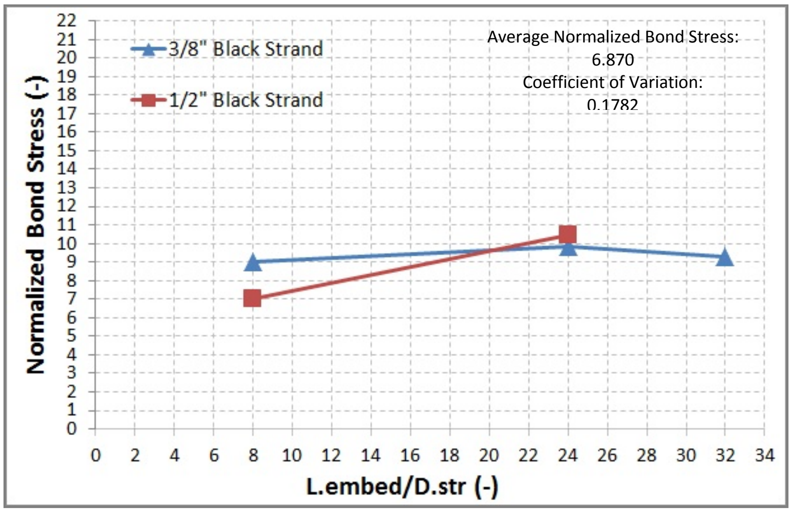


**Figure 11.28 Normalized bond stresses at 0.02 in. slip: 3/8-in. black versus 1/2-in. black strand.**

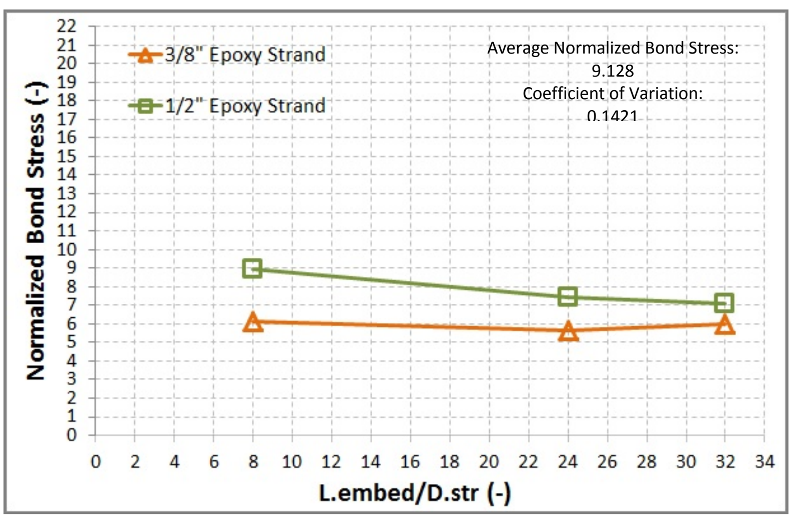


**Figure 11.29 Normalized bond stresses at 0.02 in. slip: 3/8-in. epoxy versus 1/2-in. epoxy strand.**

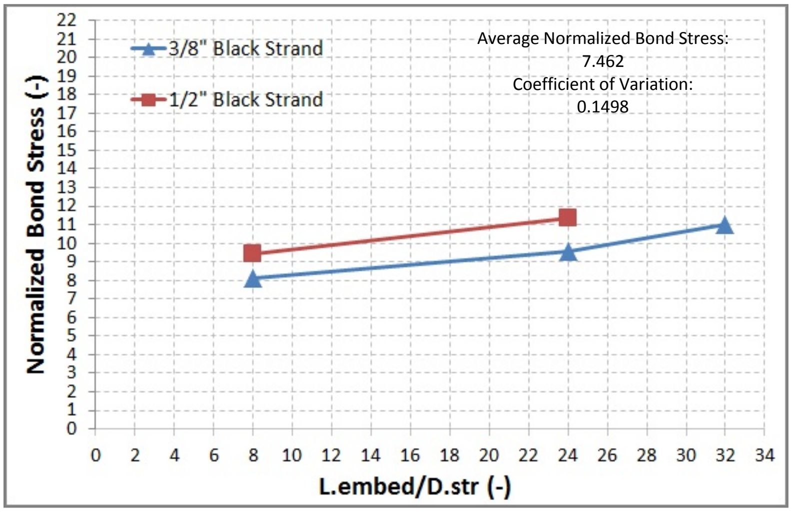


**Figure 11.30 Normalized bond stresses at 0.1 in. slip: 3/8-in. black versus 1/2-in. black strand.**

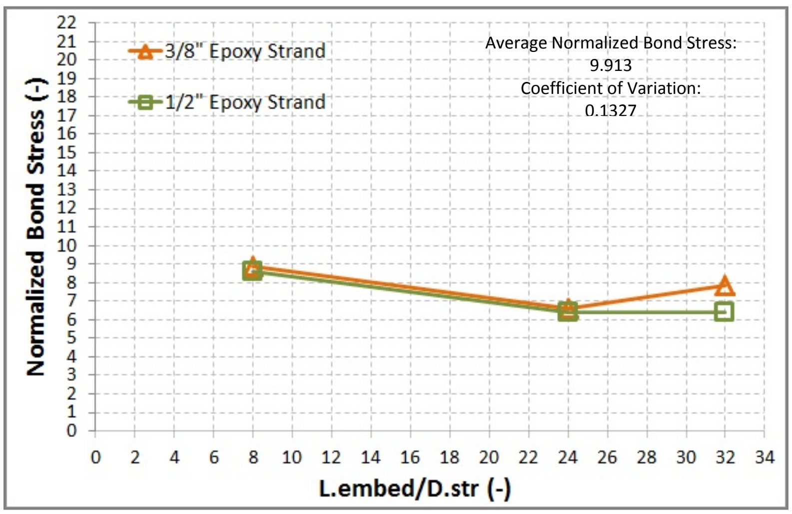


**Figure 11.31 Normalized bond stresses at 0.1 in. slip: 3/8-in. epoxy versus 1/2-in. epoxy strand.**

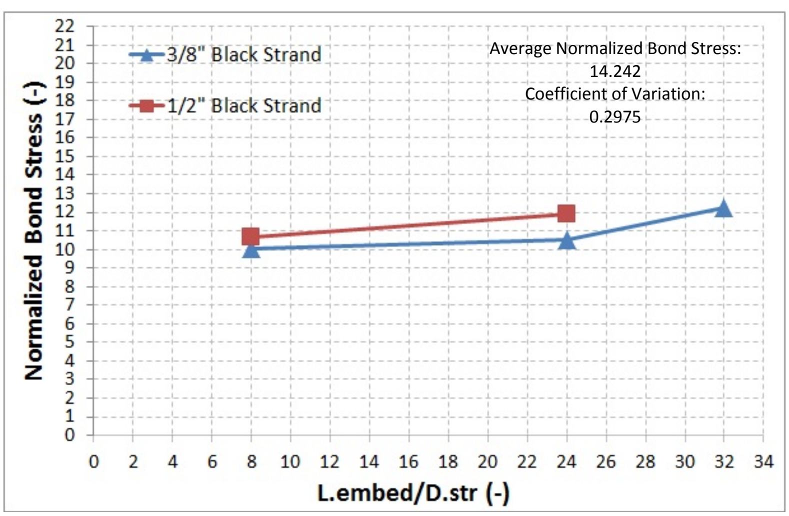


**Figure 11.32 Normalized bond stresses at the peak load: 3/8-in. black versus 1/2-in. black strand.**

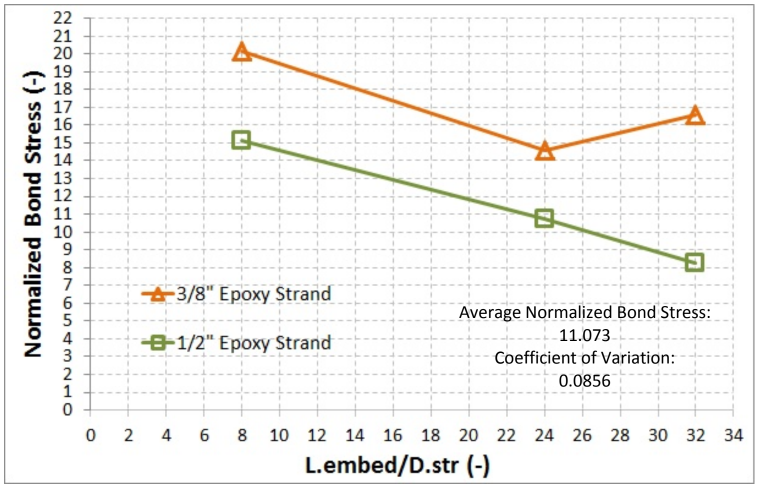


**Figure 11.33 Normalized bond stresses at the peak load: 3/8-in. black versus 1/2-in. black strand.**

To determine if the strand's embedment length affects its average normalized bond stress, it is necessary to analyze the variability in normalized bond stresses among the different embedment lengths for the black and epoxy strand. Table 11.6 summarizes the comparison of these normalized bond stresses across the strand's various embedment lengths. The last column of this table, which shows the average coefficients of variability for each strand type, suggests that a strand's embedment length does not affect its average normalized bond stress as these coefficients are consistently low.

**Table 11.6 Summary of normalized bond stresses for the 3/8-in. and 1/2-in. black and epoxy strands.**

| D.str (in.) | Type Str. | Norm. Tau @ 0.02 in. Slip | ST.DEV | Coeff. VAR. | Norm. Tau @ 0.1 in. Slip | ST.DEV | Coeff. VAR. | Norm. Tau @ Peak Load | ST.DEV | Coeff. VAR. | Avg. Coeff.VAR |
|---|---|---|---|---|---|---|---|---|---|---|---|
| 3/8 | bl. | 9.398 | 0.394 | 0.042 | 9.579 | 1.449 | 0.151 | 10.941 | 1.168 | 0.107 | 0.100 |
| 1/2 | bl. | 8.723 | 2.423 | 0.278 | 10.415 | 1.371 | 0.132 | 11.271 | 0.856 | 0.076 | 0.162 |
| 3/8 | ep. | 4.359 | 2.511 | 0.576 | 7.779 | 1.112 | 0.143 | 17.111 | 2.833 | 0.166 | 0.295 |
| 1/2 | ep. | 7.827 | 0.965 | 0.123 | 7.145 | 1.260 | 0.176 | 11.372 | 3.484 | 0.306 | 0.202 |

Since it is determined that a given strand's diameter and embedment length have little effect in its normalized bond stress capacity, the black strand's average normalized bond stresses at its two slip displacements and peak load can be compared to the epoxy strand's average normalized bond stresses. Figure 11.34 compares the black and epoxy strand's average normalized bond stresses obtained from Figures 11.28 to 11.33. By averaging the black strand's percent change in normalized bond stresses from its epoxy counterpart at a 0.02-in. and 0.1-in. slip displacement as well as the peak load, it is determined that the black strand has about a 14% larger average normalized bond stress than the epoxy coated strand.

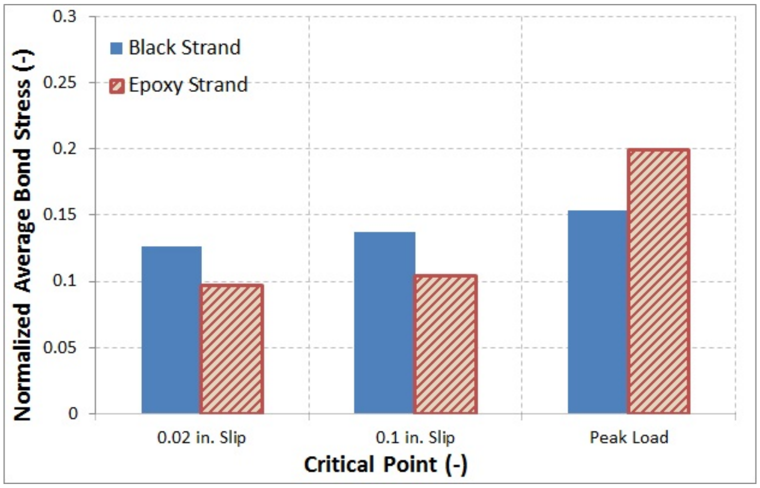


**Figure 11.34 Average normalized bond stresses at the two slip displacements and peak load: black versus epoxy strand.**

## 11.5 SUMMARY, CONCLUSIONS, AND RECOMMENDATIONS

### 11.5.1 Summary

Test data on the pull-out strength of pre-stressed strands were analyzed. The goal was to identify the major differences between the bond properties of epoxy coated and uncoated strands. All the tests were carried out by others in a previous project. While previous investigators have obtained three grades of grit embedded in the surface of the epoxy coating, only one grade was available when these tests were conducted. During fabrication, the grit application was controlled manually and the resulting grit density varied.

The specimens consisted of individual strands embedded in grout cylinders, each encased in steel tubes in accordance with the requirements for acceptance testing issued by the North American Strand Producers' Association (NASP). In all cases the strands were unstressed at the time of casting. Two strand sizes (3/8-in.- and 1/2-in.-diameter strands) were used, and the test strands were embedded for a range of different lengths. The strands were loaded in tension, and the load and displacement were recorded. The load data were converted to average bond stress in order to permit comparisons across strand diameters and embedment lengths.

### 11.5.2 Conclusions

The following conclusions were drawn from the study:

1. The average bond stress along the embedded length was almost the same regardless of embedded length for all three load levels considered (0.02-in. and 0.1-in. slip at the loaded end and at peak load). This suggests that the bond stress is almost constant along the embedment length. This was expected at peak load and for all load levels in specimens with short embedment lengths, but not when the load was low and the embedment length was long.

2. The average bond strength was not significantly affected by the strand's diameter or embedment length. It may therefore be regarded as a material property of the strand-grout interface.
3. Normalization of the bond stress with respect to either the grout strength or its square root did not affect conclusions 1 and 2 above. However, only a limited range of grout strengths was used. If a wider range were investigated, this conclusion might need to be revised.
4. Considering conclusions 1 and 2, averaging the bond stresses of the 3/8-in. and 1/2-in. black strands yields the represented average bond stress for the black strand. This can also be said about the epoxy strand. Therefore, the black strand has about a 15% larger average bond stress than the epoxy coated strand (Figure 11.21). Averaging the normalized bond stresses of the 3/8-in. and 1/2-in. black strands yields the represented average normalized bond stress for the black strand. This is also true for the epoxy strand, respectively. Based on these average values, the black strand has about a 14% larger average normalized bond stress than the epoxy coated strand (Figure 11.34).
5. These differences in normalized and non-normalized bond stresses between the two types of strands are likely influenced by the relatively small number of tests conducted (65 in all) as well as the epoxy-coated strand's grit density. Until more tests can be conducted and the epoxy strand's grit density is analyzed more thoroughly, the differences in bond strength between the two types of strand should be regarded as insignificant.

### 11.5.3 Recommendations

The number of tests conducted in the previous program and evaluated here was too small to develop firm recommendations for practice. However, the following provisional recommendations are proposed:

- Epoxy-coated strands should be treated as having the same bond properties as uncoated stands, provided that the epoxy coating is impregnated with grit.
- The average bond stress capacity for the black strand may be taken as 0.66 ksi at low loads (0.02-in. slip), 0.72 ksi at intermediate loads (0.1-in. slip), and 0.80 ksi at peak load. The corresponding coefficients of variation are 0.14, 0.13, and 0.086.
- The average bond stress capacity for the epoxy strand may be taken as 0.49 ksi at low loads (0.02-in. slip), 0.55 ksi at intermediate loads (0.1-in. slip) and 1.01 ksi at peak load, and the corresponding coefficients of variation are 0.1403, 0.1003, and 0.3112, respectively.

More strand bond tests are needed to revise the provisional conclusions above. Additional strand pull-out tests at a variety grout compressive strengths are suggested in order to determine the grout mix strength's effect on a given strand's bond stress. As pointed out by Brearley and Johnston [1990], the epoxy-coated strand's grit coating affects its bond with concrete. This point may also be true for grout, but more tests are needed to support this fact. With this in mind, for all future strand bond tests on epoxy-coated strands should consider grit density. For the best results possible, the researcher would have to document each strand's grit density prior to testing in order to diminish variation in the epoxy coated strand's bond stresses as a result of differences in grit densities.

## ACKNOWLEDGMENTS

The author would like to thank Professors Marc O. Eberhard and John F. Stanton, as well as my graduate student mentor, Olafur S. Haraldsson for the tremendous amount of help and support they gave me in completing this project. I would also like to thank Heidi Tremayne for her help in organizing the PEER internship program and the National Science Foundation, whose funding made it possible for me to conduct research at the University of Washington.

## REFERENCES

Brearley Jr LM, and DW Johnston (1990). Pull-out bond tests of epoxy-coated prestressing strand, *J. Struct. Eng*., 116(8):2236–2252.

Davis PM, T Janes, MP Eberhard, and JF Stanton (2012). Unbonded pre-tensioned columns for bridges in seismic regions, *PEER Report 2012/04*, Pacific Earthquake Engineering Research Center, University of California, Berkeley, CA.

LeClaire PJ, and AF Shaikh (1996). Effect of elevated temperature on the bond strength of epoxy-coated prestressing strand, *PCI J*., 41(4):54–61.

Pang JBP, KP Steuck, L Cohagen, JF Stanton, and MP Eberhard (2008). Rapidly constructible large-bar precast bridge-bent seismic connection, Washington State Department of Transportation, Olympia, WA.

Steuck KP, JBK Pang, JF Stanton, and MP Eberhard (2007). Anchorage of large bars in grouted ducts, *Report No. WA-RD 684.1*, Washington State Department of Transportation, Olympia, WA.

# 12. Testing the Integrity of Steel Gravity Frames subjected to Large Vertical Deflections: Connection Component and Bolt Tests

STEPHANIE LÓPEZ CRUZ


## ABSTRACT

Researchers at the University of Washington (UW), Purdue University (PU) and the University of Illinois at Urbana-Champaign (UIUC) have been studying the behavior of steel gravity frame systems subject to an event in which a column collapses or loses its ability to support gravity load. In this scenario, alternate load paths must be developed to support the gravity load and prevent collapse of the structure. At UW, various connection geometries including single plate shear bolted web-angle, and top-and-seat angle connections have been tested. Preliminary results show that single-plate shear connections fail by tear-out of the bolt edge distance on the shear plate or beam web, or by shear fracture of the bolts. These results have also shown that the return on strength diminishes with the addition of each bolt. Bolted-angle connection failures depend on the thickness of the angle. In all cases, bolted web angle connections achieved larger rotations than single-plate shear connections before initial failure. A bolt test was designed to investigate the capacity of the bolts used during the connection tests in shear. Results show that these bolts have a significantly higher shear capacity than their specified nominal shear strength.


## 12.1 INTRODUCTION

An ongoing joint research project that explores the behavior of steel gravity framing systems for a scenario in which a column loses the capacity to support its design gravity load is being conducted at the University of Washington (UW), Purdue University (PU) and the University of Illinois at Urbana-Champaign (UIUC). When a column collapse occurs, alternate load paths must be developed if the gravity load is to be supported. This causes the connections, the concrete slab on metal deck, and other frame elements to become load supporting components. The behavior of each of these critical components and the complete steel gravity frame system are studied using three independent experimental set ups. Various connection sub-assemblages tests have been completed and are still ongoing at the UW, concrete slab on metal deck configurations are being tested at PU, and a complete floor system is being constructed for future testing at the UIUC. After these tests are completed, current weaknesses in modern-day gravity frames will be identified and simple solutions to these problems will be developed to facilitate the design of next generation gravity frame systems.

This report focuses on the author's participation in the experimentation that occurred at the UW. As explained by Weigand et al. [2012], these connection component tests investigate the behavior and determine the controlling failure mechanisms of various connection geometries, which include single-plate shear, bolted web angle, and bolted top-and-seat angle connections. The connections were tested under the combined flexural, axial, and shear loading associated with large vertical deflections in steel gravity frame systems under a column collapse scenario. A bolt test was also designed and executed to test the capacity of the bolts used in the connection tests. Bolts with three different diameters—3/4 in., 7/8 in., and 1 in.—were tested to failure under double shear loading.

## 12.2 BACKGROUND

Although a column collapse scenario could occur to a building for a number of reasons, for example, earthquakes, bombings, storms, etc., the event that motivated this study was the September 11, 2001, World Trade Center (WTC) attacks. As explained in Warn et al. [2003], when a group of researchers walked through the affected area in the weeks following the attack, they encountered a building that had been badly damaged by debris ejected from the WTC Tower 2 as it collapsed. The building, known as 130 Liberty Plaza, lost a large segment of a column but did not collapse. Figure 12.1 is a picture of the building's north façade damage. The researchers determined that the use of rigid beam-to-column connections in the frame enabled the gravity load from the floors above to be transferred to neighboring undamaged vertical components. This scenario prompted the testing of gravity frame connections, concrete floor slabs, and a complete floor system to determine each component's behavior during a column collapse situation.

**Figure 102.1 130 Liberty Plaza, New York, after losing a column due to damage from the collapse of the WTC on September 11, 2001 (photo courtesy of MR38).**

Previous tests have studied the combined behavior of single plate shear connections and concrete floor slabs under similar loading conditions as a column collapse scenario. Astaneh-Asl et al. [2002] studied the behavior of single-plate shear connections with concrete floor slab on metal deck under combined gravity and lateral loading. They determined that the contribution of the floor slab roughly doubled the maximum lateral load resistance reached by the single-plate shear connection alone until the plate reached 0.04 radians lateral drift, at which point the load capacity dropped almost to that of having only the single-plate shear connection. Tests performed by Liu and Astaneh-Asl [2004] studied the effects of moment and rotation on a single-plate shear connection, with and without a concrete slab, to determine the parameters needed when constructing a basic moment-rotation curve. They used these parameters to predict moment and rotation capacities that were in agreement with experimental values from their tests. Neither of these studies assessed the effect of their respective load combinations on the concrete slab alone, nor did they take into consideration other types of connections.

Various experiments on single-plate shear connections under loading conditions similar to that of a column collapse situation have also been done. Astaneh-Asl et al. [2002] tested single-plate shear connections under gravity load and, similar to the ultimate goal of this project, they developed procedures for designing safe and economical single-plate shear connections in the form of equations with predicted the capacity of single-plate shear connections for each of six failure modes. Crocker and Chambers [2004] tested single-plate shear connection response to rotation. They determined that the connection stiffness depended on the number of bolts in the connection and suggested a maximum allowable displacement, ΔD, for the farthest bolt hole from the neutral axis.

Although the connection tests done at the UW were monotonic, past tests on bolted angles have also studied angle behavior under cyclic loading. Shen and Astaneh-Asl [1999] focused their investigation on the inelastic behavior, failure modes, and energy dissipation capacity of bolted-angle connections under cyclic loading. They found that bolted-angle connections are stable and reliably dissipate energy under cyclic loading. In addition, they identified two major deformation patterns, which depended on how strong the angle was when compared to the bolt. Even though this test was concentrated only on cyclic loading, similar failure behavior can be expected from angles under monotonic loading. Tests conducted under both cyclic and monotonic testing using blind bolts were performed by Elghzouli et al. [2009], who examined a number of connection connections with different geometric arrangements and bolt properties. They determined that top-and-set connections with or without web angles provided a rotational capacity well beyond those required under typical design scenarios.

Garlock et al. [2003] analyzed bolted top-and-seat connections to determine how the angle size and bolt gage length (the distance between the bolt line and heel of the angle) affect the connection stiffness, strength, energy dissipation, and resistance. Their test set up loaded both the top and seat angles in tension, in a way similar to the connection test at the UW, and determined that three plastic hinges would form: one in the fillet of each angle leg and another near the column bolts. They also found that the most common failure mode was a full fracture of the column leg of the angle adjacent to the fillet.

Previous testing on the behavior of bolts include the study conducted by Rex and Easterling [2003], which resulted in a model for approximating the load deformation behavior of a single bolt bearing on a single plate. Although this test had a very different objective than that of the connection component test or the bolt test administered at the UW, the reaction of the plate was very similar to that of the plates used during the bolt test and of the plates and angles during the connection component tests. This project aimed to determine the capacity of specific bolt batches used in the connection tests because the connections tested were resisting a larger load than expected; it was assumed that the bolts probably had a larger capacity than they should have. From this test a force-versus-deformation graph similar to the one presented in the elastic method for determining the combined effects of direct shear in the bolt section of the AISC manual [AISC 2011] will be produced. The relationship presented in this graph applies specifically to 3/4 in.-diameter-A325 bolts in single shear, but can be used to determine how the relationship scales with greater bolt diameters, double shear, and A490 steel.

## 12.3 CONNECTION COMPONENT TEST

### 12.3.1 Methods

A self-reacting load frame capable of delivering combined flexural, axial, and shear loading was used to test the gravity frame connection sub-assemblages. The set up for each connection test first included mounting a specimen column stub, which lay horizontal on one of its flanges, and then anchoring it to the strong floor. A specimen beam stub was then placed above the column vertically, perpendicular to the center of the column. Lastly, the connection was attached. In the single-plate shear connection case, the plate was previously welded onto the column and then bolted to the beam. In both the double web angle and top-and-seat angle connection cases, however, the connections were bolted to both the column and the beam to complete the connection sub-assemblage. The far side of the beam stub was connected to a horizontal loading beam that was attached to three actuators: two vertical 110-kip actuators and one horizontal 55-kip actuator. These provided the combined flexural, axial, and shear loading; see Figure 12.2. An additional brace frame provided lateral stability to the beam stub and enforced in plane rotation and axial deformation, as shown in Figure 12.3.

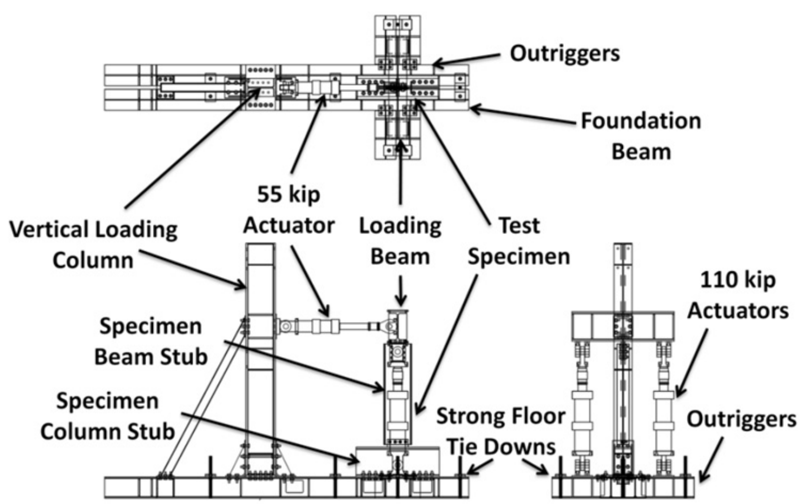


**Figure 12.2 Connection sub-assemblage experimental test set up.**

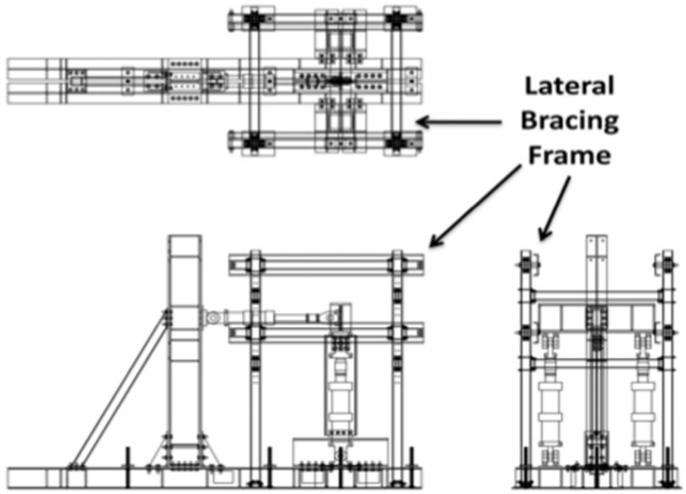


**Figure 12.3 Lateral bracing frame surrounding the connection sub-assemblage experimental test set up.**

Various connections geometries were tested: single plate shear connections, bolted web angle connections and top-and-seat angle connections. Within these designations, connection geometric parameters including plate thickness, number of bolts, edge distance, bolt spacing and bolt alignment (in bolted-angle connections) were also varied from test to test. Table 12.1 and Table 12.2 present the entire list and their properties.

## Table 12.1 Single-plate shear connection test properties.

| | System Properties | | | ASTM/AISC Desig. | | | Connection Properties | | | | Limit-State Par. | | |
|---|---|---|---|---|---|---|---|---|---|---|---|---|---|
| Exp. # | Span (ft.) | Column Shape | Beam Shape | Steel Shapes | Plate | Bolts | $n_f$ | $d_b$ | $t_p$ | Hole Type | $\frac{L_{ehp}}{L_{ehp\ min}}$ | $\frac{R_y F_y t_w}{R_y F_y t_p}$ | Purpose |
| 1 | 48.0 | W14×90 | W18×35 | A572 | A36 | A325 | 3 | 3/4 | 3/8 | STD | 1.50 | 0.849 | Comparison to Crocker 3-bolt experiment. Bearing controlled by beam web. |
| 2 | 48.0 | W14×90 | W18×35 | A572 | A36 | A325 | 4 | 3/4 | 3/8 | STD | 1.50 | 0.849 | Comparison to Crocker 4-bolt experiment. Bearing controlled by beam web. |
| 3 | 30.0 | W12×72 | W21×50 | A572 | A36 | A325 | 3 | 3/4 | 3/8 | STD | 1.50 | 1.019 | Baseline STD Specimen. Bearing controlled by shear plate. Strength controlled by bolt shear. |
| 4 | 30.0 | W12×72 | W21×50 | A572 | A36 | A325 | 3 | 3/4 | 3/8 | SSLT | 1.50 | 1.019 | Baseline SSLT Specimen. Strength controlled by bolt shear. |
| 5 | 30.0 | W12×72 | W21×50 | A572 | A36 | A325 | 3 | 3/4 | 3/8 | SSLT | 1.00 | 1.019 | Strength controlled by tearout. |
| 6 | 30.0 | W12×72 | W21×50 | A572 | A36 | A325 | 4 | 3/4 | 3/8 | SSLT | 1.50 | 1.019 | Increase in strength due to addition of fiber. |
| 7 | 30.0 | W12×72 | W21×50 | A572 | A36 | A325 | 5 | 3/4 | 3/8 | SSLT | 1.50 | 1.019 | Increase in strength due to addition of fiber and diminishing return on each additional fiber. |
| 8 | 30.0 | W12×72 | W21×50 | A572 | A36 | A490 | 3 | 3/4 | 3/8 | SSLT | 1.50 | 1.019 | Increase in strength due to bolt grade. |
| 9 | 30.0 | W12×72 | W21×50 | A572 | A36 | A325 | 3 | 3/4 | 3/8 | SSLT | 1.50 | 1.019 | Plate asymmetric to centerline of beam depth. Accentuates tendency for binding. |
| 10 | 30.0 | W12×72 | W21×50 | A572 | A36 | A325 | 4 | 7/8 | 3/8 | SSLT | 1.33 | 1.019 | Bolt-diameter correlation. Provides equal shear strength to bolted-angle specimen. |
| 11 | 30.0 | W12×72 | W21×50 | A572 | A36 | A325 | 3 | 3/4 | 1/4 | SSLT | 1.50 | 1.019 | Plate thickness correlation. Shifts failure mechanism to tearout. |
| 12 | 30.0 | W12×72 | W21×50 | A572 | A36 | A325 | 3 | 3/4 | 3/8 | SSLT | 1.50 | 1.019 | Decreased gap between column flange and beam end. Deliberately causes binding. |
| 13 | 30.0 | W12×72 | W21×50 | A572 | A36 | A325 | 3 | 3/4 | 3/8 | SSLT | 1.50 | 1.019 | Extended configuration, weak-axis single plate shear connection |
| 14 | 30.0 | W12×72 | W21×50 | A572 | A36 | A325 | - | - | - | - | - | - | Improved single plate shear connection test # 1. |
| 15 | 30.0 | W12×72 | W21×50 | A572 | A36 | A325 | - | - | - | - | - | - | Improved single plate shear connection test # 2. |
| 16 | 30.0 | W12×72 | W21×50 | A572 | A36 | A325 | - | - | - | - | - | - | Improved single plate shear connection test # 3. |
| 17 | 30.0 | W12×72 | W21×50 | A572 | A36 | A325 | 3 | 3/4 | 3/8 | SSLT | 1.50 | 1.019 | Single plate shear connection with slab component # 1. |
| 18 | 30.0 | W12×72 | W21×50 | A572 | A36 | A325 | 3 | 3/4 | 3/8 | SSLT | 1.50 | 1.019 | Single plate shear connection with slab component # 2. |
| 19 | 15.0 | W8×24 | W6×8.5 | A572 | A36 | A449 | 3 | 3/8 | 1/4 | SSLT | 1.50 | 1.019 | UIUC scaled conventional single plate shear connection |
| 20 | 15.0 | W8×24 | W6×8.5 | A572 | A36 | A449 | 3 | 3/8 | 1/4 | SSLT | 1.50 | 1.019 | UIUC scaled extended single plate shear connection |

## Table 12.2 Bolted-angle and top-and-seat connection test properties.

| | System Properties | | | ASTM/AISC Desig. | | | Connection Properties | | | | Limit-State Par. | | Other |
|---|---|---|---|---|---|---|---|---|---|---|---|---|---|
| Exp. # | Span (ft.) | Column Shape | Beam Shape | Steel Shapes | Plate | Bolts | $n_f$ | $d_b$ | $t_L$ | Hole Type | $\frac{L_{ehp}}{L_{ehp\ min}}$ | $\frac{R_y F_y t_L}{R_y F_y t_p}$ | Details |
| 1 | 30.0 | W12×72 | W21×50 | A572 | A36 | A325 | 3 | 3/4 | 2 × 1/4 , 1/2 | STD | ≥1.50 | ≫1 | Connection ductility comparison. Provides equal shear strength to single plate shear specimen. |
| 2 | 30.0 | W12×72 | W21×50 | A572 | A36 | A325 | 5 | 3/4 | 2 × 1/4 , 1/2 | STD | ≥1.50 | ≫1 | Increase in strength due to addition of fibers. |
| 3 | 30.0 | W12×72 | W21×50 | A572 | A36 | A325 | 3 | 1 | 2 × 3/4 | STD | ≥1.50 | ≫1 | Plastic hinging of angle legs at angle radius on column face. |
| 4 | 30.0 | W12×72 | W21×50 | A572 | A36 | A325 | 3 | 3/4 | 2 × 1/4 , 1/2 | STD | ≥1.50 | ≫1 | Angles asymmetric to centerline of beam depth. Accentuates tendency for binding. |
| 5 | 30.0 | W12×72 | W21×50 | A572 | A36 | A325 | 3 | 3/4 | 2 × 1/4 , 1/2 | STD | ≥1.50 | ≫1 | Decreased gap between column flange and beam end. Deliberately causes binding. |
| 6 | 30.0 | W12×72 | W21×50 | A572 | A36 | A325 | 3 | 3/4 | 2 × 1/4 , 1/2 | STD | ≥1.50 | ≫1 | Comparison of web-angle and top-and-seat angle behaviors. |
| 7 | 30.0 | W12×72 | W21×50 | A572 | A36 | A325 | 3(2) | 3/4(1) | 2 × 3/4 | STD | ≥1.50 | ≫1 | Holes at column face offset from holes at beam face. |
| 8 | 30.0 | W12×72 | W21×50 | A572 | A36 | A325 | 3 | 3/4 | 2 × 1/4 | STD | ≥1.50 | ≫1 | Angles bolted to column face and welded to beam web. |
| 9 | 30.0 | W12×72 | W21×50 | A572 | A36 | A325 | 3 | 3/4 | 2 × 1/4 | STD | ≥1.50 | ≫1 | Angles welded to column face and bolted to beam web. |
| 10 | 30.0 | W12×72 | W21×50 | A572 | A36 | A325 | 3 | 3/4 | 2 × 1/4 , 1/2 | STD | ≥1.50 | ≫1 | Weak-axis column connection. Angles bolted to column web. |

### 12.3.2 Instrumentation

Various types of instruments were utilized during each test to quantify and record how both the brace frame and the connection sub-assemblages reacted to the combined loading. The frame is instrumented to make sure it does not suffer any displacement or rotation large enough to cause out-of-plane loading on the specimen. This is monitored by using Duncan potentiometers and string potentiometers placed around the base of the frame and from the frame to the load beam. Both of these instruments measure displacement, and in this case measure horizontal displacement. A greater amount of instruments were placed on the connection sub-assemblages. Sting potentiometers kept track of the beam's vertical displacement, the beam and column's horizontal displacement, and elongation of the 110-kip actuators. Inclinometers measured the variation in inclination of all three actuators and the beam. Lastly, an OptiTrack System was used to record the initial location and track the displacement of LED targets placed on the column, connection and beam in a three-dimensional space. Cameras were used to take step-by-step pictures of the connection's progressive deformation and failure from various angles. To ensure that these measurements are recorded and verified, there were a few specimens whose displacements are measured by more than one instrument at a time. All instruments were connected to computers where LabView software was used to manage and record all the data. Figure 12.4 shows the instruments used during the connection tests.

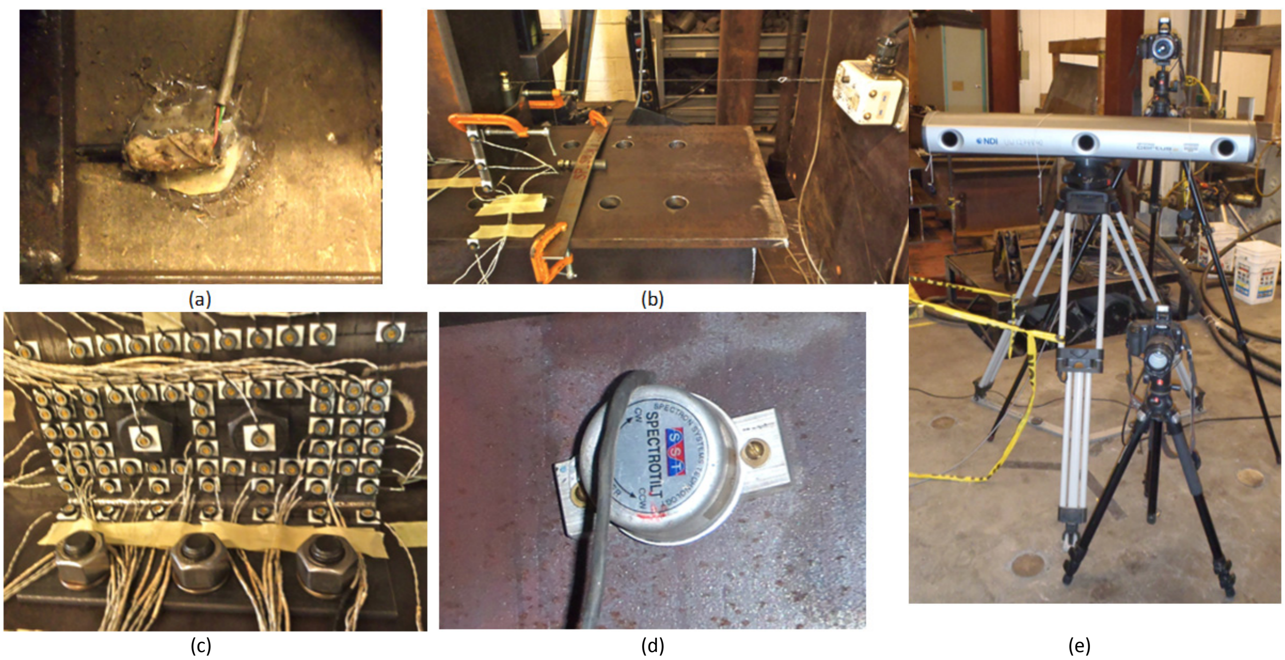


**Figure 12.4** **Instrumentation: (a) Duncan potentiometers; (b) string potentiometers; (c) LED targets; (d) inclinometer; and (e) OptiTrack system camera next to picture cameras.**

### 12.3.3 Procedure

The combined flexural, axial, and shear loading applied to the connection sub-assemblages was produced by the collective efforts of the 55-kip actuator and the two 110-kip actuators. The paths each of these actuators to produce the desired loading were determined before testing. Each loading procedure depended on the ratio of the system's vertical displacement to the connection's axial displacement and the span of the system; they were calculated based on the connection's geometry. Specimens were also loaded at a very low rate of displacement per time to eliminate possible dynamic loading effects on the results.

During the loading procedure the initially horizontal 55-kip actuator contracted as the two initially vertical 110-kip actuators elongated, and all three slowly rotated toward a point above the 55-kip actuator. The 55-kip actuator applied most of the shear load, and the two 110-kip actuators applied most of the tension load, while remaining parallel to each other and the beam stub's centerline. The test was continued until the connection failed or the actuators reached their maximum displacement.

### 12.3.4 Preliminary Results

All connection tests have not yet been completed, however, some preliminary results have been obtained from the behavior and data patterns of the configurations that have been tested. These include all single-plate shear connections, most bolted-angle connections, and one top-and-seat connection (all completed connection configurations were not tested during the author's participation).

As can be seen in Figure 12.5, which shows the progressive failure of some of the tested single-plate shear and bolted-angle connections, single-plate shear connection specimens usually fail by tear-out of the bolt edge distance on the shear plate or beam web, or by shear fracture of the bolts. This depends on the shear plate and beam web's respective thickness and steel strength. Similarly, bolted-angle connection failures depend on the angle's thickness and the diameter of the bolts. Thin-angle specimens fail by angle fracture in either the beam or column leg, starting at the toe of the angle radius on the tension end of the angle. Thick-angle specimens fail by sequential prying of the bolts propagating from tension end of the angle. In all cases bolted-angle specimens achieved larger rotations than shear plates. Bolted-angle connections reached a minimum rotation of 0.118 radians, while single-plate shear connections reached a maximum rotation of 0.110 radians. In the tests where binding was provoked, there was no change the failure mode of either type of connection.

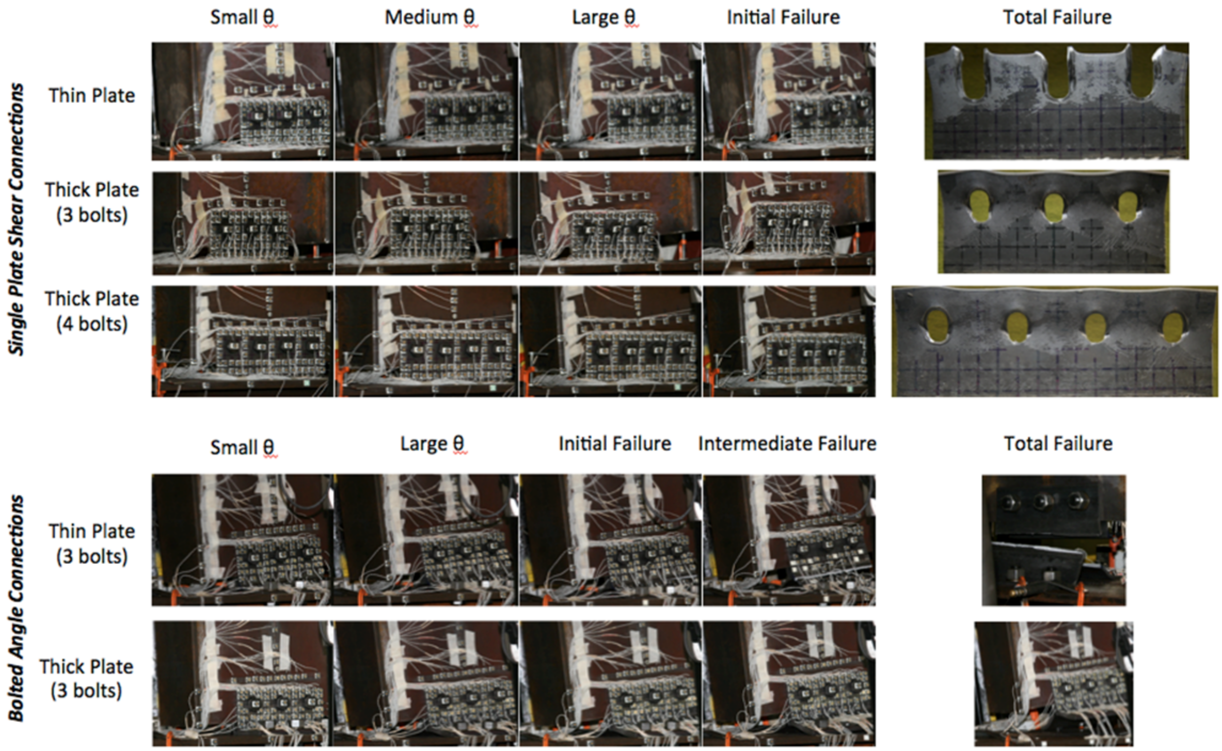


**Figure 12.5 Progressive failure of single-plate shear and bolted-angle connections.**

## 12.4 BOLT TEST

### 12.4.1 Methods

A small apparatus was designed to test the shear capacity of the bolts used during the connection tests. The connections' sub-assemblages were resisting higher loads than expected, and it was suspected that this was due to the bolts reaching higher loads than their design load. The device created to test these bolts consisted of three 1/2-in.-thick, high-strength steel vertical plates positioned between two horizontal steel plates. The vertical plates were kept in place only by compression. Railings were also added to the top and bottom horizontal plates to prevent the vertical plates from bending or slipping out during the test when under large compression load. Figure 12.6 presents a complete view of the bolt test frame. The frame was also designed to test all three of the bolt diameters under consideration. This device was then placed in a 300-kip Baldwin testing machine to apply the compression load. When compressed, the bolt placed in the frame was forced to fail in shear through both shear planes.

The tested bolt batches consisted of three different bolt diameters: 3/4 in., 7/8 in. and 1 in. A list of all five test batches and their properties can be seen in Table 12.3. In the cases where the quantity of bolts permitted, bolts from each batch were tested varying slip and tension. The tests that allowed slip used standard holes that had diameters 1/16 in. greater that the bolt diameter. Tests that did not allowed slip were done with holes that had the same size diameter as the bolt. This was done to identify the effect of slip in the capacity of the bolts. Tensioned tests were done by tightening the bolts using the same procedure as was used in the connection tests. Bolts tested without tension still contained a nut, which was lightly hand-tightened to keep the plates flush together and prevent the bolt from falling out. The tension was varied to determine the difference in the initial stiffness of tensioned and not-tensioned bolts. Table 12.4 shows a list of all the bolt tests that were done and the parameters varied in each one.

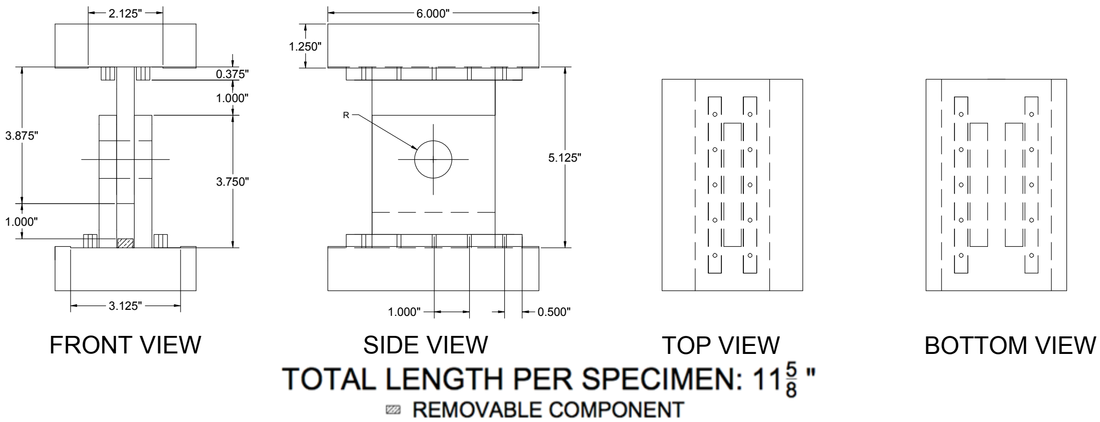


**Figure 12.6 Bolt test frame.**

**Table 12.3 Bolt test properties.**

| Diameter | Batch | ASTM Designation | Length | Quantity |
|---|---|---|---|---|
| 3/4 in. | 1a | A490 | 2 in. | 4 |
| | 1b | A325 | 2.5 in. | 4 |
| | 1c | A325 | 2 in. | 2 |
| | 2 | A325 | 2 in. | 4 |
| | 3 | A325 | 2 in. | 4 |
| 7/8 in. | 4 | A325 | 2.5 in. | 4 |
| 1" | 5 | A325 | 2.5 in. | 4 |

Table 12.4 Bolt test parameters.

| Test No. | Diameter | Batch | Slip | Tension | Plate Set | Bolt |
|---|---|---|---|---|---|---|
| 1 | 3/4 in. | 3 | NS | T | 1 | 1 |
| 2 | 3/4 in. | 3 | S | T | 3 | 1 |
| 3 | 3/4 in. | 3 | S | NT | 3 | 1 |
| 4 | 3/4 in. | 3 | NS | NT | 1 | 1 |
| 5 | 3/4 in. | 1a | NS | NT | 2 | 1 |
| 6 | 3/4 in. | 1a | NS | T | 2 | 1 |
| 7 | 3/4 in. | 1a | S | T | 4 | 1 |
| 8 | 3/4 in. | 1a | S | NT | 4 | 1 |
| 9 | 3/4 in. | 1c | NS | NT | 5 | 1 |
| 10 | 3/4 in. | 1c | NS | T | 5 | 1 |
| 11 | 3/4 in. | 2 | S | NT | 6 | 1 |
| 12 | 3/4 in. | 2 | S | T | 6 | 1 |
| 13 | 3/4 in. | 2 | NS | NT | 12 | 1 |
| 14 | 3/4 in. | 2 | NS | T | 12 | 1 |
| 15 | 3/4 in. | 1b | S | NT | 9 | 1 |
| 16 | 3/4” | 1b | S | T | 9 | 1 |
| 17 | 3/4” | 1b | NS | NT | 7 | 1 |
| 18 | 3/4” | 1b | NS | T | 7 | 1 |
| 19 | 7/8 in. | 4 | NS | NT | 13 | 1 |
| 20 | 7/8 in. | 4 | NS | T | 13 | 1 |
| 21 | 7/8 in. | 4 | S | NT | 14 | 1 |
| 22 | 7/8 in. | 4 | S | T | 14 | 1 |
| 23 | 1 in. | 5 | NS | T | 8 | 1 |
| 24 | 1 in. | 5 | NS | NT | 8 | 1 |
| 25 | 1 in. | 5 | S | T | 11 | 1 |
| 26 | 1 in. | 5 | S | NT | 11 | 1 |

### 12.4.2 Instrumentation

Three types of instruments were used to collect data during the bolt tests. The 300-kip Baldwin testing machine applied the compression load on the bolt test frame, which was the shear load applied on the bolt, and registered it in pounds. A laser extensometer was used to get precise readings of the displacement of the vertical plates relative to each other, which was due to the deformation caused by shear loading. Lastly, four Duncan potentiometers were placed near each corner of the bolt test frame to make sure the compression force was applied evenly on the top plate of the frame and was not being loaded eccentrically. Figure 12.7 shows photographs of the instruments used during the test. LabView software was used to manage and record the data.

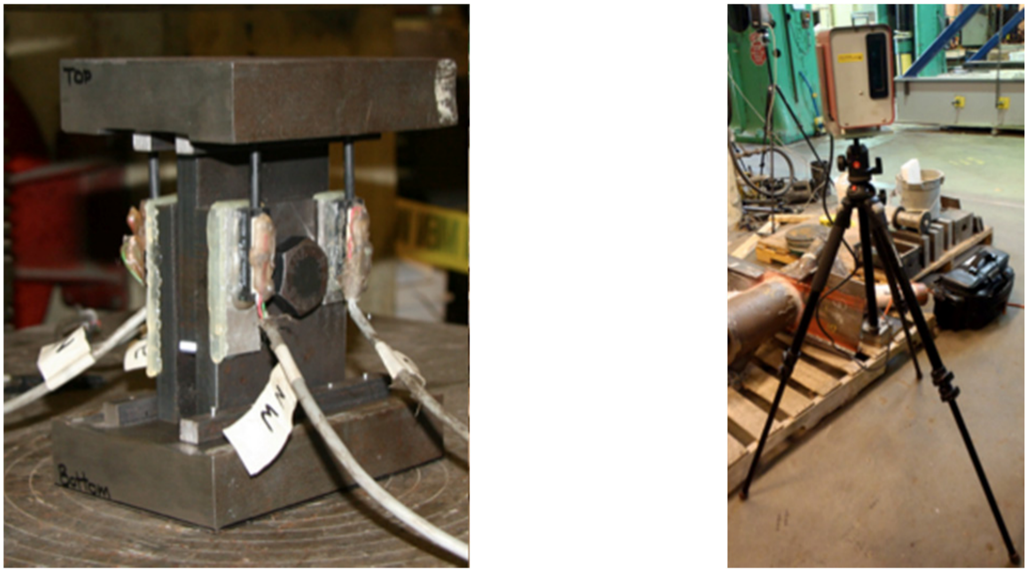


(a) (b)

**Figure 12.7 Instrumentation: (a) Duncan potentiometers; and (b) laser extensometer.**

### 12.4.3 Procedure

A set of three vertical plates was chosen before each test. Each plate set was used during two tests, one where the bolt was tensioned and another where it was not. The bolt was then placed through the holes in the plates and tightened, clamping the plates together. Four Duncan potentiometers were glued on to the vertical plates before placing them between the two horizontal plates. The completed frame was placed in the center of the Baldwin testing machine. The laser was then placed 15 in. from the vertical plates. Lastly, the Baldwin testing machine was operated to slowly apply the compression force. Figure 12.8 shows how the test set up looked before applying the compression load. The load was increased by hand at a very slow rate to eliminate any possible effects of dynamic loading and would continue to be increased until the bolt failed through both shear planes.

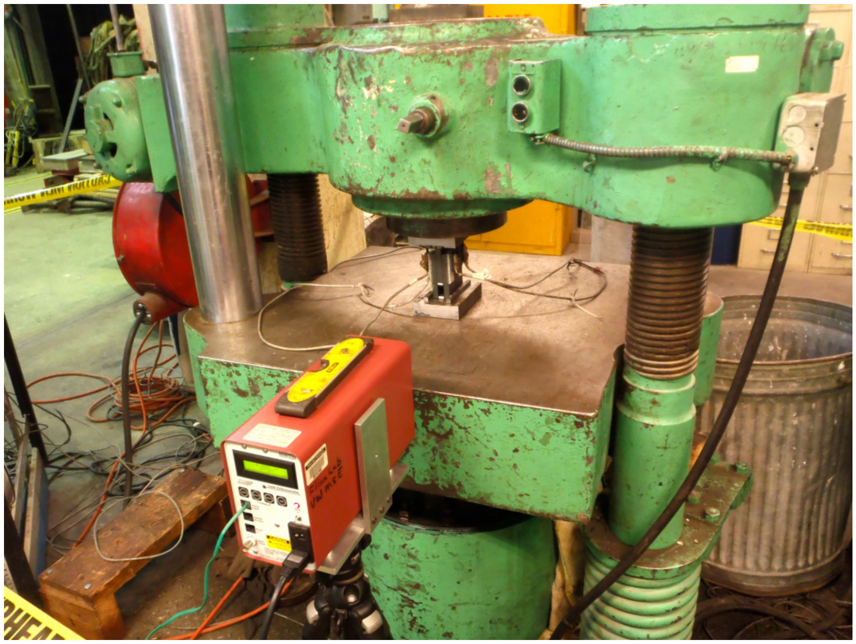

**Figure 12.8 Bolt test set up.**

### 12.4.4 Preliminary Results

Data analysis has not yet been completed but some preliminary results have been produced using information from the first nine tests. This data was frequency filtered to reduce noise, as will all subsequent test data. The data will be used to determine each bolt's initial stiffness, shear stress, maximum shear load, and displacement or deformation at maximum shear load. Force-versus-displacement graphs (see Figure 12.9) will also be produced to help determine the general behavior of the bolts during shear loading and where slip occurred. Most graphs should have a similar shape as all bolts are expected to have high initial stiffness and then slowly start deforming at a faster rate until they reach their maximum load and fail. The only variables for each graph should be the maximum load reached by the bolt before both failures and the rate at which they deform.

The first nine tests included both A325 and A490 bolts. According to ASTM Standards, their specified nominal shear strengths are 48 ksi for A325 bolts and 60 ksi for A490 bolts when threads are included in the shear plane. Results showed the average experimental maximum shear stress of the first nine tested bolts were 69.9 ksi for A325 and 72.4 ksi for A490 bolts. This proves that the bolts used during the connection tests have a significantly higher shear capacity than their specified nominal shear strength.

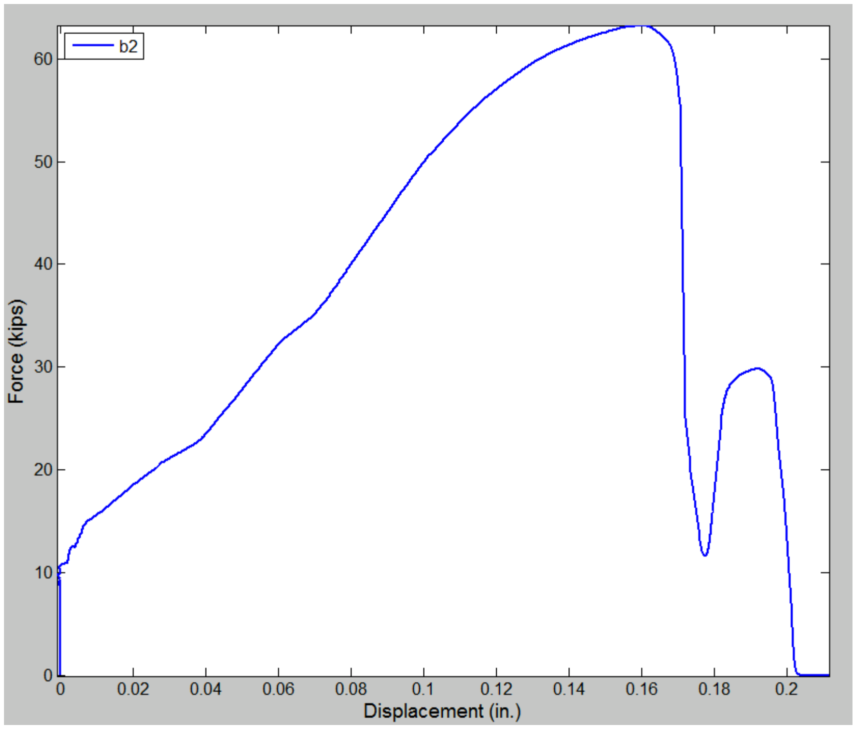


**Figure 12.9 Force versus displacement: Test #2.**

## 12.5 CONCLUSIONS

Even though data analysis has not been completed on the connection component test and the bolt test, some general conclusions have been reached based on preliminary results. In the connection component test case it was determined that for single shear plates the addition of a bolt returns a horizontal force contribution less than the capacity of that bolt in tension. There is also a diminishing return on strength with the addition of each bolt. This can be seen in Figure 12.10, which compares the loads reached by single plate shear connections with three and four bolts. Both single-plate shear and bolted-angle connections reached higher loads as their thickness increased, until the bolt capacity became the limiting state. This behavior can be seen in Figure 12.11. Bolted angles are more ductile than shear plates and reached a greater deformation before failing.

In the bolt test case, the experimental shear capacity was found to be greater than the specified shear capacity. This confirms the assumption that the bolts in the connections had a greater capacity than expected.

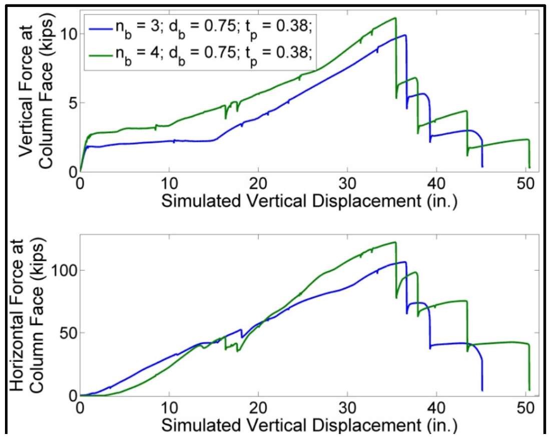


**Figure 12.10 Force versus displacement: comparing single plate shear connections with 3 and 4 bolts.**

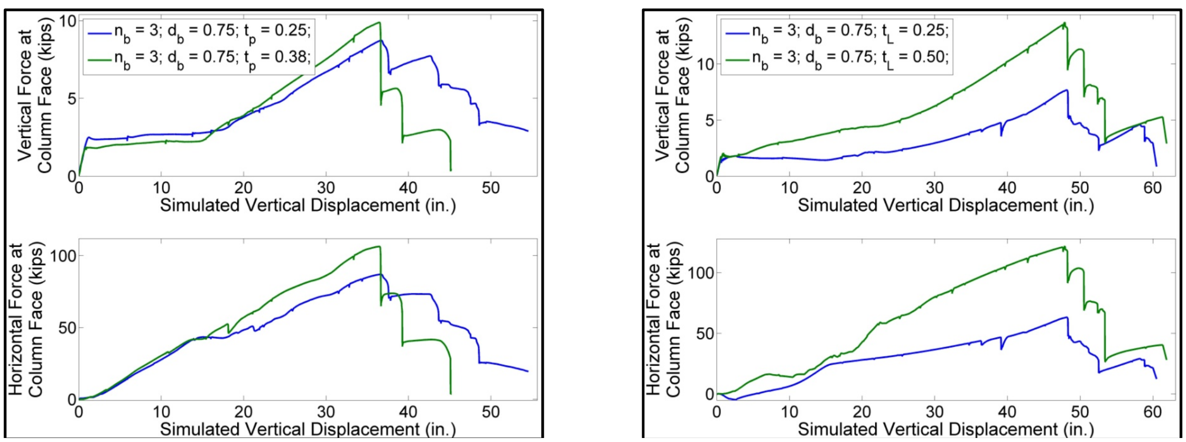


(a) (b)

**Figure 12.11 Force versus displacement: (a) comparing single plate shear connections with 0.25 in. and 0.38 in. plate thickness; and (b) comparing bolted-angle connections with 0.25 and 0.50 in. thickness.**

## 12.6 FUTURE WORK

Work will continue on all three parts of this joint project. The second stage of the connection components tests are scheduled to finish September 2012 at the UW; the concrete slab on metal deck tests are currently in progress at PU and a complete floor system is under construction at UIUC, where testing is scheduled to commence in October 2012. After this first round of tests the structural integrity of current practice steel gravity framing systems will be evaluated, and simple solutions for improving steel gravity frame performance to ensure structural integrity will be developed. Next-generation gravity frame systems will be designed and tested so that they can withstand column collapse loading. Practical computer models will also be developed for the evaluation and design of gravity frame systems.

## ACKNOWLEDGMENTS

First I would like to thank Jonathan Weigand, my graduate mentor, for being by my side, guiding and helping me throughout the summer, while at the same time challenging and motivating me to learn and grow. I would like to thank Jeffrey Berman, my faculty mentor, for giving me the opportunity of participating in so many aspects of this project and for his advice and encouragement along the way. I am very thankful for everyone I met in UW's Civil Engineering department, especially all those who helped me in some way. I wish to thank my fellow PEER interns for keeping me motivated, supporting me, and accompanying me throughout this experience. Lastly, I am very grateful to the PEER program and NSF for providing me the opportunity to participate in this research experience.

## REFERENCES

American Institute of Steel Construction (2011). *Steel Construction Manual*, 14th Edition. Chicago, IL. 7-6–7-13.

Astaneh-Asl A, J Liu, and KM McMullin (2002). Behavior and design of single plate shear connections, *J. Constr. Steel Res*., 58(5-8):1121–1141.

Crocker JP, and JJ Chambers (2004). Single plate shear connection response to rotation demands imposed by frames undergoing cyclic lateral displacements, *J. Struct. Eng*., 130(6):934–941.

Elghazouli AY, C Málaga-Chuquitaype, JM Castro, and AH Orton (2009). Experimental monotonic and cyclic behavior of blind bolted angle connections, *Eng. Struct.,* 31(11):2540–2553.

Garlock MM, JM Ricles, and R Sause (2003). Cyclic load test and analysis of bolted top-and-seat angle connection, *J. Struct. Eng*., 129(12):1615–1625.

Liu J, and A Astaneh-Asl (2004). Moment-rotation parameters for composite shear tab connections, *J. Struct. Eng*., 130(9):1371–1380.

Rex CO, and WS Easterling (2003). Behavior and modeling of a bolt bearing on a single plate, *J. Struct. Eng*., 129(6):792–800.

Shen J, and A Astaneh-Asl (1999). Hysteretic behavior of bolted-angle connections, *J. Constr. Steel Res*., 51(3):201–218.

Warn G, J Berman, AS Whittaker, and M Bruneau (2003) Reconnaissance and preliminary assessment of a damaged high-rise building near Ground Zero, *The Structural Design of Tall and Special Bldgs*., 12:371–391.

Weigand JM, JE Meissner, T Francisco, JW Berman, LA Fahnestock, and J Liu (2012). Testing the integrity of steel gravity frames subjected to large vertical deflections: Components, *Proc*., ASCE Structures Congress, Chicago, IL.

## PEER REPORTS

PEER reports are available individually or by yearly subscription. PEER reports can be ordered at http://peer.berkeley.edu/publications/peer_reports.html or by contacting the Pacific Earthquake Engineering Research Center, 325 Davis Hall mail code 1792, Berkeley, CA 94720. Tel.: (510) 642-3437; Fax: (510) 665-1655; Email: peer_editor@berkeley.edu

**PEER 2012/07** *Earthquake Engineering for Resilient Communities: 2012 PEER Internship Program Research Report Collection.* Heidi Tremayne (Editor), Stephen A. Mahin (Editor), Collin Anderson, Dustin Cook, Michael Erceg, Carlos Esparza, Jose Jimenez, Dorian Krausz, Andrew Lo, Stephanie Lopez, Nicole McCurdy, Paul Shipman, Alexander Strum, Eduardo Vega. December 2012.

**PEER 2012/06** *Fragilities for Precarious Rocks at Yucca Mountain.* Matthew D. Purvance, Rasool Anooshehpoor, and James N. Brune. December 2012.

**PEER 2012/05** *Development of Simplified Analysis Procedure for Piles in Laterally Spreading Layered Soils.* Christopher R. McGann, Pedro Arduino, and Peter Mackenzie–Helnwein. December 2012.

**PEER 2012/04** *Unbonded Pre-Tensioned Columns for Bridges in Seismic Regions.* Phillip M. Davis, Todd M. Janes, Marc O. Eberhard, and John F. Stanton. December 2012.

**PEER 2012/03** *Experimental and Analytical Studies on Reinforced Concrete Buildings with Seismically Vulnerable Beam-Column Joints.* Sangjoon Park and Khalid M. Mosalam. October 2012.

**PEER 2012/02** *Seismic Performance of Reinforced Concrete Bridges Allowed to Uplift during Multi-Directional Excitation.* Andres Oscar Espinoza and Stephen A. Mahin. July 2012.

**PEER 2012/01** *Spectral Damping Scaling Factors for Shallow Crustal Earthquakes in Active Tectonic Regions.* Sanaz Rezaeian, Yousef Bozorgnia, I. M. Idriss, Kenneth Campbell, Norman Abrahamson, and Walter Silva. July 2012.

**PEER 2011/10** *Earthquake Engineering for Resilient Communities: 2011 PEER Internship Program Research Report Collection.* Eds. Heidi Faison and Stephen A. Mahin. December 2011.

**PEER 2011/09** *Calibration of Semi-Stochastic Procedure for Simulating High-Frequency Ground Motions.* Jonathan P. Stewart, Emel Seyhan, and Robert W. Graves. December 2011.

**PEER 2011/08** *Water Supply in regard to Fire Following Earthquake.* Charles Scawthorn. November 2011.

**PEER 2011/07** *Seismic Risk Management in Urban Areas. Proceedings of a U.S.-Iran-Turkey Seismic Workshop.* September 2011.

**PEER 2011/06** *The Use of Base Isolation Systems to Achieve Complex Seismic Performance Objectives.* Troy A. Morgan and Stephen A. Mahin. July 2011.

**PEER 2011/05** *Case Studies of the Seismic Performance of Tall Buildings Designed by Alternative Means.* Task 12 Report for the Tall Buildings Initiative. Jack Moehle, Yousef Bozorgnia, Nirmal Jayaram, Pierson Jones, Mohsen Rahnama, Nilesh Shome, Zeynep Tuna, John Wallace, Tony Yang, and Farzin Zareian. July 2011.

**PEER 2011/04** *Recommended Design Practice for Pile Foundations in Laterally Spreading Ground.* Scott A. Ashford, Ross W. Boulanger, and Scott J. Brandenberg. June 2011.

**PEER 2011/03** *New Ground Motion Selection Procedures and Selected Motions for the PEER Transportation Research Program.* Jack W. Baker, Ting Lin, Shrey K. Shahi, and Nirmal Jayaram. March 2011.

**PEER 2011/02** *A Bayesian Network Methodology for Infrastructure Seismic Risk Assessment and Decision Support.* Michelle T. Bensi, Armen Der Kiureghian, and Daniel Straub. March 2011.

**PEER 2011/01** *Demand Fragility Surfaces for Bridges in Liquefied and Laterally Spreading Ground.* Scott J. Brandenberg, Jian Zhang, Pirooz Kashighandi, Yili Huo, and Minxing Zhao. March 2011.

**PEER 2010/05** *Guidelines for Performance-Based Seismic Design of Tall Buildings.* Developed by the Tall Buildings Initiative. November 2010.

**PEER 2010/04** *Application Guide for the Design of Flexible and Rigid Bus Connections between Substation Equipment Subjected to Earthquakes.* Jean-Bernard Dastous and Armen Der Kiureghian. September 2010.

**PEER 2010/03** *Shear Wave Velocity as a Statistical Function of Standard Penetration Test Resistance and Vertical Effective Stress at Caltrans Bridge Sites.* Scott J. Brandenberg, Naresh Bellana, and Thomas Shantz. June 2010.

**PEER 2010/02** *Stochastic Modeling and Simulation of Ground Motions for Performance-Based Earthquake Engineering.* Sanaz Rezaeian and Armen Der Kiureghian. June 2010.

**PEER 2010/01** *Structural Response and Cost Characterization of Bridge Construction Using Seismic Performance Enhancement Strategies.* Ady Aviram, Božidar Stojadinović, Gustavo J. Parra-Montesinos, and Kevin R. Mackie. March 2010.

**PEER 2009/03** *The Integration of Experimental and Simulation Data in the Study of Reinforced Concrete Bridge Systems Including Soil-Foundation-Structure Interaction.* Matthew Dryden and Gregory L. Fenves. November 2009.

**PEER 2009/02** *Improving Earthquake Mitigation through Innovations and Applications in Seismic Science, Engineering, Communication, and Response. Proceedings of a U.S.-Iran Seismic Workshop.* October 2009.

**PEER 2009/01** *Evaluation of Ground Motion Selection and Modification Methods: Predicting Median Interstory Drift Response of Buildings.* Curt B. Haselton, Ed. June 2009.

**PEER 2008/10** *Technical Manual for Strata.* Albert R. Kottke and Ellen M. Rathje. February 2009.

**PEER 2008/09** *NGA Model for Average Horizontal Component of Peak Ground Motion and Response Spectra.* Brian S.-J. Chiou and Robert R. Youngs. November 2008.

**PEER 2008/08** *Toward Earthquake-Resistant Design of Concentrically Braced Steel Structures.* Patxi Uriz and Stephen A. Mahin. November 2008.

**PEER 2008/07** *Using OpenSees for Performance-Based Evaluation of Bridges on Liquefiable Soils.* Stephen L. Kramer, Pedro Arduino, and HyungSuk Shin. November 2008.

**PEER 2008/06** *Shaking Table Tests and Numerical Investigation of Self-Centering Reinforced Concrete Bridge Columns.* Hyung IL Jeong, Junichi Sakai, and Stephen A. Mahin. September 2008.

**PEER 2008/05** *Performance-Based Earthquake Engineering Design Evaluation Procedure for Bridge Foundations Undergoing Liquefaction-Induced Lateral Ground Displacement.* Christian A. Ledezma and Jonathan D. Bray. August 2008.

**PEER 2008/04** *Benchmarking of Nonlinear Geotechnical Ground Response Analysis Procedures.* Jonathan P. Stewart, Annie On-Lei Kwok, Yousseff M. A. Hashash, Neven Matasovic, Robert Pyke, Zhiliang Wang, and Zhaohui Yang. August 2008.

**PEER 2008/03** *Guidelines for Nonlinear Analysis of Bridge Structures in California.* Ady Aviram, Kevin R. Mackie, and Božidar Stojadinović. August 2008.

**PEER 2008/02** *Treatment of Uncertainties in Seismic-Risk Analysis of Transportation Systems.* Evangelos Stergiou and Anne S. Kiremidjian. July 2008.

**PEER 2008/01** *Seismic Performance Objectives for Tall Buildings.* William T. Holmes, Charles Kircher, William Petak, and Nabih Youssef. August 2008.

**PEER 2007/12** *An Assessment to Benchmark the Seismic Performance of a Code-Conforming Reinforced Concrete Moment-Frame Building.* Curt Haselton, Christine A. Goulet, Judith Mitrani-Reiser, James L. Beck, Gregory G. Deierlein, Keith A. Porter, Jonathan P. Stewart, and Ertugrul Taciroglu. August 2008.

**PEER 2007/11** *Bar Buckling in Reinforced Concrete Bridge Columns.* Wayne A. Brown, Dawn E. Lehman, and John F. Stanton. February 2008.

**PEER 2007/10** *Computational Modeling of Progressive Collapse in Reinforced Concrete Frame Structures.* Mohamed M. Talaat and Khalid M. Mosalam. May 2008.

**PEER 2007/09** *Integrated Probabilistic Performance-Based Evaluation of Benchmark Reinforced Concrete Bridges.* Kevin R. Mackie, John-Michael Wong, and Božidar Stojadinović. January 2008.

**PEER 2007/08** *Assessing Seismic Collapse Safety of Modern Reinforced Concrete Moment-Frame Buildings.* Curt B. Haselton and Gregory G. Deierlein. February 2008.

**PEER 2007/07** *Performance Modeling Strategies for Modern Reinforced Concrete Bridge Columns.* Michael P. Berry and Marc O. Eberhard. April 2008.

**PEER 2007/06** *Development of Improved Procedures for Seismic Design of Buried and Partially Buried Structures.* Linda Al Atik and Nicholas Sitar. June 2007.

**PEER 2007/05** *Uncertainty and Correlation in Seismic Risk Assessment of Transportation Systems.* Renee G. Lee and Anne S. Kiremidjian. July 2007.

**PEER 2007/04** *Numerical Models for Analysis and Performance-Based Design of Shallow Foundations Subjected to Seismic Loading.* Sivapalan Gajan, Tara C. Hutchinson, Bruce L. Kutter, Prishati Raychowdhury, José A. Ugalde, and Jonathan P. Stewart. May 2008.

**PEER 2007/03** *Beam-Column Element Model Calibrated for Predicting Flexural Response Leading to Global Collapse of RC Frame Buildings.* Curt B. Haselton, Abbie B. Liel, Sarah Taylor Lange, and Gregory G. Deierlein. May 2008.

**PEER 2007/02** *Campbell-Bozorgnia NGA Ground Motion Relations for the Geometric Mean Horizontal Component of Peak and Spectral Ground Motion Parameters.* Kenneth W. Campbell and Yousef Bozorgnia. May 2007.

**PEER 2007/01** *Boore-Atkinson NGA Ground Motion Relations for the Geometric Mean Horizontal Component of Peak and Spectral Ground Motion Parameters.* David M. Boore and Gail M. Atkinson. May. May 2007.

**PEER 2006/12** *Societal Implications of Performance-Based Earthquake Engineering.* Peter J. May. May 2007.

**PEER 2006/11** *Probabilistic Seismic Demand Analysis Using Advanced Ground Motion Intensity Measures, Attenuation Relationships, and Near-Fault Effects.* Polsak Tothong and C. Allin Cornell. March 2007.

**PEER 2006/10** *Application of the PEER PBEE Methodology to the I-880 Viaduct.* Sashi Kunnath. February 2007.

**PEER 2006/09** *Quantifying Economic Losses from Travel Forgone Following a Large Metropolitan Earthquake.* James Moore, Sungbin Cho, Yue Yue Fan, and Stuart Werner. November 2006.

**PEER 2006/08** *Vector-Valued Ground Motion Intensity Measures for Probabilistic Seismic Demand Analysis*. Jack W. Baker and C. Allin Cornell. October 2006.

**PEER 2006/07** *Analytical Modeling of Reinforced Concrete Walls for Predicting Flexural and Coupled–Shear-Flexural Responses*. Kutay Orakcal, Leonardo M. Massone, and John W. Wallace. October 2006.

**PEER 2006/06** *Nonlinear Analysis of a Soil-Drilled Pier System under Static and Dynamic Axial Loading.* Gang Wang and Nicholas Sitar. November 2006.

**PEER 2006/05** *Advanced Seismic Assessment Guidelines.* Paolo Bazzurro, C. Allin Cornell, Charles Menun, Maziar Motahari, and Nicolas Luco. September 2006.

**PEER 2006/04** *Probabilistic Seismic Evaluation of Reinforced Concrete Structural Components and Systems.* Tae Hyung Lee and Khalid M. Mosalam. August 2006.

**PEER 2006/03** *Performance of Lifelines Subjected to Lateral Spreading.* Scott A. Ashford and Teerawut Juirnarongrit. July 2006.

**PEER 2006/02** *Pacific Earthquake Engineering Research Center Highway Demonstration Project.* Anne Kiremidjian, James Moore, Yue Yue Fan, Nesrin Basoz, Ozgur Yazali, and Meredith Williams. April 2006.

**PEER 2006/01** *Bracing Berkeley. A Guide to Seismic Safety on the UC Berkeley Campus.* Mary C. Comerio, Stephen Tobriner, and Ariane Fehrenkamp. January 2006.

**PEER 2005/16** *Seismic Response and Reliability of Electrical Substation Equipment and Systems.* Junho Song, Armen Der Kiureghian, and Jerome L. Sackman. April 2006.

**PEER 2005/15** *CPT-Based Probabilistic Assessment of Seismic Soil Liquefaction Initiation.* R. E. S. Moss, R. B. Seed, R. E. Kayen, J. P. Stewart, and A. Der Kiureghian. April 2006.

**PEER 2005/14** *Workshop on Modeling of Nonlinear Cyclic Load-Deformation Behavior of Shallow Foundations.* Bruce L. Kutter, Geoffrey Martin, Tara Hutchinson, Chad Harden, Sivapalan Gajan, and Justin Phalen. March 2006.

**PEER 2005/13** *Stochastic Characterization and Decision Bases under Time-Dependent Aftershock Risk in Performance-Based Earthquake Engineering.* Gee Liek Yeo and C. Allin Cornell. July 2005.

**PEER 2005/12** *PEER Testbed Study on a Laboratory Building: Exercising Seismic Performance Assessment.* Mary C. Comerio, editor. November 2005.

**PEER 2005/11** *Van Nuys Hotel Building Testbed Report: Exercising Seismic Performance Assessment.* Helmut Krawinkler, editor. October 2005.

**PEER 2005/10** *First NEES/E-Defense Workshop on Collapse Simulation of Reinforced Concrete Building Structures.* September 2005.

**PEER 2005/09** *Test Applications of Advanced Seismic Assessment Guidelines.* Joe Maffei, Karl Telleen, Danya Mohr, William Holmes, and Yuki Nakayama. August 2006.

**PEER 2005/08** *Damage Accumulation in Lightly Confined Reinforced Concrete Bridge Columns.* R. Tyler Ranf, Jared M. Nelson, Zach Price, Marc O. Eberhard, and John F. Stanton. April 2006.

**PEER 2005/07** *Experimental and Analytical Studies on the Seismic Response of Freestanding and Anchored Laboratory Equipment.* Dimitrios Konstantinidis and Nicos Makris. January 2005.

**PEER 2005/06** *Global Collapse of Frame Structures under Seismic Excitations*. Luis F. Ibarra and Helmut Krawinkler. September 2005.

**PEER 2005//05** *Performance Characterization of Bench- and Shelf-Mounted Equipment.* Samit Ray Chaudhuri and Tara C. Hutchinson. May 2006.

**PEER 2005/04** *Numerical Modeling of the Nonlinear Cyclic Response of Shallow Foundations.* Chad Harden, Tara Hutchinson, Geoffrey R. Martin, and Bruce L. Kutter. August 2005.

**PEER 2005/03** *A Taxonomy of Building Components for Performance-Based Earthquake Engineering.* Keith A. Porter. September 2005.

**PEER 2005/02** *Fragility Basis for California Highway Overpass Bridge Seismic Decision Making*. Kevin R. Mackie and Božidar Stojadinović. June 2005.

**PEER 2005/01** *Empirical Characterization of Site Conditions on Strong Ground Motion.* Jonathan P. Stewart, Yoojoong Choi, and Robert W. Graves. June 2005.

**PEER 2004/09** *Electrical Substation Equipment Interaction: Experimental Rigid Conductor Studies.* Christopher Stearns and André Filiatrault. February 2005.

**PEER 2004/08** *Seismic Qualification and Fragility Testing of Line Break 550-kV Disconnect Switches.* Shakhzod M. Takhirov, Gregory L. Fenves, and Eric Fujisaki. January 2005.

**PEER 2004/07** *Ground Motions for Earthquake Simulator Qualification of Electrical Substation Equipment.* Shakhzod M. Takhirov, Gregory L. Fenves, Eric Fujisaki, and Don Clyde. January 2005.

**PEER 2004/06** *Performance-Based Regulation and Regulatory Regimes.* Peter J. May and Chris Koski. September 2004.

**PEER 2004/05** *Performance-Based Seismic Design Concepts and Implementation: Proceedings of an International Workshop.* Peter Fajfar and Helmut Krawinkler, editors. September 2004.

**PEER 2004/04** *Seismic Performance of an Instrumented Tilt-up Wall Building.* James C. Anderson and Vitelmo V. Bertero. July 2004.

**PEER 2004/03** *Evaluation and Application of Concrete Tilt-up Assessment Methodologies.* Timothy Graf and James O. Malley. October 2004.

**PEER 2004/02** *Analytical Investigations of New Methods for Reducing Residual Displacements of Reinforced Concrete Bridge Columns.* Junichi Sakai and Stephen A. Mahin. August 2004.

**PEER 2004/01** *Seismic Performance of Masonry Buildings and Design Implications.* Kerri Anne Taeko Tokoro, James C. Anderson, and Vitelmo V. Bertero. February 2004.

**PEER 2003/18** *Performance Models for Flexural Damage in Reinforced Concrete Columns.* Michael Berry and Marc Eberhard. August 2003.

**PEER 2003/17** *Predicting Earthquake Damage in Older Reinforced Concrete Beam-Column Joints.* Catherine Pagni and Laura Lowes. October 2004.

**PEER 2003/16** *Seismic Demands for Performance-Based Design of Bridges.* Kevin Mackie and Božidar Stojadinović. August 2003.

**PEER 2003/15** *Seismic Demands for Nondeteriorating Frame Structures and Their Dependence on Ground Motions.* Ricardo Antonio Medina and Helmut Krawinkler. May 2004.

**PEER 2003/14** *Finite Element Reliability and Sensitivity Methods for Performance-Based Earthquake Engineering.* Terje Haukaas and Armen Der Kiureghian. April 2004.

**PEER 2003/13** *Effects of Connection Hysteretic Degradation on the Seismic Behavior of Steel Moment-Resisting Frames.* Janise E. Rodgers and Stephen A. Mahin. March 2004.

**PEER 2003/12** *Implementation Manual for the Seismic Protection of Laboratory Contents: Format and Case Studies.* William T. Holmes and Mary C. Comerio. October 2003.

**PEER 2003/11** *Fifth U.S.-Japan Workshop on Performance-Based Earthquake Engineering Methodology for Reinforced Concrete Building Structures.* February 2004.

**PEER 2003/10** *A Beam-Column Joint Model for Simulating the Earthquake Response of Reinforced Concrete Frames*. Laura N. Lowes, Nilanjan Mitra, and Arash Altoontash. February 2004.

**PEER 2003/09** *Sequencing Repairs after an Earthquake: An Economic Approach.* Marco Casari and Simon J. Wilkie. April 2004.

**PEER 2003/08** *A Technical Framework for Probability-Based Demand and Capacity Factor Design (DCFD) Seismic Formats*. Fatemeh Jalayer and C. Allin Cornell. November 2003.

**PEER 2003/07** *Uncertainty Specification and Propagation for Loss Estimation Using FOSM Methods.* Jack W. Baker and C. Allin Cornell. September 2003.

**PEER 2003/06** *Performance of Circular Reinforced Concrete Bridge Columns under Bidirectional Earthquake Loading*. Mahmoud M. Hachem, Stephen A. Mahin, and Jack P. Moehle. February 2003.

**PEER 2003/05** *Response Assessment for Building-Specific Loss Estimation.* Eduardo Miranda and Shahram Taghavi. September 2003.

**PEER 2003/04** *Experimental Assessment of Columns with Short Lap Splices Subjected to Cyclic Loads*. Murat Melek, John W. Wallace, and Joel Conte. April 2003.

**PEER 2003/03** *Probabilistic Response Assessment for Building-Specific Loss Estimation.* Eduardo Miranda and Hesameddin Aslani. September 2003.

**PEER 2003/02** *Software Framework for Collaborative Development of Nonlinear Dynamic Analysis Program.* Jun Peng and Kincho H. Law. September 2003.

**PEER 2003/01** *Shake Table Tests and Analytical Studies on the Gravity Load Collapse of Reinforced Concrete Frames.* Kenneth John Elwood and Jack P. Moehle. November 2003.

**PEER 2002/24** *Performance of Beam to Column Bridge Joints Subjected to a Large Velocity Pulse.* Natalie Gibson, André Filiatrault, and Scott A. Ashford. April 2002.

**PEER 2002/23** *Effects of Large Velocity Pulses on Reinforced Concrete Bridge Columns.* Greg L. Orozco and Scott A. Ashford. April 2002.

**PEER 2002/22** *Characterization of Large Velocity Pulses for Laboratory Testing.* Kenneth E. Cox and Scott A. Ashford. April 2002.

**PEER 2002/21** *Fourth U.S.-Japan Workshop on Performance-Based Earthquake Engineering Methodology for Reinforced Concrete Building Structures*. December 2002.

**PEER 2002/20** *Barriers to Adoption and Implementation of PBEE Innovations.* Peter J. May. August 2002.

**PEER 2002/19** *Economic-Engineered Integrated Models for Earthquakes: Socioeconomic Impacts.* Peter Gordon, James E. Moore II, and Harry W. Richardson. July 2002.

**PEER 2002/18** *Assessment of Reinforced Concrete Building Exterior Joints with Substandard Details.* Chris P. Pantelides, Jon Hansen, Justin Nadauld, and Lawrence D. Reaveley. May 2002.

**PEER 2002/17** *Structural Characterization and Seismic Response Analysis of a Highway Overcrossing Equipped with Elastomeric Bearings and Fluid Dampers: A Case Study.* Nicos Makris and Jian Zhang. November 2002.

**PEER 2002/16** *Estimation of Uncertainty in Geotechnical Properties for Performance-Based Earthquake Engineering.* Allen L. Jones, Steven L. Kramer, and Pedro Arduino. December 2002.

**PEER 2002/15** *Seismic Behavior of Bridge Columns Subjected to Various Loading Patterns.* Asadollah Esmaeily-Gh. and Yan Xiao. December 2002.

**PEER 2002/14** *Inelastic Seismic Response of Extended Pile Shaft Supported Bridge Structures.* T.C. Hutchinson, R.W. Boulanger, Y.H. Chai, and I.M. Idriss. December 2002.

**PEER 2002/13** *Probabilistic Models and Fragility Estimates for Bridge Components and Systems.* Paolo Gardoni, Armen Der Kiureghian, and Khalid M. Mosalam. June 2002.

**PEER 2002/12** *Effects of Fault Dip and Slip Rake on Near-Source Ground Motions: Why Chi-Chi Was a Relatively Mild M7.6 Earthquake.* Brad T. Aagaard, John F. Hall, and Thomas H. Heaton. December 2002.

**PEER 2002/11** *Analytical and Experimental Study of Fiber-Reinforced Strip Isolators*. James M. Kelly and Shakhzod M. Takhirov. September 2002.

**PEER 2002/10** *Centrifuge Modeling of Settlement and Lateral Spreading with Comparisons to Numerical Analyses***.** Sivapalan Gajan and Bruce L. Kutter. January 2003.

**PEER 2002/09** *Documentation and Analysis of Field Case Histories of Seismic Compression during the 1994 Northridge, California, Earthquake.* Jonathan P. Stewart, Patrick M. Smith, Daniel H. Whang, and Jonathan D. Bray. October 2002.

**PEER 2002/08** *Component Testing, Stability Analysis and Characterization of Buckling-Restrained Unbonded Braces™*. Cameron Black, Nicos Makris, and Ian Aiken. September 2002.

**PEER 2002/07** *Seismic Performance of Pile-Wharf Connections.* Charles W. Roeder, Robert Graff, Jennifer Soderstrom, and Jun Han Yoo. December 2001.

**PEER 2002/06** *The Use of Benefit-Cost Analysis for Evaluation of Performance-Based Earthquake Engineering Decisions*. Richard O. Zerbe and Anthony Falit-Baiamonte. September 2001.

**PEER 2002/05** *Guidelines, Specifications, and Seismic Performance Characterization of Nonstructural Building Components and Equipment*. André Filiatrault, Constantin Christopoulos, and Christopher Stearns. September 2001.

**PEER 2002/04** *Consortium of Organizations for Strong-Motion Observation Systems and the Pacific Earthquake Engineering Research Center Lifelines Program: Invited Workshop on Archiving and Web Dissemination of Geotechnical Data, 4–5 October 2001*. September 2002.

**PEER 2002/03** *Investigation of Sensitivity of Building Loss Estimates to Major Uncertain Variables for the Van Nuys Testbed.* Keith A. Porter, James L. Beck, and Rustem V. Shaikhutdinov. August 2002.

**PEER 2002/02** *The Third U.S.-Japan Workshop on Performance-Based Earthquake Engineering Methodology for Reinforced Concrete Building Structures*. July 2002.

**PEER 2002/01** *Nonstructural Loss Estimation: The UC Berkeley Case Study.* Mary C. Comerio and John C. Stallmeyer. December 2001.

**PEER 2001/16** *Statistics of SDF-System Estimate of Roof Displacement for Pushover Analysis of Buildings.* Anil K. Chopra, Rakesh K. Goel, and Chatpan Chintanapakdee. December 2001.

**PEER 2001/15** *Damage to Bridges during the 2001 Nisqually Earthquake.* R. Tyler Ranf, Marc O. Eberhard, and Michael P. Berry. November 2001.

**PEER 2001/14** *Rocking Response of Equipment Anchored to a Base Foundation.* Nicos Makris and Cameron J. Black. September 2001.

**PEER 2001/13** *Modeling Soil Liquefaction Hazards for Performance-Based Earthquake Engineering.* Steven L. Kramer and Ahmed-W. Elgamal. February 2001.

**PEER 2001/12** *Development of Geotechnical Capabilities in OpenSees.* Boris Jeremić. September 2001.

**PEER 2001/11** *Analytical and Experimental Study of Fiber-Reinforced Elastomeric Isolators*. James M. Kelly and Shakhzod M. Takhirov. September 2001.

**PEER 2001/10** *Amplification Factors for Spectral Acceleration in Active Regions.* Jonathan P. Stewart, Andrew H. Liu, Yoojoong Choi, and Mehmet B. Baturay. December 2001.

**PEER 2001/09** *Ground Motion Evaluation Procedures for Performance-Based Design.* Jonathan P. Stewart, Shyh-Jeng Chiou, Jonathan D. Bray, Robert W. Graves, Paul G. Somerville, and Norman A. Abrahamson. September 2001.

**PEER 2001/08** *Experimental and Computational Evaluation of Reinforced Concrete Bridge Beam-Column Connections for Seismic Performance.* Clay J. Naito, Jack P. Moehle, and Khalid M. Mosalam. November 2001.

**PEER 2001/07** *The Rocking Spectrum and the Shortcomings of Design Guidelines.* Nicos Makris and Dimitrios Konstantinidis. August 2001.

**PEER 2001/06** *Development of an Electrical Substation Equipment Performance Database for Evaluation of Equipment Fragilities*. Thalia Agnanos. April 1999.

**PEER 2001/05** *Stiffness Analysis of Fiber-Reinforced Elastomeric Isolators.* Hsiang-Chuan Tsai and James M. Kelly. May 2001.

**PEER 2001/04** *Organizational and Societal Considerations for Performance-Based Earthquake Engineering.* Peter J. May. April 2001.

**PEER 2001/03** *A Modal Pushover Analysis Procedure to Estimate Seismic Demands for Buildings: Theory and Preliminary Evaluation.* Anil K. Chopra and Rakesh K. Goel. January 2001.

**PEER 2001/02** *Seismic Response Analysis of Highway Overcrossings Including Soil-Structure Interaction.* Jian Zhang and Nicos Makris. March 2001.

**PEER 2001/01** *Experimental Study of Large Seismic Steel Beam-to-Column Connections.* Egor P. Popov and Shakhzod M. Takhirov. November 2000.

**PEER 2000/10** *The Second U.S.-Japan Workshop on Performance-Based Earthquake Engineering Methodology for Reinforced Concrete Building Structures.* March 2000.

**PEER 2000/09** *Structural Engineering Reconnaissance of the August 17, 1999 Earthquake: Kocaeli (Izmit), Turkey.* Halil Sezen, Kenneth J. Elwood, Andrew S. Whittaker, Khalid Mosalam, John J. Wallace, and John F. Stanton. December 2000.

**PEER 2000/08** *Behavior of Reinforced Concrete Bridge Columns Having Varying Aspect Ratios and Varying Lengths of Confinement.* Anthony J. Calderone, Dawn E. Lehman, and Jack P. Moehle. January 2001.

**PEER 2000/07** *Cover-Plate and Flange-Plate Reinforced Steel Moment-Resisting Connections.* Taejin Kim, Andrew S. Whittaker, Amir S. Gilani, Vitelmo V. Bertero, and Shakhzod M. Takhirov. September 2000.

**PEER 2000/06** *Seismic Evaluation and Analysis of 230-kV Disconnect Switches.* Amir S. J. Gilani, Andrew S. Whittaker, Gregory L. Fenves, Chun-Hao Chen, Henry Ho, and Eric Fujisaki. July 2000.

**PEER 2000/05** *Performance-Based Evaluation of Exterior Reinforced Concrete Building Joints for Seismic Excitation.* Chandra Clyde, Chris P. Pantelides, and Lawrence D. Reaveley. July 2000.

**PEER 2000/04** *An Evaluation of Seismic Energy Demand: An Attenuation Approach.* Chung-Che Chou and Chia-Ming Uang. July 1999.

**PEER 2000/03** *Framing Earthquake Retrofitting Decisions: The Case of Hillside Homes in Los Angeles.* Detlof von Winterfeldt, Nels Roselund, and Alicia Kitsuse. March 2000.

**PEER 2000/02** *U.S.-Japan Workshop on the Effects of Near-Field Earthquake Shaking.* Andrew Whittaker, ed. July 2000.

**PEER 2000/01** *Further Studies on Seismic Interaction in Interconnected Electrical Substation Equipment.* Armen Der Kiureghian, Kee-Jeung Hong, and Jerome L. Sackman. November 1999.

**PEER 1999/14** *Seismic Evaluation and Retrofit of 230-kV Porcelain Transformer Bushings*. Amir S. Gilani, Andrew S. Whittaker, Gregory L. Fenves, and Eric Fujisaki. December 1999.

**PEER 1999/13** *Building Vulnerability Studies: Modeling and Evaluation of Tilt-up and Steel Reinforced Concrete Buildings.* John W. Wallace, Jonathan P. Stewart, and Andrew S. Whittaker, editors. December 1999.

**PEER 1999/12** *Rehabilitation of Nonductile RC Frame Building Using Encasement Plates and Energy-Dissipating Devices.* Mehrdad Sasani, Vitelmo V. Bertero, James C. Anderson. December 1999.

**PEER 1999/11** *Performance Evaluation Database for Concrete Bridge Components and Systems under Simulated Seismic Loads.* Yael D. Hose and Frieder Seible. November 1999.

**PEER 1999/10** *U.S.-Japan Workshop on Performance-Based Earthquake Engineering Methodology for Reinforced Concrete Building Structures.* December 1999.

**PEER 1999/09** *Performance Improvement of Long Period Building Structures Subjected to Severe Pulse-Type Ground Motions*. James C. Anderson, Vitelmo V. Bertero, and Raul Bertero. October 1999.

**PEER 1999/08** *Envelopes for Seismic Response Vectors.* Charles Menun and Armen Der Kiureghian. July 1999.

**PEER 1999/07** *Documentation of Strengths and Weaknesses of Current Computer Analysis Methods for Seismic Performance of Reinforced Concrete Members.* William F. Cofer. November 1999.

**PEER 1999/06** *Rocking Response and Overturning of Anchored Equipment under Seismic Excitations.* Nicos Makris and Jian Zhang. November 1999.

**PEER 1999/05** *Seismic Evaluation of 550 kV Porcelain Transformer Bushings.* Amir S. Gilani, Andrew S. Whittaker, Gregory L. Fenves, and Eric Fujisaki. October 1999.

**PEER 1999/04** *Adoption and Enforcement of Earthquake Risk-Reduction Measures.* Peter J. May, Raymond J. Burby, T. Jens Feeley, and Robert Wood.

**PEER 1999/03** *Task 3 Characterization of Site Response General Site Categories*. Adrian Rodriguez-Marek, Jonathan D. Bray, and Norman Abrahamson. February 1999.

**PEER 1999/02** *Capacity-Demand-Diagram Methods for Estimating Seismic Deformation of Inelastic Structures: SDF Systems*. Anil K. Chopra and Rakesh Goel. April 1999.

**PEER 1999/01** *Interaction in Interconnected Electrical Substation Equipment Subjected to Earthquake Ground Motions.* Armen Der Kiureghian, Jerome L. Sackman, and Kee-Jeung Hong. February 1999.

**PEER 1998/08** *Behavior and Failure Analysis of a Multiple-Frame Highway Bridge in the 1994 Northridge Earthquake.* Gregory L. Fenves and Michael Ellery. December 1998.

**PEER 1998/07** *Empirical Evaluation of Inertial Soil-Structure Interaction Effects.* Jonathan P. Stewart, Raymond B. Seed, and Gregory L. Fenves. November 1998.

**PEER 1998/06** *Effect of Damping Mechanisms on the Response of Seismic Isolated Structures.* Nicos Makris and Shih-Po Chang. November 1998.

**PEER 1998/05** *Rocking Response and Overturning of Equipment under Horizontal Pulse-Type Motions.* Nicos Makris and Yiannis Roussos. October 1998.

**PEER 1998/04** *Pacific Earthquake Engineering Research Invitational Workshop Proceedings, May 14–15, 1998: Defining the Links between Planning, Policy Analysis, Economics and Earthquake Engineering.* Mary Comerio and Peter Gordon. September 1998.

**PEER 1998/03** *Repair/Upgrade Procedures for Welded Beam to Column Connections.* James C. Anderson and Xiaojing Duan. May 1998.

**PEER 1998/02** *Seismic Evaluation of 196 kV Porcelain Transformer Bushings.* Amir S. Gilani, Juan W. Chavez, Gregory L. Fenves, and Andrew S. Whittaker. May 1998.

**PEER 1998/01** *Seismic Performance of Well-Confined Concrete Bridge Columns.* Dawn E. Lehman and Jack P. Moehle. December 2000.

## ONLINE REPORTS

The following PEER reports are available by Internet only at http://peer.berkeley.edu/publications/peer_reports.html

**PEER 2012/102** *Procedure to Restart an Interrupted Hybrid Simulation: Addendum to PEER Report 2010/103.* Vesna Terzic and Bozidar Stojadinovic. October 2012.

**PEER 2012/101** *Mechanics of Fiber Reinforced Bearings.* James M. Kelly and Andrea Calabrese. February 2012.

**PEER 2011/107** *Nonlinear Site Response and Seismic Compression at Vertical Array Strongly Shaken by 2007 Niigata-ken Chuetsu-oki Earthquake.* Eric Yee, Jonathan P. Stewart, and Kohji Tokimatsu. December 2011.

**PEER 2011/106** *Self Compacting Hybrid Fiber Reinforced Concrete Composites for Bridge Columns.* Pardeep Kumar, Gabriel Jen, William Trono, Marios Panagiotou, and Claudia Ostertag. September 2011.

**PEER 2011/105** *Stochastic Dynamic Analysis of Bridges Subjected to Spacially Varying Ground Motions.* Katerina Konakli and Armen Der Kiureghian. August 2011.

**PEER 2011/104** *Design and Instrumentation of the 2010 E-Defense Four-Story Reinforced Concrete and Post-Tensioned Concrete Buildings.* Takuya Nagae, Kenichi Tahara, Taizo Matsumori, Hitoshi Shiohara, Toshimi Kabeyasawa, Susumu Kono, Minehiro Nishiyama (Japanese Research Team) and John Wallace, Wassim Ghannoum, Jack Moehle, Richard Sause, Wesley Keller, Zeynep Tuna (U.S. Research Team). June 2011.

**PEER 2011/103** *In-Situ Monitoring of the Force Output of Fluid Dampers: Experimental Investigation.* Dimitrios Konstantinidis, James M. Kelly, and Nicos Makris. April 2011.

**PEER 2011/102** *Ground-motion prediction equations 1964 - 2010.* John Douglas. April 2011.

**PEER 2011/101** *Report of the Eighth Planning Meeting of NEES/E-Defense Collaborative Research on Earthquake Engineering.* Convened by the Hyogo Earthquake Engineering Research Center (NIED), NEES Consortium, Inc. February 2011.

**PEER 2010/111** *Modeling and Acceptance Criteria for Seismic Design and Analysis of Tall Buildings.* Task 7 Report for the Tall Buildings Initiative - Published jointly by the Applied Technology Council. October 2010.

**PEER 2010/110** *Seismic Performance Assessment and Probabilistic Repair Cost Analysis of Precast Concrete Cladding Systems for Multistory Buildlings.* Jeffrey P. Hunt and Božidar Stojadinovic. November 2010.

**PEER 2010/109** *Report of the Seventh Joint Planning Meeting of NEES/E-Defense Collaboration on Earthquake Engineering. Held at the E-Defense, Miki, and Shin-Kobe, Japan, September 18–19, 2009.* August 2010.

**PEER 2010/108** *Probabilistic Tsunami Hazard in California.* Hong Kie Thio, Paul Somerville, and Jascha Polet, preparers. October 2010.

**PEER 2010/107** *Performance and Reliability of Exposed Column Base Plate Connections for Steel Moment-Resisting Frames.* Ady Aviram, Božidar Stojadinovic, and Armen Der Kiureghian. August 2010.

**PEER 2010/106** *Verification of Probabilistic Seismic Hazard Analysis Computer Programs.* Patricia Thomas, Ivan Wong, and Norman Abrahamson. May 2010.

**PEER 2010/105** *Structural Engineering Reconnaissance of the April 6, 2009, Abruzzo, Italy, Earthquake, and Lessons Learned.* M. Selim Günay and Khalid M. Mosalam. April 2010.

**PEER 2010/104** *Simulating the Inelastic Seismic Behavior of Steel Braced Frames, Including the Effects of Low-Cycle Fatigue.* Yuli Huang and Stephen A. Mahin. April 2010.

**PEER 2010/103** *Post-Earthquake Traffic Capacity of Modern Bridges in California.* Vesna Terzic and Božidar Stojadinović. March 2010.

**PEER 2010/102** *Analysis of Cumulative Absolute Velocity (CAV) and JMA Instrumental Seismic Intensity ($I_{JMA}$) Using the PEER–NGA Strong Motion Database.* Kenneth W. Campbell and Yousef Bozorgnia. February 2010.

**PEER 2010/101** *Rocking Response of Bridges on Shallow Foundations.* Jose A. Ugalde, Bruce L. Kutter, and Boris Jeremic. April 2010.

**PEER 2009/109** *Simulation and Performance-Based Earthquake Engineering Assessment of Self-Centering Post-Tensioned Concrete Bridge Systems.* Won K. Lee and Sarah L. Billington. December 2009.

**PEER 2009/108** *PEER Lifelines Geotechnical Virtual Data Center.* J. Carl Stepp, Daniel J. Ponti, Loren L. Turner, Jennifer N. Swift, Sean Devlin, Yang Zhu, Jean Benoit, and John Bobbitt. September 2009.

**PEER 2009/107** *Experimental and Computational Evaluation of Current and Innovative In-Span Hinge Details in Reinforced Concrete Box-Girder Bridges: Part 2: Post-Test Analysis and Design Recommendations.* Matias A. Hube and Khalid M. Mosalam. December 2009.

**PEER 2009/106** *Shear Strength Models of Exterior Beam-Column Joints without Transverse Reinforcement.* Sangjoon Park and Khalid M. Mosalam. November 2009.

**PEER 2009/105** *Reduced Uncertainty of Ground Motion Prediction Equations through Bayesian Variance Analysis.* Robb Eric S. Moss. November 2009.

**PEER 2009/104** *Advanced Implementation of Hybrid Simulation.* Andreas H. Schellenberg, Stephen A. Mahin, Gregory L. Fenves. November 2009.

**PEER 2009/103** *Performance Evaluation of Innovative Steel Braced Frames.* T. Y. Yang, Jack P. Moehle, and Božidar Stojadinovic. August 2009.

**PEER 2009/102** *Reinvestigation of Liquefaction and Nonliquefaction Case Histories from the 1976 Tangshan Earthquake.* Robb Eric Moss, Robert E. Kayen, Liyuan Tong, Songyu Liu, Guojun Cai, and Jiaer Wu. August 2009.

**PEER 2009/101** *Report of the First Joint Planning Meeting for the Second Phase of NEES/E-Defense Collaborative Research on Earthquake Engineering.* Stephen A. Mahin et al. July 2009.

**PEER 2008/104** *Experimental and Analytical Study of the Seismic Performance of Retaining Structures.* Linda Al Atik and Nicholas Sitar. January 2009.

**PEER 2008/103** *Experimental and Computational Evaluation of Current and Innovative In-Span Hinge Details in Reinforced Concrete Box-Girder Bridges. Part 1: Experimental Findings and Pre-Test Analysis.* Matias A. Hube and Khalid M. Mosalam. January 2009.

**PEER 2008/102** *Modeling of Unreinforced Masonry Infill Walls Considering In-Plane and Out-of-Plane Interaction.* Stephen Kadysiewski and Khalid M. Mosalam. January 2009.

**PEER 2008/101** *Seismic Performance Objectives for Tall Buildings.* William T. Holmes, Charles Kircher, William Petak, and Nabih Youssef. August 2008.

**PEER 2007/101** *Generalized Hybrid Simulation Framework for Structural Systems Subjected to Seismic Loading.* Tarek Elkhoraibi and Khalid M. Mosalam. July 2007.

**PEER 2007/100** *Seismic Evaluation of Reinforced Concrete Buildings Including Effects of Masonry Infill Walls.* Alidad Hashemi and Khalid M. Mosalam. July 2007.

The Pacific Earthquake Engineering Research Center (PEER) is a multi-institutional research and education center with headquarters at the University of California, Berkeley. Investigators from over 20 universities, several consulting companies, and researchers at various state and federal government agencies contribute to research programs focused on performance-based earthquake engineering.

These research programs aim to identify and reduce the risks from major earthquakes to life safety and to the economy by including research in a wide variety of disciplines including structural and geotechnical engineering, geology/seismology, lifelines, transportation, architecture, economics, risk management, and public policy.

PEER is supported by federal, state, local, and regional agencies, together with industry partners.

PEER Core Institutions:
University of California, Berkeley (Lead Institution)
California Institute of Technology
Oregon State University
Stanford University
University of California, Davis
University of California, Irvine
University of California, Los Angeles
University of California, San Diego
University of Southern California
University of Washington

PEER reports can be ordered at http://peer.berkeley.edu/publications/peer_reports.html or by contacting

Pacific Earthquake Engineering Research Center
University of California, Berkeley
325 Davis Hall, mail code 1792
Berkeley, CA 94720-1792
Tel: 510-642-3437
Fax: 510-642-1655
Email: peer_editor@berkeley.edu

ISSN 1547-0587X